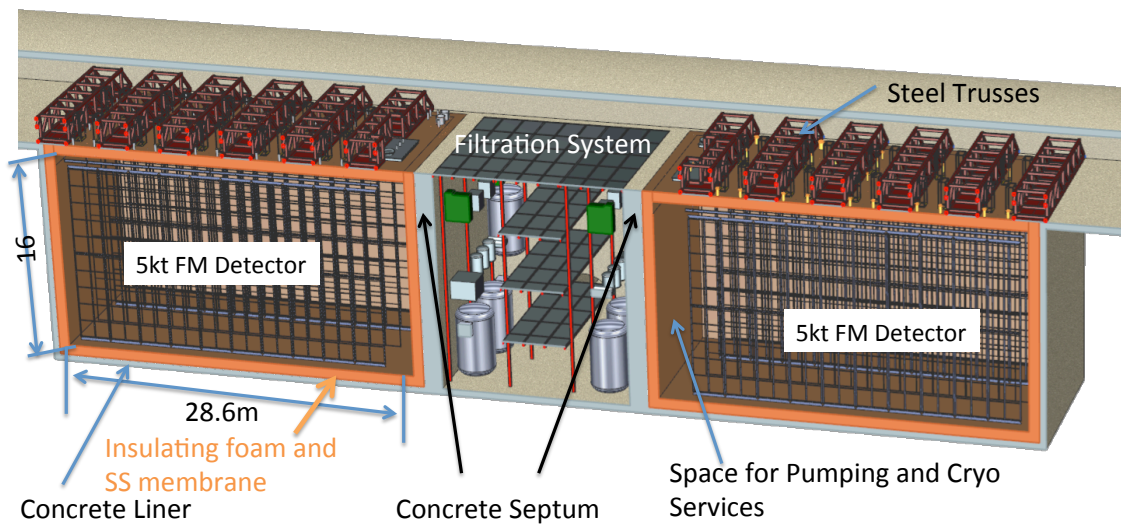


1 Annex 4A: The LBNE Design for a Deep  
2 Underground Single-Phase Liquid Argon  
3 TPC

4 Annex to the  
5 LBNF/DUNE Conceptual Design Report



6

7

April 30, 2015





# Contents

2	<b>1 Introduction</b>	<b>1</b>
3	1.1 Overview . . . . .	1
4	1.2 LAr-FD Components and Activities . . . . .	3
5	1.2.1 Time Projection Chamber . . . . .	3
6	1.2.2 Electronics, Readout and Data Acquisition . . . . .	5
7	1.2.3 Photon-Detection System . . . . .	7
8	1.2.4 Detector Installation and Operation . . . . .	8
9	1.3 Far Detector Requirements . . . . .	8
10	1.3.1 Detector Requirements: Beam Neutrino Physics . . . . .	9
11	1.3.2 Detector Requirements: Supernova Burst Neutrino Physics . . . . .	10
12	1.3.3 Detector Requirements: Atmospheric Neutrino Physics . . . . .	11
13	1.3.4 Detector Requirements: Nucleon Decay Physics . . . . .	11
14	1.3.5 Derived Detector Performance Requirements . . . . .	11
15	1.3.6 Engineering Requirements . . . . .	12
16	1.4 Principal Parameters . . . . .	13
17	1.5 Design Considerations . . . . .	13
18	<b>2 Time Projection Chamber</b>	<b>18</b>
19	2.1 Introduction . . . . .	18
20	2.2 Design Considerations . . . . .	22
21	2.3 Anode Plane Assemblies . . . . .	23
22	2.3.1 Wires . . . . .	23
23	2.3.2 Wire Planes . . . . .	24
24	2.3.3 APA Frame . . . . .	28
25	2.3.4 Wire Wrapping Around an APA . . . . .	29
26	2.3.5 Wire Supports on Inner Frame Members . . . . .	30
27	2.3.6 Wire-Winding Machines . . . . .	31
28	2.4 Cathode Plane Assemblies . . . . .	35

1	2.5	Field Cage . . . . .	37
2	2.6	High-Voltage Components . . . . .	38
3	2.7	TPC Assembly in the Cryostat . . . . .	40
4	2.8	TPC Prototyping, Test and Checkout . . . . .	40
5	2.8.1	TPC Prototyping . . . . .	40
6	2.8.2	Assembly Testing . . . . .	44
7	2.8.3	Checkout . . . . .	45
8	<b>3</b>	<b>Cold Electronics</b>	<b>46</b>
9	3.1	Introduction . . . . .	46
10	3.2	Design Considerations . . . . .	48
11	3.3	Architecture . . . . .	49
12	3.4	CMOS Circuit Design . . . . .	52
13	3.4.1	Cold Analog ASICs . . . . .	55
14	3.4.2	Cold Digital Data ASICs . . . . .	60
15	3.5	Signal Feedthroughs, Cabling, and Power . . . . .	61
16	3.5.1	Signal Feedthroughs . . . . .	62
17	3.5.2	Cabling for the Cold Electronics . . . . .	63
18	3.5.3	Power for the Cold Electronics . . . . .	65
19	3.5.4	Wire-Bias Voltages . . . . .	66
20	3.6	CE Installation . . . . .	66
21	3.6.1	Prototype Testing . . . . .	66
22	3.6.2	Assembly Testing . . . . .	67
23	3.6.3	Commissioning . . . . .	68
24	<b>4</b>	<b>Data Acquisition</b>	<b>69</b>
25	4.1	Introduction . . . . .	70
26	4.1.1	System overview . . . . .	70
27	4.1.2	Physics Considerations . . . . .	73
28	4.1.3	Event Rates and Timing . . . . .	74
29	4.1.4	Architecture Summary . . . . .	76
30	4.2	TPC Readout . . . . .	76
31	4.3	Photon Detector Readout . . . . .	78
32	4.4	Timing System . . . . .	79
33	4.4.1	Beam Triggers and Time Stamps . . . . .	80
34	4.4.2	Front-End Clocks . . . . .	80
35	4.4.3	Time stamping and synchronization . . . . .	81
36	4.4.4	Dynamic Synchronization and Executes . . . . .	82

1	4.5	Readout of Auxiliary Signals . . . . .	82
2	4.6	Event Building and Triggering . . . . .	82
3	4.6.1	artDAQ . . . . .	83
4	4.7	Run Control . . . . .	85
5	4.7.1	Control and Monitoring of LBNE Components . . . . .	85
6	4.7.2	Display of Component Monitoring and Alerts . . . . .	85
7	4.7.3	Management of Per-Run Information . . . . .	87
8	4.7.4	Run-Control Technology . . . . .	87
9	4.8	Online Monitoring . . . . .	87
10	4.9	Slow Control Systems . . . . .	88
11	4.9.1	Monitoring . . . . .	88
12	4.9.2	Slow Control . . . . .	88
13	4.10	Interface between DAQ and Offline Computing . . . . .	89
14	4.11	DAQ Infrastructure . . . . .	90
15	4.11.1	Wide Area Network . . . . .	90
16	4.11.2	Online Data Storage . . . . .	90
17	4.11.3	Power and Cooling . . . . .	90
18	4.12	Modular DAQ Design . . . . .	90
19	<b>5</b>	<b>Photon Detector</b>	<b>93</b>
20	5.1	Introduction . . . . .	93
21	5.2	Requirements and Goals . . . . .	93
22	5.2.1	Beam-based physics . . . . .	93
23	5.2.2	Proton Decay and Atmospheric Physics . . . . .	94
24	5.2.3	Low-energy Physics . . . . .	94
25	5.2.4	Required Performance . . . . .	94
26	5.2.5	General Considerations . . . . .	96
27	5.3	Photon Detector Prototype Designs . . . . .	96
28	5.3.1	Cast or Bulk Doped Acrylic Bars . . . . .	97
29	5.3.2	Fiber-embedded Bulk Acrylic Plate . . . . .	99
30	5.3.3	Bulk panel production . . . . .	99
31	5.3.4	Prototype Detector Test Results . . . . .	101
32	5.3.5	R&D Work in Progress and Present Plans . . . . .	102
33	5.3.6	Fiber Bundle with WS-coated Radiator . . . . .	104
34	5.3.7	Technology Selection . . . . .	106
35	5.4	Silicon Photomultipliers . . . . .	106
36	5.4.1	Requirements . . . . .	109
37	5.4.2	Test Results . . . . .	109

1	5.5	Mechanical Support . . . . .	113
2	5.6	Photon System Readout Electronics . . . . .	119
3	5.6.1	Reference Design . . . . .	119
4	5.6.2	Alternatives . . . . .	124
5	5.7	Photon Detector Calibration . . . . .	126
6	5.8	Installation . . . . .	131
7	<b>6</b>	<b>Installation and Commissioning</b>	<b>134</b>
8	6.1	Introduction . . . . .	134
9	6.2	Integration - Permanent Equipment . . . . .	136
10	6.2.1	Relay Racks and cable management . . . . .	136
11	6.2.2	Detector Electrical Ground . . . . .	137
12	6.2.3	TPC support rails . . . . .	139
13	6.2.4	Discussion of ports in the top of the cryostat . . . . .	139
14	6.3	Installation Equipment - Temporary Equipment . . . . .	141
15	6.3.1	Clean Area Outside cryostat . . . . .	141
16	6.3.2	Inside cryostat . . . . .	143
17	6.3.3	Full-scale Mockup . . . . .	144
18	6.3.4	Surface at SURF . . . . .	146
19	6.4	Far Site Installation . . . . .	146
20	6.4.1	Far site activities overview . . . . .	146
21	6.4.2	Detector material storage /testing above ground . . . . .	150
22	6.4.3	Material movement to cavern . . . . .	152
23	6.4.4	TPC installation details . . . . .	152
24	6.5	Training . . . . .	156
25	6.6	Far Detector commissioning . . . . .	158
26	6.6.1	Argon receipt . . . . .	160
27	6.6.2	Testing . . . . .	160
28	6.6.3	ES&H . . . . .	161
29	<b>7</b>	<b>Detector Development Program</b>	<b>163</b>
30	7.1	Introduction . . . . .	163
31	7.2	Materials Test System . . . . .	164
32	7.3	TPC Design . . . . .	167
33	7.4	35-ton Prototype: Phase 1 . . . . .	168
34	7.4.1	Phase 1 Construction . . . . .	168
35	7.4.2	Phase 1 Cryogenics Instrumentation . . . . .	171
36	7.4.3	Phase 1 Operations . . . . .	171

1	Gas Phase . . . . .	172
2	Cooldown and LAr Fill . . . . .	172
3	LAr Purification . . . . .	175
4	7.4.4 Phase 1 Stability of Operation . . . . .	175
5	7.4.5 Phase 1 Conclusions . . . . .	179
6	7.5 35t Prototype Phase 2 . . . . .	179
7	7.5.1 35t Phase 2 TPC Design . . . . .	179
8	7.5.2 Phase 2 Simulation, Reconstruction and Analysis . . . . .	182
9	7.6 Prototype Detector at CERN to Test Physics Sensitivity . . . . .	183
10	7.7 Summary . . . . .	183



# List of Figures

2	1.1	Underground detector illustration . . . . .	2
3	1.2	Detector Overview Slide for January 2015 configuration . . . . .	4
4	1.3	Fiducial mass of 10-kton detector . . . . .	6
5	2.1	Cross section of the TPC inside the cryostat . . . . .	20
6	2.2	Illustration of the APA wire wrapping scheme . . . . .	21
7	2.3	Plot of electric potential distribution near the wire planes . . . . .	25
8	2.4	TPC APA wire wrapping illustration . . . . .	27
9	2.5	Conceptual design of a wire frame . . . . .	28
10	2.6	Conceptual design of a wire-bonding board for the x wires . . . . .	29
11	2.7	Design of a wire wrapping board for the U wires on a long edge of an APA . . . . .	31
12	2.8	Closeup view of a partially assembled corner of an APA . . . . .	32
13	2.9	Conceptual design of the wire support for the U, V & X wires . . . . .	33
14	2.10	Winding machine concepts . . . . .	34
15	2.11	Conceptual design of the cathode plane assembly . . . . .	36
16	2.12	35T field cage . . . . .	37
17	2.13	FCA with resistive coating . . . . .	39
18	2.14	Concept of new feedthrough . . . . .	39
19	2.15	A partial assembly of the TPC showing all major components . . . . .	41
20	2.16	APA prototype used to study the support structure and wire wrapping . . . . .	42
21	2.17	Trial assembly of the APAs, CPAs and field cage panels into the 35-t TPC . . . . .	43
22	3.1	The front end electronics as mounted on an APA . . . . .	47
23	3.2	The CE Architecture . . . . .	50
24	3.3	The Front End Mother Board (FEMB), as used in the early set of tests . . . . .	51
25	3.4	Lifetime at different temperatures vs $V_{DS}$ . . . . .	53
26	3.5	The layout of the 16-channel analog FE ASIC . . . . .	56
27	3.6	Measured pulse response with details . . . . .	57
28	3.7	Measured ENC vs filter time constant . . . . .	58

1	3.8	The layout of the 16-channel ADC ASIC . . . . .	59
2	3.9	Functional Block Diagram of the Cold Digital Data (COLDATA) ASIC .	61
3	3.10	Conceptual design of signal/power feedthrough . . . . .	63
4	3.11	The 35 Ton "Flange Board", without the Conflat flange . . . . .	64
5	4.1	DAQ subsystem block diagram . . . . .	72
6	4.2	The COB (left) and RTM (right) . . . . .	77
7	4.3	A front view of the ATCA crate with a COB in the top slot. . . . .	78
8	4.4	Run control system . . . . .	86
9	5.1	Probability of photon being detected in detectors when depositing energy	96
10	5.2	Schematic drawing of a light guide with its photosensors . . . . .	97
11	5.3	LSU photon-detection panel . . . . .	100
12	5.4	Light yield for the fiber LSU PD panels with alpha source in LAr . . . .	102
13	5.5	Summed charge plots of SiPMs in response to muon hodoscope trigger .	103
14	5.6	Fiber-bundle PD prototype (early one-sided version) . . . . .	105
15	5.7	SiPM signals as function of bias voltage in liquid nitrogen. . . . .	108
16	5.8	The schematics of the PCB board and the PCB as built . . . . .	110
17	5.9	Acrylic holder for SiPMs and assembly prior to lowering in the dewar . .	111
18	5.10	Gain test of SenSL C series SiPM in LN <sub>2</sub> and numbers of p.e.'s . . . . .	112
19	5.11	SiPM SenSL C series dark rate, two data runs in LN <sub>2</sub> . . . . .	112
20	5.12	SenSL C series SiPM afterpulsing fraction comparison, with system cooled	113
21	5.13	SenSL C series SiPM cross-talk measurement based on two runs in LN <sub>2</sub> .	114
22	5.14	Full APA frame with ten photon detectors mounted inside the frame . . .	115
23	5.15	Photograph of 40 cm long bar-based prototype mounted in test frame . .	116
24	5.16	Mechanical assembly drawing of frame system . . . . .	117
25	5.17	Blow up of APA fram showing PD insertion location . . . . .	118
26	5.18	Slot and rail showing mounting location of photon detector . . . . .	118
27	5.19	Picture of the SSP module . . . . .	122
28	5.20	Block diagram the SSP module . . . . .	123
29	5.21	Concept of the UV-light calibration system . . . . .	128
30	5.22	Diagrams of diffusers, their locations and UV light transport . . . . .	128
31	5.23	Photon detector calibration module (PDCM) layout . . . . .	129
32	5.24	Simulated light distributions of the 35t APA, two cases . . . . .	130
33	5.25	Cable assembly for each photon detector readout channel. . . . .	132
34	5.26	Connection between the PD twisted-pair cable and SiPM mounting board.	133
35	5.27	Insertion of one PD paddle . . . . .	133
36	6.1	Support rails inside cryostat . . . . .	140



1	6.2	Feedthroughs . . . . .	142
2	6.3	Raised-panel floor to protect the cryostat's primary membrane . . . . .	145
3	6.4	Installation equipment mockup to be built and tested . . . . .	147
4	6.5	Underground clean area arrangement . . . . .	148
5	6.6	TPC panels installed in cryostats . . . . .	149
6	6.7	Concept for APA shipping containers . . . . .	151
7	6.8	Warehouse arrangement . . . . .	153
8	6.9	The three main work zones for TPC Installation . . . . .	157
9	6.10	Startup and Commissioning Sequence . . . . .	159
10	7.1	Liquid argon area at the Proton Assembly Building at Fermilab . . . . .	165
11	7.2	Schematic of the Materials Test System (MTS) cryostat at Fermilab . .	166
12	7.3	35t prototype at Fermilab's PC-4 facility, layout . . . . .	169
13	7.4	35t Cutaway view . . . . .	170
14	7.5	35t Gas Ar Purge and Recirculation . . . . .	173
15	7.6	35t Cooldown and Fill . . . . .	174
16	7.7	35t Vapor Flow . . . . .	176
17	7.8	35t Electron Lifetime . . . . .	177
18	7.9	35t Temperature Stability . . . . .	178
19	7.10	35t Vertical Temperature Profile . . . . .	180
20	7.11	35t with TPC . . . . .	181



# 1 List of Tables

2	1.1	LAr-FD Principal Parameters for 10-kt Detector . . . . .	13
3	4.1	Rates and data sizes/rates for various processes. . . . .	75
4	4.2	DAQ subsystem component counts . . . . .	76
5	5.1	Individual photon collection efficiencies . . . . .	95
6	5.2	Light guide technologies . . . . .	97
7	5.3	Physics requirements for the photon detector electronics . . . . .	119
8	7.1	35t Details and Dimensions . . . . .	170
9	7.2	35t Design Elements . . . . .	181



# <sup>1</sup> **Todo list**

- <sup>2</sup> add ref? CERN prototype proposal doesn't have one, as was suggested . . . . . 163

# Chapter 1

## Introduction

### 1.1 Overview

The former LBNE Far Detector Project team has prepared this design document which describes the single-phase liquid argon time projection chamber (LArTPC) that was being developed for the LBNE experiment. This report reflects the design status of January 2015, which marks the end of the LBNE collaboration and the start of the new DUNE collaboration. As the DUNE collaboration moves forward, it is anticipated that the collaboration will grow and the scope of the experiment will increase. The LBNE detector consisted of two detector modules each with a fiducial volume of 5 kt to be located at the 4850L of the Sanford Underground Research Facility (SURF). Figure 1.1 shows the 3D model of the detector. Throughout this document the detector is referred to as the LAr-FD.

The LAr-FD is proposed as the starting point for the design of the DUNE single-phase far detector. The full scope of the DUNE experiment consists of four 10-kt detector modules to reach the desired fiducial mass of 40 kt, which would enable a compelling research program in long-baseline and underground neutrino physics and in nucleon decay studies. The ultimate goal in the operation of the facility and experimental program is to measure fundamental physical parameters, explore physics beyond the Standard Model and better elucidate the nature of matter and antimatter.

The basic components of this detector type are a cryostat to contain the liquid argon (LAr), a Time Projection Chamber (TPC) detector mechanism immersed in the LAr to detect charge deposited in the detector, a photon system to register light, a readout electronics system and a cryogenic system to keep the LAr temperature at 89 K and maintain the required purity. The cryostat and cryogenics systems will

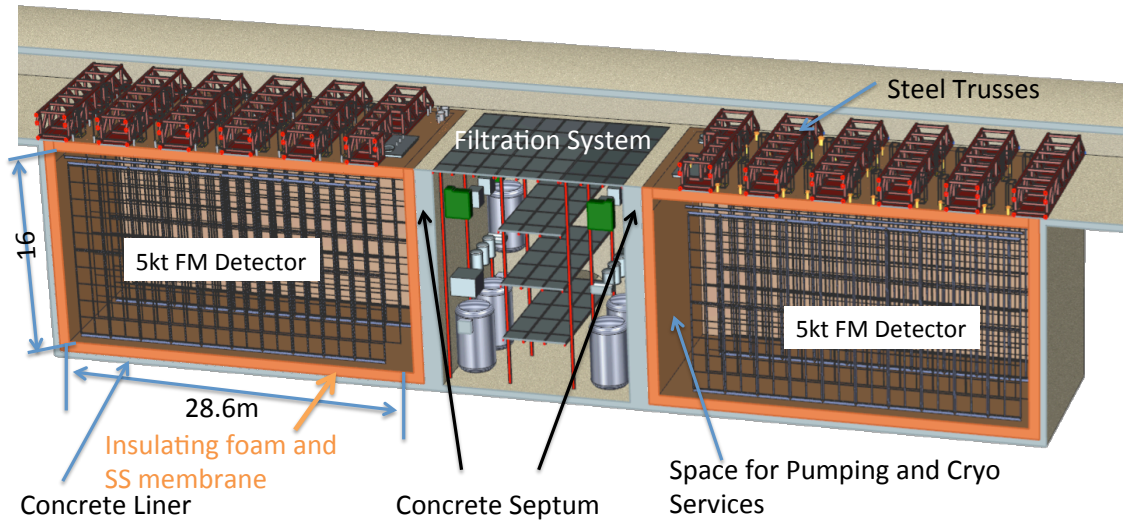


Figure 1.1: The LBNE underground liquid argon detector design as of January of 2015. The design consisted of two liquid argon detector module each with 5 kt fiducial volume.

fig:2x5kt-3d

1 be managed by the LBNF project, therefore descriptions of these systems are not  
2 included in this document.

3 In a single-phase LArTPC, a uniform electric field is created within the TPC  
4 volume between cathode planes and anode wire planes. Charged particles passing  
5 through the TPC interact with the argon and generate both VUV photon and ion-  
6 ization electrons. The electrons drift in the applied electric field to the anode planes.  
7 The anode planes consist of (listed in order from the outside in) four wire planes,  
8 a grid plane, two stereo induction planes and a collection plane. The bias voltage  
9 to each plane is set so that ionization electrons drift between the grid and the two  
10 induction planes, to be collected on the last plane. Readout electronics amplify and  
11 continuously digitize the induced waveforms on the sensing wires at 2 MHz, and  
12 transmit these data to the data acquisition (DAQ) system for processing. The wire  
13 planes are oriented at different angles allowing a 3D reconstruction of the particle tra-  
14 jectories. In addition to these basic components, a photon-detection system provides  
15 a trigger for proton decay and galactic supernova neutrino interactions.

16 The design of the LAr-FD has been developed and refined over the past five  
17 years. The starting point was the ICARUS T600 system [1], and the process was  
18 informed and guided by the experience with small LArTPCs in the U.S., particularly

ArgoNeuT [2] and MicroBooNE [3]. The LAr-FD concept is designed for assembly from small, independent units that can be repeated as many times as necessary in any dimension to form the entire assembly within a large cryostat. Each of the units provides an independent mechanical structure to support the elements it contains. The size of the units is defined by the restrictions placed by the local site and logistical issues. The detector units will be manufactured in advance of the detector installation, so they must be small enough to be shipped and stored using standard transport containers. They must physically fit in the shafts at SURF and be transported underground.

The modular design offers several advantages. The units can be thoroughly tested prior to installation, reducing installation time. Construction of the major components can be done at multiple sites. The design can accommodate a wide range of detector volumes, containing anywhere from a few to several hundred units in a straightforward way, with small and predictable risk. Scaling in other areas of LArTPC detector technology, namely cryostat construction, LAr purification and electronics readout has been incorporated into the design.

## 1.2 LAr-FD Components and Activities

### 1.2.1 Time Projection Chamber

The Time Projection Chamber (TPC) is the active detection element of the LAr-FD. The construction concept is shown schematically in the upper right illustration of Figure 1.2. A TPC is located inside each cryostat vessel and is completely submerged in LAr at 89 K. Five planes line up across the width: three Cathode Plane Assemblies (CPA) interleaved with two Anode Plane Assemblies (APA). These planes are oriented vertically and parallel to the beamline such that the electric fields applied between them are perpendicular to the beamline. Sufficient space is maintained between the detector and the cryostat walls to prevent high voltage discharge.

As seen on the left of Figure 1.2 the APAs are constructed as 2.3-m-wide, 6-m-tall units. Each APA has three wire planes that are connected to readout electronics; two induction planes (labeled “U” and “V” in Figure 1.2) and one collection plane (“X”). A fourth wire plane, grid plane (“G”), is held at a bias voltage but is not instrumented with readout electronics. The grid plane improves the signal-to-noise ratio on the U plane and provides electrostatic discharge protection for the readout electronics. The electronic readout is from a single end so that two units can be hung together with minimal gap between the top and bottom units. The APAs are mounted inside the cryostat on rails which run the length of the cryostat (Figure 1.2



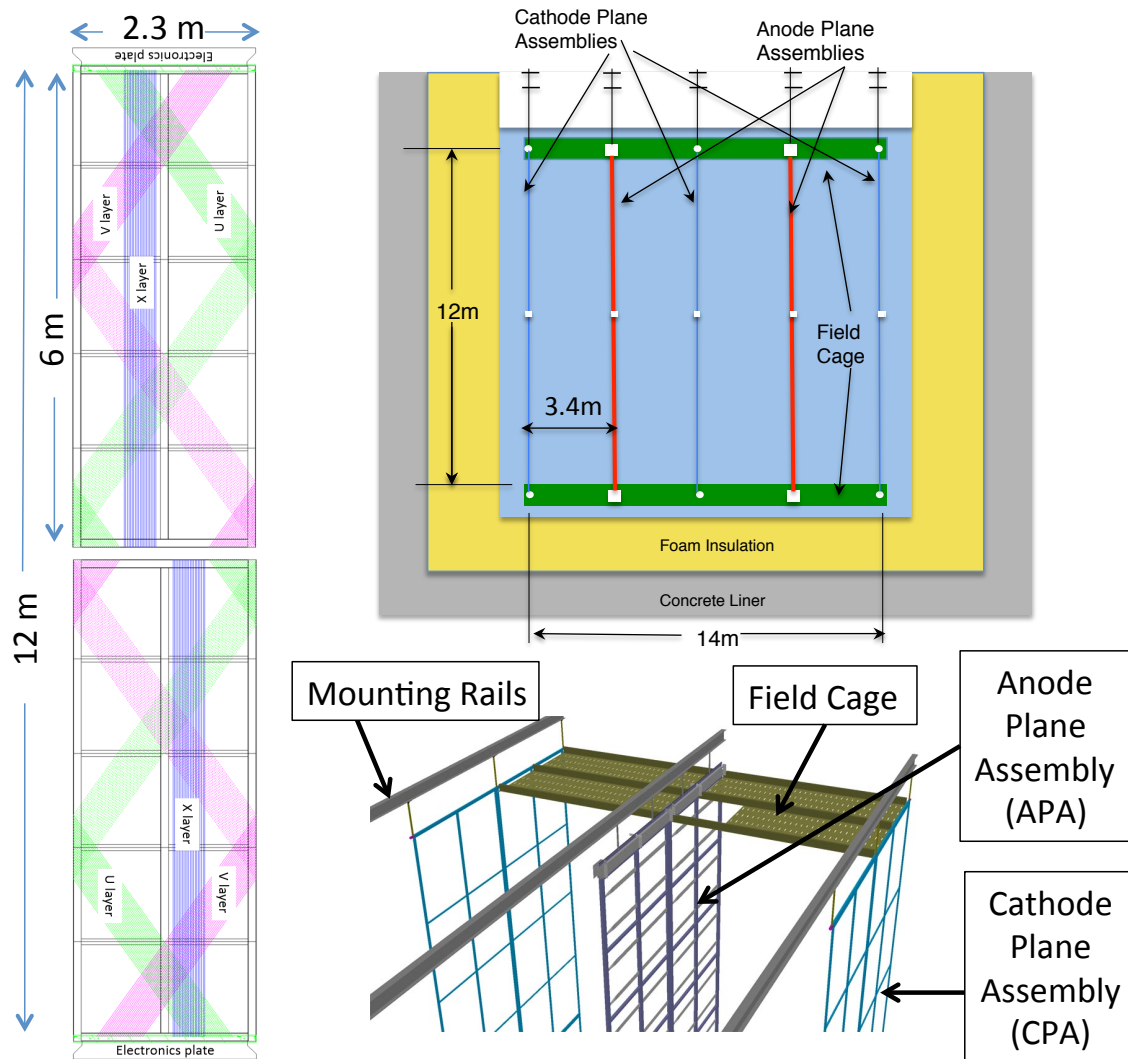


Figure 1.2: Left: Illustration of the APA design. 2.3-m by 6-m steel frames form the core of the APAs. Wires are wound about the planes to form the grid plane (not shown), the U and V induction planes and the collection plane. Electronic readout is mounted on one end. The lower APA plane is hung from the top plane to form a 12-m-tall unit. Upper-Right: Schematic showing the orientation of the TPC inside the Cryostat. Lower-Right: The APAs and CPAs are hung from the top of the cryostat using mounting rails. The rails also are used in the installation process to move the planes to the final position.

fig:single-pha

lower-right). Two rows of wire planes, each two APAs high and 13 deep, instrument each cryostat forming a 30-m-long detector. A total of 52 APA are needed for a 5-kt fiducial volume detector.

The CPAs are also manufactured in 2.3-m-wide stainless steel units and are hung from similar mounting rails as the APAs. Insulating G-10 rods connect the CPAs to the rails and provide the needed electrical isolation. Each cryostat needs 78 CPAs for the three rows. The maximum electron-drift distance between a CPA and an adjacent APA is 3.4 m. A “drift cell” is associated with the volume between any APA and CPA. As seen in Figure 1.2, each of the far detector modules has four drift cells each 3.5 m wide 12 m high and 30 m deep. A “field cage” surrounds the top and ends of the cryostat to ensure uniformity of the electric field. The field cage is assembled from panels of FR-4 sheets with parallel copper strips connected to resistive divider networks.

The size of a liquid argon detector is normally quoted in terms of its mass. However, several metrics are used and need to be clearly defined if comparisons are to be made. The total liquid volume and mass of a detector module are defined by the total amount of liquid argon contained, 9.2 kt per cryostat in this case. Space inside the cryostat is needed for the membrane convolutions, cryogenic services, installation, the volume of the APAs themselves, and an insulation region for HV protection, which is 0.5 m for the LAr-FD. These volumes reduce the total instrumented volume for each cryostat to 6.9 kt. Finally, in any physics analysis fiducial volume cuts will need to be applied to the data. The cuts will depend on the physics process itself but for the purpose of defining the detector size, the cuts for the oscillation physics are used. These cuts lead to a total fiducial mass of two 5-kt detector modules, as shown in Figure 1.3. A cut of 10 cm on the upstream end of the detector is applied to ensure that a given event originated inside the detector and not from a muon generated in the rock. A cut of 140 cm downstream of the detector is applied so that muon momentum can be determined by multiple scattering. Finally, a cut of 30 cm on each side of the APAs is applied to ensure that a neutrino interacting in the fiducial volume will be sufficiently contained to have a good energy measurement.

## 1.2.2 Electronics, Readout and Data Acquisition

CMOS technology, with a noise minimum at 89 K, permits the front-end electronics to reside in the LAr (henceforth “cold electronics”), as close to the anode wires as is practical. This minimizes capacitance and therefore signal noise, and benefits LAr purity by not residing in the ullage gas. The cold electronics architecture is composed of a front-end shaping/filtering stage (FE ASIC), an analog-to-digital

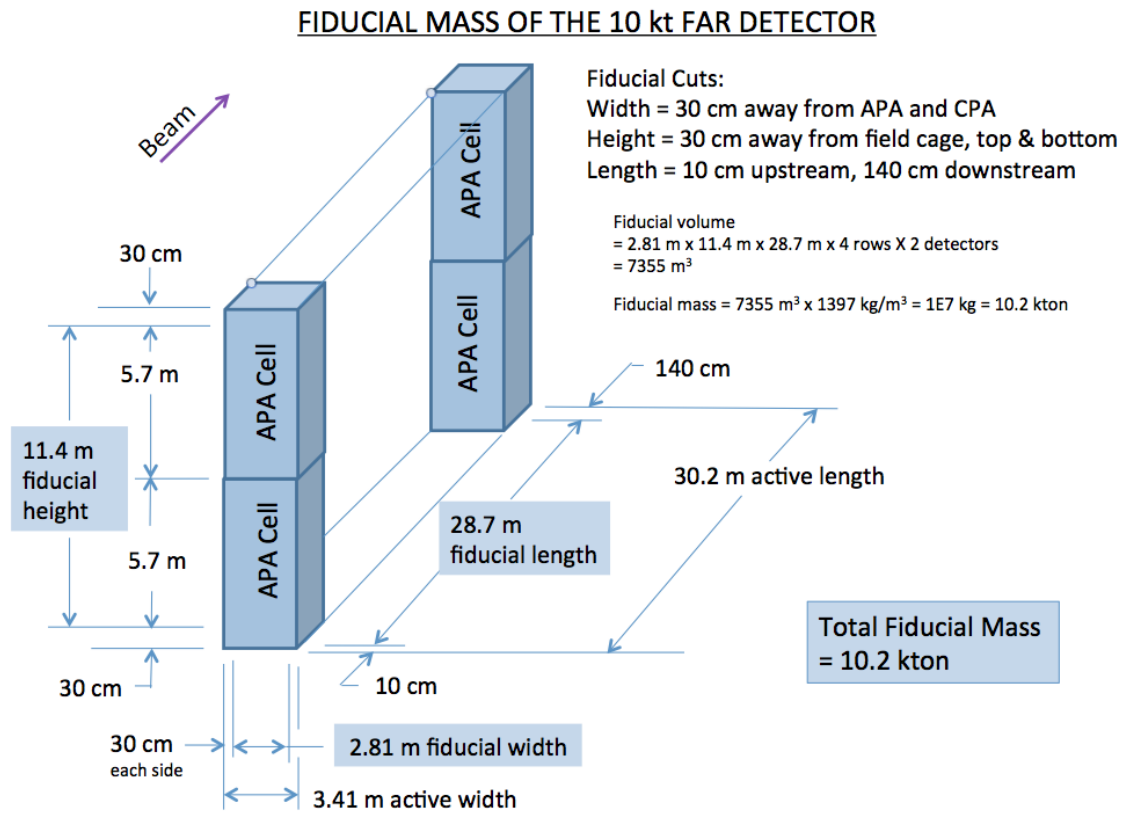


Figure 1.3: Fiducial mass of 10-kton detector

fig:10kt-fiduc

conversion stage (ADC ASIC), and a communication/control stage (digital ASIC). The signal feedthroughs are all located on top of the cryostat, where they are most accessible, are at low hydrostatic pressure, and pose no risk of LAr leakage. The cold electronics multiplex at 1:32, which lowers the cable count to what can be accommodated by the planned number of feedthroughs, and mitigates contamination from cable outgassing by reducing the volume of cables in the ullage gas.

The data acquisition system (DAQ) handles the signals from the LArTPC and photon detection once they are outside the cryostat and packages the data into events within runs for offline analysis. The logic runs in FPGAs extensively use the Ethernet protocol, which feeds data to commodity computers and network switches for event building and triggering. This uses a modern software framework that capitalizes on scalable parallelization with multicore machines. The primary data transfer path in the DAQ reads out interactions from neutrinos (beam and atmospheric), proton decay and other underground physics phenomena and cosmic-ray muons with no zero suppression — these events occur rarely (the most frequent are the cosmic muons at a rate of about one per minute). A separate data-transfer path works with zero-suppressed data to provide both the triggering for the above events and a continuous readout of all data, which can be filtered for study of low-energy physics phenomena. These two readout paths are used in combination for supernova events to maximize the information collected, which is dependant on the space available for buffering. The DAQ is partitioned into sections that are more independent than in most HEP experiments; this is done to practically eliminate periods of downtime of more than one section of the detector at a time, which is important for supernova detection.

### 1.2.3 Photon-Detection System

Identification of the different possible charged-particle types depends on accurate measurements of ionization along tracks. This requires accurate determination of the time of interaction, or event time,  $t_0$ , which leads to the absolute location of the event along the drift axis, and allows the determination of  $Q_0$ , the true ionization charge.

For non-accelerator physics events,  $t_0$  is not known a priori. However, LAr is an excellent scintillator, generating of order  $10^4$  128-nm photons per MeV of deposited energy. Detection of scintillation photons provides a prompt signal that allows unambiguous location of particle positions along the drift axis.

The reference design for the photon detection system is based on acrylic bars, which are either coated in TPB or doped in bulk. The 128-nm photons interact with the TPB on the surface and 430-nm light is re-emitted. The signals will be routed

1 out of the cryostat to standard readout electronics.

2 Twenty light-guide and SiPM assemblies, or “paddles”, will be installed within  
 3 each APA frame prior to wire winding. The SiPM signals will be used as a software  
 4 “trigger” in the DAQ to define the event time,  $t_0$ , for non-accelerator events. This  
 5 system provides a  $t_0$  signal throughout the entire detector in contrast to a system  
 6 similar to that used in MicroBooNE and ICARUS, where light is detected outside  
 7 the detector volume.

## 8 1.2.4 Detector Installation and Operation

9 Detector components will be shipped in sealed containers to the far site by truck  
 10 and lowered to the cavern. Shipping containers will be moved to a clean area over  
 11 the septum between the cryostats. There the components will be unpacked from the  
 12 sealed container and lowered through an access hatch into the cryostat.

13 The construction of the two cryostats and the installation and commissioning  
 14 activities will be staged such that both TPCs can be tested cold while one cryostat  
 15 still remains available as a potential LAr storage vessel. The LAr in one cryostat can  
 16 be transferred to the other, and back again, if necessary, until all the tests complete  
 17 successfully. Once both TPCs are known to work properly at LAr temperature, the  
 18 second fill will take place.

19 To protect the membrane on the floor of the cryostat during TPC installation,  
 20 a temporary floor will be installed. After each pair of APAs is installed, they will  
 21 be connected to the DAQ system and the wire integrity will be tested. All wires on  
 22 previously installed APA pairs will also be tested. The wire integrity test will be  
 23 performed during cryostat cool-down as well. A relatively slow cool-down rate will  
 24 ensure that the temperature-induced stresses in the APA frames and wires are kept  
 25 well below the level experienced during testing.

26 An installation and integration detector mock-up will be constructed at Fermilab  
 27 to confirm that interfaces between detector systems are well defined and to refine  
 28 the installation procedures.

## 29 1.3 Far Detector Requirements

30 The requirements for the far detector TPC can be found in the requirements docu-  
 31 mentation [4] and are summarized in the following sections. A particularly important  
 32 requirement for physics studies involving SNB, nucleon decay, atmospheric neutri-  
 33 nos and beam neutrinos is reduction of cosmogenic backgrounds. To meet this, the  
 34 detector is to be situated at the 4850 ft level of the SURF facility.

### 1.3.1 Detector Requirements: Beam Neutrino Physics

In order to be sensitive to the mass hierarchy, the baseline of the experiment is required to be in excess of 1000 km [5, 6]. To optimize the simultaneous constraint on the mass hierarchy and the ability to measure  $\delta_{CP}$ , a baseline of 1300 km is needed.

The sensitivity of the experiment scales with the product of the fiducial mass, the event-detection efficiency, and the efficiency of the event selection requirements. The fiducial volume cuts are set so that events with primary vertices within the fiducial volume are detected with high efficiency and are contained well enough to contribute to the oscillation analysis. The fiducial volume definition is shown in Figure 1.3. The volume inside the wire planes is to be defined as non-fiducial. The event timing for beam-induced neutrino scatters shall be precise enough to correlate the events with the beam spill times.

Events will be selected and classified in order to reduce the backgrounds of the analyses and to focus attention on only those events with well-modeled efficiency; thus the efficiency for selecting an analysis-quality event is not expected to be 100%. The event-selection efficiency for  $\nu_e$  CC interactions shall be at least 80% after selection requirements for incident neutrinos with energies above 100 MeV. For  $\nu_\mu$  CC interactions, the selection efficiency shall be at least 85% for the same range of neutrino energies. For neutral current events, a selection efficiency of 90% is required.

The determination of the physics outputs requires a very small systematic uncertainty on the event detection and selection efficiency, as much of the information is carried by the rates of  $\nu_e$  and  $\bar{\nu}_e$  appearance events and their ratios to the  $\nu_\mu$  and  $\bar{\nu}_\mu$  samples. The total uncertainty on the signal yields is required to be less than 1% from far-detector-related uncertainties. For all of these efficiencies, fractional systematic uncertainties of less than 0.5% are required. These uncertainties will require the formation of control samples in the data, therefore events that are not selected as analysis quality still will need to be detected and counted as such. A neutrino interaction of any sort with its vertex in the fiducial volume, depositing above 50 MeV of ionization energy in the detector is required to be detected by charge signals on the wires in the TPC, even if they are not selected by the analysis cuts. The systematic uncertainty on the fiducial mass of the detector, the product of the fiducial volume and the density of the liquid argon, is required to be less than 0.5%. Because the fiducial volume cuts are applied to the primary vertex location, the resolution on the primary vertex is thus required to be better than 25 mm.

The background rates for  $\nu_e$ -CC and  $\nu_\mu$ -CC events are required to be no more than half of the relevant signal rates, and the relative systematic uncertainties on the predictions of the background rates are required to be no larger than 5%. The

misidentification rate of neutral-current neutrino scatters as  $\nu_e$ -CC events is required to be less than 1%. The misidentification rate of  $\nu_\mu$ -CC events as  $\nu_e$ -CC events is required to be less than 1%. For  $\nu_\mu$  disappearance studies, the misidentification rate of neutral-current neutrino scatters as  $\nu_\mu$ -CC events is required to be less than 1%.

As more data are collected, the shapes of the distributions of the reconstructed neutrino energies become increasingly important in reducing the uncertainties in the measured parameters. The event-by-event resolution on the reconstructed neutrino energy for  $\nu_e$ -CC events shall be no wider than  $15\%/\sqrt{E(\text{GeV})}$ , and for  $\nu_\mu$ -CC, no wider than  $20\%/\sqrt{E(\text{GeV})}$ . The resolution of the reconstructed neutrino energy in neutral-current interactions is required to be no wider than  $30\%/\sqrt{E(\text{GeV})}$  for neutrinos with energies between 200 MeV and 6 GeV. The energy resolution on stopping hadrons (protons and kaons) is required to be 1-3% based on the measured ionization and range.

The average neutrino energy-scale calibration is required to be better than 5% for both  $\nu_e$ -CC and  $\nu_\mu$ -CC events [7]. The calibration of the energy resolution function is required to be better than ??% for both electron and muon events (“needs study”).

### 1.3.2 Detector Requirements: Supernova Burst Neutrino Physics

In order to perform measurements of supernova-burst neutrinos, the detection efficiency (including hardware and analysis selection effects) for a single 5-MeV electron is required to be in excess of 90% averaged over the active volume of the detector, and that for the scintillation light flash from a 10-MeV electron to be in excess of 50% averaged over the active volume of the detector. The energy resolution of electron tracks in SNB neutrino events is required to be better than 15% in the range 5-100 MeV in order to study the properties of SNB neutrino spectra. The cosmic-ray and radiological background to low-energy  $\nu_e$ -CC events shall be low enough to measure a supernova burst within the Milky Way.

The far detector is required to be able to collect data continuously, in order to maximize the acceptance of atmospheric neutrino scatters, SNB events, and nucleon decays. The data-acquisition system is required to be able to buffer at least two minutes of continuous, untriggered data for long-term storage in order to preserve a detailed record of a supernova burst. These data are to be collected with minimal impact from zero suppression, either with a lower threshold, or a generous amount of samples in both time and space near triggered signals. The detector, data-acquisition system, and online processing shall be able to trigger a supernova-burst event and provide a prompt alert. The absolute time of arrival of SNB neutrino

events is required to be known to 0.1 ms. The relative time difference between any two SNB events is also required to be known to 0.1 ms. The angular resolution on supernova-burst neutrinos shall be sufficient to point them to a common location in the sky. Prompt de-excitation gammas produced in association with low-energy charged-current interactions shall be identified and separated from radiological backgrounds and electronics noise.

### 1.3.3 Detector Requirements: Atmospheric Neutrino Physics

The detection efficiency for neutrino interactions is required to be independent of energy, angle, and arrival time, for events with primary vertices within the fiducial volume. The cosmic-ray backgrounds for atmospheric neutrino physics shall be small enough so as not to impact the analysis's sensitivity significantly. The more stringent requirements on cosmic-ray backgrounds for proton decay will suffice for the atmospheric neutrino analyses, which are less sensitive to backgrounds.

### 1.3.4 Detector Requirements: Nucleon Decay Physics

The separation of charged kaons from protons, pions, and muons shall be unambiguous and accomplished via  $dE/dx$  vs. residual range measurements, as well as interactions at the ends of the tracks. The cosmic-ray background shall be low enough to achieve the proton decay science objective.

### 1.3.5 Derived Detector Performance Requirements

The detection efficiency for a minimum-ionizing particle (MIP) traveling close to the CPA is required to exceed 99%. The signal-to-noise ratio for a MIP traveling close to the CPA is thus required to be 9:1 or better, in all three detection planes, regardless of the orientation of the track.

The detector uptime shall be greater than 90% during beam running. At least part of the detector shall be operational at all times.

The uncertainty on the electron loss due to the finite electron lifetime shall be known to better than 1%. This requirement can be satisfied with a high electron lifetime, a stable electron lifetime, and regular monitoring with purity monitors and *in situ* measurements.

Electromagnetic showers shall be identified by their topology. The energy resolution on individual EM showers is required to be  $3\%/\sqrt{E(\text{GeV})}$ . The muon momentum resolution is required to be better than 5% for fully-contained muon tracks, and



1 better than 15% for partially-contained muon tracks.

2 The misidentification rate of photons from  $\pi^0$  as electrons is required to be less  
3 than 2% from measuring the  $dE/dx$  in the beginning of the electromagnetic shower,  
4 coupled with reconstructed event topological information, such as the identification  
5 of second electromagnetic showers and the displacement of the shower start from the  
6 primary vertex.

7 Single-track events shall be separated from multi-track events with a high effi-  
8 ciency. Protons, pions, and kaons recoiling from charged-current interactions with  
9 kinetic energies above 21 MeV [?] shall be counted and identified. This requirement is  
10 coupled to similar requirements on the near detector, where a closer match between  
11 identification efficiencies of each final state in the far and the near detector pro-  
12 vides better cancellation of systematic uncertainty. Energy deposits from neutrons  
13 originating in neutrino scatters shall be recorded.

14 The far detector shall communicate the data to the DUNE global DAQ, which  
15 shall record the data on long-term storage media easily accessible to the collaboration.

16 The detector shall retain its resolution on  $dE/dx$  up to  $15 \times \text{MIP}$ , in order to  
17 separate heavily-ionizing particles from one another, and to measure overlapping  
18 particles.

19 Reconstruction ambiguities arising from wrapped wires shall not degrade the  
20 pattern-recognition abilities of the far detector and its software such that the above  
21 requirements are not met. In order for each event to be reconstructible without  
22 ambiguity, each induction-plane wire may intersect any collection-plane wire at most  
23 once. More ambiguity may result in charge deposits reconstructed far away from their  
24 true locations, worsening the particle counting, energy, and particle identification  
25 performances.

26 Studies have shown that the separation of electrons from photons using the ioniza-  
27 tion density of the first portion of an electromagnetic shower depends most critically  
28 on the first 2.5 cm of the shower. That, and the need to identify low-energy electrons,  
29 protons, and pions gives a wire pitch requirement of no more than 5 mm.

30 The electric field shall be sufficiently uniform and the detector alignment suffi-  
31 ciently stable and well known in order for the muon momentum measurement from  
32 multiple scattering requirement to be met.

### 33 1.3.6 Engineering Requirements

34 In order to limit radiological contamination from dust in the detector, the far de-  
35 tector underground hall shall accommodate the construction of a class 100,000 clean  
36 room for detector construction. Concrete floors shall be sealed in clean room envi-

ronments and in the high bay of the cavern. Showers are to be provided for workers underground to remove dust and debris. A solid waste disposal station consisting of a pad large enough to accommodate two 4'×6' dumpsters shall be provided near the surface support buildings.

There shall be control rooms both on the surface and underground, with monitoring of detector parameters and data flow. Adequate electrical power, water, air, cryogenics support, and networking shall be provided via the shafts. In case one shaft becomes inoperable, the other shaft is required to provide egress, ingress, and sufficient services to ensure the safety of the staff and equipment. Sufficient airflow is required to reduce buildup of radioactive radon gas.

## 1.4 Principal Parameters

The principal parameters of the LAr-FD are given in Table 1.1.

Table 1.1: LAr-FD Principal Parameters for 10-kton Detector

Parameter	Value
Active (Fiducial) Mass	13.8 (10.2) kton
Number of Detector Modules (Cryostats)	2
Drift Cell Configuration within Module	2 wide × 2 high × 13 long
Drift Cell Dimensions	2 × 3.4 m wide (drift) × 6 m high × 2.3 m long
Detector Module Dimensions	14 m wide × 12 m high × 30 m long
Anode Wire Spacing	~4.8 mm
Wire Planes (Orientation from vertical)	Grid (0°), Induction 1 (36°), Induction 2 (-36°), Collection (0°)
Drift Electric Field	500 V/cm
Maximum Drift Time	2.1 ms

## 1.5 Design Considerations

TPCs operated to date have been constructed with an anode wire spacing in the range of 3 mm (ICARUS) to 4.8 mm (Fermilab cosmic-ray stand). The amount of ionization charge collected on the wires increases with larger wire spacing, resulting

in a better signal-to-noise ratio without serious consequences (the radiation length of LAr is  $\sim 30$  times larger than the typical wire spacing). The electron- $\pi^0$  separation efficiency of a TPC with 5-mm wire spacing is only a few percent lower than one with 3-mm wire spacing. It is also clear that a TPC with larger wire spacing requires fewer wires and readout channels, resulting in lower cost. As the wire spacing becomes larger, however, spatial resolution degrades in the plane parallel to the wires, while resolution remains good in the remaining axis pointing along the electric field as that axis is digitized in time samples. This difference in resolutions along the three axes, if too big, will lead to anisotropy in efficiencies, resolutions, and particle ID performance. The 5-mm wire spacing is expected to be adequate for discerning short stubs from supernova neutrino scattering electrons which should create signals in approximately ten adjacent wires for a 10-MeV electron. Counting short protons near the interaction vertex requires good resolution for short tracks. Furthermore, ambiguities in associating features between planes become easier to break when the spatial resolution is better.

If hits can be unambiguously reconstructed and associated between planes, then only two wire planes are required to reconstruct events in three dimensions. However, three wire planes are needed in order to break ambiguities and provide  $N + 1$  redundancy. In many events, one or more tracks will travel parallel or nearly parallel to the wires in one or more of the planes, reducing one plane's contribution to the spatial resolution. The other two planes' hits will be able to reconstruct these tracks in three dimensions. Furthermore, the wrapping of the induction-plane wires introduces a discrete ambiguity in interpreting the hits on these wires. Hits that arrive on different wires at similar times, because they come from portions of tracks and clusters that are similar distances from the anode plane, create ambiguity in the association of hits between planes. The wrapping allows for more combinations, as tracks and clusters from either side of the APA can contribute to the signals on any induction wire.

The collection-plane wires are oriented vertically ( $0^\circ$ ) in order to minimize both the wire length and the electronics noise, as well as to provide readout on the ends of the APA frames for each wire. These wires do not wrap around the APA frames and so they provide unambiguous two-dimensional information about the event. Calorimetry is most commonly performed using the collection-plane wires, therefore low noise is important, though induction-plane wires provide additional measurements of the same drifting charge [8, 9, 10].

A study of wire orientation [11] was performed that uses the sum of the numbers of wires a photon from  $\pi^0$  decay traverses in all three planes before it converts. This figure of merit is designed to optimize topological separation of neutral-current

events from charged-current electron neutrino scatters. In this study, the optimum orientation of the induction plane wires should be between  $\pm 40^\circ$  and  $\pm 60^\circ$  when the collection plane wires are at  $0^\circ$  for beam neutrino physics. The ideal orientation for the more isotropic low-energy events, e.g., supernova-neutrino interactions, is  $\pm 60^\circ$ . Selecting induction-plane wire angles in this range necessitates wrapping the wires around the sides of the APA frames so that readout electronics can be located on the top or bottom of the TPC. As a result, it is natural to arrange the APA's vertically in a two-high configuration.

Wrapping the induction-plane wires however creates pattern-recognition difficulties arising from the discrete ambiguity in determining which segment of the wire contributed any given signal. If the wires wrap around more than once, so that a particular induction-plane wire intersects a particular collection-plane wire more than once, then the ambiguity is unresolvable with two readout planes; a third one is then required, with a slightly different angle so as to create repeated solutions of three wires intersecting. Even with the proposed  $44.3^\circ$  and  $45.7^\circ$  solution of the initial (2012) design, however, ambiguities resurface when multiple hits arrive on different wires at similar times. Misassociating hits between views can result in displacement of the 3D reconstructed location of the charge deposit by the vertical distance required to wrap an induction-plane wire around once; this was approximately five meters in the 2012 design. Even with the most sophisticated reconstruction algorithms, it is expected that even a small fraction of misassigned hits will create difficulties in energy reconstruction, track identification and particle ID, which may be difficult to simulate to the accuracy required by the physics program.

In order to reduce the impact of hit-assignment ambiguity on reconstruction, an angle of  $\pm 35.71^\circ$  was chosen for the induction-plane wires [8, 9, 10]. The APA design with this angle improves on the CD-1 design in a number of ways. The length of the APA is shorter at 6 meters, allowing it to be stiffer using the same materials. The 2.3-meter APA width was chosen to facilitate construction and allow standard, over-the-road transport. The wire angle is such that no induction-plane wire intersects any given collection-plane wire more than once, significantly reducing the categories of events for which combinations of hits can be misassigned. The exact wire angle and APA dimensions were further constrained by the desire to have an integer multiple of 128 readout channels per APA so as to efficiently assign channels to front-end boards. In this design, the collection-plane wires are 6 m long and the induction-plane wires are 7.3 m long.

A drift field of 500 V/cm was chosen based on experience from similar detectors such as ICARUS, ArgoNeuT and the Fermilab cosmic-ray test stand. At this electric field,  $\sim 30\%$  of the ionization electrons produced by the passage of a minimum

ionizing particle (MIP) recombine and create scintillation light that provides a fast trigger. The remaining ionization electrons drift to the APA and produce wire-plane signals. The TPC could function at higher or lower drift fields but the relative yields of scintillation light and ionization electrons would change. The use of a higher drift field would require more care in the design of the high-voltage systems. The electron drift velocity is  $1.6 \text{ mm}/\mu\text{s}$  at  $500 \text{ V/cm}$ .

The 14 m width of the the detector can be divided into four drift cells with a maximum drift length of 3.41 m each. This drift cell length was chosen based on experience from other detectors, the required minimum signal-to-noise ratio and high-voltage considerations. The required minimum signal-to-noise ratio of 9:1 ensures that the tracking efficiency will be 100% throughout the entire drift cell. The TPC must be capable of detecting the smallest signal (1 MeV) produced in interactions that DUNE will study. This situation occurs when a MIP travels parallel to a wire plane and perpendicular to the orientation of the wires in the plane. A MIP loses 2.1 MeV of energy in each cm of travel, producing  $\sim 40,000$  ionization electrons along every 5 mm section of the track. About 28,000 electrons escape recombination and, ignoring the effects of LAr purity and diffusion, would all drift to one collection plane wire. The capacitance due to the maximum-length 7.3 m wire is 164 pF resulting in an equivalent noise charge (ENC) of 500 electrons in the CMOS amplifiers. The signal-to-noise ratio would therefore be 53:1 if all of the ionization electrons arrived at the wire. For a maximum drift distance of 3.41 m and a drift field of  $500 \text{ V/cm}$ , the required voltage on the cathode plane is 173 kV. This is within the range of commercially available high-voltage cables and within the range of current designs for cryogenic feedthroughs. Additional R&D would be needed for longer maximum drift lengths.

Ionization electrons will be lost due to impurities in the LAr. The fraction that survive passage to the anode planes is  $e^{t/\tau}$ , where  $t$  is the drift time and  $\tau$  is the drift-electron lifetime. The maximum drift time is the maximum drift length divided by  $1.6 \text{ mm}/\mu\text{s}$  which equals 2.3 ms for DUNE. The ICARUS detector has achieved a drift electron lifetime of 6 – 7 ms. The Materials Test System (described in Section 7.2) regularly achieves a drift-electron lifetime of 8 – 10 ms. The Fermilab Liquid Argon Purity Demonstrator achieved a lifetime of  $> 3 \text{ ms}$  during initial tests. Based on this experience, and by careful selection of materials in the ullage, a drift-electron lifetime at least as good as ICARUS is expected. The signal-to-noise ratio would be 36:1 for a drift electron lifetime of 6 ms. A minimum lifetime of 1.4 ms is required to meet the 9:1 signal-to-noise ratio requirement.

The cloud of drifting ionization electrons will spread out in space due to the effects of diffusion. The maximum transverse *RMS* width of the electron cloud is

- <sub>1</sub> 2.4 mm for the chosen drift distance and drift field. This is well matched to the
- <sub>2</sub> 5 mm wire spacing.

# Chapter 2

## Time Projection Chamber

ch:tpc

The scope of the Time Projection Chamber (TPC) subsystem includes the design, procurement, fabrication, testing, delivery and installation of the mechanical and high voltage components of the TPC:

- anode plane assemblies
- cathode plane assemblies
- field cage
- feedthroughs, filtering networks, cables and power supplies for the cathode high voltage system

This chapter describes the reference design for the TPC that meets the required performance for charge collection in the single-phase liquid argon far detector, LAr-FD, developed for the former LBNE experiment.

### 2.1 Introduction

The Time Projection Chamber (TPC) is the active detector element of LAr-FD. It is located inside the cryostat vessel and is completely submerged in liquid argon at 89 K. The TPC consists of alternating anode plane assemblies (APAs) and cathode plane assemblies (CPAs), with field-cage panels enclosing the four open sides between the anode and cathode planes. When proper bias voltages are applied to the APAs and CPAs, a uniform electric field is created in volume between the anode and cathode planes. A charged particle traversing this volume leaves a trail of ionization in the ultra-pure liquid argon. The electrons drift toward the anode wire planes,

inducing electric current signals in the front-end electronic circuits connected to the sensing wires. The current signal waveforms from all sensing wires are amplified and digitized by the front-end electronics, and transmitted to the data acquisition system (Chapter 4) outside of the cryostat [12].

The front-end mother boards and digital multiplexer boards from the Cold Electronics subsystem (Chapter 3) are directly mounted on the APAs as part of the APA assembly (shown in Figure 3.1). The Photon Detectors (Chapter 5) are also mounted inside the APAs' frame openings before the APAs are installed into the cryostat. The TPC subsystem also interfaces to the cryostat and cryogenics system [12] through the TPC mounting fixtures, and to the DAQ subsystem through the signal feedthroughs. The installation of the TPC inside the cryostat is the responsibility of the Installation subsystem (Chapter 6).

The TPC's active volume (Figure 2.1) is 12 m high, 14 m wide and 30 m long in the beam direction. Its three rows of CPA planes interleaved with two rows of APA planes<sup>1</sup> are oriented vertically, with the planes parallel to the beamline. The electric field is applied perpendicular to the planes. The maximum electron-drift distance between a cathode and an adjacent anode is 3.4 m. The anode plane assemblies are 2.3 m wide and 6 m high. Two 6-m modules stack vertically to instrument the 12-m active depth. In each row, 13 such stacks are placed edge-to-edge along the beam direction, forming the 30-m active length of the detector. Each CPA has the same width, but half the height ( $\sim 3$  m) as an APA, for ease of assembly and transportation. Four CPAs stack vertically to form the full 12-m active height. Each cryostat houses a total of 52 APAs and 156 CPAs. Each facing pair of cathode and anode rows is surrounded by a "field cage," assembled from panels of FR-4 sheets with parallel copper strips connected to resistive divider networks.

On each APA, four planes of wires cover each side of a frame (the "wire frame"); see Figure 2.2. The inner three planes of wires are oriented, in order from the inside out, vertically, and at  $\sim \pm 36^\circ$  to the vertical, respectively. Each wire is connected to a front-end readout channel. The wires on the outermost plane are oriented vertically, and are not connected to the readout electronics. At a nominal wire pitch (center-to-center separation) of 4.8 mm, the total number of readout channels in an APA is 2560, for a total of 133,120 in each cryostat.

As shown in Figure 2.2, the readout electronics reside only along one narrow edge of an APA. During installation, two APAs are interconnected on their non-readout ends, leaving the readout ends completely outside of the TPC's active volume. Cables from the bottom APAs can be routed either through the hollow vertical APA frames, or down along the floor and up along a side wall of the cryostat.

<sup>1</sup>Note that the APA and CPA positions are exchanged in the DUNE design.



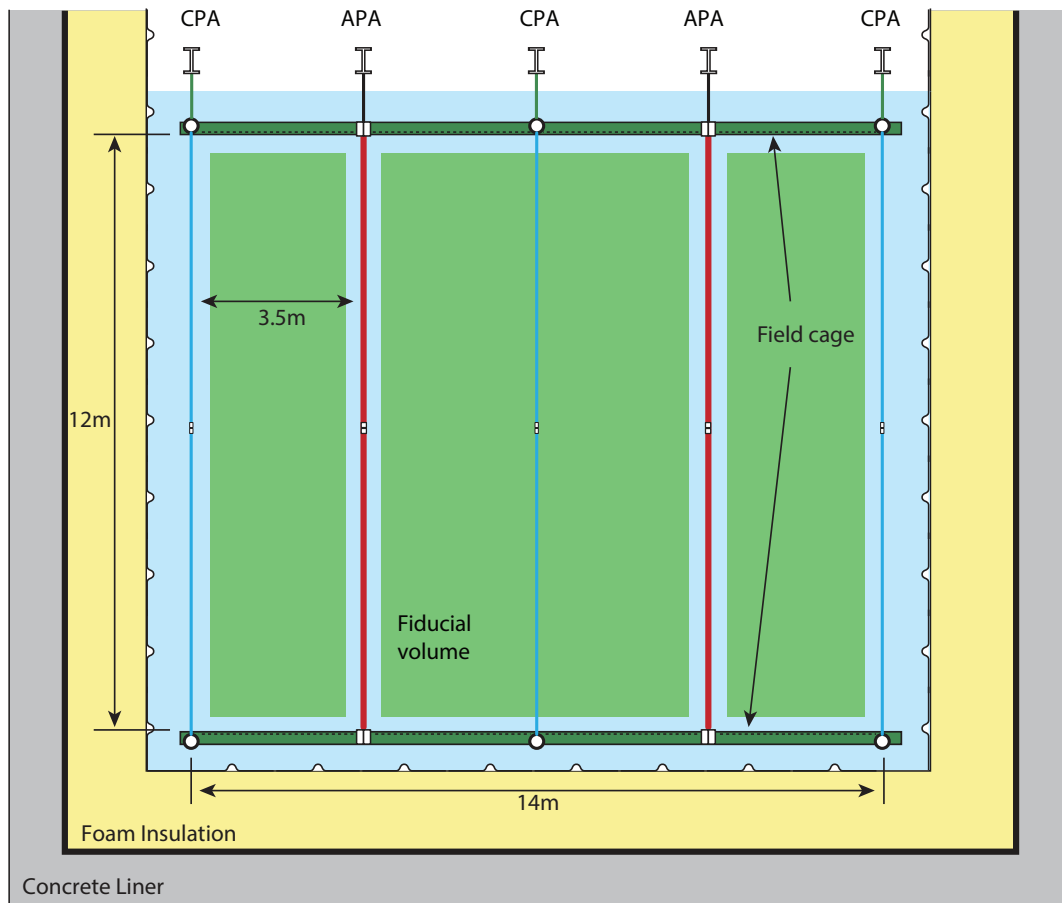


Figure 2.1: Cross section of the 5-kt fiducial mass LBNE TPC inside the cryostat. The length of the TPC is 30 m along the direction of the neutrino beam (into the paper)

fig:tpc-xsect1

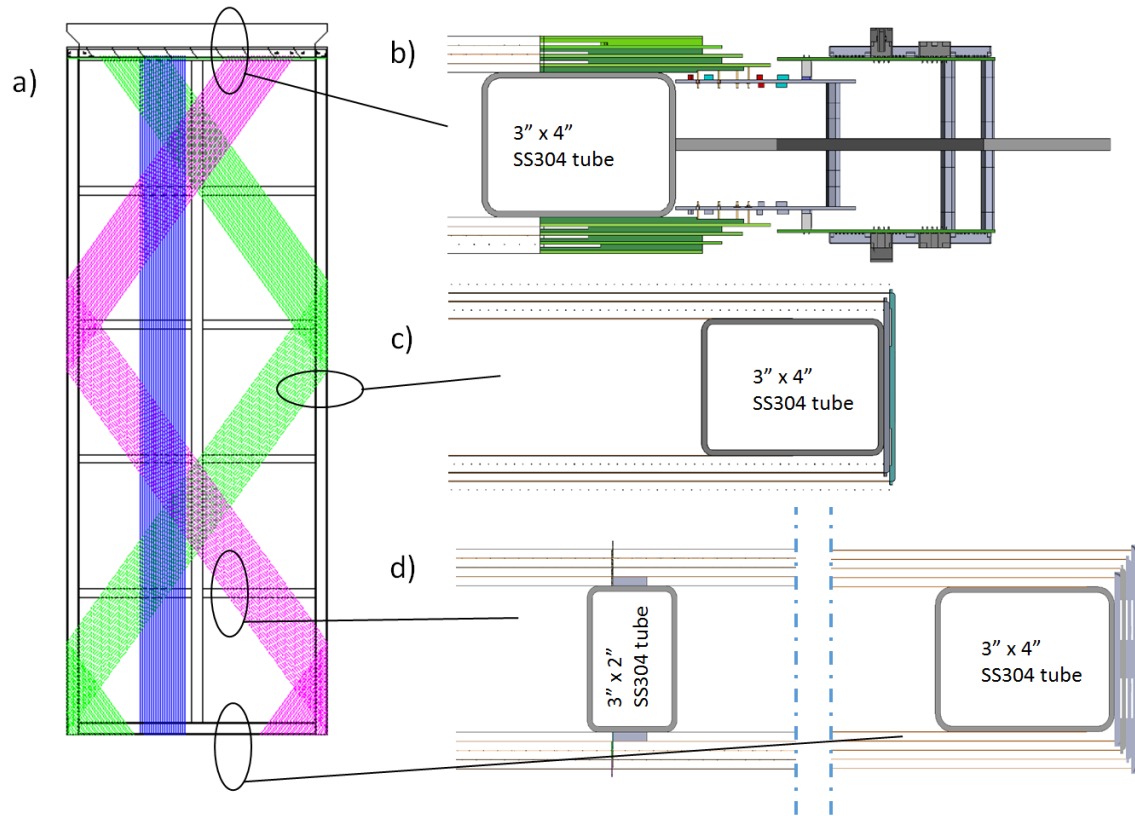


Figure 2.2: a) Illustration of the APA wire wrapping scheme. b) cross section of the 'readout end' of the APA. Front-end readout electronics boards are plugged in to the wire-bonding boards. c) cross section of a long edge of the APA where the two induction wire planes wrap around the edge boards. d) cross section view of an intermediate wire support structure, and the non-readout end of the APA.

fig:tpc-wire-f

## 2.2 Design Considerations

The requirements for the TPC can be found in the requirements documentation [4].

The most significant ones are the following. The TPC shall:

- Provide the means to detect charged particles in the detector and transmit the detector signals to the Data Acquisition System (DAQ)
- Meet the physics requirement for electron/photon discrimination; the TPC wire spacing will be  $< 5$  mm
- Limit variation in the wire sag to  $< 0.5$  mm such that it does not significantly impact the position and energy resolution of the detector
- Provide redundancy in the discrimination of electrons from photon conversions and ensure long-term reliability over the life of the experiment; the configuration will use three instrumented wire planes
- Optimize the measurement of high-energy and low-energy tracks from accelerator-neutrino interactions; the wire-plane orientation is optimized for neutrinos in the LBNE energy range
- Enable the detector to distinguish a Minimum Ionizing Particle (MIP) from noise with a signal-to-noise ratio  $> 9:1$
- Enable the detector to measure the ionization up to 15 times that of a MIP particle; this is necessary to perform particle identification of stopping kaons from proton decay
- Enable the in-vessel electronics to operate for the life of the facility
- Record the wire-signal waveforms continuously without dead time
- Use only materials that are compatible with high-purity liquid argon

The TPC is composed of several interconnected subsystems — APAs, CPAs, a Field Cage, and High Voltage Feedthroughs. A systems-engineering design and development approach will be taken to ensure that the various subsystems are properly integrated and the system is designed end-to-end to meet performance requirements. This approach will be led by a systems engineer who will ensure that interfaces are defined and managed, that requirements for each subsystem and the TPC as a whole

are defined and understood, that analyses are performed where needed, that prototyping is performed to retire or mitigate risk, and that test plans meet verification and validation requirements. The most significant challenge for the TPC is the LAr cryogenic environment. The TPC architecture will handle the cryogenic thermal cycles, accommodate the cryostat roof motion, and mitigate potential microphonics noise generated by wire vibrations.

The design approach will take inputs from several sources. These sources include requirements from the scientific collaboration to ensure integrity of the physics data, studies of what has been successful in smaller scale TPCs, sharing of knowledge, ideas, and concepts with others in the LArTPC community, and analysis and evaluation of the performance of the 35-t prototype (Sections 7.4 and 7.5). These inputs will be distilled into functional requirements. These functional requirements will be used to define alternative concepts or architectures for the TPC, which in turn will drive preliminary requirements for the TPC interface with the cryostat and the conventional facilities. They will also be used to define the preliminary interface requirements between the structural components and the modular subassemblies of the TPC. These alternate concepts will be tested and analyzed as needed, and reviewed with the physicists, conventional facilities engineers, the cryostat manufacturer and the TPC engineers. Based on analysis and feedback, the preferred concept will be further developed and detailed into final requirements and specifications for the physical internal and external interfaces. These requirements and specifications will be clearly communicated to the responsible engineering groups.

## 2.3 Anode Plane Assemblies

The APAs are 2.3 m wide, 6.3 m long, and 12 cm thick. The length is chosen for fabrication purposes and compatibility with underground transport limitations. The 2.3-m width is set to fit in a standard HiCube container for storage and transport with sufficient shock absorbers and clearances. Each APA is constructed from a framework of light-weight, stainless-steel rectangular tubing, with four layers of wires wrapped over both sides of the frame. The front-end electronics boards are mounted on one end of the wire frame and protected by a metal enclosure.

### 2.3.1 Wires

The wires used in the TPC must provide:

- High break load to withstand the applied tension

- Good conductivity to minimize noise contribution to the front-end electronics
- A thermal-expansion coefficient comparable to that of the stainless-steel frame to avoid tension change after cool-down

Both stainless-steel and copper-beryllium (CuBe) wires are potential candidates. Stainless steel was the choice of ICARUS [1], while a copper-plated stainless-steel wire was chosen by MicroBooNE [13] (to reduce resistance). Both experiments use a wire-termination technique that is labor-intensive and impractical for LAr-FD. Previous experience from FNAL [14] has shown that a CuBe wire under tension can be reliably bonded to a copper-clad G10/FR4 (glass epoxy material) surface by a combination of epoxy (mechanical bonding) and solder (electrical connection). This bonding technique greatly simplifies the electrical connection to the readout electronics and it can be easily automated with commercial equipment. Therefore CuBe wire is selected as the reference design wire of choice.

At 150  $\mu\text{m}$  diameter, the breaking tension of a hardened CuBe wire is  $\sim 30$  N. To ensure no wire breakage in the TPC, e.g. during cryostat cool-down, the nominal operating tension of the wire will be set at 5 N. Periodic support structures on the wire frame will limit the unsupported wire length to less than 1.5 m, resulting in less than 0.2 mm deflection due to gravitational or electrostatic forces. Wire ends will be glued and soldered (if electrical connection is needed) onto printed circuit boards attached to the wire frame.

### 2.3.2 Wire Planes

Four planes of wires are installed on each side of an APA as shown in Figure 2.2. A nominal wire pitch of 4.7 mm is selected to meet the position resolution and signal-to-noise ratio requirement. The distance between wire planes is set to 4.8 mm (3/16 in) to use standard printed circuit board thickness, while maintaining optimal signal formation. These four planes (along the direction of electron drift) are labeled as: the *grid plane* (G), the *first induction plane* (U), the *second induction plane* (V), and the *collection plane* (X). The wires on the grid and the collection planes are vertically oriented, while the two induction planes are oriented at  $\pm 35.71^\circ$  to the vertical. This wire layout is shown to be very good for reconstructing beam-neutrino events [11]. The wires on the grid plane are not connected to the readout electronics; they shield the first induction wire plane from being influenced by distant arriving ionizations. The four wire planes will be electrically biased so that electrons from an ionizing-particle track completely drift past the first three planes and are collected by the fourth plane. Calculations show that the minimum bias voltages needed to achieve

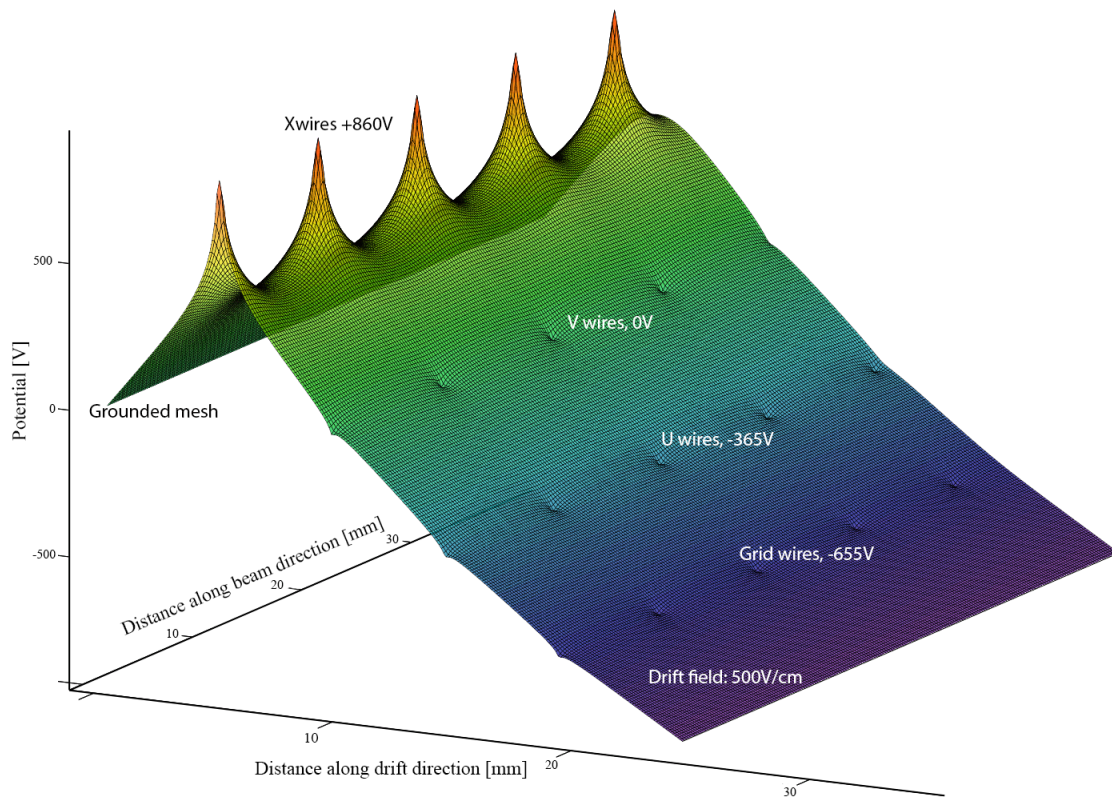


Figure 2.3: A surface plot of the electric potential distribution near the wire planes. The voltages on the wire planes are biased to provide complete electron transparency through the first three planes, and complete collection on the fourth plane.

fig:tpc-bias-v

1 this goal are  $V_G = -655\text{V}$ ,  $V_U = -365\text{V}$ ,  $V_V = 0\text{V}$  and  $V_X = 860\text{V}$  respectively.  
 2 A grounded mesh plane, located 4.8 mm behind the collection plane, prevents the  
 3 electric field around this set of wires from being distorted by the metal frame structure  
 4 and the wires on the opposite side of the frame. It also shields the sensing wires from  
 5 potential EM interferences from the silicon photomultipliers (SiPMs), discussed in  
 6 Chapter 5, mounted within the frame. The mesh should have a wire pitch less than  
 7 2 mm to ensure a uniform electric field and a high optical transparency. Figure 2.3  
 8 shows the electric potential distribution near the APA frame with the wire planes  
 9 biased with the appropriate voltages.

10 The V wire plane is directly connected to the front-end electronics, i.e.  $V_V = 0\text{V}$ ,  
 11 to simplify the coupling and reduce the maximum bias voltages on the other planes.  
 12 The wires on the two induction planes (U and V) are wrapped in a helical pattern  
 13 around the long edges of the wire frame (Figure 2.2a). This technique makes it  
 14 possible to place readout electronics only at one short edge of a wire frame, enabling  
 15 joining the APAs on the other three sides with minimal dead space. It slightly  
 16 complicates the track reconstruction because the U and V wires are sensitive to  
 17 tracks on both sides of the APA. The upper APAs in the cryostat will have their  
 18 readouts at the top edge of the frame (as shown in Figure 2.2), while the lower  
 19 APAs will mount their electronics at the bottom edge. These readout electronics are  
 20 located outside of the TPC's active volume.

21 The wire angle and overall APA length are chosen so that the angled wires wrap  
 22 less than one full wrap around the APA between its head and foot (Figure 2.4). This  
 23 avoids an ambiguity problem that would arise if a pair of angled wires and a vertical  
 24 wire coincided at more than one location on an APA face. A particle arriving at  
 25 one of the locations would be indistinguishable from a particle arriving at the other.  
 26 The multiple photon detectors embedded in the APA frame also help to identify the  
 27 vertical location of an ionizing track.

28 Precise values of wire angle and wire pitch were chosen to give an integral number  
 29 of wires across the wire-bonding boards at the electronics end of the APA as well as  
 30 an integral number of wire slots in the boards along the sides of the APA. A solder  
 31 pad spacing of 5.75 mm at the electronics end and a wire slot spacing of 8.00 mm  
 32 along the sides results in a wire-to-wire pitch of 4.67 mm and a wire angle of  $35.71^\circ$   
 33 to the long axis of the APA.

34 The 5.75 mm pitch of solder pads across the electronics boards of the U and V  
 35 layers results in 40 channels per 230-mm-wide board. The 4.79 mm pitch in the X  
 36 layer gives 48 channels per 230 mm wide board. Each 230-mm-wide stack of boards  
 37 has, therefore,  $40+40+48=128$  channels. There are 10 of these boards distributed  
 38 per side along the readout edge of an APA for a total of 2560 signal wires on the

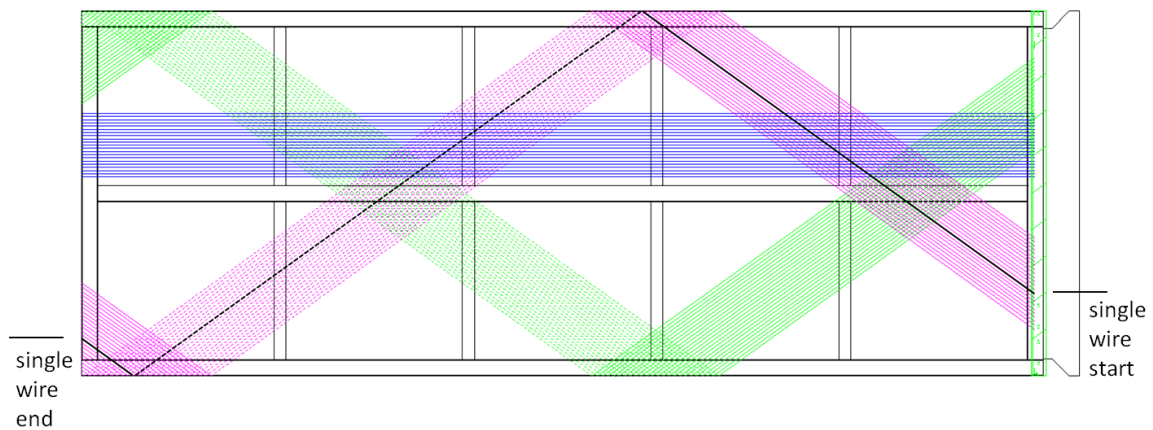


Figure 2.4: An illustration of a few wire paths on the APA. The length and width of the APA, and the wire angle, are chosen so that in the angled layers the wires wrap less than once around the APA. This can be seen from a single wire (shown in black in the magenta group) in the illustration. Small portions of the wires from the three signal planes are shown in color: magenta (U), green (V), blue (X). There is a fourth (G), un-shown wire plane above these three, and parallel with X, which is present to improve the pulse shape on the U plane signals.

fig:tpc-wire-a



- 1 APA. With the additional 48 G wires per board stack, the total number of wires per
- 2 APA is 3520.

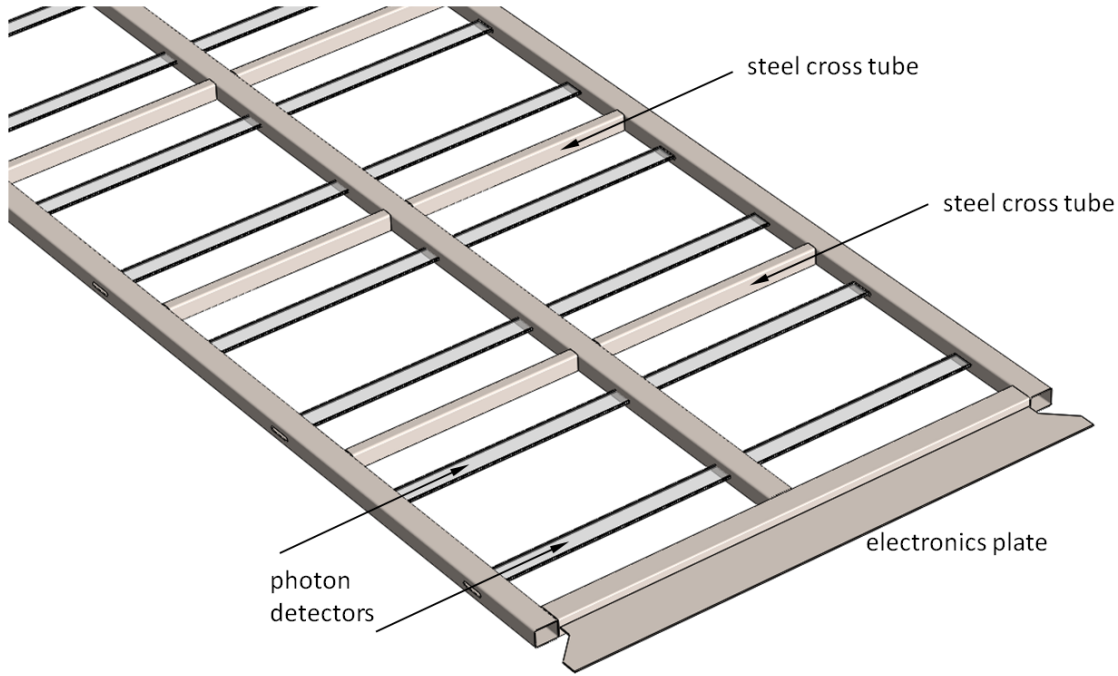


Figure 2.5: The stainless steel APA frame (shown without wires or boards). The photon detectors are shown in place — although the APA is designed so that the photon detectors can be inserted into the APA after the wires are wound.

fig:tpc-wire-f

### 3 2.3.3 APA Frame

4 At a nominal wire tension of 5 N, the 3520 wires exert a force of  $\sim 7.0$  kN/m on the  
 5 short edges of the APA, and a  $\sim 1.5$  kN/m force on the long edges. The wire frame  
 6 must be able to withstand the wire tension with minimal distortion, while minimizing  
 7 the thickness of the frame to reduce the resulting dead space. A conceptual design  
 8 of the wire frame is shown in Figure 2.5. It is constructed from all stainless-steel  
 9 tubes welded in a jig. Structural analysis has shown that the maximum distortion  
 10 of the frame due to wire tension is less than 0.5 mm. The total mass of a bare frame  
 11 is  $\sim 260$  kg.

Lengthwise buckling is not an issue, both because of the strength of the frame and because the wires are maintained at an approximately uniform distance from the frame by periodic comb-like structures (Figure 2.9).

All three long tubes have slots cut in them so the photon detectors can be inserted into the APAs after the wires are installed. The two long outer members of the frame are open-ended, so the photon detector cables can be threaded through them. All tube sections are vented to prevent the creation of trapped volumes.

### 2.3.4 Wire Wrapping Around an APA

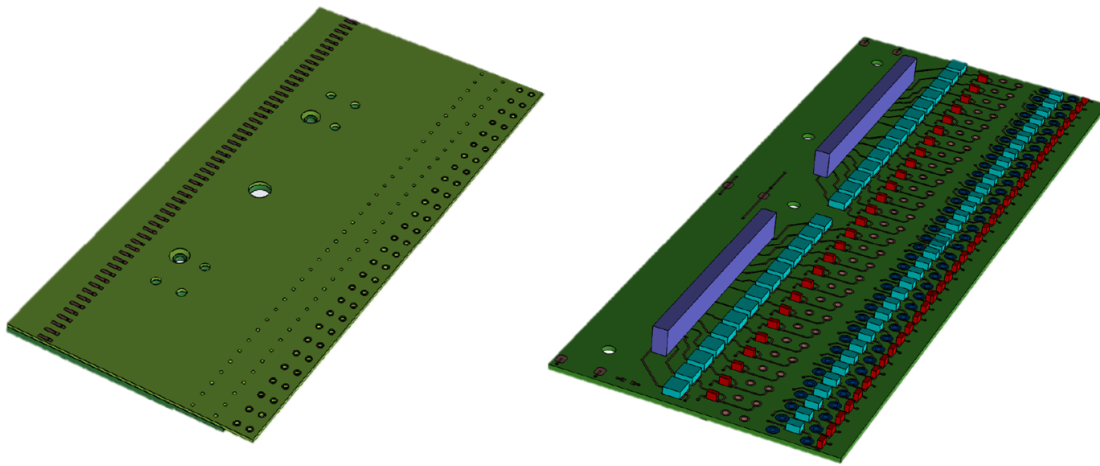


Figure 2.6: Left: Design of a wire-bonding board for the x wires. The wires are glued on the leading edge of the top surface, and then soldered to the soldering pads. Right: Another board, located underneath the four wire-bonding boards, carries the RC network for the bias voltages.

The wire-bonding boards are the interface between the wires and the front-end electronics. Also, they physically anchor the wires at the top end of the APA. The four planes of wires are attached to their respective wire-bonding boards through a combination of epoxy and solder. During winding of the X layer onto the APA the wires are placed across the top surface of the X wire-bonding board. The wires are then glued down with a strip of epoxy at the leading edge of the board. After the epoxy has cured, the wires are soldered onto the copper pads under each wire, and then the wires are cut beyond the pads. The V, U and G planes are attached on top

of the X boards and similarly populated with wires, one layer at a time. An array of pins is pushed through holes in the stack of wire-bonding boards, making electrical connections between the wires and the CR board. Figure 2.6 shows one of the X boards and an intermediate board, the capacitor-resistor (or CR) board, which is located between the wire-bonding boards and the front end electronics boards.

In this way the wire-bonding boards are connected to the bias voltage supply through the resistor-capacitor network on the CR board. The resistors in this network have values around 20 M $\Omega$ , so that in the event that a wire from a different plane breaks and is shorted to these wires, the bias voltages on the rest of the wires will not be affected. The AC-coupled signals from the RC network are connected to sockets that will mate with the front-end readout boards.

These readout boards, as described in Chapter 3, process the analog signals from the wires and transmit the digital information via feedthroughs to the DAQ system outside the cryostat. The electronics on the readout boards generate an estimated  $\sim 160$  W of heat per APA which may produce a small quantity of argon bubbles. Stainless-steel covers are placed over the readout boards to contain the bubbles and direct them to the gas volume of the cryostat. In the case of the lower APAs, the bubbles, if not already re-condensed, will be funneled through the vertical hollow frame members to the top of the cryostat.

Figure 2.8 is a close-up view of a corner of an APA frame with some wires and various wire-bonding boards to demonstrate the assembly.

After the grid plane wires are placed on the APA, and fiberglass cover sheets placed over the edge boards, metal guards are placed along the three wrapped edges of an APA. These guards protect the fragile wires during APA handling, storage and transport.

### 2.3.5 Wire Supports on Inner Frame Members

Figure 2.9 shows the comb set that provides intermediate support to the long wires. Combs are located on each of the 4 cross beams so that the longitudinal wires are supported every 1.2 m and the angled wires about every 1.5 m while introducing only millimeter-scale dead regions.

The support structure is composed of strips of thin G10 sheet, with notches machined at correct intervals. The support strips for the X plane are mounted on the surface of the cross tubes. After all X wires have been placed into the slits, the V support strip (shown in green) is glued onto the tips of the X strips, trapping the X wires in position. After the V wire are placed into the slits, the U support strip (identical to the V strip) is glued to the V strip, trapping the V wires. These wire

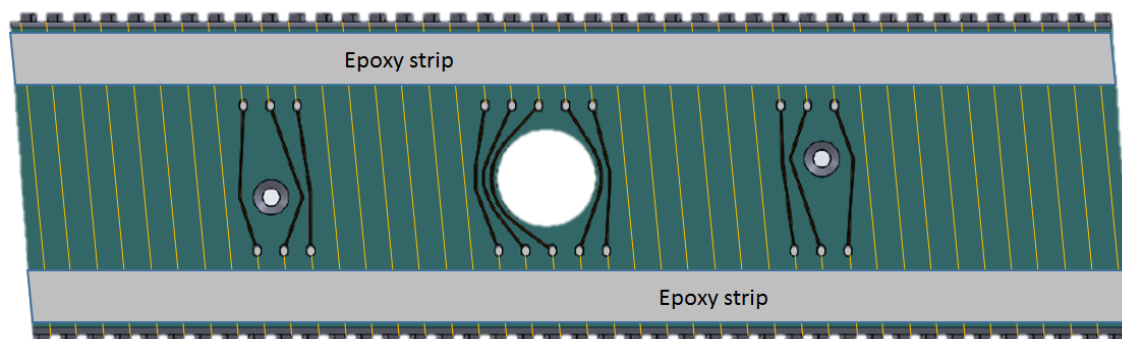


Figure 2.7: Design of a wire wrapping board for the U wires on a long edge of an APA. The light, angled lines represent the wires wrapped over the board surface. Some wires near the mounting holes must be soldered to the copper traces and then cut. An epoxy strip attaches the wires to the board so the solder is only critical for the electrical connection.

fig:tpc-wire-b

- 1 supports play a key role in minimizing wire deflection due to gravity and electrostatic
- 2 force, enabling the use of a moderate wire tension and reducing the risk of wire
- 3 breakage.

## 4 2.3.6 Wire-Winding Machines

5 A winding machine will be constructed to lay the 3520 wires onto each APA. It  
 6 has sufficient versatility that the same mechanism can wind both the angled and  
 7 the longitudinal layers. This was not a deliberate goal in the beginning but it has  
 8 turned out that the method chosen for winding the angled layers will work for the  
 9 longitudinal layers as well.

10 Its working concepts are illustrated in Figure 2.10. The wire tensioner is a self-  
 11 contained unit that includes the wire spool. It is designed so that tension is main-  
 12 tained, not just when wire is pulled out, but also if wire is let back into the tensioner.  
 13 The APA is held off the ground by a couple of posts, with one of its long edges down.  
 14 There are X-Y positioners on either side of the APA; the tensioner is moved across  
 15 the face of the APA by one of these positioners — unspooling tensioned wire as it  
 16 moves. When the tensioner arrives at the edge of the APA it is passed across to  
 17 the positioner on the other side of APA. This is done in the correct position so that  
 18 wire is placed into the appropriate slots of the edge boards. The new positioner then  
 19 moves it to the next location on the edge — where it is passed back around the edge

fig:tpc-winding-machine

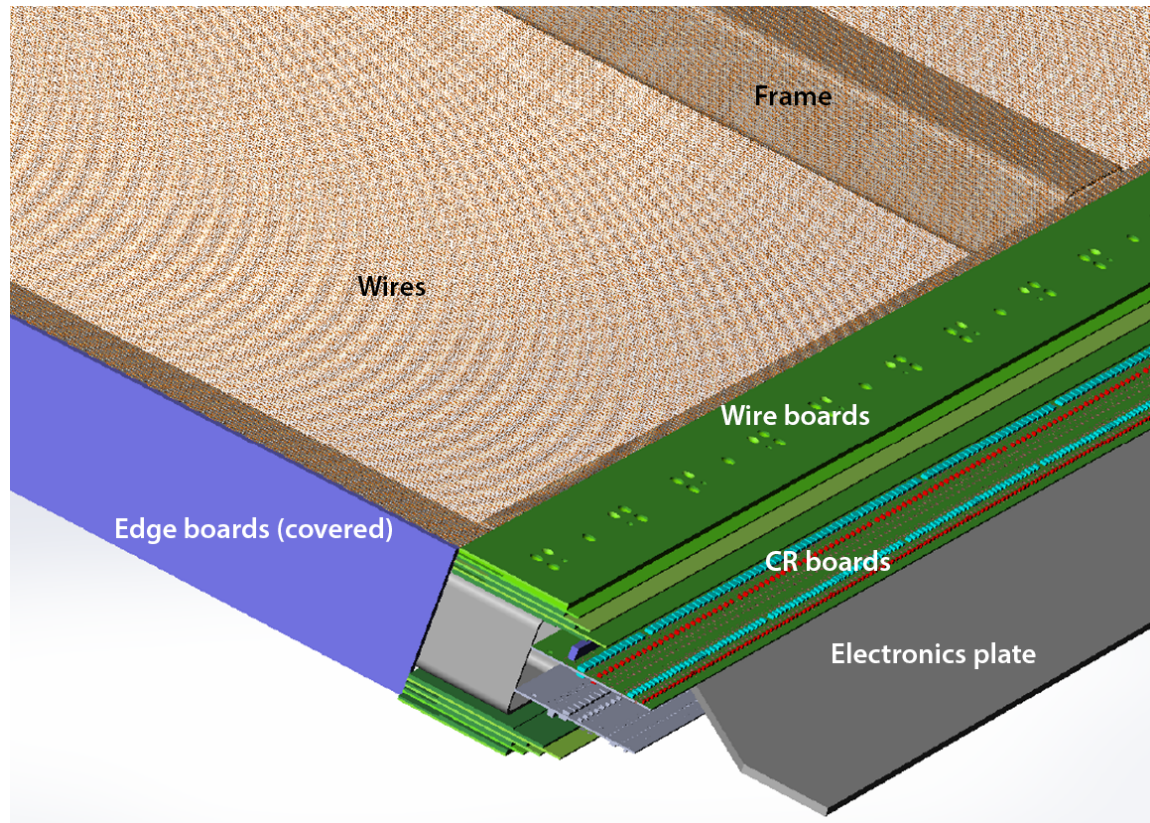


Figure 2.8: A close-up view of a partially assembled corner of an APA. The wire-bonding boards and CR boards are shown but the “cold electronics boards”, for data acquisition, are not shown. They mount on the electronics plate and connect electrically to the CR boards.

fig:tpc-APA-co



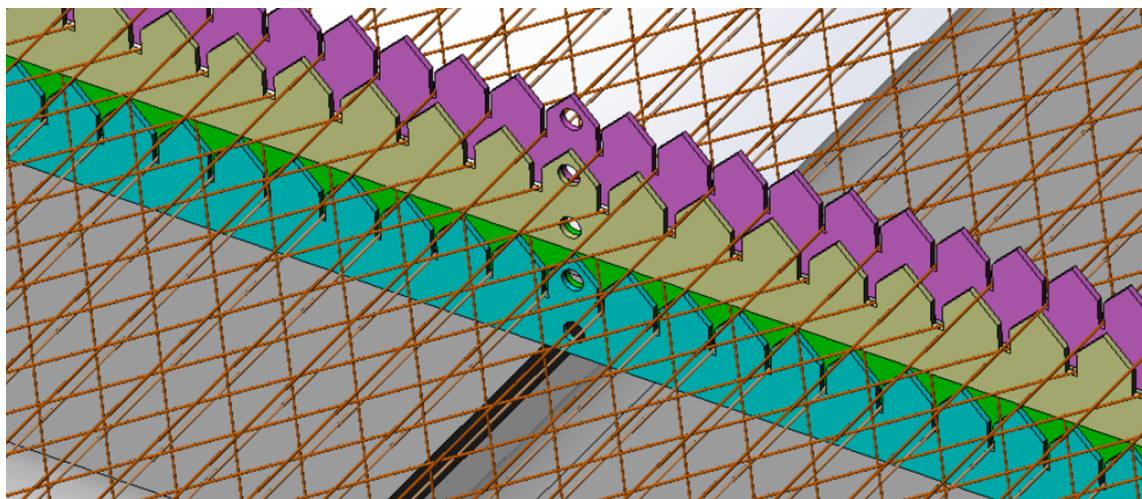


Figure 2.9: Intermediate wire support combs. A set of thin G10 combs is located on each cross bar of the frame. Each layer of wire has its own comb and, as each new comb is glued to the previous one, it locks in the previous layer of wire. In this view the tips of the second layer (green) combs are hidden behind the body of the third layer (tan) combs. One more retainer strip would be added to the above combs to hold the top wire layer in place. The row of holes in the comb are used with a registration/alignment fixture.

fig:tpc-wire-s

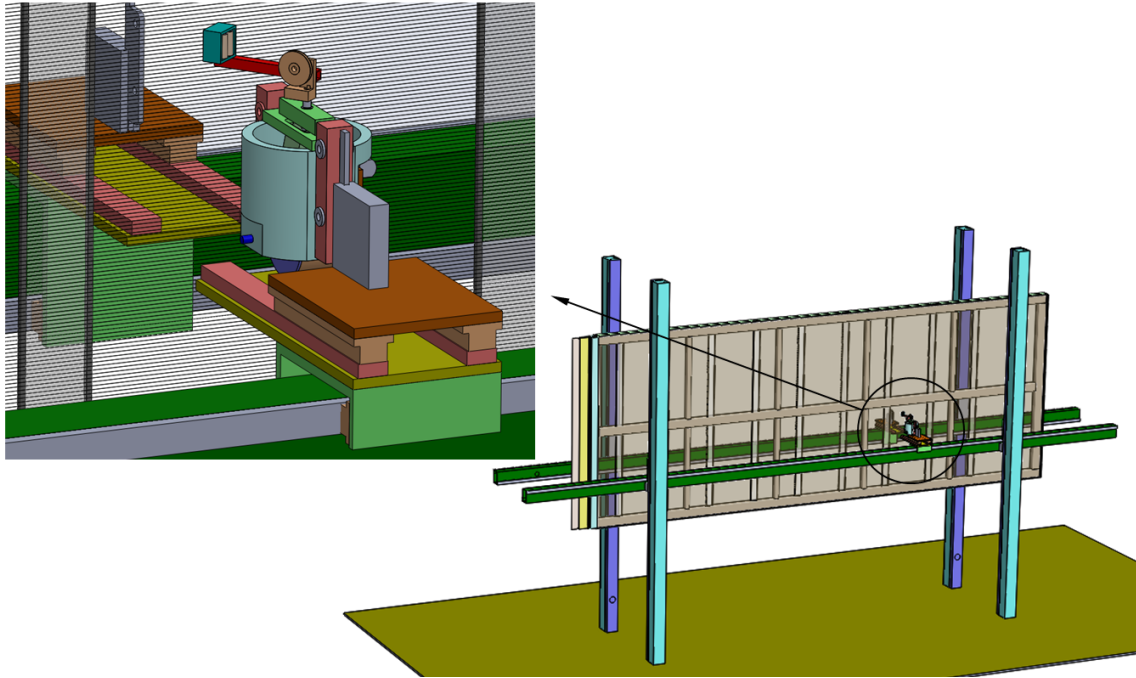


Figure 2.10: The tensioner head is passed from one side of the APA to the other as it is moved around the APA to wind wire onto the APA frame. The horizontal/vertical positioning systems on each side of the APA are made of commercial linear motion components. Much or all of the positioning systems should be available from commercial vendors

fig:tpc-windin

of the APA. In this way half the wires in a layer can be wound on with only occasional stops for temporary soldering to prevent loosening in case of a broken wire. After the supports at the end of the APA are relocated out of the winding path, the rest of the wires in the layer can be wound on in the same manner. (A layer in this case refers to the pair of identical wire planes in an APA - one on each side.)

Although a large part of an entire plane of wires can be wound in one continuous process, a more fault-tolerant procedure would be to pause the winding machine periodically and solder the last wire. This intermediate soldering step will prevent the unwinding of a large section due to an accidental broken wire. An automatic soldering robot will solder the wire ends after the wires have been laid down on the APA. A wire-tension measuring device will scan the newly placed wires and record the wire tension of each wire. Any wires with abnormal tension will be replaced manually.

## 2.4 Cathode Plane Assemblies

There are three walls of cathodes in each TPC. Each wall is tiled from a four-unit-high by 13-unit-wide array of cathode plane assemblies (CPAs). Figure 2.11 shows a corner of a cathode plane. Each CPA is 2.3 m wide (identical to the APA width) and 3 m tall (half of APA height) for ease of fabrication, assembly and handling. Each CPA is made of a stainless-steel framework, with panels of solid stainless steel sheets mounted between the frame openings. Along each vertical column of the four CPAs, there are two slightly different versions, one for the edge CPAs (top and bottom rows), and one for the non-edge CPAs (2nd and 3rd rows). The non-edge CPAs use all square tubes for the frame structure, while the edge CPAs use a round tube on the floor- or ceiling-facing edge of the CPA to minimize the surface electric field. Two sets of field-shaping end pieces are installed at the two ends of the CPA wall to properly terminate the cathode wall with rounded edges. All CPAs are suspended from the ceiling using G10 hangers to electrically insulate the CPA from the cryostat.

The impact of the square tube frame on the drift field near the cathode will be evaluated in the 35-ton TPC study (see Section 7.4). If necessary, strips of field shaping electrodes with a suitable bias voltage can be attached to the raised square tube surfaces to correct the field distortions.

This CPA design forms a highly conductive wall at  $-170$  kV facing the grounded cryostat wall with a  $\sim 0.6$  m clearance. As a result, the stored energy on this cathode is more than 100 joules. There is a risk of damage to the cryostat membrane or other TPC components if a high-voltage discharge develops, and dumps all the energy quickly onto a very small surface area. To mitigate this risk, the electrical



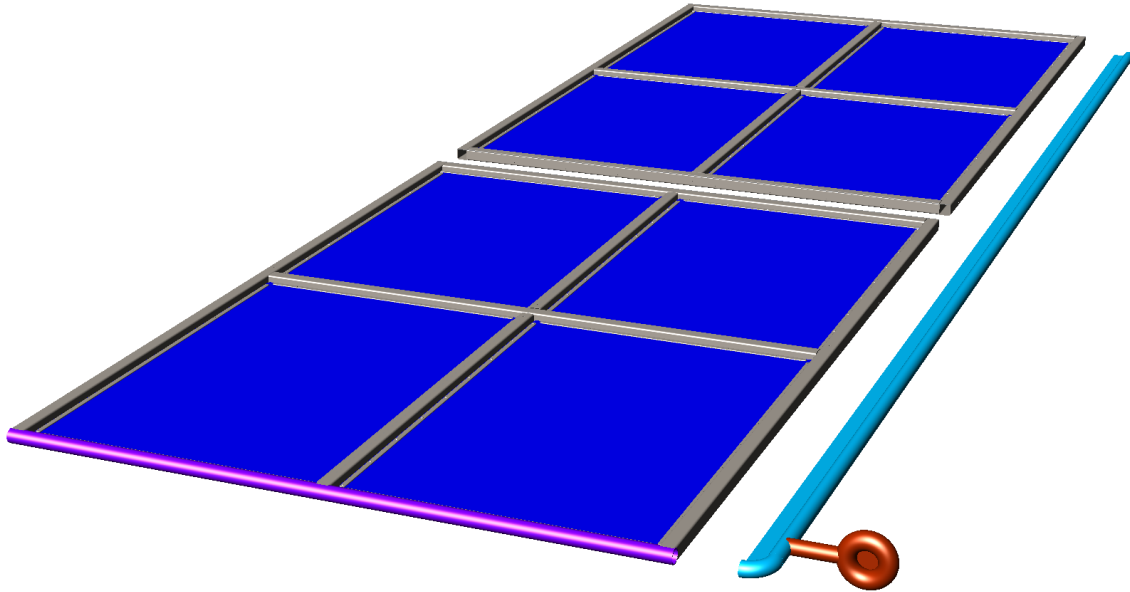


Figure 2.11: Conceptual design of the different cathode plane components near a corner of a cathode wall. Two flavors of CPAs (edge unit and non-edge unit) make up the entire wall of a cathode plane, terminated at both ends by the end pieces (cyan colored). A high voltage receptacle (orange) connects with the HV feedthrough from the cryostat ceiling. Each CPA is roughly 2.3m wide by 3m tall.

fig:tpc-cathod

1 properties of the cathode are currently being analyzed, and cathode designs that  
 2 will substantially slowdown the total energy release in case of a discharge are being  
 3 developed. Possible choices include a highly resistive coating on all non-conductive  
 4 cathode surface panels as well inner frame members; or conductive panels with robust  
 5 resistive coupling to the frame structures.

## 6 2.5 Field Cage

7 Each facing pair of CPA and APA rows forms an electron-drift region. A field cage  
 8 completely surrounds the four open sides of this region to provide the necessary  
 9 boundary conditions to ensure a uniform electric field within, unaffected by the  
 10 presence of the cryostat walls.

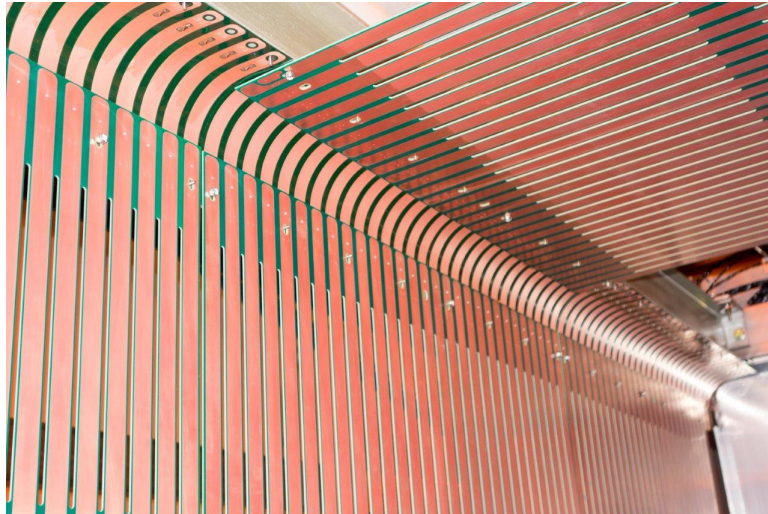


Figure 2.12: A corner of the 35ton TPC field cage as it is being constructed

fig:tpc-field-

11 The entire TPC requires  $\sim 1,100 \text{ m}^2$  of field cage material per 5-kt detector.  
 12 The field cages are constructed using copper-clad FR4 sheets reinforced with fiber  
 13 glass I-beams to form panels  $2.3 \text{ m} \times 3.4 \text{ m}$  in size. Parallel copper strips are  
 14 etched/machined on the FR4 sheets. Strips are biased at appropriate voltages pro-  
 15 vided by a resistive-divider network. These strips will create a linear electric-potential  
 16 gradient in the LAr, ensuring a uniform drift field in the TPC's active volume.  
 17 Simulations have shown that the drift-field non-uniformity quickly drops below 1%,  
 18 roughly a strip pitch away from the field-cage surface.

Since the field cage completely encloses the TPC drift region on four sides, while the solid cathodes block the remaining two, the FR4 sheets must be frequently perforated to allow natural convection of the liquid argon. The “transparency” of the perforation will be determined by a detailed LAr computerized fluid dynamic (CFD) study.

The resistor-divider network will be soldered directly onto the field-cage panels. Multiple resistors will be connected in parallel between any two taps of the divider in order to provide fault tolerance. One end of the divider chain is connected directly to the cathode, while the other end is connected to ground at the APA through resistors of the appropriate value. In addition to the resistor network, surge suppressors such as varistors and gas discharge tubes will be installed between field cage strips to avoid an over-voltage condition that occurs between field cage electrodes and the cathode in a high-voltage discharge.

The major challenge of this field cage design is to minimize the electric field exposed to the liquid argon near the thin copper strips. One solution is to cover all copper edges with a thick layer of solder mask (an acrylic-based polymer with a high dielectric strength) as part of the standard PCB fabrication steps. This construction is currently being implemented in the 35-ton TPC. Figure 2.12 shows a section of the partially constructed field cage. The 35-ton TPC test results will be evaluated to determine if this technique is suitable for the much larger far detector. In the meantime, collaborators are also investigating new concepts to minimize the electric field at the copper edges (see, for example, Figure 2.13).

## 2.6 High-Voltage Components

The cathode planes are biased at  $-170$  kV to provide the required  $500$  V/cm drift field. At a minimum, three high-voltage (HV) power supplies, each connecting through its own feedthrough, will be used. Each supply will provide high voltage to one of the three rows of the cathode plane assemblies.

The power supplies for the TPC cathode planes must be able to provide  $-200$  kV at  $1$  mA current. The output voltage ripple must not introduce more than 10% of the equivalent thermal noise from the front-end electronics. The power supplies must be programmable to trip (shutdown) their output at a certain current limit. During power on and off, including output loss (for any reason), the voltage ramp rate at the feedthrough must be controllable to prevent damage to the in-vessel electronics through excess charge injection.

HV feedthroughs must be able to withstand  $-250$  kV at their center conductors in 1 atm air or argon gas environment when terminated in liquid argon.

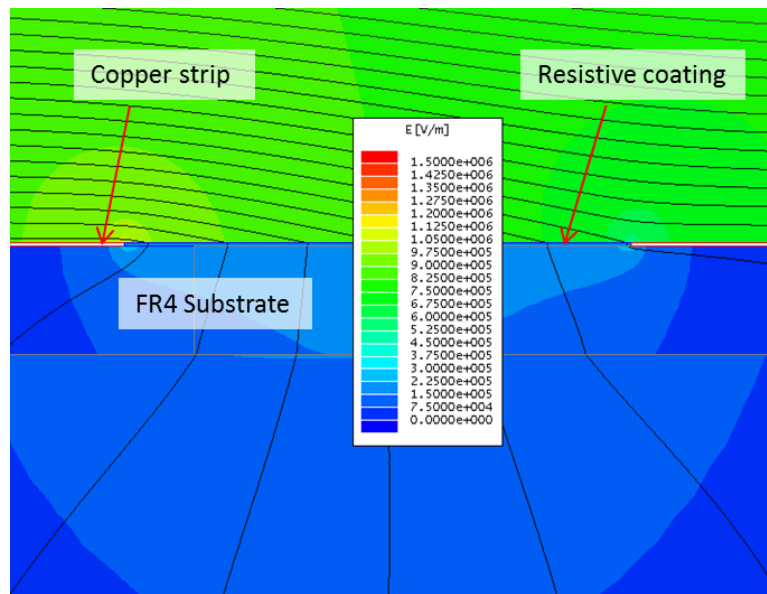


Figure 2.13: Electrostatic simulation of a field cage design that uses a layer of resistive coating between the conductive copper strips to eliminate the high field regions near the copper edges.

fig:tpc-field-

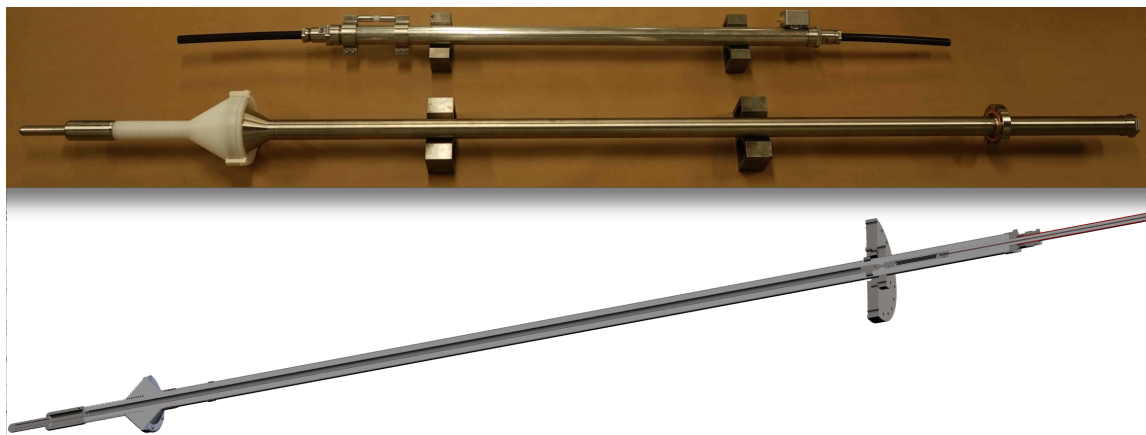


Figure 2.14: Top: The high voltage feedthrough and filter developed by the UCLA group for the 35ton TPC. It was tested up to 150 kV. Bottom: a conceptual design of a new feedthrough for the LAr-FD.

fig:tpc-UCLA-f

The current candidate for the high-voltage power supplies is the Heinzinger PNChp series, which is used by the ICARUS experiment. Additional filtering of the voltage ripples is done through the intrinsic HV cable capacitance and series resistors installed inside the filter box. Established techniques and practices will be implemented to eliminate micro-discharges and minimize unwanted energy transfer in case of an HV breakdown.

To ensure safe and reliable operation, the HV feedthroughs will be tested at a much higher voltage than expected in routine operation ( $\sim 250$  kV) in liquid argon. The feedthroughs will be mounted on the ceiling of the cryostat, their cold ends reaching through the gas ullage space and submerging into the liquid argon. The center conductor on the cold side of a feedthrough will be insulated and shielded by a grounded shroud at least 50 cm below the surface of the liquid. Connections between a feedthrough and a CPA row is made through a specially designed high voltage receptacle attached to the end of a CPA row and the retractable tip located at the end of the feedthrough to ensure good electrical contact throughout the temperature range. Figure 2.14 shows an example of the feedthrough and filter box made by the UCLA group for the 35-ton TPC, as well as the conceptual design of a feedthrough suitable for the far detector TPCs.

## 2.7 TPC Assembly in the Cryostat

Figure 2.15 shows a partial assembly of a section of the TPC. The finished cryostat has five rows of anchor points distributed along the ceiling (not shown in the figure). A mounting rail is suspended through stainless-steel rods to each row of the anchor points. Under these five mounting rails, rows of CPAs and APAs are suspended in an interleaved fashion. Because the cathodes are at a high voltage, the CPAs are attached to their mounting rails through G10 rods. The distance between the facing anode-cathode pair is maintained by the pultruded fiberglass I-beams holding the FR4 sheets forming the field cage. The TPC installation procedure is discussed in Chapter 6.

## 2.8 TPC Prototyping, Test and Checkout

### 2.8.1 TPC Prototyping

Several prototype TPC modules have been constructed during the design phase. The initial prototypes were fractional scale or partial models of the APA and CPA. The

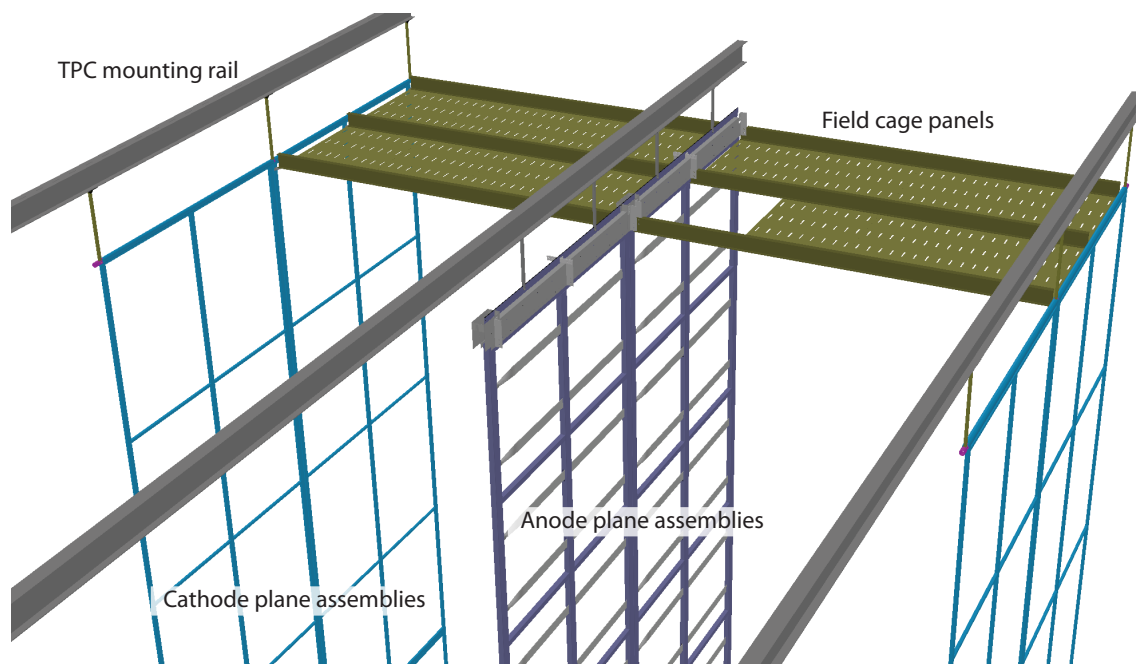


Figure 2.15: A partial assembly of the TPC showing all major components

fig:tpc-partia



- 1 CPA prototype was used to evaluate field-shaping electrode attachment techniques.
- 2 The APA prototype that was used to study the placement of the wire-wrapping
- 3 boards and wire-support structures is shown in Figure 2.16. It was also used to
- 4 develop the prototype winding machines. These prototypes were subjected to nu-
- 5 merous thermal cycles down to liquid-nitrogen temperature to test the integrity of
- 6 the wire-to-board and board-to-frame bonds.



Figure 2.16: APA prototype used to study the support structure and wire wrapping

fig:tpc-apa-40

- 7 The current set of prototypes are scale models of the APA and CPA. They are
- 8 being used to validate the designs and to evaluate production procedures. Pro-
- 9 totype front-end electronics boards for the scale APAs are currently being tested.
- 10 Figure 2.17 shows the trial assembly of these functional prototypes into the TPC
- 11 that will be installed in the 35-ton prototype cryostat. This TPC is expected to be
- 12 operational in 2015.



Figure 2.17: Trial assembly of the APAs, CPAs and field cage panels into the 35-t TPC

fig:tpc-35ton-

Design for a Deep Underground Single-Phase LArTPC



A future TPC prototype, proposed for testing in the CERN neutrino beam, will require three full-size APAs with fully instrumented readout electronics, six full-size CPAs, and complete field-cage coverage. The TPC will be constructed using identical APAs, CPAs and field-cage panels as designed for the far detector. Additional features will be installed to ensure proper TPC operation given the half-height cryostat configuration. The construction and assembly of all TPC mechanical components will use the same materials and techniques as designed for LAr-FD, with the exception of a reduced degree of automation than will be used to wire APAs for the LAr-FD.

This TPC prototype will have a complete set of cold electronics installed on the APAs. The electronics components will closely resemble those designed for the LAr-FD. All key features of the LAr-FD electronics chain, including preamp, shaper, ADC, digital buffer, zero suppression and multiplexing will be implemented. Some electronics may be in prototype or functional-equivalent form.

## 2.8.2 Assembly Testing

The components and the completed APAs will undergo thorough testing. In particular:

- The wire-carrier boards will be thermally cycled and HV stressed to check for excess leakage current.
- The CR boards will be fully tested at the rated bias voltages of the capacitors at warm and cold. Components showing excess leakage current at bias will be replaced.
- The tension and electrical continuity of each wire will be measured after the plane of wires is bonded to the frame.
- After the front-end electronics boards have been installed on the APA, an initial calibration of all electronic channels will be performed. The electronic gains and noise levels of all channels will be recorded in a database.
- A cool-down stress test will be performed on each completed APA in a liquid-nitrogen environment. Electronic calibration on all channels will be performed while the APA is cold and again after it is warmed up. Significant differences in the cold and warm calibration results will be investigated and remediated.

A cool-down stress test will also be performed on each completed CPA in a LN<sub>2</sub> environment to verify its flatness at cryogenic temperature. If resistive surfaces are

1 used on the cathode, its contact resistivity to the outer metal frame at warm and  
2 cold temperatures will be verified to be within spec.

3     Regarding the field cages, the resistance will be measured along each copper  
4 strip, and between strip pairs. The resistance between two strips should exceed 50  
5  $G\Omega$  without the resistive divider. All resistors will be thermal cycled before installing  
6 on the divider. Any resistor with resistance beyond spec in the cold will be rejected.  
7 All varistors will be also be thermal cycled, and their leakage current at nominal  
8 operating voltage as well as their clamping voltages at cold will be verified. High-  
9 voltage tests may be performed on all field cage assemblies to identify manufacturing  
10 defects on the surfaces.

### 11 2.8.3 Checkout

12 After passing the tests at the assembly level, the APAs will be put into storage, and  
13 later transported to the Far Site. Prior to installation, another round of electronic  
14 calibration will be performed on the APAs to validate their acceptable status.

15     During installation, the DAQ system will be running continuously. As soon as  
16 each stack of APAs is connected to the pre-routed cables, a suite of calibration runs  
17 will be performed to validate that all connections have been made properly. Repair  
18 or replacement at this stage will still be straightforward.

19     After the entire TPC is assembled, a system-wide calibration will be performed  
20 at room temperature and again at cryogenic temperature in argon gas. Repair or  
21 replacement would require partial disassembly of the TPC and should be avoided  
22 unless absolutely necessary.

23     The responsibility and authority for the design, installation and use of the detec-  
24 tor quiet-power distribution and detector-grounding system is held by the subproject  
25 electrical engineer. This engineer has oversight responsibility for all electrical and  
26 electronics design and installation tasks, including all attachments to the detector  
27 that create an electrical connection.

ckout-checkout

# Chapter 3

## Cold Electronics

ch:ce

### 3.1 Introduction

sec:ce\_intro

The TPC read-out electronics are referred to as the “Cold Electronics” (CE) because they will reside in LAr, mounted directly on the APA front-end (Figure 3.1). This will minimize channel capacitance and noise by keeping the length of the connection between an anode wire and its corresponding electronics input to an absolute minimum. The CE will be implemented as ASIC chips using CMOS technology, which performs well at cryogenic temperatures, and will provide amplification, shaping, digitization, buffering and multiplexing (Mux) of the signals. Because it is not possible to form a trigger for some important measurements, such as proton decay and supernova bursts, the CE will be continuously read out, with a digitized ADC sample from each APA channel (wire) every 500 ns. For each of the 104 APAs in a 10-kt fiducial cryostat, one cable bundle will connect to the outside of the cryostat through a feedthrough, with one feedthrough servicing two APAs. Each of these cable bundles consists of wires for low-voltage power, TPC wire-bias voltages, data-out, clock-in and digital-control IOs.

The scope of the CE subsystem includes the design, procurement, fabrication, testing, delivery and installation of the CE, the components of which are:

- Front-end cards installed on the APAs
- All electronics on those cards
- Feedthroughs (a single type, henceforth “signal feedthroughs”) which handle the signal, low-voltage power, TPC bias voltage and control lines
- External interface crates

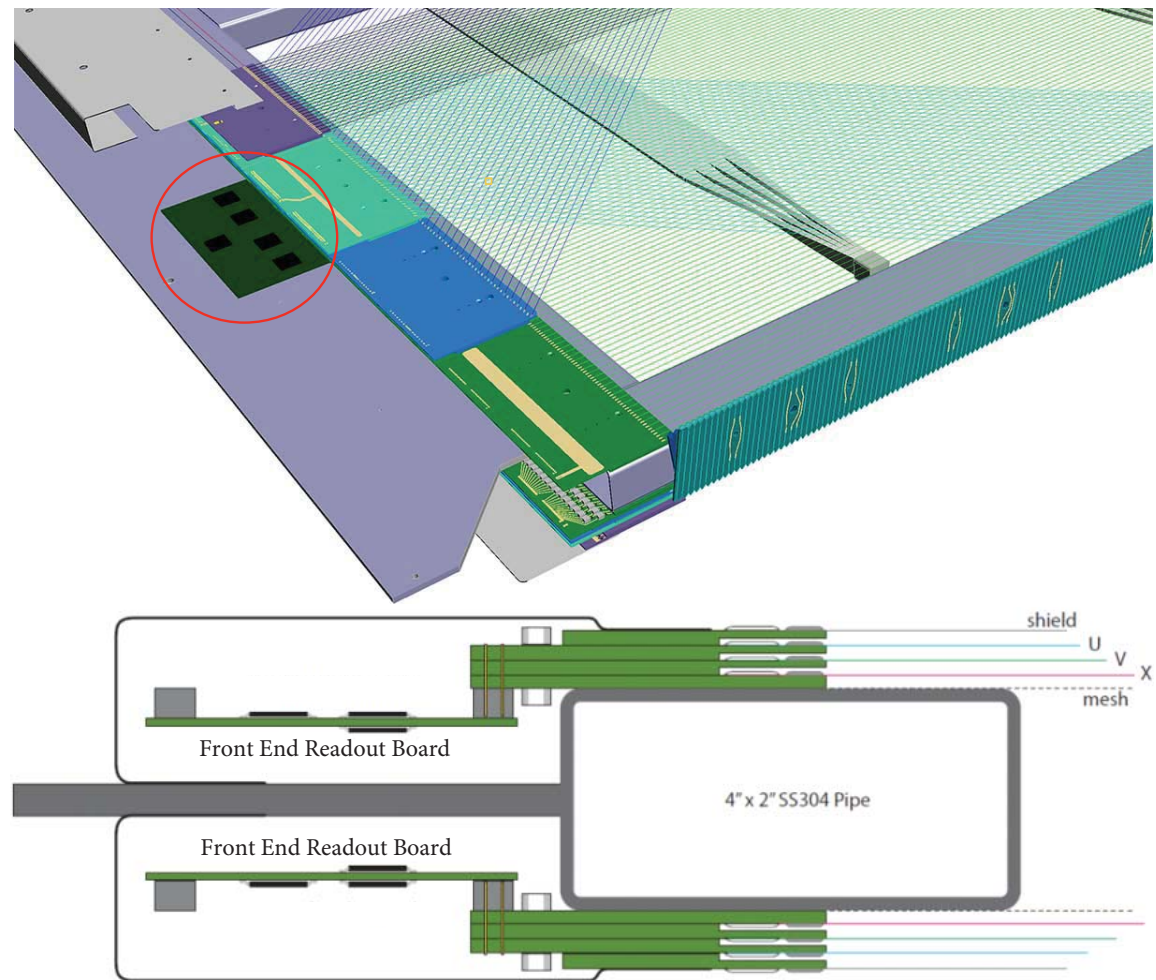


Figure 3.1: The front end electronics as mounted on an APA. **Top:** The front end electronics is shown in the red circle. **Bottom:** Cross section view.

fig:elec\_CMBon

- Power supplies, including low-voltage supplies for the CE and bias-voltage supplies for the TPCs
- Signal, control and power cabling between the front-end cards and the feedthroughs, and between the feedthroughs and external power supplies and interface crates

## 3.2 Design Considerations

The requirements for the CE can be found in the requirements documentation [4].

The most significant ones are listed here. The CE shall:

- Provide the means to read out the TPCs and transmit their data in a useful format to the Data Acquisition System (DAQ).
- Operate for the life of the facility without significant loss of function.
- Record the channel waveforms continuously without dead time.
- Use only materials that are compatible with high-purity liquid argon.
- Provide sufficient precision and range in the digitization to:
  - Discriminate electrons from photon conversions;
  - Optimize for high- and low-energy tracks from accelerator-neutrino interactions;
  - Distinguish a Minimum Ionizing Particle (MIP) from noise with a signal-to-noise ratio  $> 9:1$ ;
  - Measure the ionization up to 15 times that of a MIP particle, so that stopping kaons from proton decay can be identified.
- Ensure that all power supplies have:
  - Local monitoring and control
  - Remote monitoring and control through DAQ
  - Over-current and over-voltage protection circuits
- Ensure that the low-voltage (signal) feedthroughs are able to withstand twice their nominal operating voltages with a maximum specified leakage current in 1-atm argon gas.

The responsibility and authority for the design, installation and use of the detector quiet-power distribution and detector-grounding system is held by the subproject electrical engineer. This engineer has oversight responsibility for all electrical and electronics design and installation tasks, including all attachments to the detector that create an electrical connection.

### 3.3 Architecture

The CE architecture is manifested in the Front End Mother Board assembly (FEMB), which consists of an analog mother board with a digital ASIC mezzanine (Figure 3.2). Each APA is instrumented with 20 FEMBs, for a total of 2,560 channels per APA.

The analog mother board is instrumented as a 128-channel board which uses eight 16-channel FE ASICs, eight 16-channel ADC ASICs, low-voltage regulators, and input-signal protection. The 16-channel FE ASIC provides amplification and pulse shaping. The 16-channel ADC ASIC comprises a 12-bit digitizer, local buffering, and an 8:1 Mux stage with two pairs of serial readout lines in parallel. This has already been prototyped and tested, using a commercial FPGA to perform the role of the digital ASIC (Figure 3.3).

The Cold Digital Data (COLDATA) ASIC and its voltage regulators are mounted on the digital ASIC mezzanine. The COLDATA ASIC provides:

- The communication protocol with the data acquisition system (DAQ)
- The control required to program and read out the FE and ADC ASICs
- The system clock interface
- Four 4:1 Muxs that combine 16 serial lines from the ADCs of eight channels each into four serial lines of 32 channels each
- Four 1-Gbps serial drivers that form the data link to DAQ

If it is demonstrated that the COLDATA ASIC can achieve 2 Gbps, then the 4:1 Mux will be increased to 8:1 and only two serial drivers will be implemented, with a subsequent reduction in cabling, etc. In either case, the data rates will not be high enough to require the use of optical fibers in the cold, nor is there a need for zero suppression or data compression. This greatly reduces the complexity of the COLDATA ASIC, with a corresponding decrease in overall risk, including risk of failure-to-implement (within a fixed schedule and budget) and risk of device failure during long-term operation. Data will be driven to DAQ through copper cable

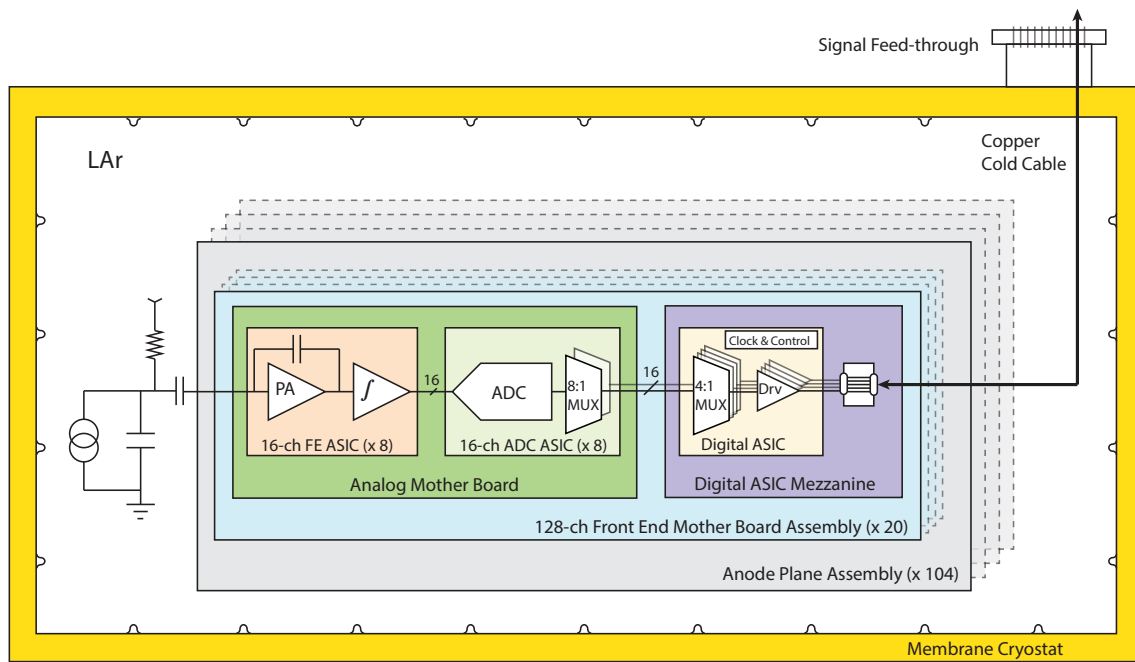


Figure 3.2: The CE Architecture. The basic unit is the 128-channel FEMB

fig:elect\_sche

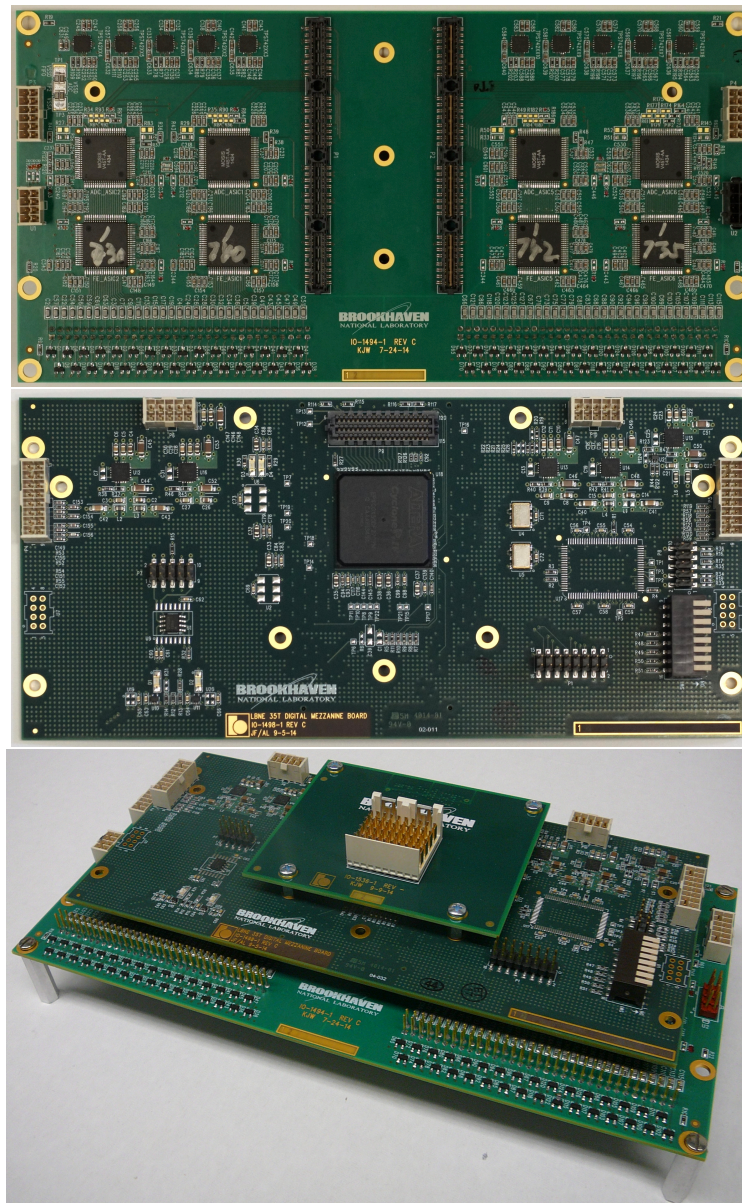


Figure 3.3: The Front End Mother Board (FEMB), as used in the early set of tests. **Top:** The analog mother board, showing four ADC ASICs and four FE ASICs surface mounted. The other side of the board has another four ADC and FE ASICs. Except for anticipated small modifications, this board is essentially the final version. **Middle:** The FPGA mezzanine, used in place of the digital ASIC mezzanine for the early set of tests. **Bottom:** The complete FEMB assembly as used in the early set of tests. The uppermost mezzanine board is the cable connection.

fig:elec\_CMBpi



utilizing low-voltage differential signaling (LVDS). Output data cables will go to a signal feedthrough and from there to an external crate mounted nearby. Under DAQ scope, further data processing is done in the external crate and data is transmitted via optical fiber to front-end computers.

The analog FE ASIC has 16 channels. Each channel includes a charge amplifier with a gain selectable from one of 4.7, 7.8, 14 and 25 mV/fC (full scale charge of 55, 100, 180 and 300 fC), a high-order anti-aliasing filter with adjustable time constant (peaking time 0.5, 1, 2, and 3  $\mu$ s), an option to enable AC coupling, and a baseline adjustment for operation with either the collecting or the non-collecting wires. The 16-channel FE ASICs then transmit the shaped pulse to a 16-channel 12-bit 2 MS/s ADC ASIC. Shared among the 16 channels in the FE ASIC are the bias circuits, programming registers, a temperature monitor, an analog buffer for signal monitoring, and the digital interface. The estimated power dissipation of FE ASIC is about 6 mW per channel at 1.8 V supply. Shared among the 16 channels in the ADC ASIC are the bias circuits, programming registers, an 8:1 Mux, and the digital interface. The estimated power dissipation of FE ASIC is below 5 mW per channel at 1.8 V supply.

## 3.4 CMOS Circuit Design

sec:fe\_CMOS

Compared to the situation at 300 K, charge-carrier mobility in silicon increases at 89 K while thermal fluctuations decrease with  $kT/e$ . These effects result in a higher gain (transconductance/current ratio =  $g_m/i$ ), higher speed, and lower noise at 89 K than at 300 K. For a given drain-current density, the same degree of impact ionization (measured by the transistor substrate current) occurs at a somewhat lower drain-source voltage at 89 K than at 300 K. The charge trapped in the gate oxide and its interface with the channel causes degradation in the transconductance (gain) of the transistor and a threshold shift. The former is of major consequence as it limits the effective lifetime of the device (defined in industry and the literature as 10% degradation in transconductance). Thus, an MOS transistor has equal lifetime due to impact ionization at 89 K and at 300 K, but at different drain-source voltages  $V_{DS}$ , as illustrated in Figure 3.4. This property can be exploited to stress the transistor with both increased current and increased voltage while monitoring the substrate current and the change in  $g_m$  due to impact ionization. Under these conditions, the lifetime can be reduced arbitrarily by many orders of magnitude, and the limiting operating conditions for a lifetime in excess of  $\sim 20$  years can be determined. With this foundation, more conservative design rules (lower current densities and voltages) can be derived and applied in the ASIC design. With this accelerated testing the

- 1 expected lifetimes can be verified for the several widely available CMOS technologies  
 2 under consideration (TSMC, IBM, AMS). It should be noted that this is a standard  
 3 test method used by the semiconductor industry; it is used to qualify electronics for  
 4 deep space NASA missions as well as commercial PCs.

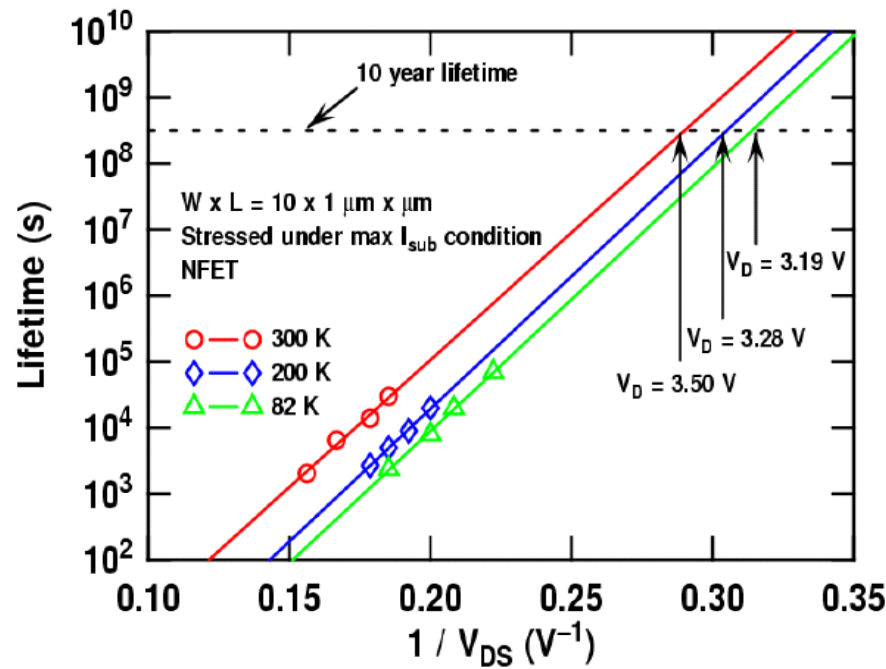
Figure 3.4: Lifetime at different temperatures vs  $V_{DS}$ 

fig:Lifetime

- 5 To successfully design CMOS circuits that will operate at cryogenic temperatures,  
 6 two critical issues must be addressed and resolved. The first issue is the need for  
 7 realistic models at the operating temperature of all active and passive components  
 8 in order to reliably predict operating points, signal response and noise during the  
 9 design process. The second issue is that the design must ensure a long operational  
 10 lifetime, since once the TPC is filled with LAr the detector must operate for about  
 11 15 years without any access to the electronics for repair or replacement. Concerning  
 12 the availability of realistic models, our preliminary results from the cryogenic char-  
 13 acterization (down to 40 K) of a complete mixed-signal ASIC [15] in a commercial  
 14 CMOS 0.25  $\mu\text{m}$  technology, originally developed for room-temperature applications,

indicates that the models are useful to first order. To refine these models, several single-transistor test structures were fabricated on the first prototype of the  $0.18\ \mu\text{m}$  device. Measurements of the properties of these structures at cryogenic temperatures have been used to refine the device models at 89 K.

The lifetime of CMOS circuits is limited by several mechanisms which degrade the performance over time, eventually causing the circuit to fail to perform as specified. The rates of most degradation mechanisms in CMOS, such as electro-migration (EM), stress migration (SM), time-dependent dielectric breakdown (TDDB), thermal cycling (TC), and negative bias-temperature instability (NBTI), all scale with temperature such that cryogenic operation is favored [16][17]. The only mechanism that could affect the lifetime at cryogenic temperature is the degradation due to impact ionization, which causes charge trapping in the MOSFET gate oxide at large drain-current densities (the “Hot Carrier” effect). Results from a CMOS reliability study [18] provide general design guidelines (for device geometry, bias and current density) that should guarantee a lifetime well in excess of 15 years for continuous cryogenic operation. These design guidelines also provide information for designing test conditions to observe the deterioration mechanism and to extrapolate from accelerated deterioration rates, measured under stressed conditions within practical times, to the ultimate lifetime under normal operation.

A monitor of the impact ionization is the bulk current, which reaches a maximum at  $V_{DS} = V_{DD}$  and at  $V_{GS} = 0.5V_{DD}$ . When operating constantly in this condition at room temperature, a properly designed device will typically have a lifetime (defined as a 10% degradation in  $g_m$ ) of about 10 years. The bulk current (i.e., the impact ionization) increases by roughly a factor of four from 300 K to 77 K [18] and a circuit designed for operation at room temperature would have a proportionately shorter useful life at cryogenic temperature. As stated above, in order to guarantee the required lifetime at cryogenic temperatures, design guidelines must be modified for both analog and digital circuits. For analog circuits, this is done by operating the devices at moderate-to-low drain current densities, where impact ionization becomes negligible. For digital circuits, operating the devices with reduced  $V_{DD}$  (about 20%) and using non-minimum channel length  $L$  is easily accommodated since at cryogenic temperature the speed of the digital circuit increases, compensating for the increased  $L$ . These guidelines will be verified with accelerated aging tests, at increasing values of  $V_{DD}$ , on dedicated structures. Such tests also will be conducted on prototype samples throughout the development process to verify the long-term reliability of the final ASICs.

### 3.4.1 Cold Analog ASICs

The development of the readout ASIC has begun by designing and fabricating in a commercial CMOS process (0.18  $\mu\text{m}$  and 1.8V) a 16-channel ASIC implementing the complete analog front-end section. The FE ASIC layout is shown in Figure 3.5. This process is expected to be available for at least another 10 years. The charge amplifier input MOSFET is a p-channel biased at 2 mA with a L/W (channel length/width) ratio of 0.27  $\mu\text{m}$  / 10  $\mu\text{m}$ , followed by dual cascade stages. The charge amplification and shaping filter have digitally programmable gain and peaking time (as listed in Section 3.3). Each channel also implements a high-performance output driver, which is used to drive a long cable when it is used in a standalone mode, as it is in MicroBooNE.[3] The buffer can be disabled when it is interfaced to an ADC ASIC to reduce the power consumption. The ASIC integrates a band-gap reference (BGR) to generate all the internal bias voltages and currents. This guarantees a high stability of the operating point over a wide range of temperatures, including cryogenic. The ASIC is packaged in a commercial, fully encapsulated plastic QFP 80 package.

This ASIC has now been through four design/fabrication/testing revision cycles. Prototypes from each cycle have been evaluated and characterized at room (300 K) and liquid nitrogen (77 K) temperatures. During these tests the circuits have been cycled multiple times between the two temperatures and operated without any change in performance. Figure 3.6 shows the measured pulse response, along with details on the adjustability of the gain, peaking time and baseline. These results are in close agreement with the simulations and indicate that both the analog and the digital circuits and interface operate as expected in a cryogenic environment. Also reported in Figure 3.6 are the outputs of the BGR and temperature sensor, which are in close agreement with the simulations as well.

Figure 3.7 shows the measured ENC versus filter-time constant (peaking time). At 1  $\mu\text{s}$  about 650  $e^-$  was measured, to be compared to the simulated value of 500  $e^-$ . The difference is mainly due to the thermal noise from a  $\sim 11$ -ohm parasitic resistance of the input line (shown in the detail of Figure 3.7), which contributes about 350 electrons at 77 K. The width of the line has been increased in a revision in order to make this contribution negligible. A second contribution, on the order of 100  $e^-$ , was due to the dielectric loss from the capacitor (220 pF) used to simulate the wire (the cases of MICA and NPO ceramic were compared). This contribution would not be present with the input connected to a sense wire in the TPC.

Each channel is equipped with an injection capacitor which can be used for test and calibration and can be enabled or disabled through a dedicated register. The injection capacitance has been measured using a calibrated external capacitor. The measurements show that the calibration capacitance is extremely stable, changing

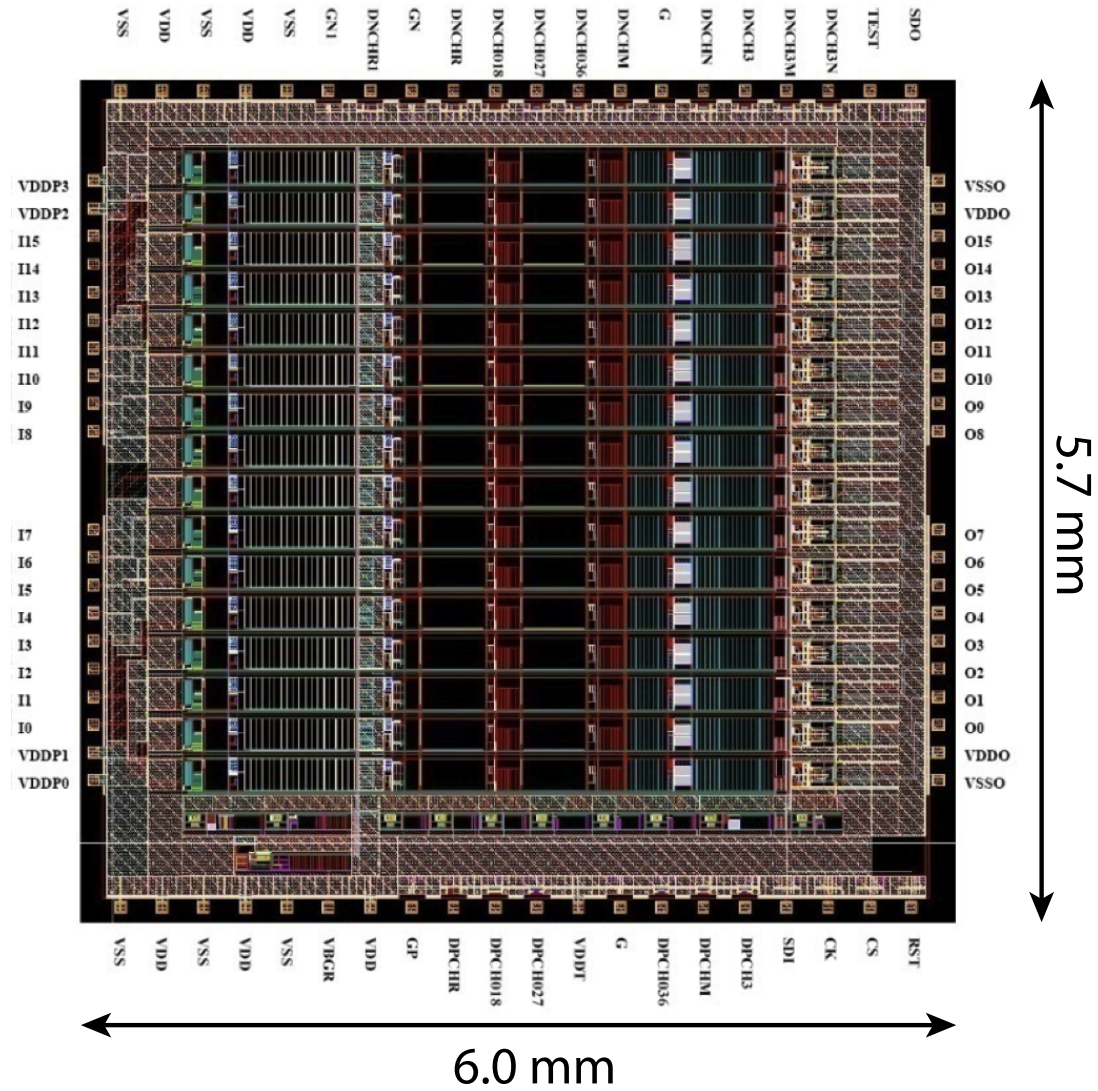


Figure 3.5: The layout of the 16-channel analog FE ASIC

fig:elec\_FE\_AS

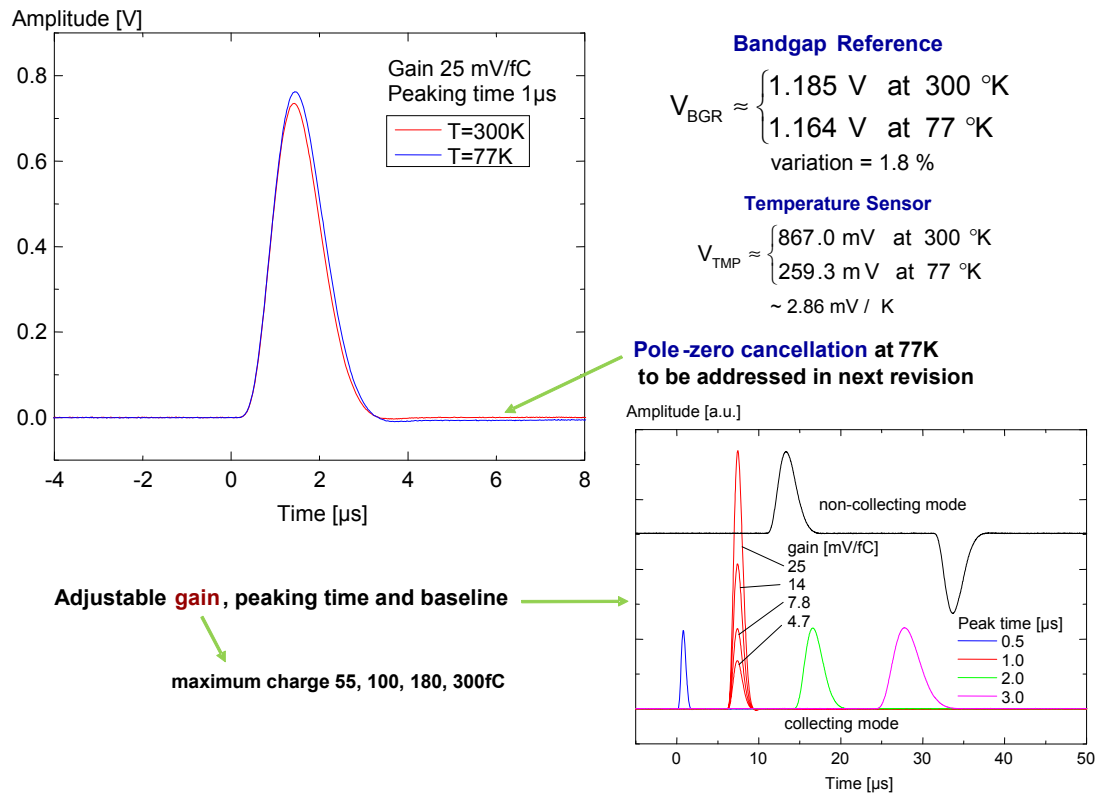


Figure 3.6: Measured pulse response with details on gain, peaking time and baseline adjustments

fig:ce\_elec\_sh

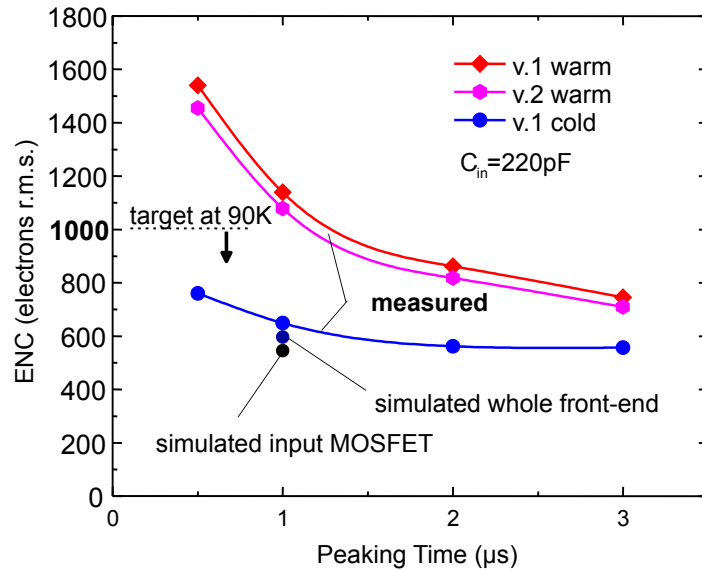


Figure 3.7: Measured ENC vs filter time constant from the first two versions of the analog front end ASICs

fig:ce\_elec\_en

from 184 fF at room temperature to 183 fF at 77 K. This result and the measured stability of the peaking time demonstrate the high stability of the passive components with the temperature. Channel-to-channel and chip-to-chip variation in the calibration capacitor are typically less than 1%. Measurements are being carried out on the individual test structures fabricated on this ASIC to confirm device models and design guidelines.

The development of the ADC ASIC is also using CMOS process (0.18  $\mu\text{m}$  and 1.8V). A 16-channel ASIC has been prototyped and tested. The layout of the ADC ASIC is shown in Figure 3.8. The ADC ASIC has 12-bit resolution, 2 MS/s sampling rate, built in FIFO, two 8:1 multiplexing and two pairs of serialized output. The ADC is a complex design, which has more than 300,000 transistors. All of the transistor design has been done following the rules for long cryo-lifetime.

The ADC ASIC has an input buffer with offset compensation to match the output of the FE ASIC. The input buffer first samples the input signal (with a range of 0.2 V to 1.6 V), then provides a current output after compensating for offset voltage error. This current output is then supplied to the ADC which converts the input to digital in two phases. The MSB (Most Significant Bit) 6 bits are first determined followed by the LSB (Least Significant Bit) 6 bits. After the conversion the thermometer code is



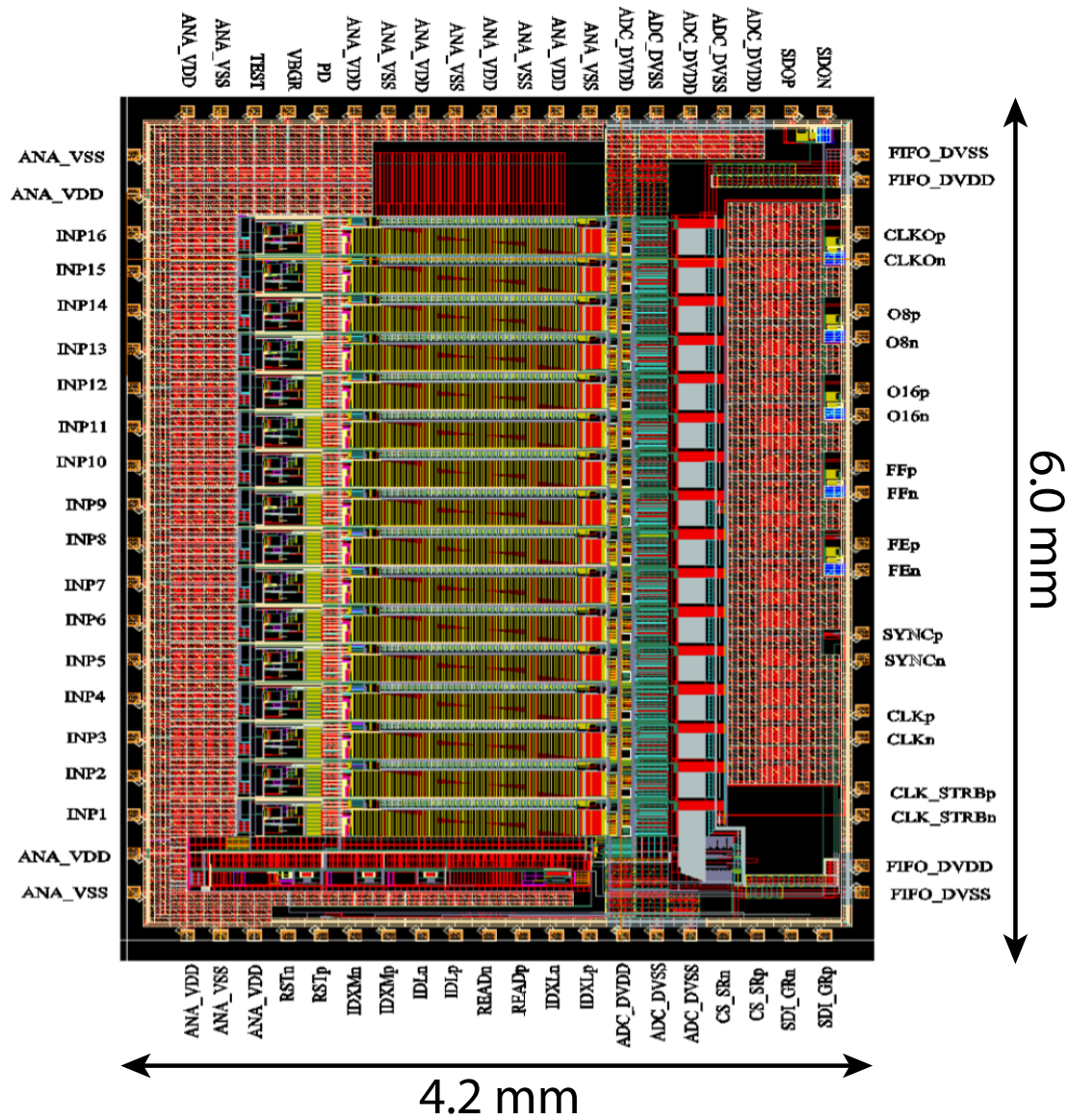


Figure 3.8: The layout of the 16-channel ADC ASIC

fig:elec\_ADC\_A



converted to binary and latched. The output of ADC 16 can be monitored externally. The data from the 16 ADCs is transferred in parallel to the FIFO block. The built-in FIFO is 32 bits wide and 192 bits long, it has the full and empty indicator flags to make it easy to interface to FPGA or digital ASIC. The ADC along with the input buffers are biased internally using a bias generator and a bandgap voltage reference. The bandgap voltage (VBGR) can be monitored and/or controlled externally. It can be put in the low-power sleep mode, and woken up in less than 1  $\mu$ s.

The ADC ASIC has now been through four design/fabrication/testing revision cycles. Prototypes from each cycle have been evaluated and characterized at room (300 K) and liquid nitrogen (77 K) temperatures. During these tests the circuits have been cycled multiple times. The effective resolution with reference to the input referred noise is  $\sim 11.6$  bits at both 300 K and 77 K. The differential non-linearity (DNL) is less than 4 LSBs for 99% of ADC bins at both 300 K and 77 K. The performance of the ADC meets the far detector requirements.

An analog front-end ASIC was adopted by the MicroBooNE experiment in 2010.<sup>[3]</sup> The fabrication and installation was successfully completed in early 2014, and now a total of 8,256 channels (516 FE ASICs) instrument the MicroBooNE TPC. A total of 2,048 channels (on 128 FE ASICs and 128 ADC ASICs) are used to instrument the 35-ton LArTPC. The FEMBs have been produced and tested at 300 K and are currently being tested at 77 K before final installation.

### 3.4.2 Cold Digital Data ASICs

The development of the COLDATA ASIC will follow the same general guidelines developed for the cold analog ASICs, but will differ from the analog design in a couple of aspects. It is anticipated that the digital ASIC will make use of a 65-nm CMOS technology and require a digital library with accurate cold timing models allowing for high-level language design and automated place-and-route for design blocks using extensive digital logic.

A block diagram of the COLDATA ASIC is presented in Figure 3.9. The major components of the COLDATA ASIC include a downlink which is required to receive the system clock and the control/download information transmitted from the DAQ. The download data must be transmitted to the FE and ADC ASICs on the FEMB. The system clock will provide a frequency reference to a crystal-based Phase Lock Loop (PLL) which will generate a low-jitter stable clock to the high-speed serializer.

A single COLDATA ASIC on each FEMB will also be receiving the data from each of the eight ADCs on a board. Each ADC will transmit two streams of data at 192 Mbps for a total data input of 3.072 Gbps. All data will be transmitted

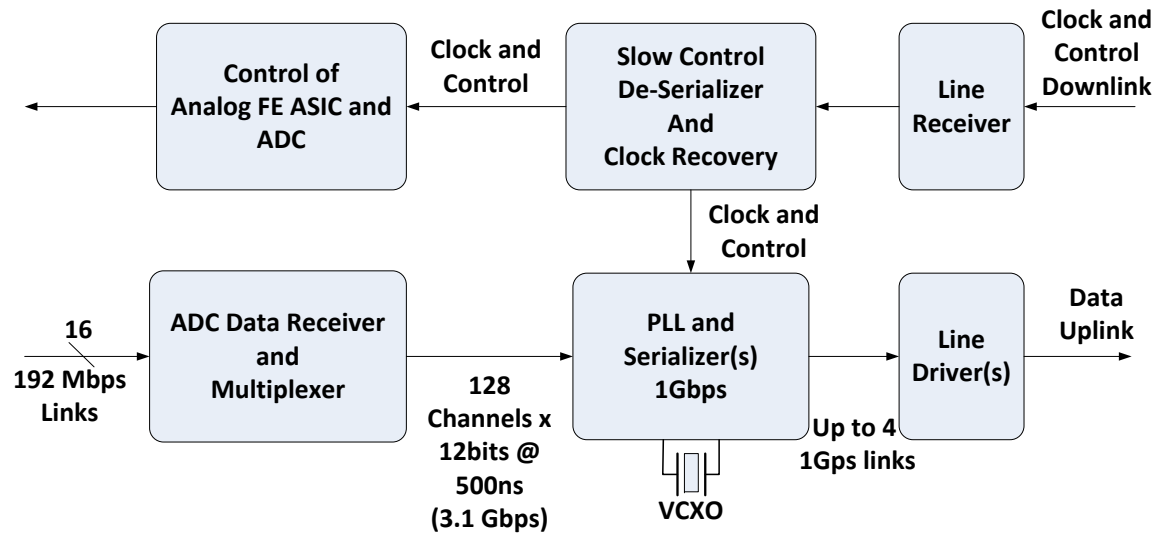


Figure 3.9: Functional Block Diagram of the Cold Digital Data (COLDDATA) ASIC

fig:elec\_COLDDATA

1 off-board to DAQ. Twelve bits of ADC data per APA channel every 500 ns yields  
 2 a single-channel bit rate of 0.024 Gbps. With 8B10B encoding, for example, this  
 3 increases to 0.03 Gbps, plus some overhead for frame data to indicate event blocks.  
 4 Assuming a conservative serial-link transmission speed of 1 Gbps, a single link can  
 5 therefore handle 32 channels. Thus, it is planned to drive four 1 Gbps links from  
 6 each COLDDATA ASIC. A line driver will be designed that is capable of driving a  
 7 copper link for the approximate 20 m required to exit the LAr environment. If a  
 8 speed of 2 Gbps can be achieved, which is possible but not yet demonstrated, the  
 9 number of serial links for data transmission will be cut in half.

### 3.5 Signal Feedthroughs, Cabling, and Power

11 A single type of feedthrough, henceforth “signal feedthrough”, will handle the sig-  
 12 nals, supply voltages and control lines. The TPC data rate per APA, using the full  
 13 event-buffer scheme described earlier, is sufficiently low that it is within the capa-  
 14 bility of a single LVDS channel on copper, with an overall 32:1 Mux and 80 LVDS  
 15 channels per APA. There is, therefore, no need for high-speed optical links inside  
 16 the cryostat, so all cables inside the cryostat will be copper. This has the significant  
 17 benefit of avoiding a major R&D effort which would be required to demonstrate both  
 18 functionality and adequate lifetime of optical converters in LAr. In addition to the

1 high-speed data-output channels, LVDS connections will be made to each APA to  
 2 distribute a clock signal and control information. These data can be transmitted at  
 3 a lower bit rate. Optical fiber will be employed externally to the cryostat, under  
 4 DAQ scope.

### 5 3.5.1 Signal Feedthroughs

6 No specific design for the Far Detector signal feedthroughs exists at this time. We  
 7 are currently exploring the possibility of working in tandem with the Near Detector  
 8 group, which has similar feedthrough needs. This group is starting with a concept  
 9 based on the feedthrough design that has been successfully running in the Atlas  
 10 experiment for about 15 years[19], demonstrating both longevity and reliability. A  
 11 somewhat different conceptual design of a signal feedthrough flange is shown in  
 12 Figure 3.11. Based on a standard 8-in conflats flange with all commercial off-the-shelf  
 13 components, each of these feedthroughs would serve the bias/power/digital IO needs  
 14 of two APAs.

15 All cables inside the cryostat will be attached to their corresponding feedthroughs  
 16 distributed throughout the cryostat roof. The other ends of the cables will be con-  
 17 nected to the matching connectors on the APAs in the cryostat. The cables for the  
 18 lower APAs must be carefully threaded through the hollow frames of the APA stacks;  
 19 these cables will be strain-relieved on the mounting rails above the APAs.

20 The 35-ton prototype detector requires a feedthrough and cable plant similar to  
 21 what a single full-size APA will require and can serve as a model for at least one  
 22 possible solution to the feedthrough problem. In the 35-ton case, a custom printed  
 23 circuit embedded in a single 10-in Conflat flange handles all the cabling associated  
 24 with the TPC and photon detector cabling as well as a small number of cables for a  
 25 specialized camera system to monitor the cathode connection. For the 35-ton APAs  
 26 there are, in addition to the TPC bias voltages, 16 cold electronics boards with data,  
 27 power and control wires plus some 74 photon detector signals on individual cables.  
 28 For a full-size far detector APA there would be 20 electronics boards with simpler  
 29 control and power wiring requirements and rather fewer photon detector cables so  
 30 the 35-ton feedthrough will serve as a good model for what might be done for the  
 31 far detector. While the electrical connection requirements are straightforward, the  
 32 reliable gas tightness of the flange with an embedded circuit board needs to be fully  
 33 verified. Also the planned method of reducing contamination from the cable plant  
 34 in the ullage (the warmer gas phase at the top of the cryostat) needs to be studied  
 35 carefully, as does that for the 35-ton cryostat, which has a much larger ullage  
 36 than that planned for the far detector.

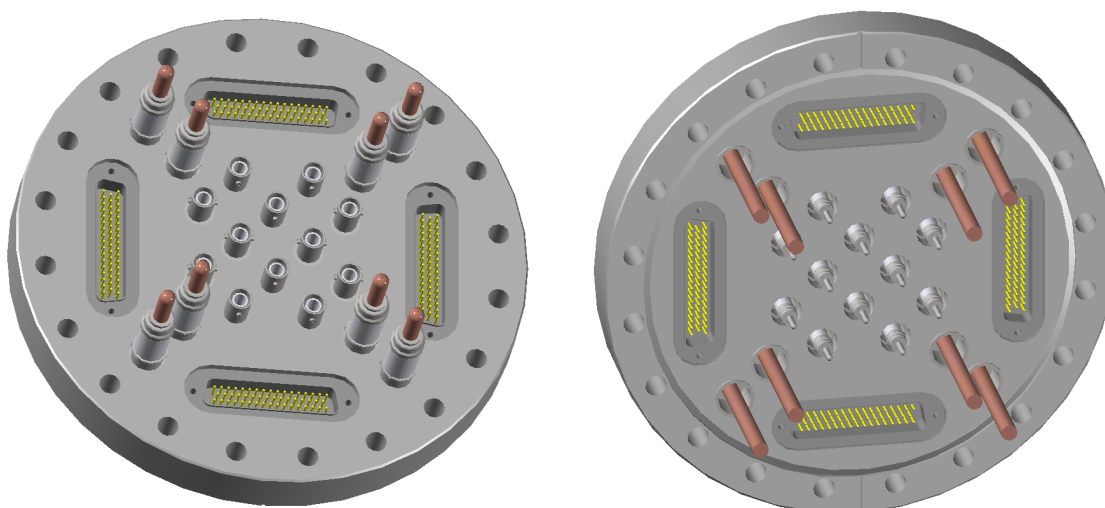


Figure 3.10: A conceptual design of a signal/power feedthrough using all off-the-shelf commercial components

fig:ce\_feedthr

1 Measurements in the Materials Test Stand at Fermilab (described in Section 7.2)  
 2 have shown that impurities (principally  $O_2$  and  $H_2O$ ) embedded in objects submerged  
 3 in the liquid argon do not result in a decrease in electron-drift lifetime, whereas  
 4 impurities in objects located in the ullage do. This indicates the importance of  
 5 minimizing the amount of material in the ullage. It also indicates that it would be  
 6 desirable to connect all cables to feedthroughs below the liquid surface, and then  
 7 pass the cables out of the cryostat, through an evacuated volume that traverses the  
 8 gas and cryostat insulation, to a matching set of feedthroughs to the outside. In the  
 9 35-ton design, a stainless steel tube surrounds the cable bundle in the ullage and  
 10 is partially sealed off below the liquid level to limit contamination. Understanding  
 11 whether a scheme like this would be sufficient for the longer drift lengths in the far  
 12 detector is an important question to be addressed.

### 3.5.2 Cabling for the Cold Electronics

13  
 14 Five basic types of cables will be required to penetrate the cryostat and service the  
 15 Cold Electronics. We will require low-voltage cables to power the FE boards, wire  
 16 bias cables to provide the reference voltages for the wire planes, moderate-speed  
 17 cables for a communication downlink to the FE boards, high-speed cables to carry  
 18 the data out of the cryostat and signal cables to carry the photon detection out.

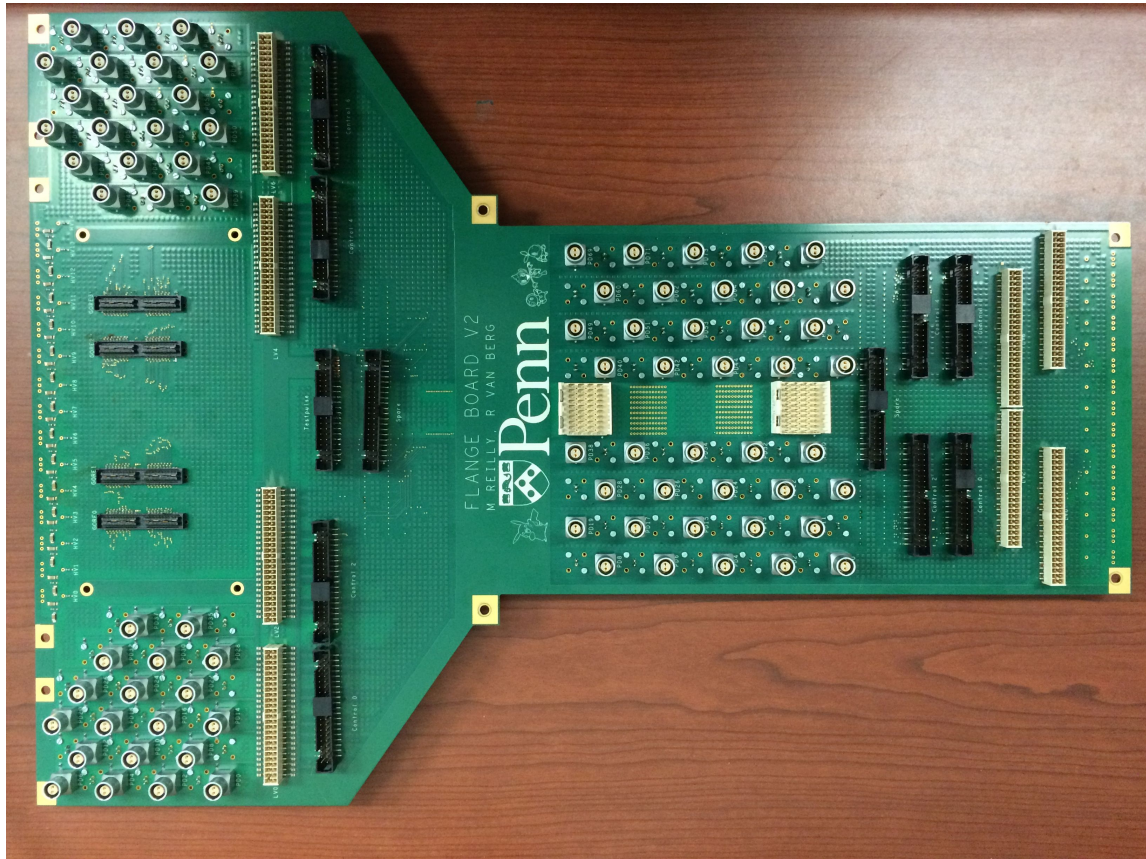


Figure 3.11: Photograph of the 35 Ton “Flange Board”, without the Conflat flange which will be epoxy potted near the center of the printed circuit. This board carries all the electrical connections for the four small APAs in the 35 Ton test cryostat and is similar to the number of connections needed for a Far Detector APA

fig:ce\_feedthr

1 All of these cables will pass through the feedthrough port provided for each pair of  
2 stacked APAs.

3 The cables — and connectors — will be selected to have a low outgas and provide  
4 minimal contamination to the LAr environment. Connectors will also need to be  
5 tested for usage in LAr to make sure that a low ohmic contact is maintained in the  
6 cryogenic environment.

7 We are looking into several types of cables and connectors. The low-voltage  
8 cabling will be chosen based on power needs and whether we decide to go with a  
9 higher-voltage/lower-current feed using DC/DC convertors or a low-voltage/higher-  
10 current feed used by low-voltage regulators. Studies will take place to decide the  
11 most efficient and practical usage.

12 The wire-bias cables must deliver voltages up to two or three thousand volts with  
13 less than a couple of milliamps. We anticipate using a coaxial cable and connectors  
14 which have been tested and found sufficient to provide this load.

15 The cables for the moderate speed downlink could utilize LVDS signaling and low-  
16 skew pairs. Again, testing will be required to select the final cable and connectors.

17 For the high-speed data links, we anticipate using a low-skew copper twinax cable.  
18 We have prototyped such a cable and found that we can drive data at 2 Gbps for a  
19 20 m length.

20 Finally, the photon detector cables currently make use of shielded twisted pair  
21 cables which carry both the DC bias voltage as well as the signals. Future work  
22 involving these cables is described in Chapter [?].

23 It will be important that all cables and connectors be somewhat rugged, locking  
24 and able to withstand a minimum of several tens of mating cycles. This is in addition  
25 to concerns about material compatibility and the fact they must work in the cryogenic  
26 environment.

### 27 3.5.3 Power for the Cold Electronics

28 The power-per-channel for the FE electronics is designed be about 25 mW and the  
29 total low-voltage power requirement for each APA is expected to be about 64 W.  
30 Power will be supplied to the electronics on each APA separately by low-noise power  
31 supplies outside the cryostat, either directly by low-voltage (1.8 V), high-current (36  
32 A) conductors or by high-voltage (48 V) low-current (2 A) conductors to DC-DC con-  
33 verters placed locally in the LAr. The use of DC-DC converters requires conductors  
34 with smaller cross section, minimizing heat input to the cryostat (and ice formation  
35 on the feedthroughs). However, the power dissipated by the (somewhat inefficient)  
36 converters in the LAr will create boiling which may introduce contamination directly

into the high-purity LAr, and if enough LAr is vaporized, may also produce strong mixing of the ullage gas, driving more impurities into the liquid. These effects of boiling LAr, unless they can be demonstrated to be harmless, will drive a preference for eliminating DC-DC converters, and directly powering the front-end readout boards.

Heat conduction through the high-current feedthroughs and the self-heating ( $I \cdot R$ ) of the wires are the factors contributing to additional heat load on the cryogenic system. The sum of these two factors as a function of the wire gauge, however, has a minimum due to the two opposing dependencies on the copper-wire cross section. An optimum wire gauge can be chosen to minimize heat input to the cryostat.

### 3.5.4 Wire-Bias Voltages

Each anode plane assembly requires three bias voltage connections at +820V, -370V, and -665V. The current on each of these supplies is expected to be zero at normal operation. However the ripple voltage on the supply must be carefully controlled to avoid noise injection into the front-end electronics.

The power supplies for the wire bias will be similar to those used for conventional multi-wire proportional chambers. Additional filtering networks will be needed to further reduce voltage ripples. The default feedthroughs are the commercial SHV type. However, other, higher-density multi-channel feedthroughs capable of withstanding the maximum voltage are under investigation.

## 3.6 CE Installation

Cold electronics will be mounted on the TPC and installed inside the cryostat. Because access to the cold electronics is not possible after the cryostat is sealed, a full complement of tests will be performed during the development stage and before the final installation (Figure 3.1).

### 3.6.1 Prototype Testing

Dedicated test boards for the FE ASIC and ADC ASIC, were used to characterize the performance of prototype ASICs at both 300 K and 77 K, and taking them through multiple thermal cycles. An automated test board was built for the FE ASIC to evaluate large numbers of FE ASICs at room temperature, and another such board is currently being designed for the ADC ASIC.

The development of the FE and ADC ASICs has proceeded through a series of prototype designs. A 128-channel prototype analog mother board has been developed and tested in the lab. Together with an FPGA mezzanine in place of the digital ASIC mezzanine, they form a FEMB for use in the 35-ton prototype TPC. A test stand has been developed to test the FEMB using a commercial FPGA evaluation board as a mini-DAQ system. All evaluation test data are stored on a desktop PC and analyzed to determine whether the board is ready to be installed on the detector.

During the prototype testing, a procedure has been developed for the production test of the cold electronics boards. This includes key parameters (gain, noise, non-linearity, etc.) that should be tested, detailed steps of the test to collect data and extract these parameters, and also the work flows to perform the test at both 300 K and 77 K.

Prototype cold electronics has been tested with prototype TPC and DAQ system, to evaluate the performance of the APA assembly, and help the development of the DAQ software. A vertical slice test has been used as the test bed for the integration test. It is an important step to identify potential issues, check out system integration and performance before the installation into the cryostat.

### 3.6.2 Assembly Testing

The front-end readout boards will be thoroughly tested. A testing program has been identified:

- A small number of the ASICs will undergo a complete suite of tests, including thermal cycling to determine the batch yield.
- If the yield is high ( $> 95\%$ ), all ASICs will be mounted on the front-end boards. Tests will be performed on each board and bad chips replaced as needed.
- If the yield is not high, an automated test fixture will be fabricated to validate every ASIC chip before mounting on the readout boards. Board-level tests after mounting the ASICs will be conducted.
- The fully assembled front-end boards will be thermally cycled multiple times while connected to a simple DAQ system to ensure reliable operation.
- After the front-end electronics boards have been installed on an APA, an initial calibration of all electronic channels will be performed. The electronic gains and noise levels of all channels will be recorded in a database.



- Electronic calibration on all channels will be performed while the APA is cold and again after it is warmed up. Significant differences in the cold and warm calibration results will be investigated and remediated.

### 3.6.3 Commissioning

During installation, the DAQ system will be running continuously. As soon as each stack of APAs is connected to the pre-routed cables, a suite of calibration runs will be performed to validate that all connections have been made properly. Repair or replacement at this stage will still be straightforward.

Following the installation of the APAs and the sealing of the cryostat, another complete test will be performed to verify the integrity of the cold electronics before the filling with argon. After the cryostat is filled with LAr and the detector is cooled down, an electronics calibration test will be performed to evaluate the detector performance prior to data taking.

# Chapter 4

## Data Acquisition

ch:trig

The data acquisition (DAQ) subsystem provides the data collection in a robust fashion and optimized for the specific needs of the long-baseline neutrino and underground physics of the experiment. The scope includes design, procurement, fabrication, testing, delivery and installation of a combination of custom and commercial electronics modules, (including commodity computing and networking hardware), as well as both commercial and internally developed software.

The LBNE DAQ must collect data from (a) interactions which are associated with the beam, (b) high energy ( $> 100$  MeV) interactions which are asynchronous such as atmospheric neutrinos, proton decay, cosmic ray muons etc., and (c) low energy interactions such as those from diffuse supernova neutrinos or a possible supernova explosion in our galaxy. For case (a) and (b), it is essential to record the maximum information about each event — the design presented allows collection of all the LArTPC data with no zero suppression whatsoever. For supernova physics, it is essential to have the maximum possible uptime, to be sure data is being collected when a supernova occurs. The sensitive time needed for a supernova is at least 10 seconds, during which the data flow will increase dramatically, and zero suppression of some form will be required. The design follows many of the principles of other neutrino and collider experiments with scope for a multi-level trigger and continuous readout to cope with events, such as atmospheric neutrinos, that are asynchronous with the beam.

An innovation of the LBNE DAQ is a modular DAQ design, as described in Section 4.12, which extends the modularity of the LBNE far detector design and facilitates both staging and a possible distributed (worldwide) approach to design and procurement. It allows the different detector sections to be operated independently, and in so doing allows an added degree of robustness to data collection, in particular

supernova burst detection, by giving a method for eliminating entirely even short periods when the entire detector is off. It also allows for unique design features in the different detector sections of LBNE.

The majority of this chapter describes the full conceptual design for the main data acquisition which could be used in all, or just some of the detector sections of the experiment. This is the reference design, used in the 2015 cost and schedule estimations for LBNE.

The main data acquisition is introduced in Section 4.1. It is composed of a readout for the LArTPC based on Cluster-On-Board (COB) modules (Section 4.2), a readout for the photon detectors based on SSP modules (Section 4.3), a time synchronization system (Section 4.4) and a readout and trigger generator for auxiliary signals associated with the experiment (Section 4.5). The real time data collection is performed by a toolkit called artDAQ (Section 4.6) that will implement two arms of data collection, event-building and processing; one of these is primarily dedicated to collection of full non-zero suppressed data for the most important triggered events such as beam or atmospheric neutrino candidates; the other arm receives zero-suppressed data from the whole detector for all times, it is responsible for deadtimeless triggering in software of these important events, has ring-buffers to store potential supernova events, and records low energy physics events. The run control (Section 4.7), online monitoring (Section 4.8), slow control (Section 4.9) and infrastructure for the DAQ subsystem (Section 4.11) are also described. There follows the description of the modular DAQ design approach as introduced above, in Section 4.12. This allows a heterogeneous approach to different detector sections of the DAQ and gives the ability to keep the majority of the detector running when one part needs to stop data taking for maintenance.

## 4.1 Introduction

### 4.1.1 System overview

The DAQ subsystem will perform the primary functions of:

- Readout of raw data from the LArTPC electronics and the photon detector subsystem,
- Continuous filtering and assembly of data to be treated offline as individual events, including receiving and using the Fermilab beam-spill signal,
- Logging data to persistent storage media,

- 1     • Configuration, online calibration/checkout, and control of operations of detec-  
2       tor electronics, including the generation and distribution of timing and control  
3       signals,
- 4     • Control of, and readout of data from, devices providing real-time information  
5       on detector, subsystem and environmental conditions, and
- 6     • Providing user/operator interfaces for these functions via a run control system.

7     A reference design for the DAQ subsystem is presented in this chapter. The  
8     development of this design is guided by recent experience gained in the development  
9     of relevant systems for the MINOS, NO $\nu$ A [20] and MicroBooNE [13] experiments,  
10    as well as from experiments with comparable channel counts and/or experimental  
11    conditions, such as D-Zero, CDF, NA48 and ICARUS. Guidance and experience is  
12    also available from the design and operation of the LBNE 35t prototype and the  
13    future CERN testing program.

14    The DAQ subsystem is to be located external to the cryostat vessel, with compo-  
15    nents in the detector halls (sharing rack space near the cryostat feedthroughs with  
16    the photon readout, and the power supplies for components inside the cryostat) and  
17    in an underground computer room for the trigger and data collection computers. A  
18    small computer room on the surface will also be required for GPS units and network  
19    connections between the fiber underground and the network to connect to Fermilab.  
20    It is not decided yet whether a larger control room or computer room on the surface  
21    is needed in addition to the one underground. The interfaces to this work package  
22    are with the front-end electronics for the LArTPC, the photon-detector subsystems  
23    and the offline computing.

24    To increase robustness and up-time, the modular DAQ design concept makes a  
25    comparatively loose coupling between the DAQ subsystems in each detector hall, to  
26    allow calibration or maintenance to proceed in one, while data collection continues in  
27    the others. The DAQ subsystem includes the run of optical fibers to the surface for  
28    transfer of data, GPS time synchronization and e.g., telephone. The DAQ subsystem  
29    interfaces with the Fermilab Accelerator complex (the beam-spill signal), and has a  
30    read-only interface with the cryogenics subsystem for logging of conditions.

31    The DAQ subsystem reference design described in this chapter is shown in Fig-  
32    ure 4.1 and consists of the following components:

- 33    • logic and processing elements called “Reconfigurable cluster elements” (RCE)  
34      residing on daughter cards in standard ATCA crates located in the detector  
35      hall to receive data from the LArTPC; these carry out data merging, buffering

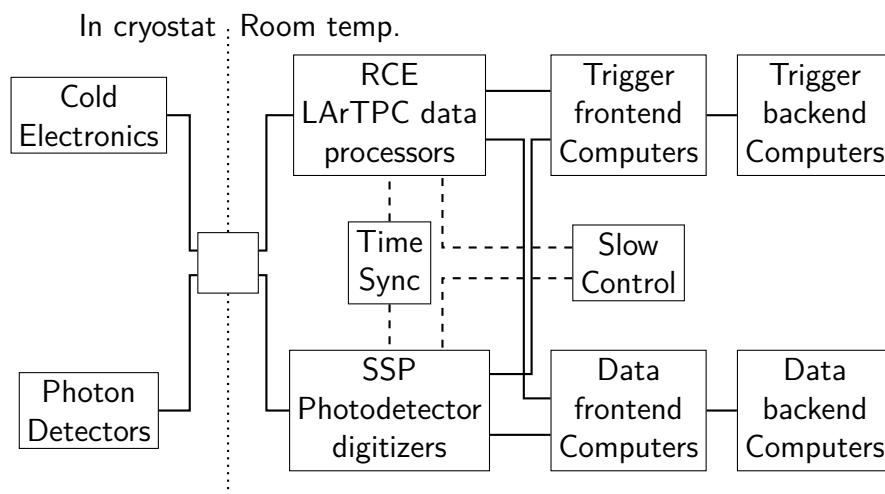


Figure 4.1: Block diagram layout of the main components of the DAQ subsystem.

fig:daq15\_main

1 and compression and transmission to the local farms of commodity computers  
 2 (see Section 4.2)

3 • custom ‘SSP photon detector digitizers’ which digitize and process the light  
 4 signals (described in Section 4.3)

5 • two local farms of commodity computers providing two separate branches of  
 6 readout, triggering, event processing and logging of the detector computers;  
 7 these use the artDAQ toolkit for data acquisition systems (see Section 4.6)

8 • a custom timing system consisting of a master unit, situated on the surface, that  
 9 locks onto a GPS clock and distributes timing signals to the data concentrator  
 10 modules via slave units (see Section 4.4)

11 • dedicated computer nodes that host run control, online monitoring, database  
 12 services and slow controls processes

13 The DAQ subsystem does not include power-supply hardware for the LArTPC or  
 14 front-end electronics, nor does it include the cryogenics subsystem process-control  
 15 and monitoring functions. The SSP readout modules for the photon detector sub-  
 16 system is included in that part of the project.

## 4.1.2 Physics Considerations

The physics considerations determine the scale of the primary tasks of digitizing the LArTPC data readout, merging the photon system data, event building and online processing. In addition to rates for processes of interest, the DAQ subsystem design depends critically on the specifications for the LArTPC and front-end electronics systems, chosen to satisfy the LBNE physics requirements. The sampling rate of 2 MHz has been chosen so as to achieve the required position resolution along the ionization drift direction. Obtaining sensitivity to signals that occur independently of the LBNE beam spill, such as those from nucleon decay, atmospheric neutrinos or supernova-neutrino bursts, requires a free-running transmission of data from the LArTPC front-end electronics. In principle, this same technique can be used to collect the beam events as well, however the robustness of the beam data collection will be supplemented by transferring knowledge of the spill times from Fermilab to the far detector site using GPS.

The task of data transfer is facilitated by multiplexing and utilizing high-speed data lines (1Gbps) in front-end ASICs in the LAr, and by data lines that provide connection to data-acquisition hardware located outside the cryostat. The hardware receiving the raw TPC data then perform zero-suppression and/or data compression, as desired. A challenge in real-time is to use the information of the channels which have hits on them in a particular interaction to determine a larger set of channels, which includes the surrounding ones, that should be read out. The design, as depicted in Figure 4.1, addresses this difficulty by using two data paths. The trigger data path continuously receives the data from the channels that the online hardware determines have hits on them. This determines whenever an event occurs and designates regions of interest that are to be read out in more detail. Ring buffers in the RCEs store the non-zero suppressed data until the region-of-interest information is received. At that point they transmit non-zero-suppressed data to the second path, the data path, which, within the entire event drift window period, reads out the interesting events (all candidates of cosmic rays, beam events, atmospheric neutrinos, proton decays, etc.) for all channels within active APAs with no zero suppression. This allows the maximum available information for these, the most important LBNE events, to be recorded for offline analysis using e.g., Fourier transform deconvolution techniques.

The trigger data path handles all the zero-suppressed data and can store it for long periods, either in  $\mathcal{O}(\text{hours})$ -long ring buffers or in permanent offline storage for collection of data from a supernova neutrino burst. Experience from Micro-BooNE, which has a similar division of lossy-compressed and lossless-compressed data readout, will be vital in optimizing this feature of the data acquisition. During a supernova neutrino burst, the data path may also be used for data collection; the

optimum way for utilizing this is still to be studied.

In addition to physics considerations, the DAQ design goals include minimizing the impact of single-point failures, maximizing the uptime and maximizing the use of commercial components. The robustness is addressed in part by some redundancy (and ability to cross-check) between the two arms of data transfer shown in Figure 4.1, and by the separation of sub-system control in different detector sections of the experiment (Section 4.12).

### 4.1.3 Event Rates and Timing

For the reference design described here, sited at the 4850L of the Sanford Laboratory, the atmospheric-muon rate is small enough — 0.1 Hz within the full LAr-FD active volume — to contribute only negligibly to the DAQ bandwidth requirement.

Signals associated with beam events will be localized within the LArTPC and synchronous with discrete ( $\mathcal{O}(1\text{ s})$  rep rate) beam-spill intervals spanning approximately  $10\mu\text{s}$  and will take  $\mathcal{O}(2\text{ ms})$  for the ionization drifting in the LArTPC to take place. However, other physics events of interest will occur at random times, and can be dispersed throughout the TPC volume as in the case of neutrino bursts from supernovae. Other specific signatures, such as very slow-moving magnetic monopoles ( $\beta < 10^{-3}$ ) may involve signals spanning sample times exceeding the ionization-drift time.

Cosmic-ray muons dominate the physics rate, even at the proposed 4850L site. However, this rate is negligible with respect to noise sources. The reference design proposed here would be capable of operation at shallower depths, up to about the 800L, without significantly impacting the design.

As described in Section 3.3, the cold electronics for a single Anode Plane Assembly will consist of twenty 128-channel Front-End Readout Boards, each providing four digital inputs to the RCEs. The Front-End Boards will generate non-zero-suppressed data, i.e., a constant data rate of  $(1.5\text{ bytes/sample} \times 32\text{ wires/link} \times 2 \times 10^6\text{ samples/wire/s}) = 96\text{ MB/s}$ .

Radioactive decay from  $^{39}\text{Ar}$  and  $^{85}\text{Kr}$  in the LAr, and to a lesser extent from detector materials (U/Th/Co/K), is estimated to provide a 65-kHz/APA rate of activity of energy above about 300 keV (0.3 MIPs) but less than  $\sim 5\text{ MeV}$ , while electronics noise (assuming 10:1 S/N for 1 MIP, and a threshold of 0.3 MIPs) will contribute a relatively low rate per APA of singles. The data rate from cosmic ray muons at the 4850L is considerably lower. Table 4.1 provides a summary of these rate estimates.

The conclusion from Table 4.1 is that the average data rates out of the front-end

Table 4.1: Per-APA estimates of rates and data sizes/rates for various processes. Mbps denotes millions of *bits* per second. Unless otherwise stated, estimated numbers of samples and data rates assume suppression of signals below 0.3 MIP. ‘Inst. Data Rate’ refers to the number of bits in a 2.3-ms long data block divided by this time interval, while ‘Avg. Data Rate’ factors in the process rate. A 12-bit ADC is assumed, and no allowance is made for data items such as time-stamp, etc.

Process	Rate (kHz/APA)	Samples (per APA)	Inst. Data Rate (Mbps)	Avg. Data Rate (Mbps)
Generic 2.3 ms interval (not zero-suppressed)	0.43	$1.06 \times 10^7$	55,000	55,000
Cosmic ray muons (4850L)	$6 \times 10^{-7}$	$5 \times 10^4$	260	$1 \times 10^{-4}$
10 GeV EM shower	—	$1 \times 10^6$	5,200	—
Radioactivity: $\gamma$ : U/Th	$\sim 1$	40	0.48	0.48
$\beta$ : $^{39}\text{Ar}$ , $^{85}\text{Kr}$	63	24	18	18
Electronics noise (not common mode)	$\sim 1$	15	0.2	0.2

q-signal-rates



electronics system are manageable: about 20 Mbps of ‘salt and pepper’ per APA due to radionuclides in the Ar and LArTPC materials. Large beam- or atmospheric-neutrino interactions or showering ultra-high-energy cosmic-ray muons will result in high (Gbps-level) instantaneous rates on the scale of the maximum ionization drift period, but contribute negligibly to the average rate.

#### 4.1.4 Architecture Summary

The reference design of the DAQ system is summarized in block-diagram form in Figure 4.1. Component counts are given in Table 4.2.

Table 4.2: DAQ subsystem component counts for one 10-kt module/cryostat.

Quantity	Description
250	COBs (Cluster on Board) each with 8 RCEs,
26	14-slot ATCA Shelves
27	Ethernet Switches (one 10G, 26 1G)
26	TPC Readout Compute Nodes
1	Master Timing Unit with GPS Receiver
27	Slave Timing Units
11	Event Builder Compute Nodes
8	Other computing nodes (server, run control, slow control etc)

## 4.2 TPC Readout

The primary interface between the TPC front-end electronics (FE) and the DAQ subsystem consists of an ATCA-based system of RCEs (Reconfigurable Cluster Elements). The RCE system receives the serialized raw data for the FE, stores it with no zero suppression in ring buffers for later retrieval if a valid trigger is received, performs zero suppression on it to send to the trigger-arm. It packetizes and transmits the resulting data to the back-end farms for event building and further processing. Additionally, the RCE system transmits timing and control signals to the FE and forwards configuration data to them at start-up.

The RCE system consists of the following components: a commercial ATCA shelf (2-, 6-, or 14-slot), a Cluster-On-Board (COB) which is the “front board” in ATCA terms, and a Rear Transition Module (RTM) which is the “rear board.” The COB is a custom board, developed by SLAC, which holds the processing power of

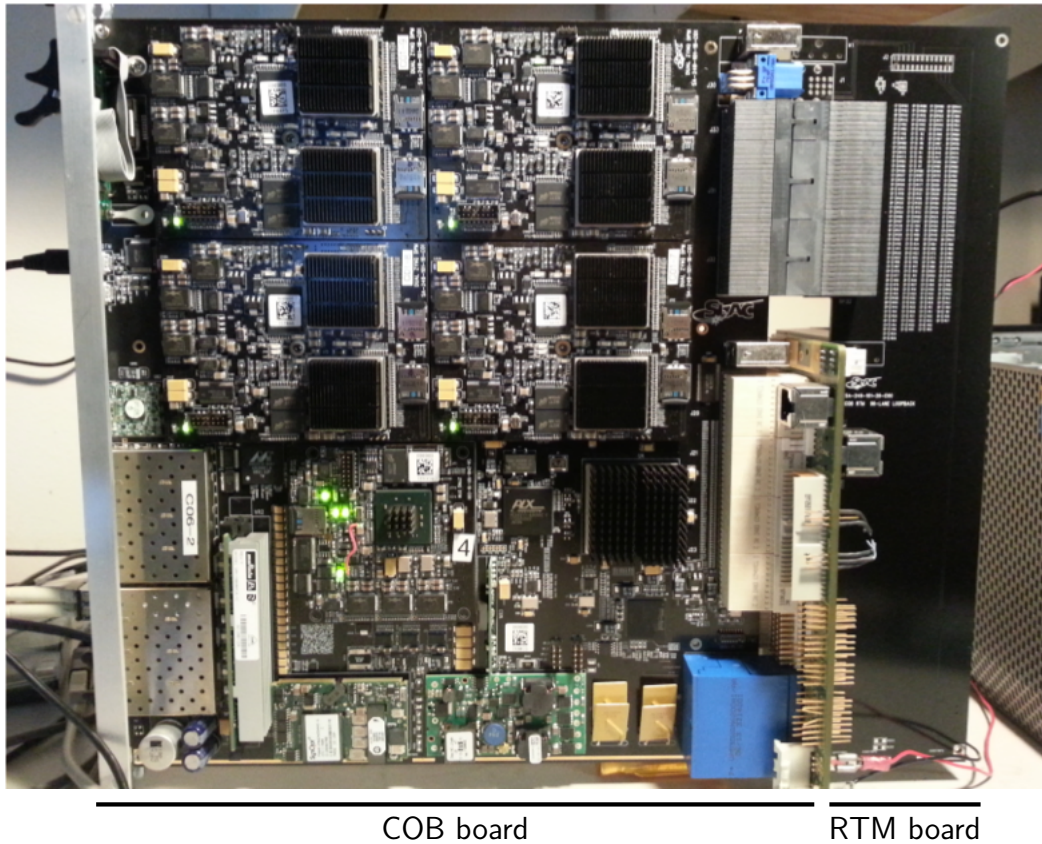


Figure 4.2: The COB (left) and RTM (right). The eight black square units near the upper-left of the COB modules are the RCEs.

the system. The COB (see Figure 4.2) consists of five bays for holding daughter boards, an onboard 10-GbE switch, and both 10- and 1-Gb ethernet connections for communications with the back-end system. Four of the daughter-board bays are for Data Processing Modules (DPM), each of which can hold up to two RCEs. The RCE is the core processing unit of the system; it is made up of a modern “system-on-chip” (SoC) — currently, the Xilinx Zynq-7045 — with multiple high-speed I/O ports (up to 10-Gbps each) and 1 GBytes of external DRAM and flash memory controllers. The other bay on the COB contains the Data Transmission Module (DTM), which is responsible for distributing timing and trigger information to and between the DPMs.

While the COB hardware is application-agnostic, the firmware and software on

the RCE and the RTM boards are application-specific. The RTM provides the mechanical and electrical interfaces between the front-end (or, in our case, the flange electronics) and the back-end, as well as other external sources such as the timing or trigger systems. In the case of LBNE, fiber optic connections are used between the flange and the TPC DAQ using QSFP+ connectors. This provides the required ground isolation. These links are used for data transmission from the cryostat and also provide the synchronization clock to run the ADCs. Currently, each RTM can accommodate up to 16 QSFP+ connections.

With the assumption that each cold FE board multiplexes its 128 wire channels to four outputs at 1-Gbps each, the non-zero-suppressed data for one APA can be fed into a single COB (containing eight RCEs). Each RCE would receive data from two FE boards, perform zero suppression, and send the result to the trigger front-end computers. There would also be a large DRAM ring buffer to store a non-zero-suppressed copy of the data, which would be read out on request (see Figure 4.1) to the data front-end computers.

Figure 4.3 shows a COB in a two-slot ATCA shelf. There are some options regarding the physical distribution of the shelves. One option is to have a smaller shelf at each flange port, each shelf collecting data from the two or four APAs accommodated by that port. Alternatively, the fibers from all APAs could be routed to a central location into a smaller number of large ATCA-shelves.



Figure 4.3: A front view of the ATCA crate with a COB in the top slot.

## 4.3 Photon Detector Readout

The photon detection system is digitized and readout by a custom module called the SIPM signal processor (SSP) which is described in detail in Section 5.6. The module has ADC- and signal-processing hardware. The output of the SSP is Ethernet, interfaced with the same Xilinx Zynq architecture as the COB that is used for the

1 LArTPC data. The SSP therefore is able to provide control, data and slow-control  
2 monitoring independently of each other, which facilitates a consistent interface be-  
3 tween the hardware and software parts of the DAQ.

## 4.4 Timing System

sec:daq\_time  
5 The requirements of LBNE for timing are comparable to those of the NO $\nu$ A experi-  
6 ment. NO $\nu$ A uses a Global Positioning System (GPS) receiver on the surface, in a  
7 module called the Master Timing Unit (MTU), and a protocol that uses four twisted-  
8 pair connections (on a standard RJ45 connector) to fan out and then daisy-chain  
9 these signals to the electronics. LBNE proposes using the same concept with poten-  
10 tial enhancements and modernization, for distribution of the surface-to-underground  
11 timing among the readout modules for the photon detector and also for distribution  
12 to the COBs for the LArTPC readout. This will maintain a 64-bit counter synchro-  
13 nized to the absolute GPS time on each of these readout modules. In addition, a  
14 separate protocol for synchronization of the cold electronics boards from the coun-  
15 ters on the COBs will be used; this uses the same optical links as the data path  
16 described in Section 4.2. For simplicity, the full 64-bit counter is not used in the  
17 cold electronics, instead, the 64 MHz clock is supplied to the cold electronics and the  
18 higher-order bits on the timestamp added when the data reach the COBs.  
sec:daq\_cob

19 The timing link is the only physical link other than the communications network.  
20 The system described here provides several essential functions:

- 21 • Provides a time stamp so that data can be associated with a specific accelerator  
22 extraction cycle.
- 23 • Provides a common 64-MHz clock to all front-end electronics boards.
- 24 • Synchronizes the data acquisition system so that all data from a given time  
25 period is sent to the same event builder.
- 26 • Provides dynamic synchronization to the cold electronics so that glitches in the  
27 clock signal are detected promptly.
- 28 • Enables calibration and test pulses to be generated simultaneously for multiple  
29 channels.

### 4.4.1 Beam Triggers and Time Stamps

A similar GPS-based system will be used at Fermilab to record the times of the accelerator spills that generate the 10- $\mu$ s bursts of neutrinos. There should be sufficient buffering in the trigger path of the readout system shown on Figure 4.1 so that all data can be buffered while the time stamp of the spill is sent to the far detector over the internet.

Since the Fermilab accelerator complex is timed off the 60-Hz electric line frequency from the local power company, and the time between accelerator cycles is a variable number of 60-Hz periods, it may be possible to predict the time of the spills and avoid the need for such a long ring buffer. Experience on MINOS and NO $\nu$ A have shown that the variability in the 60 Hz is too great to accurately predict the arrival time of a burst of neutrinos in the future for those scintillation detectors, however LBNE has a considerably longer readout window (several drift times) — long enough that it could work.

A 64-bit time stamp has been chosen for the 64-MHz clock so that all detector and accelerator data will have unique times throughout a 20-year run of the experiment. This will allow correlation with non-accelerator physics events such as supernovae as well as such things as equipment failures.

### 4.4.2 Front-End Clocks

The LBNE detector has very low noise front-end amplifiers. The APA system is connected to 7-meter-long wires so that noise pick up from the clock is a significant concern. One way to nearly eliminate this noise is to select a clock frequency that is well outside the bandwidth of the front-end electronics. This has proven to be very effective in several other experiments. A frequency of 64 MHz has been chosen for this design. The internal capacitance of the SiPMs in the photon system limits the useful frequency range to below about 30 MHz. Thus, a double-pole (6 db/octave) filter can be placed in front of the digitizers. This reduces any noise from the clock system by 12 db. The SiPM's have large internal gain, so 12 db coupled with careful cable design should be adequate to eliminate any possible clock noise.

The LArTPC front-end amplifiers digitize at 2 MHz. The Nyquist frequency is 1 MHz, so a 4-MHz single-pole filter is quite adequate. Any noise from the clock system is then suppressed by 48 db, which should be adequate for this system.

### 4.4.3 Time stamping and synchronization

The transfer of counter synchronization from the master timing unit (containing the GPS receiver) to the 64-bit counters in the readout modules is achieved using the four twisted-pair lines. Three of the four lines send signals from the master to the readout modules and are used for (a) the continuous 64-MHz clock, (b) a serial command line and (c) a SYNC line. The fourth line, operating in the opposite direction, is (d) a return-SYNC. The synchronization procedure occurs in a similar manner to the NO $\nu$ A experiment; The master loads a predetermined time in the near future over the serial command line to a time-load register in all the readout modules. A specific time  $T$  (described in the next paragraph) before the GPS time reaches the predetermined time, the master sends a SYNC to all the modules. The SYNC causes each front end to load its time-stamp register from the time-load register. The time-stamp register then increments on each 64-MHz cycle. This register is 64 bits wide and it is appended to each data packet.

To compensate for the delay in the cables, the SYNC pulse is delayed by a preprogrammed number of 64 MHz steps at the receiving end of each fan-out and daisy chain step. The time  $T$  is chosen so that the loading in each readout module reflects the correct GPS time. As in the NO $\nu$ A timing system, the cable delays are determined automatically with a special delay-calibration sequence in which outgoing SYNC pulses are returned immediately over the return-SYNC line to the preceding fanout which measures twice the delay. As the detector is nearly a mile underground, the four signals (a)-(d) will be converted to optical for the journey down the shaft. The delay on this link will be large, and will be measured and corrected by the same procedure as described above.

The data rates at the far detector are low enough that a software trigger can be used instead of a dedicated hardware trigger. This system operates by sending data to a special trigger farm. This requires that all the data come from the same physical time period. The time stamp system easily provides this synchronization. Each front end has a “data enable” bit that must be set before any data is recorded. At initialization, this bit is turned off. When the synch signal arrives to load the time stamp register, it also sets the “data enable” bit. Since this occurs at the same physical time for the entire detector, it provides the necessary synchronization. The data acquisition software need only monitor the “data enable” to know when data taking has started. It can read the time load register to know the time that data taking started.

#### 4.4.4 Dynamic Synchronization and Executes

For the LArTPC readout, 64-bit registers exist in each of the COBs. For simplicity, only the 64-MHz clock is transmitted upstream and fanned-out to the cold electronics, not the absolute synchronization to GPS of any counters. To insert time markers on this clock line, phase encoding (or equivalently, modification of the mark-space ratio) is used. The first use of this technique is to detect and correct for possible glitches on the clock line that could put the data stream off by one or more bits resulting in lost data. This is achieved by phase-encoding the start of a 16-channel conversion cycle on the clock line. If the front end was not internally at the start of a conversion cycle, it would reset its internal clock and send out an error message. The warm electronics would also check the phase-encoding to spot failures in the clock distribution system. The second use of the phase encoding is to send an ‘execute’ pulse to the cold electronics which can be used to cause calibration pulses to appear all at the same time. These techniques are used successfully on the MINOS experiment.

### 4.5 Readout of Auxiliary Signals

In addition to the main readout of the LArTPC and photon detector systems, a certain number of auxiliary signals may need to be read out. A trigger module, designed for the 35t test, will be used to perform trigger counter logic and supply external calibration pulsers with triggers at predetermined times. This module is connected to the time-synchronization network as described in Section 4.4. It is read out using a Xilinx Zynq FPGA using the same techniques as for the RCE system. At the CERN single-phase test, this module will also be used to record beam counter information and to digitize the warning of extraction from the SPS accelerator. The module will be retained for the far detector operation for calibration triggers and to readout auxiliary information into the data stream such as e.g., the phase of the 60-Hz line voltage for correlated noise studies.

### 4.6 Event Building and Triggering

Subsequent to the data collection and processing by the RCE system (for the LArTPC), the SSP (for the photon detectors) and the auxiliary readout module, the data is passed to the two local data processing farms, as described in Section 4.1.2 and shown in Figure 4.1, to perform the triggering and event building. Event data will be staged locally before being transmitted in quasi real time for archival to persistent storage

1 (nominally the primary store will be at Fermilab, and the responsibility of the DAQ  
 2 will end when it reaches this store; it will then be copied to further locations).

### 3 4.6.1 artDAQ

4 The data acquisition software in both of the local processing farms of commodity  
 5 computers will be based on artDAQ, which is a toolkit for building DAQ systems.  
 6 It has been developed at Fermilab, written in C++11 and is in use in several other  
 7 experiments. Within artDAQ, core DAQ functions are provided by the toolkit, and  
 8 experimenters develop the modules that perform the functions specific to the ex-  
 9 periment. For the 35t detector, LBNE collaborators have developed modules that  
 10 configure and read out the RCE and SSP boards that are connected to the LArTPC  
 11 and photon system detectors, respectively. Other members of the experiment are de-  
 12 veloping reconstruction and filtering software modules that will analyze the data as  
 13 it is acquired. The artDAQ-based DAQ system for the 35t detector has been success-  
 14 fully used to acquire data in electronics and detector-integration tests, and artDAQ  
 15 has been the default choice for the DAQ framework for the full LBNE detector for  
 16 some time.

17 ArtDAQ uses the concept of *fragments*. These are used in different ways in the  
 18 triggering processing farm and in the data processing farm. In the triggering process-  
 19 ing farm, in order to implement a completely deadtimeless trigger, the data are read  
 20 in a continuous stream with no interruption. This is done by reading blocks of data,  
 21 called millislices, corresponding to fixed windows of time immediately adjacent to  
 22 each other. The boundaries between one millislice and the next are at precisely the  
 23 same time across all the subcomponents of the readout, as determined by the 64-bit  
 24 time counters, which are synchronized as described in Section 4.4. The triggering  
 25 front-end computers (Figure 4.1) receive zero-suppressed data from one particular  
 26 part of the readout of the detector and parcel it up into blocks corresponding to  
 27 the millislice interval. These are the fragments in artDAQ terminology. The data  
 28 from the beginning of the time interval of one fragment is copied into the end of  
 29 the preceding fragment to provide sufficient overlap for correct treatment of neutrino  
 30 events close to the boundary of the millislices.

31 ArtDAQ designates a back-end trigger farm node for each millislice in the se-  
 32 quence to allow parallelization of the triggering and event-building processing. One  
 33 fragment from each front-end is sent to each back-end node in sequence so that the  
 34 back-end node receives all the data from the whole detector for one millislice period.  
 35 The number of back-ends operating in parallel can be extended if the processing  
 36 required is large. The trigger farm back-end then runs triggering algorithms on the



1 data to recognize periods of time with clusters of hits corresponding to neutrino,  
2 cosmic ray and other interactions in the detector. The times and locations within  
3 the detector corresponding to interactions are communicated to a centralized trigger  
4 master.

5 In addition, the trigger back-end nodes store all the zero-suppressed hit data in  
6 data files locally, in order to provide a historical buffer of hits for supernova studies.  
7 As storage costs decrease, it may become possible to store this data indefinitely, but  
8 even with current disk storage capability, the history of many hours of data may be  
9 buffered in case a supernova is detected by some other group elsewhere in the world.  
10 The trigger master will also provide a self-trigger mode for supernova detection by  
11 receiving a summary of the number of hits above a threshold from the back-ends  
12 for each millisecond. If an increase in interactions, integrated over  $O(100\text{ ms})$  or  $O(1\text{ s})$   
13 indicates a possible supernova, the data in the data storage for that period will be  
14 retained indefinitely.

15 The second local data processing farm operates in a similar way to the first, except  
16 the object of this farm is to collect *all* the data, rather than just the zero-suppressed  
17 data, during the full drift time for the interesting interactions (beam or atmospheric  
18 neutrinos, proton decay candidates, cosmic muons, etc.). The data is stored in ring  
19 buffers in the RCEs while the trigger processing farm is working on the data. The  
20 trigger master will communicate trigger information (including a mask indicating  
21 the ‘regions of interest’, i.e. which APAs), which determines the time interval and  
22 which APAs to readout as a complete event. The *fragment* in the data processing  
23 farm corresponds to one trigger. The fragments are merged in exactly the same way  
24 as in the trigger farm, i.e., all the fragments corresponding to one event are sent to a  
25 particular data farm back-end for merging. Further trigger processing is possible at  
26 this stage. The events are written to disk file and transferred to the host laboratory  
27 for data archival.

28 In thinking about the data acquisition system for a reconfigured long-baseline  
29 neutrino experiment, it is recognized that using a toolkit such as artDAQ has advan-  
30 tages in that it allows experimenters to leverage existing infrastructure and focus on  
31 developing only the components that are necessary for their experiment. In addition,  
32 there are advantages to using the same event analysis framework online and offline  
33 (artDAQ uses art). This allows experimenters to develop and substantially test their  
34 software in an offline environment and only include the full DAQ infrastructure for  
35 final testing.

## 4.7 Run Control

The LBNE run-control system will be the primary control and monitoring interface to all data acquisition detector systems for use by detector operators and other users. This run-control system will provide several key functions that will make the collections of specific data acquisition and monitoring systems (referred to as “components”) appear as a single, integrated system with a common control, monitoring, alert and information display interface. If the modular DAQ design concept described in Section 4.12 is adopted, the run control will independently control each detector section, with a separate run-state while an overall user interface will give an overview of the state of all the detector sections. This common view of the “system of systems” will ease the training burden on detector shift operators, allowing for rapid response in the event of system error conditions.

The design is modeled on the successful IceCube Neutrino Observatory experiment-control system, known as IceCube Live[21]. The overall design presented here is simplified, since the geographical and networking constraints for LBNE are considerably more straightforward than for the extremely remote South Pole site.

The run-control system has a modular design, which is shown in Figure 4.4. It has a dedicated Run Control server, which handles the control messages and communication with the components, the GUI and command line front-end control interfaces, and the database server to manage recording of reported information in an organized form.

### 4.7.1 Control and Monitoring of LBNE Components

The run-control system provides a control and monitoring interface that can be integrated into each component. This allows operators to monitor and change the state (for example: Running, Stopped, or Error) of each component. This component control will be available by both command line interface and a web GUI. This centralized control of all components that make up DAQ systems will support complicated dependencies between components, for example a requirement that the DAQ be in a running mode before starting a calibration system.

### 4.7.2 Display of Component Monitoring and Alerts

During normal operation, all LBNE components will report system monitoring and health values to the run control and will be available for graphical display. These values can include items such as overall component health, trigger rates, memory

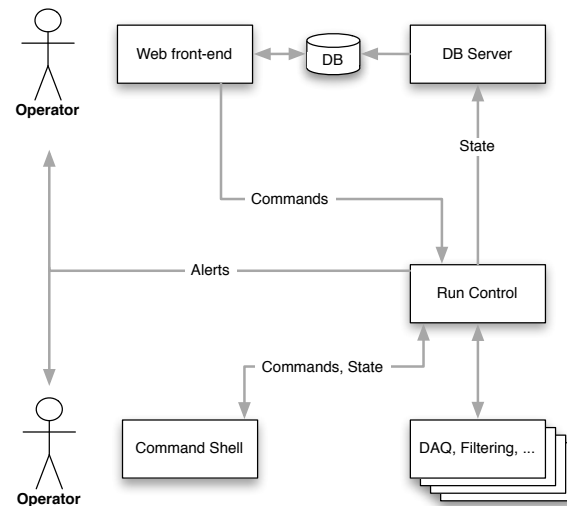


Figure 4.4: LBNE run control system design.

fig:expcont

1 buffer status or rack temperatures. These values will be archived in a database and  
 2 be presented in a detailed GUI. This interface can be customized to the intended  
 3 audience, with shift operator pages presenting just high-level status information,  
 4 and expert views that show detailed, per-channel information for use in detector  
 5 debugging.

6 Historical views of component monitoring information will also be available via  
 7 the user interface. This enables exploration of historical reported information and  
 8 correlation analysis between detector components. Detector components are not  
 9 required to be under LBNE run-control-state control, but can simply report useful  
 10 information. This type of reporting-only integration could potentially be useful for  
 11 offline systems, and would allow the creation of a more complete historical view of  
 12 detector history, with information from data collection displayed side-by-side with  
 13 information from offline data analysis.

14 The LBNE run control can also generate alerts to detector operators and/or  
 15 component experts if reported monitoring information is outside expected ranges or  
 16 a system component is in an error state. These alerts can take any form (email, SMS,  
 17 etc.) and will be a unified mechanism for alerting operators/experts of operational  
 18 issues.

### 4.7.3 Management of Per-Run Information

Run control is responsible for assigning a unique number to each segment of data collected by the data acquisition system (commonly referred to as a run number), as well as collecting all user settings selected for a run. This information will include identifiers for the configurations used, components selected for operation during a run, and any provided operator comments. This information will be stored in a database, and made available for collaboration-wide use in online and offline analysis processes.

### 4.7.4 Run-Control Technology

The run control uses several standard network and web technologies. These include:

- XML-RPC - A remote procedure-calling library using XML-formatted messages to issue commands to remote processes, allowing the run-control server to remotely control components
- JSON - An open standard for message formatting that allows arbitrary data to be packaged in a human-readable format using name-value pairs for transmission. Used by the run-control components to format and send arbitrarily complex monitoring records.
- ZeroMQ - A high-performance message transport system that allows a large number of clients to report information to the run-control server.
- DJANGO - A graphical web content framework that can easily query and display information from database records. The run-control server stores recorded monitoring information in database tables, which are available for graphical presentation within the web-base user interface.

While these technology choices are selected for their robust designs, the modular design of the LBNE run-control system allows for flexibility in utilizing other technologies as replacements.

## 4.8 Online Monitoring

Rapid access to the data during data collection will be provided by the artDAQ framework and used for making online monitoring histograms and event display. The online monitoring histograms will be used to display the performance of the detector

sec:daq\_om

1 including e.g., noise rates, dead channels and the online drift-velocity measurement.  
2 A framework based on the ATLAS LHC experiment online monitoring will be used to  
3 display the histograms and associated historical data. Since the data are presented  
4 in the art framework online, the development of new histograms can be easily made  
5 offline first.

## 6 **4.9 Slow Control Systems**

### 7 **4.9.1 Monitoring**

8 The slow-controls system will allow monitoring of data both within and outside  
9 normal data taking. The central server is based on the same infrastructure as the  
10 run control described in Section 4.7. It will accept individual ZeroMQ messages  
11 from subsystem components containing measurement readings and will store them  
12 in a database on a server at the far detector. This database will be replicated to  
13 a server at Fermilab which will allow access via the standard offline interface being  
14 developed at Argonne National Lab, based on the NO $\nu$ A database system.

15 The slow control will generate status and historical plots of the monitored values  
16 on demand from the run control DJANGO system so that shift-takers and experts  
17 can access the information easily through the same framework as the run control.  
18 Alarms will be used to notify shift-crew and experts of values that are beyond their  
19 normal range.

20 Several example data collection routines which send the zeroMQ message to the  
21 central control will be provided, e.g., for the Wiener power supplies, the rack pro-  
22 tection units, the SSP monitoring functions, the GPS time synchronization and the  
23 ATCA crate managers. Storage of performance parameters derived from inside art-  
24 DAQ, or from the data analysis in the trigger or the online monitoring, will also be  
25 reported by zeroMQ messages to the slow-control infrastructure. Collaborators who  
26 supply nonstandard equipment will be able to provide their own software to send  
27 the zeroMQ messages. A centralized program will harvest read-only data about the  
28 cryogenics and about the beam at Fermilab which will also be available for status  
29 and historical display. All this data will be replicated to Fermilab and accessible  
30 offline through the LBNE offline database framework.

### 31 **4.9.2 Slow Control**

32 The control functions of the LBNE slow control will allow experts to power off/on  
33 crates and racks remotely when it is necessary to restart the experiment after a crash,

1 and no DAQ expert is present underground, e.g., during off hours. The rack protec-  
2 tion system will automatically shut down electronics if a smoke, over-temperature or  
3 absence of cooling condition is detected (independently of the slow controls). The  
4 slow controls will provide the interface to set up the rack protection thresholds and  
5 to send reset commands after a trip.

6 The slow control will have no control over the cryogenics system or the beamline  
7 at Fermilab; it will only provide a display of harvested monitoring data.

## 8 4.10 Interface between DAQ and Offline Computing

9 The online DAQ system must be closely coupled to the offline data processing and  
10 analysis software in order that the data that is collected can be studied easily.  
11 Although there are some software libraries in common between online and offline, the  
12 requirement that the online should have a high uptime means it must be ready to  
13 run on demand, whereas the offline code can wait for short periods if bugs in the  
14 latest code need to be fixed. Therefore the online will use relatively stable, frozen  
15 versions of the software packages.

16 The default output format for artDAQ is readable by the art framework directly.  
17 As described in Section 4.12, the data will be stored briefly at each detector section  
18 and then a merging job will form complete ‘runs’ corresponding to all the data in the  
19 entire detector for a given running period. This will be archived to Fermilab, recorded  
20 in the run control database and accessible directly by the offline reconstruction and  
21 analysis programs.

22 As described in Section 4.9, the access offline to the slow-control monitoring data  
23 will be handled via replication of the online slow-control database tables to Fermilab  
24 where they will be accessible via the standard database-access tools developed for  
25 LBNE. The data will be accessible using the time as a key, rather than e.g. the run  
26 number so that the slow control can provide monitoring information independent of  
27 whether a run is in progress or not.

28 This method will also be used to give offline access to the run-logging database  
29 table that provides information about each run taken by the DAQ. The values of  
30 parameters used to configure the experiment at the start of each run will also be  
31 stored in database tables and made available in this way.

## 4.11 DAQ Infrastructure

### 4.11.1 Wide Area Network

As in the case of MINOS and NO $\nu$ A, it is expected that event data can be transmitted over the network to Fermilab. Although rates for events of interest are comparable, data throughput for the LBNE LArTPC is expected to be at least an order of magnitude higher. A bundle of single-mode fibers (the latest estimate is a 96-fiber bundle) should be sufficient for transmitting the data from all four 10-kt modules to the surface, for transmitting the GPS synchronization underground (independently for each of the four 10-kt modules) and to provide expansion capacity.

### 4.11.2 Online Data Storage

To protect against significant periods of absent network connectivity, it is desired to store a significant amount of the data emerging from the DAQ to local storage. A local data storage facility of  $\sim 100$  TB is expected to be more than adequate for five days worth of detector data, even without prescaling cosmic-ray muon events. This storage is provided by a RAID disk array on one of the computing nodes in the trigger farm.

### 4.11.3 Power and Cooling

Power and cooling requirements for the DAQ system described here are fairly modest. COB modules operate at around 100 W each and the commodity computers for the data collection and triggering operate at around 200 W each. More detailed power measurements will be provided by the 35t test to refine these numbers and add the other electronics components into the estimate.

## 4.12 Modular DAQ Design

The modular DAQ design concept described here allows the detector sections of the experiment to have semi-independent and autonomous data taking — essentially each detector section has sufficient components (timing system, readout of detectors, data storage and database storage) to run on its own, and also to maintain an independent run-control state. The modular DAQ design allows the detector modules to be monitored and controlled as a single big detector, for simplicity in operation. It also allows triggers in one detector section to initiate data collection in the other

1 detector sections. This strategy addresses the problem of ensuring that the possibility  
2 of a supernova occurring while data is not being collected is very close to zero,  
3 as long as power is present underground. It leverages the inherent redundancy,  
4 without increasing cost, in the modular nature of the experiment. It also has benefits  
5 in staging and allowing different detector sections to implement different readout  
6 features.

7 The essential difference between the modular design and a single data acquisition  
8 for the entire far detector is that if one detector section needs maintenance, or if the  
9 data collection stops due to a communication problem or other reason, the unaffected  
10 detector sections will continue data collection uninterrupted. If the complete detector  
11 is not in data taking mode, this will be indicated on the operations status and  
12 alarms screen, and the operator will be able restart the detector section and add  
13 it back into the overall run. The run-log database will indicate the periods when  
14 any compartment is missing from the overall data collection. Given the rarity and  
15 scientific value of a supernova event, it is deemed essential to do everything possible  
16 to ensure continuous operation of at least part of the detector at all times. The  
17 modular DAQ design concept will improve overall uptime of the detector.

18 Each detector section runs as a separate data acquisition system with all the real-  
19 time functions capable of being run independently. Each compartment has its own  
20 run-start and run-stop mechanisms (with a standardized interface for initiating these  
21 commands and obtaining state status information); its own timing system (required  
22 to be synchronized to UTC to within  $10\ \mu\text{s}$ , although it is likely with GPS that a more  
23 stringent limit will be met by the individual detector sections); its own data storage  
24 and data catalogue (with a standard format for data and for indicating the period  
25 of collection in each file). Each detector section will also have its own independent  
26 storage for slow-control measurements.

27 A centralized ‘manager’ for triggers across the entire detector will be imple-  
28 mented. The timing requirements for the communications protocol with the manager  
29 should not be more stringent than needed for operating an individual detector sec-  
30 tion alone. The individual detector sections are able to report when they detect an  
31 activity that warrants triggering of the adjacent (or all) detector sections; this could  
32 be detection of e.g., a cosmic muon, atmospheric or beam neutrino. These reports  
33 are likely to occur only once every minute, and a maximum acceptable reporting  
34 rate will be about one every five seconds. The reports should arrive at the central  
35 manager within 150 ms of the event occurring.

36 The readout in the detector sections should be capable of storing the complete set  
37 of signals for at least 200 ms. The central manager will report back to the detector  
38 sections within this time any requests from adjacent detector sections to collect data



1 within a certain period. The central manager will also distribute the spill timing  
2 from the beam to the detector sections. It is likely that the communication between  
3 the detector sections and the central manager will be implemented via a dedicated  
4 Ethernet network. To establish a connection setup to the central management service  
5 the individual detector section will subscribe to it; if the central management is not  
6 present or stops, the detector section can run independently (although, in this case,  
7 it will not receive trigger requests from the other detector sections).

8 The modular run control will consist of a dedicated run control for each detector  
9 section that permits run-starts, run-stops, monitoring, logging, run-mode selection  
10 and configuration. The run control functionality can vary between detector sections,  
11 but will conform to a standard overall scheme to allow control and monitoring of the  
12 entire experiment via a single interface. A separate section of the run-control will  
13 give the overall status of the detector sections. All detector sections are expected to  
14 be taking data in production configurations; anything else will be regarded as a fault  
15 situation.

16 The ability for the run-control to treat the detector sections as autonomous and to  
17 provide an overall status are the required features of the real-time portion of the DAQ.  
18 The status portion runs offline, shortly after the data collection has been completed,  
19 operating as a batch system on a farm of computers. The individual detector sections  
20 will have data files spanning different periods of time; this operation combines the  
21 data into a single sequence of time-ordered files for archival and production use  
22 offline. The beamline status and monitoring data will be transferred from Fermilab  
23 and incorporated into the files as if this data came from another detector section.

# Chapter 5

## Photon Detector

ch:photon

### 5.1 Introduction

Liquid argon is an excellent scintillating medium. With an average energy needed to produce a photon of 19.5 eV (at zero field) a typical particle depositing 1 MeV in liquid argon will generate 40,000 photons with a wavelength of 128 nm. At higher fields this will be reduced but at 500 V/cm the yield is still about  $\sim 20,000$  photons per MeV. Roughly  $1/4$  of the photons are promptly emitted after about 6 ns while the rest are emitted with a delay of 1100-1600 ns. LAr is highly transparent to the 128 VUV photons with a Rayleigh scattering length and absorption length of <sup>1</sup> 95 cm and  $>200$  cm respectively [?]. The relatively large light yield makes the scintillation process an excellent candidate for determination of  $t_0$  for non-beam related events. Detection of the scintillation light may also be helpful in background rejection.

### 5.2 Requirements and Goals

#### 5.2.1 Beam-based physics

There are no requirements for the beam-based physics program, as the accelerator clock will provide a  $t_0$  with roughly  $10 \mu\text{s}$  resolution. Given that the electron drift is  $1.6 \text{ mm}/\mu\text{s}$  the uncertainty to the electron lifetime correction is small when the beam timing is used. The photon system can be useful in determining the  $t_0$  of cosmic ray events and events from radiological decays as well as giving a handle to the location of beam events in the LAr volume with respect to fiducial boundaries. The impact

<sup>1</sup>A new result determines the Rayleigh scattering length to be 55 cm [22] RAYLEIGH NEW

of the LAr scintillation light on the detector performance needs to be determined, but it is expected that its role in reducing backgrounds for the oscillation program will not introduce additional requirements to the photon system design.

## 5.2.2 Proton Decay and Atmospheric Physics

The photon detector system must provide the  $t_0$  for non-beam related physics channels if a correction for electron recombination during drift is to be applied. The requirements for electronics and hadronic energy resolution for the proton decay and the atmospheric neutrino program are  $1\%/\sqrt{E(\text{GeV})} \oplus 1\%$  and  $30\%/\sqrt{E(\text{GeV})}$  respectively [5]. With these resolutions the collected charge must be accurately corrected for recombination. Therefore the photon system must provide a  $t_0$  for particles with  $>100$  MeV with  $>95\%$  efficiency in the fiducial volume of the detector.

## 5.2.3 Low-energy Physics

Supernova events will produce neutrinos down to about  $\sim 5$  MeV. Studies have estimated the momentum resolution for 5 MeV electrons to be 20% using only TPC information and assuming a highly efficient trigger and an electron lifetime of 5 ms. The impact of various detector resolutions on the physics potential of LBNE has not been studied in detail. At present there is no strong requirement that the energy resolution must be better than 20%, so no requirement on the photon system trigger efficiency is set at this time. However it is clear that if a better detector design, with higher photon collection efficiency, can be found then the energy resolution could be significantly improved. A goal of the photon detection R&D is to develop a system with the lowest possible threshold for a reasonable cost.

## 5.2.4 Required Performance

To achieve the physics goals in the previous section the performance of the photon detection system must be understood. The prototype readout electronics described in Section 5.6 have been shown to detect the single photoelectron (p.e.) signals associated with the late scintillation light but future versions may sacrifice this ability to mitigate high channel costs. It is assumed that the physics goals of the photon detection system will be met using the prompt scintillation light.

The performance, or overall photon collection efficiency, is given by the following, where it is assumed only prompt light is collected:

$$\frac{N_{pe}}{MeV} = N_{128} \cdot \epsilon_{geom} \cdot \epsilon_E \cdot \epsilon_{mesh} \cdot \epsilon_{conv} \cdot \epsilon_{capt} \epsilon_{tran} \cdot \epsilon_{QE} \quad (5.1)$$

eff\_eqn

1 The efficiencies leading to the overall number of photo-electrons collected by the  
 2 photon detection system,  $\frac{N_{pe}}{MeV}$ , are given in table ??.

Table 5.1: Individual photon collection efficiencies

Factor	Description	Value	Comments
$\epsilon_{geom}$	geometric acceptance	0.0023	FD optical simulation
$\epsilon_E$	field correction	0.6	500 V/cm
$\epsilon_{mesh}$	TPC wire shadowing	.83 (30-150°)	falls off sharply [23]
$\epsilon_{conv}$	TPB conversion	1	see ref. [24]
$\epsilon_{capt}$	waveguide incident	0.5	about half converted photons travel into waveguide
$\epsilon_{tran}$	waveguide transmission	TBD	prototype dependent
$\epsilon_{QE}$	SiPM QE	.41	SensL C-series

tab:example

3 Using Equation 5.1, and only looking at the prompt photons for a 20 MeV elec-  
 4 tron, it is seen that to detect a 2 p.e. signal, which is likely to be discriminated from  
 5 noise, the required transport efficiency is 5.7%. Of course this value is very position-  
 6 dependent, as the geometric acceptance, wire shadowing and transport corrections  
 7 all depend on the location of the event. It is also expected that there will be a thou-  
 8 sand or so events in 10 kt during the SN burst neutrino arrival and hence detection  
 9 efficiency may be higher due to the increase in number of photons - although for  
 10 triggering the leading edge of neutrino arrivals is most important.

11 An additional possibility is to utilize the delayed photons to increase the number  
 12 of collected photons and effectively reduce the detection energy. As the delayed  
 13 photons are typically detected as single photo-electrons due to the spread over time  
 14 it is important to understand the contrinution of backgrounds coming from SiPM  
 15 dark rate and  $^{39}\text{Ar}$  during the integration window.

16 Figure 5.1 shows the probability of energy deposition from MIPs being detected  
 17 in the photon detectors.

18 The TPC wire mesh shadowing is also quite location-dependent as photon an-  
 19 gles, relative to the wire plane, lead to rapid loss in transmission below 30° and  
 20 greater than 150°. Lastly, the photon detector paddles themselves can have position-  
 21 dependent response to incident photons due to the attenuation length of the wave-

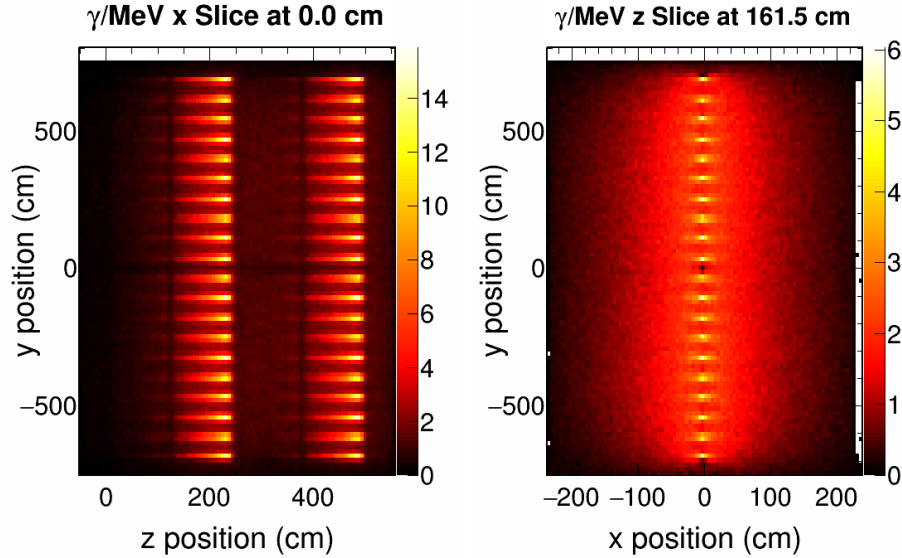


Figure 5.1: Photon map giving the number of photons expected per MeV deposited energy accounting for the efficiencies listed in table ??

fig:photon\_map

- 1 uide. The photon detector simulation, which is nearing stable operation, will be able
- 2 to better estimate the efficiencies coming from geometric acceptance correction.

### 3 5.2.5 General Considerations

- 4 In the event that higher photon collection efficiencies can be achieved it should be
- 5 possible to improve the energy resolution of the detector by adding the photon yield
- 6 to the electron yield information. However this requires significant improvement in
- 7 light collection efficiency, so it is beyond the scope of the present design.

## 8 5.3 Photon Detector Prototype Designs

- 9 All designs considered for the photon detector have been based on the use of wavelength-
- 10 shifting coating, or bulk doping, of plastic materials coupled to silicon photomulti-
- 11 pliers (SiPMs). The reference design utilizes a coated acrylic waveguide coupled
- 12 to SiPMs. This waveguide is described in Section 5.3.1. Alternate waveguide de-
- 13 signs, described in the following sections, have been developed in an effort to optimize
- 14 coverage, cost and attenuation length.

### 5.3.1 Cast or Bulk Doped Acrylic Bars

The reference design for the photon detection system is based on light guides that are coated with wavelength shifter. The 128-nm scintillation photons from liquid argon interact with the wavelength shifter on the light guide surface and light peaking at 430-nm is re-emitted in the bar. The light guide channels the light to photodetectors at its end.

A schematic drawing of a light guide with its photosensors is shown in Figure 5.2. The prototype light guides are bars with a footprint  $2.54 \text{ cm} \times 0.6 \text{ cm}$ . The concept is described in Ref. [25].

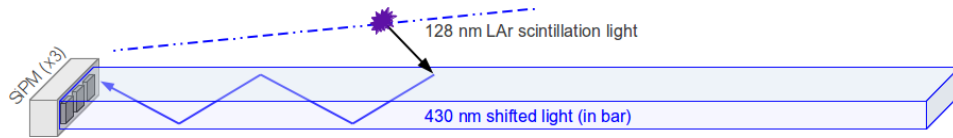


Figure 5.2: Schematic drawing of a light guide with its photosensors. The bars have embedded wavelength shifter (WLS), either TPB or bis-MSB. Three SiPMs collect the waveshifted photons that have been internally reflected to the bar's end.

The wavelength shifter converts incident VUV scintillation photons that strike it into 430 nm photons inside the bar, with an efficiency of  $\sim 50\%$  for converting a VUV to an optical photon [24]. A fraction of the waveshifted optical photons are internally reflected to the bar's end where they are detected by SiPMs whose QE is well matched to the 430-nm waveshifted photons. The light guides were made with one of two wavelength shifters: the conventional TPB (1,1,4,4-tetraphenyl-1,3-butadiene) and the less expensive alternative bis-MSB (1,4-bis-(o-methyl-styryl)-benzene). Preliminary studies with a VUV monochromator show that the two wavelength shifters compare favorably in their waveshifting efficiency [26]. A testing program is currently underway to compare their relative performance in liquid argon.

A team at Indiana University is studying prototype light guides made with three different technologies. These technologies are listed in Table 5.2.

Table 5.2: Light guide technologies

Label	Light Guide Technologies
(a)	clear acrylic, dip-coated
(b)	doped Eljen PVT light guide, dip-coated
(c)	doped Eljen polystyrene light guide, dip-coated

The clear acrylic bars (a) are made from blanks of commercially available Lucite-UTRAN cast UVT acrylic sheet that has been laser-cut and diamond-polished into bars of the proper size. Lucite-UTRAN has the longest attenuation length of the acrylics tested [27]. The Eljen<sup>2</sup> bars (b and c) are commercial light guides that are doped with J2 green fluor (equivalent to Y11). Two types of light guides were purchased from Eljen. The light guides (b) were fabricated from polyvinyl toluene (PVT); these are the standard Eljen product EJ-280. The quantum efficiency of the fluorescent dopant in EJ-280 is 0.86, so the second shift in wavelength does not markedly degrade the photon detector efficiency. The light guides (c) were fabricated from polystyrene; these light guides were ordered because PVT bars can craze if cooled too rapidly. Although the PVT light guides may be brighter, no instance of crazing has ever been observed in polystyrene light guides.

For the acrylic light guides, the WLS must be embedded in the plastic at the bar's surface so that 128-nm scintillation photons can generate optical 430-nm photons within the volume of the plastic. Otherwise the VUV photons will not be trapped by the light guide. For the Eljen bars, the wavelength shifter can either be embedded in the plastic, as with the acrylic, or it can be deposited on a plate or film placed in proximity to the light guides. The J2 wavelength shifter then converts the resulting 430-nm photons inside the light guides where they are channeled to the photodetectors.

To embed the WLS at the surface of the light guides, a “dip-coating” process was developed at Indiana University. Before the WLS was applied to the acrylic bars, the bars were annealed at 80°C for one hour. (The Eljen bars were not annealed.) The WLS was dissolved in the organic solvent, dichloromethane, or DCM, ( $\text{CH}_2\text{Cl}_2$ ). For these waveguides 5 g of wavelength shifter was dissolved in 1,000 gm of DCM. A series of experiments showed that this concentration was optimum. A bar was first dipped into the WLS mixture for 15 seconds and then removed. It was then hung in the dark for at least two hours to dry. Once dry, the ends of the bars were flycut. Currently designs are being fabricated that put an acrylic plate painted with WLS or a thin film impregnated with WLS in front of the Eljen light guides.

In summer 2015 these designs will all be tested side-by-side at the TallBo dewar facility at Fermilab under uniform, low-contamination conditions. In addition to the designs described above, these tests will include photon detector designs from Colorado State University and Louisiana State University. This experiment will compare the relative performance and the absolute efficiency for all designs scaled to 1.5 m.

---

<sup>2</sup><http://www.eljentechnology.com>

### 5.3.2 Fiber-embedded Bulk Acrylic Plate

The LSU group has developed a VUV photon detector design for a large LAr detector that overcomes some of the shortcomings of the present LBNE reference design photon detectors. The LSU photon detector design allows for coverage of a very large area, thereby increasing the geometrical acceptance of the photon detectors. The number of required SiPMs and readout channels per unit detector area covered with photon detection panels has been significantly reduced to keep the overall cost for the photon detection system at or below the present design while increasing the geometrical acceptance at the same time.

The photon detection system consists of a TPB-coated acrylic panel with an embedded S-shaped wavelength shifting (WLS) fiber. The fiber is read out by two SiPMs, which are coupled to either end of the fiber, and serves to transport the light over long distances with minimal attenuation. The double-ended fiber readout has the added benefit of providing some position dependence to the light generation along the panel by comparing relative signal sizes and arrival times in the two SiPMs. Figure 5.3 shows a drawing of the layout and a photograph of a prototype photon detection panel in the test stand at LSU. The incoming 128-nm VUV Ar scintillation light will be converted by the thin TPB layer on the acrylic panel and re-emitted with wavelength peaking at 430 nm in an isotropic way. About 50% of the light is emitted into the acrylic panel where some fraction will be absorbed by the WLS fiber and converted to light with a peak intensity of about 480 – 500 nm. The green light exiting the fiber is well matched to the peak photon detection efficiency of typical SiPMs.

### 5.3.3 Bulk panel production

The photon detection panels are produced from 0.25-inch-thick sheet UVT acrylic and cut to size. For a first series of prototypes the acrylic panel dimensions were chosen to closely match the area of four bars of the LBNE baseline photon detection system described in the previous section. The groove is cut with a CNC mill in several passes to achieve good groove surface quality, which is important for good light transmission from the bulk acrylic to the fiber. The panels are dip coated with TPB and left to dry prior to insertion of the WLS fiber. Panels with two and three layers of fibers inserted and glued into the groove have been produced. Fiber ends are cut and polished. The resulting acrylic panels are then inserted into a custom-made mechanical frame, which was designed by David Warner at CSU. The end caps of the mechanical frame house one SiPM on either end. The presently used  $6 \times 6\text{mm}^2$  active-area SiPMs are spring-mounted to ensure good contact between



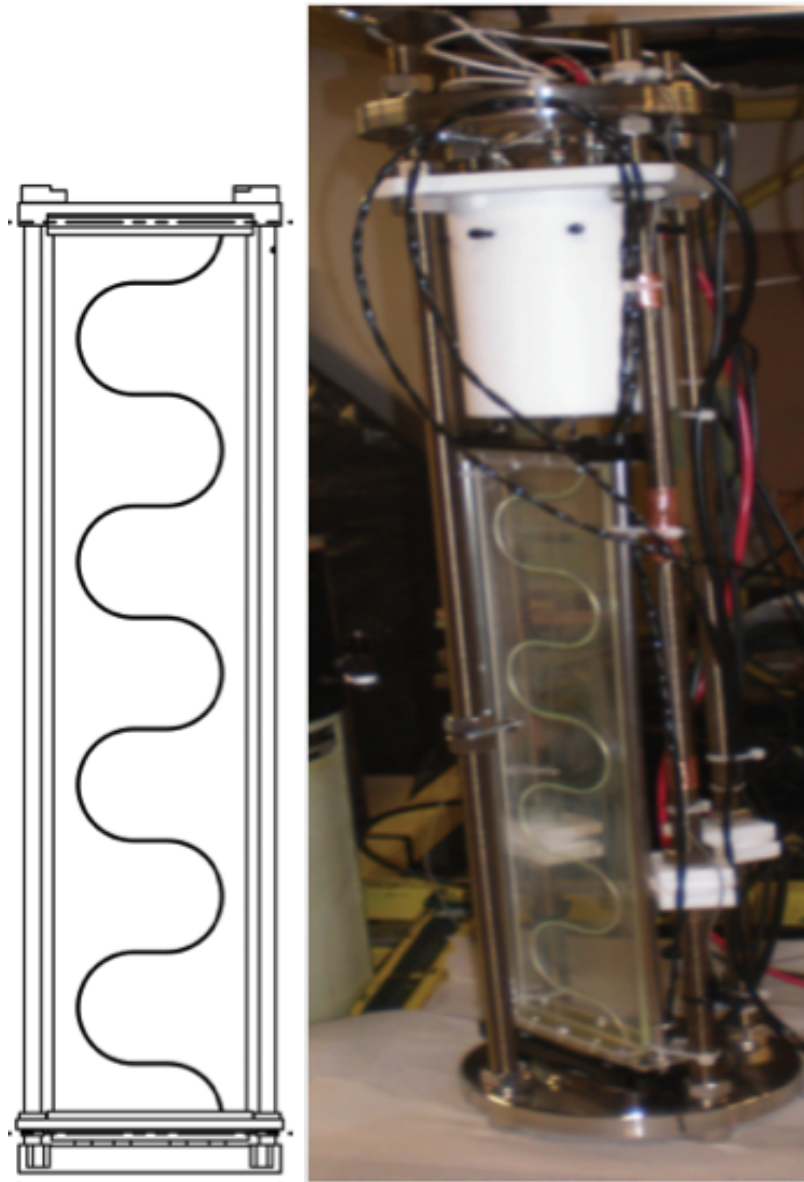


Figure 5.3: LSU photon-detection panel. Technical drawing of a 20''  $\times$  4.33'' acrylic panel with embedded WLS fiber (left) and picture of a prototype in test set-up at LSU (right) with the same dimensions.

fig:1-LSU

the active area and the fiber ends. The leads of the SiPMs are connected to a small Printed Circuit Board (PCB) onto which  $\sim 2$ -m-long twisted-pair coax cables are soldered to supply the SiPM with a bias voltage and to read out signals. The other cable ends are typically connected to pre-amplifiers before leading to a DAQ system. Components for the photon detection panels are inspected at all stages of the manufacturing process for quality. Due to the small number of panels produced to date, no quantitative quality control parameters have been defined yet. Proper connectivity of the fully assembled units are tested in a setup at LSU using a LED flasher. If LED light signals are seen, the panel is successively immersed in gaseous argon (GAr) along with an alpha source. The observation of argon scintillation light originating from alpha particles and cosmic rays penetrating the GAr volume allows for a relatively quick quality-control check of a completed photon detector at room temperature.

### 5.3.4 Prototype Detector Test Results

Several photon detector panels of  $20 \times 4.33 \text{ in}^2$  have been produced and two have been tested in a LAr test stand at CSU. The detectors submitted to the cold test have three and two embedded fibers, respectively, but are otherwise produced in the same way. The data taken in LAr included self-triggered alpha source scans as well as cosmic runs with a muon hodoscope providing a trigger for near-vertical muons penetrating the LAr volume.

**Alpha source runs:** The alpha source was placed at a distance of about 1 inch in front of the center line of the photon panel and moved to 20 different positions spaced about 1 inch apart from neighboring positions. At each position 5000 signal traces were recorded and measurements were repeated for three of the positions to check the reproducibility of the measured light yield. Figure 5.4 shows results for both successively measured panels. The red and blue dots show the mean light yield values in units of p.e. (photo electron equivalents = no. of fired SiPM pixels) for the SiPM on the top and bottom end of the panel as function of source position. Green dots show the sum of both channels. The summed signals provide indicate a very uniform detector response for the entire panel, independent of the alpha source position. The data also indicate good reproducibility for the doubly measured positions. The three-fiber panel shows about 50% more light when compared to the two-fiber panel, which is in good agreement with expectations. It needs to be pointed out that the LAr purity was not monitored and that measurements for the two panels were performed sequentially after refilling the dewar with LAr. However, the liquid argon for both

- 1 measurements came from the same batch, which motivates the assumption that the
- 2 purity for both measurements was very similar.

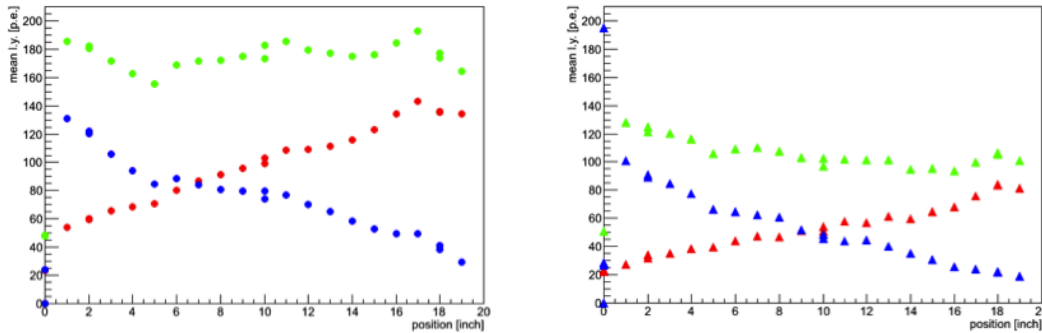


Figure 5.4: Light yield for the three (left) and two (right) fiber LSU photon detection panels in response to a 1-in distant alpha source in LAr. Red and blue symbols represent the mean light yield over 5000 trigger events from a single SiPM each and green points represent the summed signal from both SiPMs.

fig:2-LSU

3 **Cosmic trigger runs:** Two 1"  $\times$  10" wide scintillator counters were placed above  
 4 and below the dewar to form a muon hodoscope and to select near-vertical muons  
 5 traversing the LAr volume. The three-fiber LSU panel and one LBNL/Elgin Bis-  
 6 MSB doped polystyrene bar of LBNE baseline dimensions and read out by three  
 7 SiPMs were simultaneously inserted in the LAr. The setup allowed the study of  
 8 the response of these photon detectors to scintillation light created by penetrating  
 9 cosmic muons. A detailed quantitative comparison of the relative light yield was  
 10 not possible with this setup due to large systematic uncertainties in the position  
 11 dependence of the scintillation light generation by the triggering cosmic muons. A  
 12 qualitative comparison of the detector responses, taken as the signal sum of three  
 13 and two SiPMs for the Elgin bar and the LSU panel, respectively, shows comparable  
 14 light yields as shown in Figure 5.5.

### 15 5.3.5 R&D Work in Progress and Present Plans

16 After the construction and proof-of-principle test of the Lbulk acrylic prototype pho-  
 17 ton detection panels we manufactured several 2.17-m-long and 110-mm-wide (=4.33")  
 18 panels were manufactured to demonstrate the scalability of the design. At the time of  
 19 writing, tests in the large LAr dewar at CSU are in progress. The team is performing

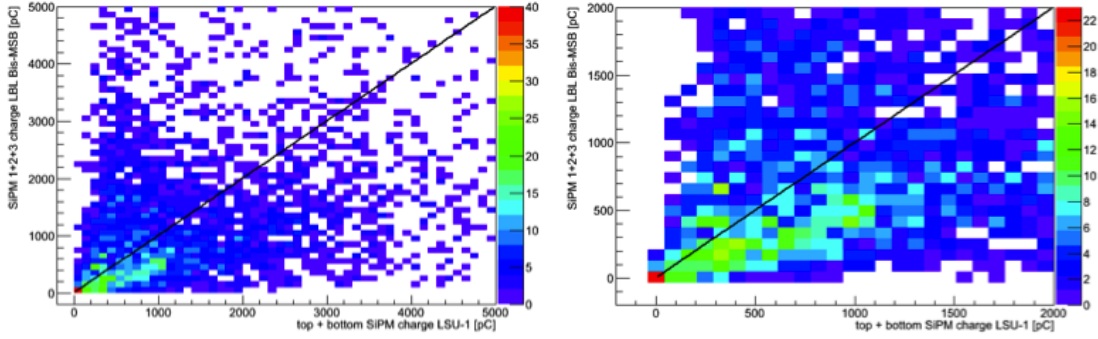


Figure 5.5: Scatter plot of the summed charge of three SiPMs coupled to the LBNL/Elgin Bis-MSB doped bar and the summed charge of two SiPMs for the three-fiber LSU panel in response to an external muon hodoscope trigger. The right plot shows a zoomed version of the left plot.

fig:3-LSU

1 alpha source scans and cosmic muon runs. The alpha source scan runs are arranged  
 2 such that the source illuminates two photon detectors at the same time. This setup  
 3 facilitates quantitative and relative light yield comparison between different photon  
 4 detector designs in the same LAr bath with a well-defined VUV light source.

5 Manufacturing and testing of wider panels is under consideration to maximize  
 6 the photon detector panel area in the DUNE LAr far detector. The goal is to cover  
 7 the entire anode plane assembly (APA) area with photon detectors embedded into  
 8 the APA frame. Another important measurement goal is to establish the energy  
 9 threshold of the photon detection panels. A study will be conducted for the photon  
 10 detectors presently installed in the 35t detector (Chapter 7) using Michel electrons.  
 11 The 35t detector contains one of the three-fiber LSU photon detection panels. In  
 12 addition, performing alpha source runs in a well-controlled and monitored LAr setup  
 13 may provide information on the particle energy threshold for observation of VUV  
 14 scintillation light. The measurement of a photon detector panel's light yield as  
 15 function of the source distance is another key measurement to estimate the response  
 16 and sensitivity of the full photon detection system in a LAr detector. Results will be  
 17 useful to validate MC simulations. We are exploring options to perform these tests  
 18 in the large dewar setup at CSU or alternatively in the TallBo setup [28] at FNAL.

19 The TPB coating procedure of the acrylic panels has not yet been optimized and  
 20 improvements may be possible. A systematic study is foreseen to identify parameters  
 21 in the TPB dip and in the evaporation coating procedure to maximize the light yield  
 22 of resulting samples. These tests will be performed on small  $10 \times 10 \text{ cm}^2$  acrylic

panels with a U-shaped embedded WLS fiber. On the software and analysis side, tools are being improved to study position dependence for alpha-source run data using relative signal timing and size. Furthermore, it is planned to continue work on analysis algorithms to identify the late light component from argon scintillation.

Finally, early exploratory work on wallpapering the TPC cathode planes with TPB coated Tetratex foils and observing the shifted light with suitably installed photon sensors in combination with light collector cones will be pursued and explored more rigorously to provide timely results.

### 5.3.6 Fiber Bundle with WS-coated Radiator

A reduction in attenuation length has been observed in acrylic waveguides that have been doped with TPB. One possible way to address this reduction would be to populate the PD system with half-length paddles. However, this would lead to an increase in the number of readout channels, and readout electronics is the driving cost of the photon detector system. While it may be possible to combine readout channels to improve the increase in overall number, a more desirable solution would be to address issue with short attenuation length.

To mitigate the reduced attenuation length coming from acrylic and polystyrene doped or coated with TPB the CSU group has been developing an alternative design based on UV-to-blue wavelength shifting fiber (Y11) that has not been treated with TPB. A thin TPB-coated acrylic radiator located in front of a close-packed array of WLS fibers. Figure 5.6 shows a photograph of the fiber-bundle prototype.

The VUV photons are incident on the TPB-coated plastic radiator and roughly half of the photons converted in the radiator are incident on the fiber bundle. The photons in the Y11 fiber are then directed onto SiPMs at one end. The Y11 fiber (from Kuraray) have mean absorption and emission wavelengths of about 440 nm and 480 nm respectively. The attenuation length of the Y11 fibers is given to be greater than 3.5 m at the mean emission wavelength, which allows production of full-scale (2.2-m length) photon detector paddles.

First prototypes of this design utilized two rows of fibers with a reflector behind the double row used to redirect the unabsorbed  $\sim 400$  nm photons back through the two rows if they weren't absorbed on the first pass through. Based on data taken at the CSU Cryogenic Detector Development Facility (CDDF) and the Fall 2014 FNAL Tallbo test it was apparent that the front row of fibers collected twice as much light as the back row, thus only a single row design can be considered — this is currently under development. The current design utilizes two single rows of fibers back-to-back with layers of Tyvek diffuse reflector between them.



Figure 5.6: Photograph of fiber-bundle PD prototype (early one-sided version). The thin TPB-coated radiator is mounted on top of the prototype in the image.

fig:fiber\_bund

In this design the fiber bundles would face into different TPC cells, allowing additional information to be used in the disambiguation of the TPC signals coming from wires wrapped around the APA frames. A possible further benefit of the design could be its compatibility with concepts where the walls of the detector are covered with TPB-coated material shifting the VUV photon to blue, the WS-fiber in this design could capture the emitted light, offering a further benefit. Further study is required to determine the effect these enhancements would have on the physics reach of the detector.

To fully exploit this approach several design optimizations need to be examined, including the following:

- TPB coating thickness on thin radiator
- Double-ended readout; if the fibers are read out from both ends and the corresponding channels are ganged onto one readout channel, an increase in channel output can be obtained without significant cost
- Use of custom-doped fibers to best match the QE response of the SiPMs and the emission spectrum of the TPB

- Removal of the radiator and coating the TPB directly onto the outer fiber-cladding of the Y11 fibers. Since the fibers are double-clad it may be the case that the attenuation length of the fibers is not altered by the TPB application. The geometry of the close-packed fiber row may lead to increased photon (400 nm) collection

The cost of this design is comparable to that of the bar-based design but is slightly more complex to fabricate — although the Y11 fibers are commercially available, which is an attractive feature. The engineering aspects of the design will be discussed in the appropriate section of this chapter ??.

### 5.3.7 Technology Selection

As has been mentioned in the previous sections, the current reference design for the photon detector suffers from a reduction in attenuation length for the light guides when VUV-Blue wavelength-shifters like TPB are used on them. It may be beneficial to use one of the alternative designs above to mitigate this effect, as well as potentially reduce the cost of the photon detector system while preserving the detector performance.

The primary criteria for the PD technology decision is cost-normalized performance - assuming that the PD system requirements put forward by the DUNE collaboration are met. In addition to this criteria it is also important that the chosen design is robust and does not introduce significant difficulties in interfacing with the TPC, manufacture, procurement, or handling. In addition one has to consider the ramifications of reducing the readout channels per PD to the point where a failed channel could lead to significant holes in detector acceptance or large variations in detector response.

A testing program is underway at Fermilab, CSU, and IU to provide data to aid with the technology decision. Once DUNE has established a technical board, or similar body, this entity will decide whether it the technology used for the PD system will be based on the current reference design, or one of the alternatives. It is expected that a decision on technology will be made toward the end of FY 2015 so that the overall far detector project schedule can be met.

## 5.4 Silicon Photomultipliers

Silicon Photomultipliers (SiPMs) have been selected as the reference design photon detectors for the far detector photon detection system. An SiPM is a photo detection

1 device sensitive to single photons with excellent linear response in collecting multiple  
2 photons.

3 SiPMs have been developing at a very fast pace in recent years, largely in response  
4 to the needs of the medical industry. As a result, the price of SiPMs has reduced con-  
5 siderably, while their performance has greatly improved. A number of characteristics  
6 make SiPMs an attractive choice as photon detectors for the PD system:

- 7 • High photon-detection efficiency (PDE), up to 40-50% at the peak detection  
8 wavelength.
- 9 • High intrinsic gain ranging from  $10^5$  to  $10^7$  depending on the overvoltage
- 10 • Low dark rate at cryogenic temperatures — less than 50 Hz even at the maxi-  
11 mum overvoltage
- 12 • Insensitivity to external magnetic field
- 13 • Extremely linear gain vs. overvoltage
- 14 • Low cost per sensitive area compared to small cryogenic photomultiplier tubes  
15 (PMTs)
- 16 • Small dimensions allowing a simple, compact and robust design
- 17 • No need for high voltage (HV) power.
- 18 • Low bias voltage, typically less than 100 V required, and even less than 30 V  
19 in some cases, resulting in low peripheral costs
- 20 • Maintenance of high gain and PDE at cryogenic temperatures

21 In short, SiPMs have demonstrated performance comparable to traditional PMTs,  
22 but at a significantly reduced cost. As a result, they have become the photon-detector  
23 of choice for PD system of the far detector.

24 The main risk associated with using SiPMs is that they have not generally been  
25 designed for operation at LAr temperature. None of the SiPM data sheets show nor  
26 guarantee the device's performance at cryogenic temperatures. This was the main  
27 motive for testing SiPMs at LAr temperatures. Most of the low-temperature tests  
28 performed by LBNE teams on SiPMs in the last two years have been done using  
29 LN<sub>2</sub>, as it has similar temperature (10 K below LAr) but costs much less.

30 A number of manufacturers offer SiPMs, such as SenSL, Hamamatsu, KETEK,  
31 AdvanSiD, CPTA (Photonique), Philipis, Novel Device Laboratory (NDL), Zecotek,



Voxtel, Amlification Technologies, Excelites, etc..., but only a fraction of them offer SiPMs suitable for the PD system – large area ( $6 \times 6\text{mm}^2$  or  $3 \times 3\text{mm}^2$ ), large fill factor, pin or surface mount and no housing. An exhaustive search of suitable SiPMs was conducted in 2012 and sample SiPMs were obtained from SenSL, Hamamatsu, CPTA and AdvanSID. It should be noted, however, that although one should keep in mind, that in this rapidly developing field, manufacturers come up with new models regularly.

Preliminary tests included models from SenSL (MicroSM-600-35-X13), Hamamatsu (MPPC S10985-100C), CPTA (SSPM-0710G9MM) and AdvanSID (ASD-SiPM3S-P). In these tests, SiPMs were cooled in liquid nitrogen and laser light pulses at 400 nm wavelength were used as the light source. Signal output as a function of overvoltage was recorded. Results can be seen in Figure ??.

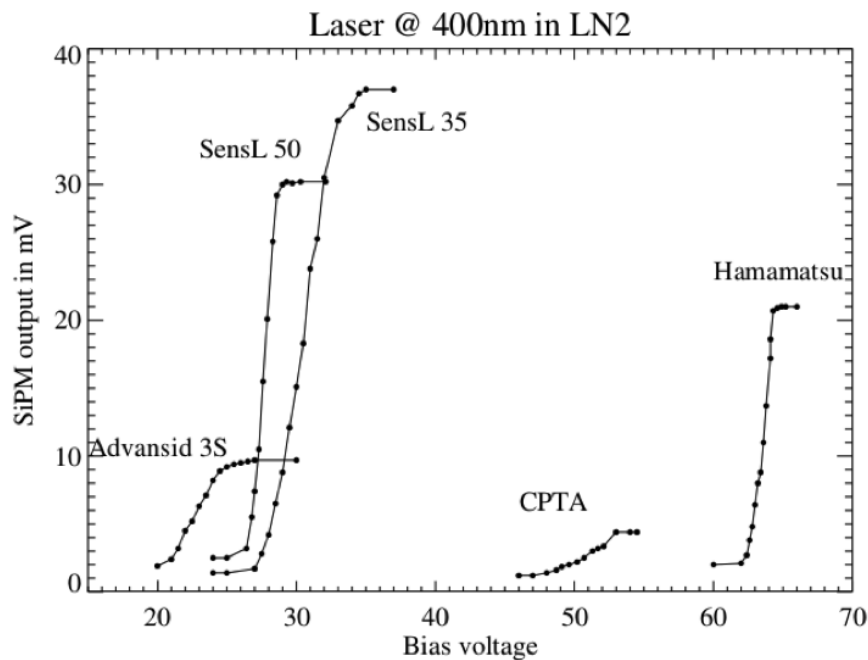


Figure 5.7: SiPM signals as function of bias voltage in liquid nitrogen. Liquid nitrogen has 10 K lower temperature than liquid argon, making the measurement applicable. In all cases there is a significant increase in gain with increasing bias voltage, but difference in gain among different samples is clearly visible.

fig:laser400

Based on these preliminary tests and high price quotes received at the time from AdvanSiD and CPTA, the follow-up tests focused only on SenSL and Hamamatsu

1 models.

2 Following initial tests, SenSL released a new model of the device we had been test-  
 3 ing (MicroFB-600-35-SMT followed by improved MicroFC-600-35-SMT) and follow-  
 4 up tests were performed on these new models. Hamamtsu's MPPC S12895- 0404-  
 5 PB50 has been on the market for a long time and the Indiana group has measured  
 6 very high cross-talk and afterpulsing rates. Hamamtsu has released a new, improved  
 7 model in 2015, S13360, that will be tested in 2015 and compared with SenSL models.

8 The C-Series SensL device has the same low after-pulsing and gain characteristics  
 9 as the earlier SensL device being tested while having a larger detection efficiency (41%  
 10 vs. 31%) and lower dark noise.

### 11 5.4.1 Requirements

12 Despite liquid argon's excellent scintillation yield, the PD system requires high-  
 13 efficiency photon detection due to the very small surface area of the SiPMs. Further-  
 14 more, the late scintillation light in argon represents 3/4 of the total, but it is spread  
 15 over 1100 – 1600 ns, making the individual late-light signals very small on average.

16 SiPM data sheets for the devices of interest indicate that PD system requirements  
 17 are satisfied, but it is important to determine that performance required by the PD  
 18 system is observed at LAr temperatures in terms of high gain, sensitivity to single  
 19 photoelectrons, high PDE, linearity of response, stability of breakdown voltage, long-  
 20 term stability, low afterpulsing and low cross-talk. In addition, SiPMs must exhibit  
 21 mechanical robustness and low dark rate as they undergo cryogenic cooling and  
 22 cycling. Finally, the cost must be low enough. To avoid sole-sourcing, it is required  
 23 devices must have low cost and we need to identify at least two choices that meet all  
 24 requirements.

25 Institutions designing different PD prototypes (IU, CSU and LSU) have con-  
 26 ducted a number of tests of PDs that include SiPMs. Additional, specifically targeted  
 27 tests have been conducted at LSU and University of Hawaii (UH) in recent months.  
 28 The importance of selecting the best photo-sensors for the PD motivates the need  
 29 for the parallel tests conducted at LSU and UH will ensure important cross-checks  
 30 and reduce possible testing biases.

### 31 5.4.2 Test Results

32 In the last 18 months, a test setup for SiPM evaluation has been built, that includes  
 33 Belle experiment [29] electronics to power and record signals coming from the SiPMs.  
 34 Over the past year a new board similar to the SenSL testing board has been designed

- 1 to address noise problems and low amplification found on the Belle board, issues that  
 2 become critical at low light levels. This new board is currently being used to conduct  
 3 dark rate and single-photoelectron studies. Figure ?? shows the layout of this board  
 4 and a picture of the actual circuit as built.

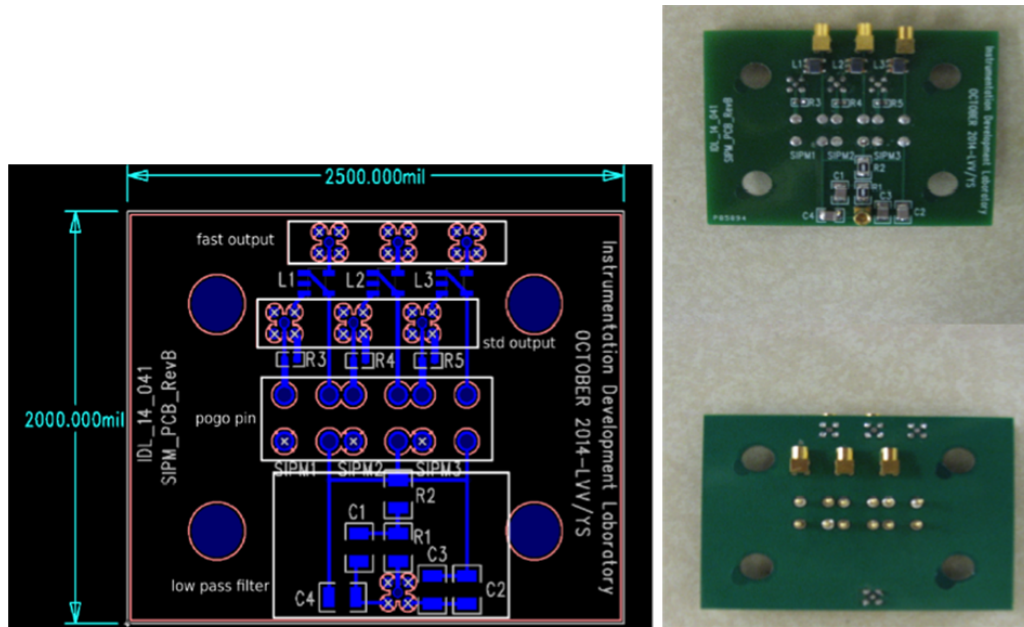


Figure 5.8: The diagram on the left shows the schematics of the PCB board. The picture on the right shows the PCB as built. This PCB can accommodate three SiPMs for testing.

fig:sipm\_schem

- 5 As previously mentioned, tests focused on devices from Hamamatsu and  
 6 SenSL FOr testing the SiPMs are placed in a dewar inside a copper plated dark box  
 7 and cooled with LN<sub>2</sub>. SiPMs are held in place on the PCB with acrylic holder as  
 8 shown in the Fig ??.

- 9 The different contraction rates of materials in LN<sub>2</sub> produced mechanical damage  
 10 to some of the SiPMs. To address this issue, a PCB board with spring-loaded POGO  
 11 pins is used (based on the previous design by the CSU group) to provide contact to  
 12 SiPMs and hold them in place with an acrylic housing rather than solder joints.  
 13 Special cryo-rated, compact MMCX connectors have been acquired, as the solder  
 14 joints of the signal and power wires have been breaking from repeated usage.

- 15 The SiPM bias voltage is delivered via the POGO pins and the SiPM signal is sent  
 16 via these pins to the DAQ. The signal is amplified via two inline low-noise amplifiers  
 17 and read out by an oscilloscope. The SiPMs are illuminated by 1-ns-long laser pulses

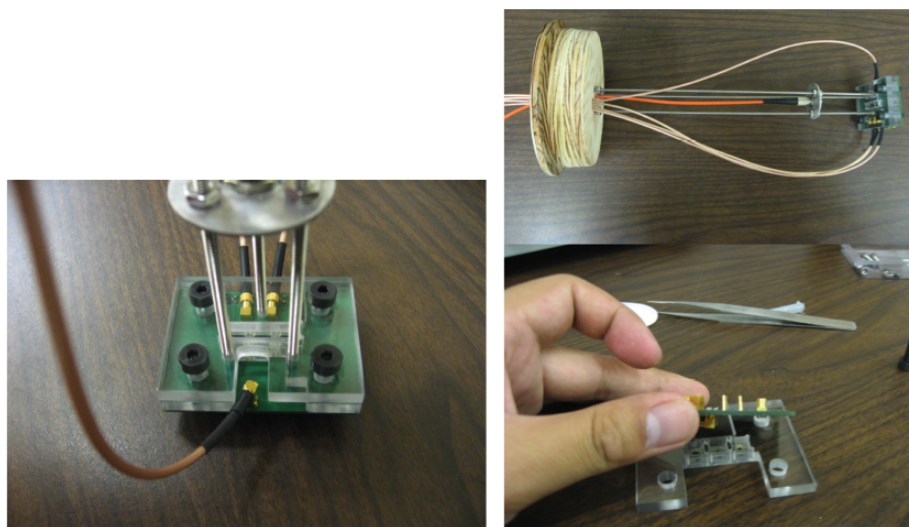


Figure 5.9: Picture on the left shows acrylic holder that secures SiPMs to the PCB while figure on the top right shows the entire assembly prior to lowering in the dewar. Orange cable delivers laser or LED light that shines on the SiPMs. Everything is secured to the wooden lid that closes the dewar.

fig:sipm\_mount

1 from a tunable wavelength laser system. Laser light intensity is regulated with a  
 2 Fine Laser Intensity Controller (FLIC), a computer-controlled system that allows  
 3 tuning of laser intensity through several orders of magnitude with various stages;  
 4 this is important for linearity measurements. Signal waveforms from a Waverunner  
 5 LeCroy oscilloscope are recorded and analyzed.

6 It has also been noted that the SiPMs require lower bias voltage when cooled  
 7 in  $\text{LN}_2$ , which requires determination of the optimal operating voltage at LAr tem-  
 8 perature, since dark rates also increase with bias voltage. Additional tests showed  
 9 excellent gain at cryogenic temperatures, as can be seen from the tests conducted  
 10 on the SenSL C series SiPM MicroFC-600-35-SMT (previous M and B series were  
 11 also tested) shown in Figure ??, along with clearly distinguished pulses for one, two,  
 12 three and four photoelectron pulses.

13 The dark rate increases significantly with bias voltage, but the overall rate is very  
 14 small when SiPMs are cooled to 80 K, as can be seen in Figure ??.

15 Afterpulsing is another important aspect of SiPM performance. Afterpulsing  
 16 increases noise and obstructs detection of late argon scintillation light. Results of  
 17 the afterpulsing measurement performed on the cooled SenSL C series SiPM show  
 18 a very small afterpulsing fraction below 1% for most overvoltage values, as can be

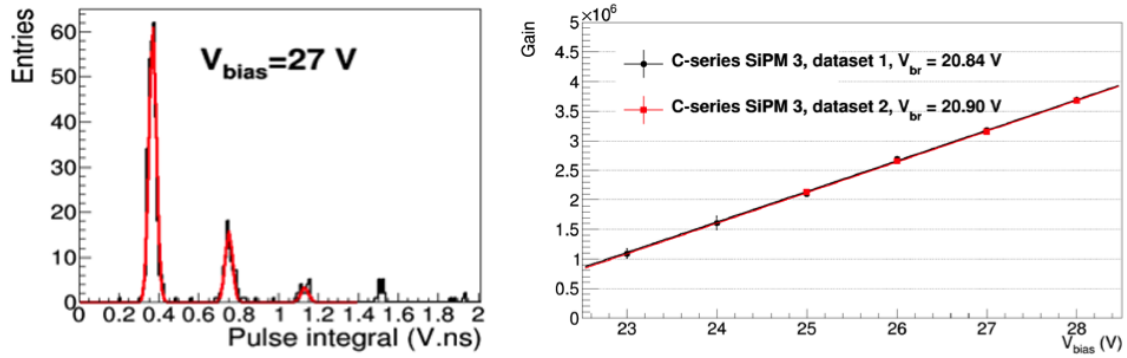


Figure 5.10: SiPM SenSL C series gain tested in LN2 is shown on the right hand side. Excellent linearity over the entire overvoltage range observed. There is a significant change of gain with increasing bias voltage, effectively doubling between the minimum and maximum tested bias voltage. Clearly distinguished numbers of photoelectrons can be seen in the left hand figure.

fig:sipm\_gain

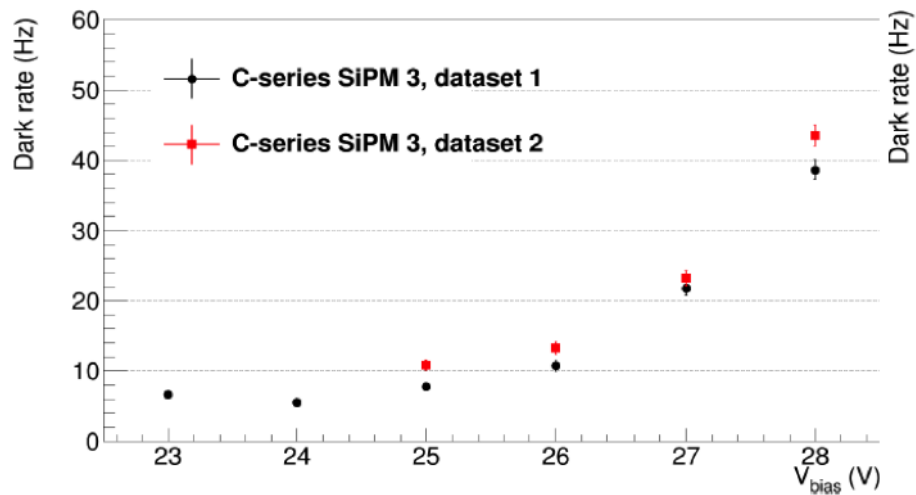


Figure 5.11: SiPM SenSL C series dark rate with two different data runs in LN2. While dark rate increases for an order of magnitude, it is still less than 50 Hz even at the highest bias voltage setting.

fig:sipm\_dark

1 seen in Figure `fig:sipm_after`.

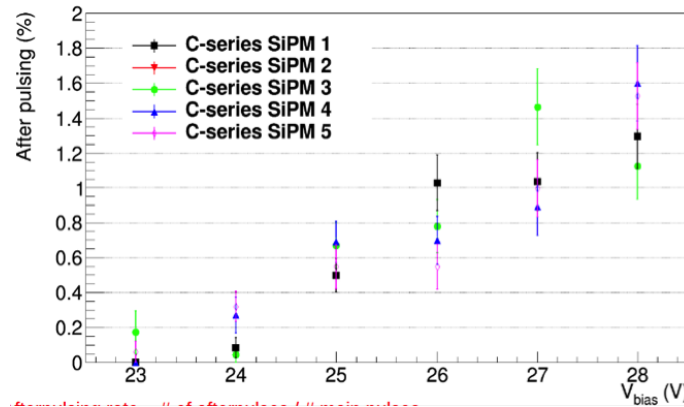


Figure 5.12: SenSL C series SiPM afterpulsing fraction for 5 different SiPMs, with system being completely cooled down.

`fig:sipm_after`

2 SenSL C series SiPMs were also tested for cross-talk. Cross-talk is effect of light  
 3 hitting one pixel producing a signal in and adjacent pixel, which effectively distorts  
 4 the device response. Figure 5.13 shows the test results. Cross-talk is a strong function  
 5 of overvoltage, which will be another criterion in choosing the operating overvoltage  
 6 for the PD system.

7 Although not presented here, SenSL B series SiPM MicroFB-600-35-SMT were  
 8 also tested and satisfy our requirements, based on the tests conducted so far. How-  
 9 ever, we have not yet performed full set of tests including mechanical integrity from  
 10 thermal cycling and cross-checks, although a testing program is underway.

11 In parallel with performance tests, mechanical cryogenic tests are being conducted  
 12 where the number of cycles and time spent at LN<sub>2</sub> temperature is being logged. This  
 13 important test has started recently, but will involve testing a number of devices for  
 14 extended period of time and examining their mechanical status under the microscope,  
 15 along with the performance tests.

16 Future steps involve increasing the testing sample of C series SiPMs and evalu-  
 17 ating several alternatives to avoid the risk of sole-source vendor.

## 18 5.5 Mechanical Support

`MECH_SECTION`

19 ??

20 Mechanically supporting the PD systems in the APA frames presents several  
 21 challenges, including the need to be able to support three different light-collecting

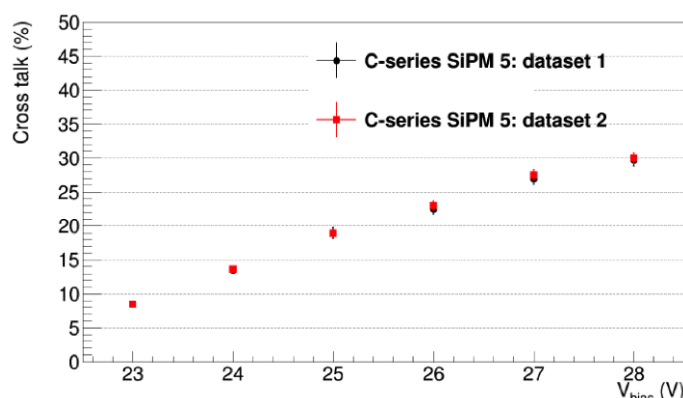


Figure 5.13: SenSL C series SiPM cross-talk measurement based on two separate runs in LN2. Cross-talk is a strong function of overvoltage and is very consistent between the runs.

fig:sipm\_cross

and wavelength-shifting technologies (individually) in a package utilizing the same mounting features in the APA frames, and the effects of varying thermal contraction of various materials at 80 degrees Kelvin which complicated both light collector and SiPM mounting.

The reference design for mounting the PDs into the APA frames calls for ten PD modules, approximately 2.2 m long, mounted with roughly equal spacing along the full length of the APA frame (Figure 5.14). The PD modules are read out using individual twisted-pair cable, one per SiPM. These cables (120 of them in the original reference design) are routed through the APA side tubes to a connector at the cold electronics readout end of the APA. Initially it was decided that it would be too complicated to design the APA frames to allow PD module installation following APA wire-wrapping, so it was planned to install the PD modules prior to this step. The wavelength-shifting elements in the light collectors of the PD modules are sensitive to heat, humidity and most critically to exposure to ambient light, which places significant requirements on the environment in which the APAs are assembled and stored.

A universal PD frame assembly was devised to hold all three PD design variations under consideration. Figure 5.15 shows an example of a short (400-mm-long active area) version of this frame manufactured for the 35t test, and Figure 5.16 shows a mechanical assembly drawing of the frame system for one of the candidate light collector choices. The frame consists of two plastic (acetal) end caps mounted to the inside of the APA frame, joined by 10-mm-diameter stainless steel tubes that run the full width of the APA frame, providing intermediate support for the PD modules.

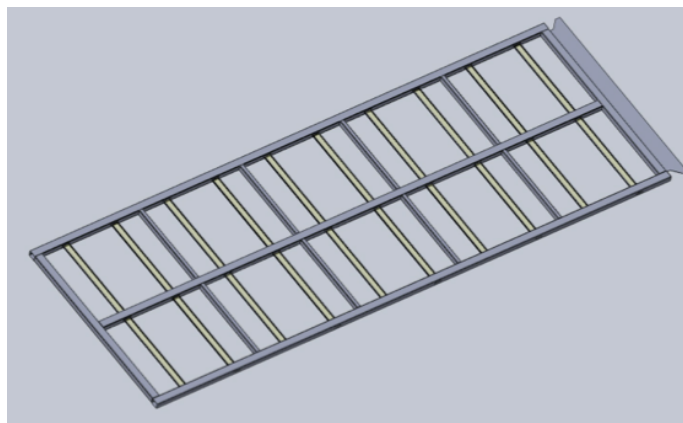


Figure 5.14: Full APA frame with ten photon detectors mounted inside the frame.

fig:5.5-1

1 The PCBs in which the SiPMs are mounted mount PCBs are incorporated into one  
 2 of the end blocks, along with the cable connections for the twisted-pair cables. Due  
 3 to the significant differences between the coefficients of thermal expansion for the  
 4 stainless steel frame and the plastic WLS elements, a relative difference in thermal  
 5 contraction of  $\sim 1\%$  is expected at LAr temperatures. The far endblock assembly  
 6 provides the balancing forces to the light collector elements required to ensure these  
 7 elements remain in good contact with the SiPMs.

8 Testing of the PD mount scheme in many test setups (at IU, CSU and FNAL),  
 9 as well as experience APA assembly, have led to a re-evaluation of the PD mounting  
 10 scheme. The revised reference design has PD installation occurring after APA wire  
 11 wrapping, through slots left in the side of the APA frame (Figure 5.17). As shown  
 12 in the figure, the plan still calls for ten PDs per APA frame. Five of the PDs will  
 13 be installed through each side of the APA frame, and the cables for each of the PDs  
 14 will be routed to the cold-electronics end of the APA, inside the side tube through  
 15 which the PD was inserted. Stainless steel c-channels mounted into the APA frames  
 16 prior to wire wrapping will guide and support the PDs during and after installation.  
 17 The PD will only be attached to the APA frame at one end, so the purely plastic  
 18 PD module will be free to slide in the track to allow for the differential contraction  
 19 (Figure 5.18). Tests of the 2.2-m prototype assemblies of both fiber hybrid and the  
 20 LSU-proposed monolithic acrylic bar design in the CSU CDDF have demonstrated  
 21 significant promise.

22 Thermal contraction at cryogenic temperatures also complicates the mounting  
 23 of the SiPMs in the PD modules. The baseline SensL SiPMs are surface-mount  
 24 components, with four  $0.5 \times 0.5$ -mm pads for making electrical contact. Reliability



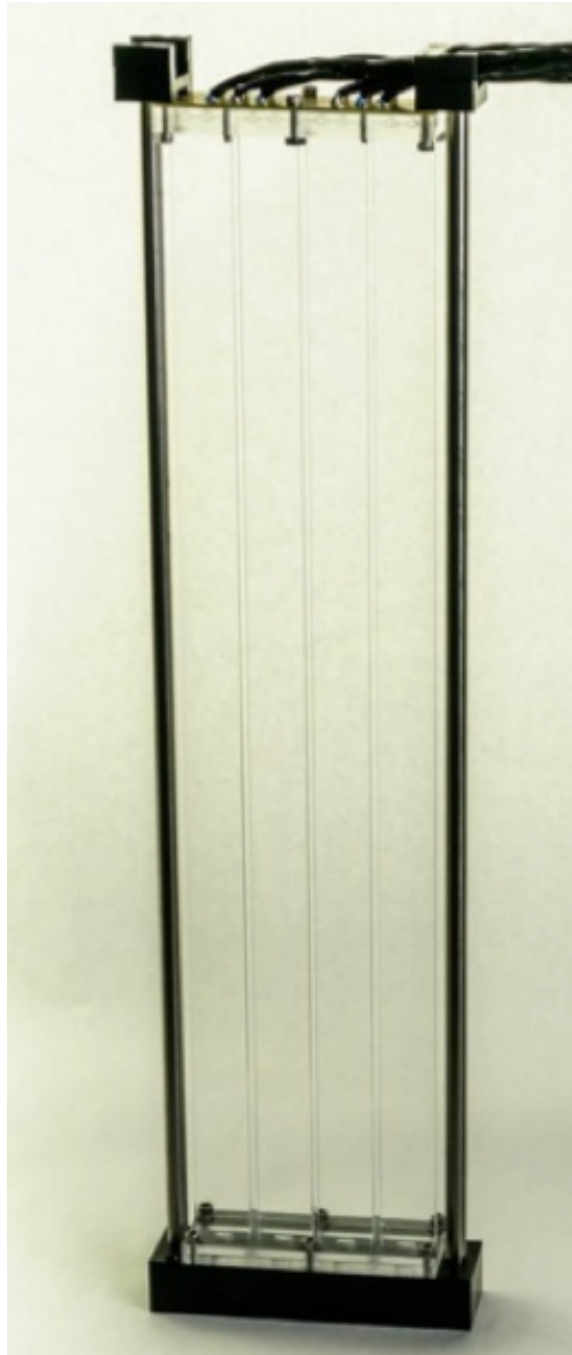


Figure 5.15: Photograph of 40 cm long bar-based prototype mounted in test frame

fig:5.5-2

Design for a Deep Underground Single-Phase LArTPC

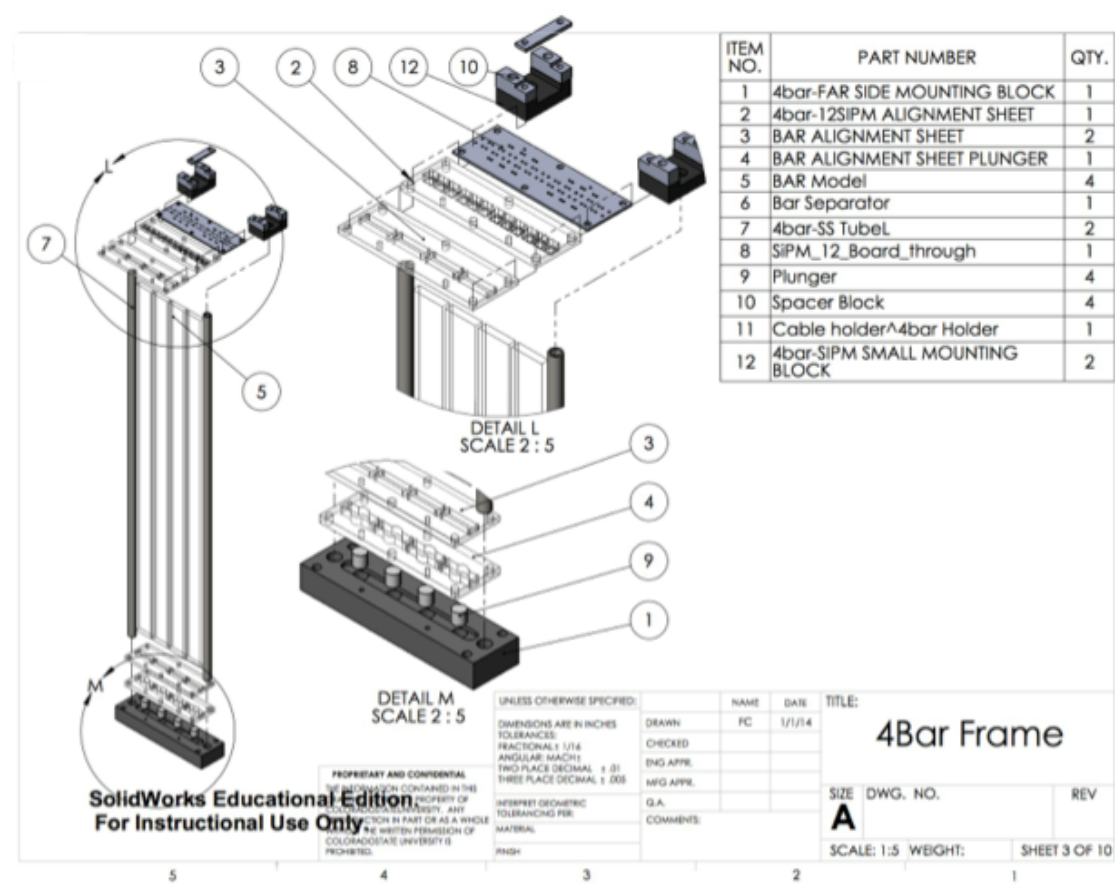


Figure 5.16: Mechanical assembly drawing of frame system

fig:5.5-3

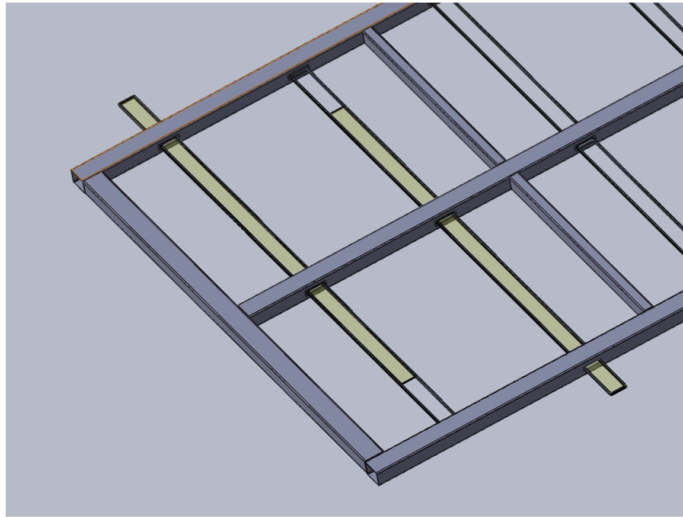


Figure 5.17: Blow up of APA fram showing PD insertion location

fig:5.5-4

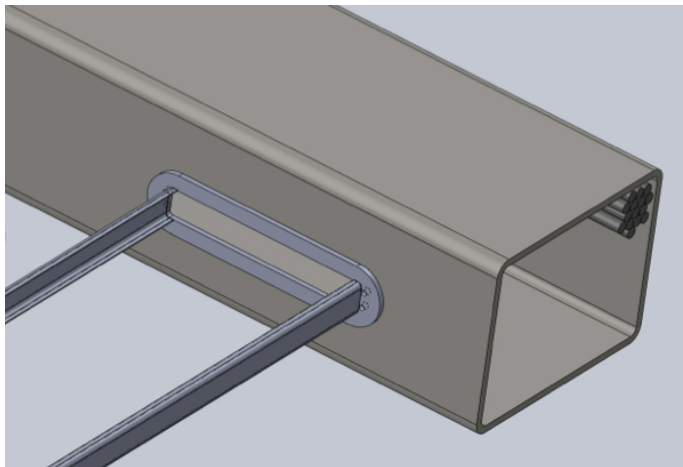


Figure 5.18: Slot and rail showing mounting location of photon detector

fig:5.5-5

issues and elevated dark count rate problems, as well as physical delamination of the SiPM front face from the silicone substrate, were observed early in cryogenic testing of SiPMs, and suspicion fell on the mechanical contact between the mounting PCB and the SiPM itself.

Three different methods of making these electrical contacts have been studied:

- Soldering the SiPMs directly to the PCBs (fig 5.5-6a),
- using commercial spring-loaded electrical contacts or “Pogo pins” (Figure ??), fig:5.5-6b
- soldering short wires to the SiPM pads and thence to the PCB (Figure ??). fig:5.5-6c

Each of these methods provides assembly challenges, and cryogenic testing has not suggested a clear choice so far. Testing and development are still underway to resolve this issue.

## 5.6 Photon System Readout Electronics

### 5.6.1 Reference Design

Due to the geometric acceptance of the system, only a fraction amount of scintillation light is collected by the PD system, so the electronics must be designed to collect the light from both excited states. A summary of the general requirements for the system, including requirements from a physics performance perspective, are given in Table 5.3.

Table 5.3: Physics requirements for the photon detector electronics

Performance Parameter	Target
Time Resolution	Better than 30 nS wrt event time zero ("t0")
Charge Resolution	0.25% photo-electron equivalent
Dynamic Range	$\sim \times 10$ better than detector (1000:1)
Linearity	Sufficient to resolve 1 photo-electron signals
Multi-Hit Capability	Sufficient to measure Triplet (late) Photons
Dead Time	Live up to 2 drift times either side of beam spill
Bias Control	0.1 V resolution up to 30 V per channel
Calibration	On-board Charge Injection
Timing	Events time-stamped using NO $\nu$ A Timing syst.

1 The plans for the electronics for the photon detection subsystem include a ref-  
2 erence design with several options that remain R&D activities. There alternative  
3 implementations of electronics are described in Section 5.6.2.

4 In the reference design there are no front-end electronics in the cold volume. In-  
5 stead, the unamplified signals from the SiPMs are transmitted to outside the cryostat  
6 on cables for processing and digitization. There are advantages and disadvantages  
7 to this approach. The advantages are that the infrastructure required for inside  
8 the cryostat is reduced (power, data cables, precision clocks, data protocols, etc.);  
9 reliability is improved (no single-point failures of multi-channel devices inside the  
10 cryostat); serviceability and accessibility to the front-end electronics are improved;  
11 and the need to develop cold electronics, possibly a custom ASIC, is eliminated. The  
12 disadvantages are that the cable plant inside the detector is increased, which can cre-  
13 ate mechanical challenges and installation difficulties; the flange board (warm/cold  
14 interface) is more complex; there are generally more connectors in the system; and  
15 signal-to-noise considerations are more difficult. The reference design favors simplic-  
16 ity, reliability and reduced R&D time and costs, and also meets the performance  
17 requirements of the electronics.

18 In the 35t prototype, each SiPM signal is transmitted on an individual shielded  
19 twisted-pair cable fitted with individual LEMO-style connectors. The bias voltage  
20 was coupled onto the signal cable, using AC-coupling on the receiving end to mea-  
21 sure the SiPM signal. The use of high-quality cable with point-to-point connections  
22 between an individual SiPM inside the cryostat and the front-end electronics resid-  
23 ing outside the cryostat, combined with good differential signal processing on the  
24 receiving end, enabled the demonstration of the principle that single photo-electron  
25 signals could be measured accurately without the need for cold electronics. In order  
26 to address the problems with the cable plant as identified above, the following ideas  
27 are being pursued:

- 28 • Ganging together several SiPM outputs from a given PD detector into one  
29 output cable. This increases the detector capacitance, affects the pulse shape,  
30 and could spoil the timing resolution of the measurement. Also, the SiPMs  
31 may have to be preselected, since there will be only one bias voltage for three  
32 devices, and it may be important to match the overvoltage characteristics.  
33 Studies are in progress to find a compromise between data precision and cabling  
34 issues. One approach is to add a cold pre-amplifier if the ganging together of  
35 several SiPMs result in performance that is too degraded to meet specifications.  
36 The infrastructure requirements (cables, connectors, power, cold performance,  
37 reliability, mechanical mounting, etc.) would have to be considered.

- 1     • Use of multi-conductor, individually shielded pair cable. A candidate cable  
2       containing four individually shielded twisted pairs has been identified and tests  
3       are in progress. The cable is in Teflon jacket, which has been found to be  
4       acceptable for use in LAr.
- 5     • Use of mass-terminated connectors. Several candidate connectors for use with  
6       the cable described above are being pursued.

7       The reference design assumes that three SiPM signals can be ganged together into  
8       one readout channel. By using the multi-conductor cable with four twisted pairs,  
9       this results in one cable per PD consisting of 12 SiPMs. The use of this cable will  
10      reduce the cable plant by  $\sim \times 10$  compared to that used in the 35t detector. The cost  
11      of the connectors also decreases by  $\sim \times 10$ . Lastly, the ease in making connections  
12      at the flange board will be improved by the use of a mass-terminated connector.

13     In the reference design, the front-end electronics reside outside of the cryostat  
14     in instrumentation racks. A custom module for receiving SiPM signals has been  
15     designed and built, and signal processing is being performed in the front-end as  
16     preprocessing for trigger and DAQ. The module is called the SiPM Signal Processor  
17     (SSP). An SSP consists of 12 readout channels packaged in a self-contained 1U  
18     module. Each channel contains a fully differential voltage amplifier and a 14-bit,  
19     150 MSPS analog-to-digital converter (ADC) that digitizes the waveforms received  
20     from the SiPMs. The front-end amplifier is configured as fully differential with high  
21     common-mode rejection, and receives the SiPM signals into a termination resistor  
22     that matches the characteristic impedance of the signal cable. Currently there is no  
23     shaping of the signal, since the SiPM response is slow enough relative to the speed  
24     of the digitization to obtain several digitized samples of the leading edge of the pulse  
25     for the determination of signal timing.

26     The digitized data is stored in pipelines in the SSP for up to  $\sim 13 \mu\text{s}$ . The  
27     processing is pipelined, and performed by a Xilinx Artix-7 Field-Programmable Gate  
28     Array (FPGA). The FPGA implements an independent Data Processor (DP) for  
29     each channel. The processing incorporates a leading-edge discriminator for detecting  
30     events and a constant fraction discriminator (CFD) for sub-clock timing resolution.  
31     Because the FPGA is programmable and accessible, it is possible to explore different  
32     data processing algorithms and techniques, and even customize the readout for a  
33     given type of event (e.g., supernova). A picture of the module is shown in Figure 5.19.  
34     A block diagram of the system is shown in Figure 5.20.

35     In the simplest mode of operation, the module can perform waveform capture,  
36     using either an internal trigger or an external trigger. Up to 2046 waveform samples  
37     may be read out for each event. When waveform readouts overlap, the device can

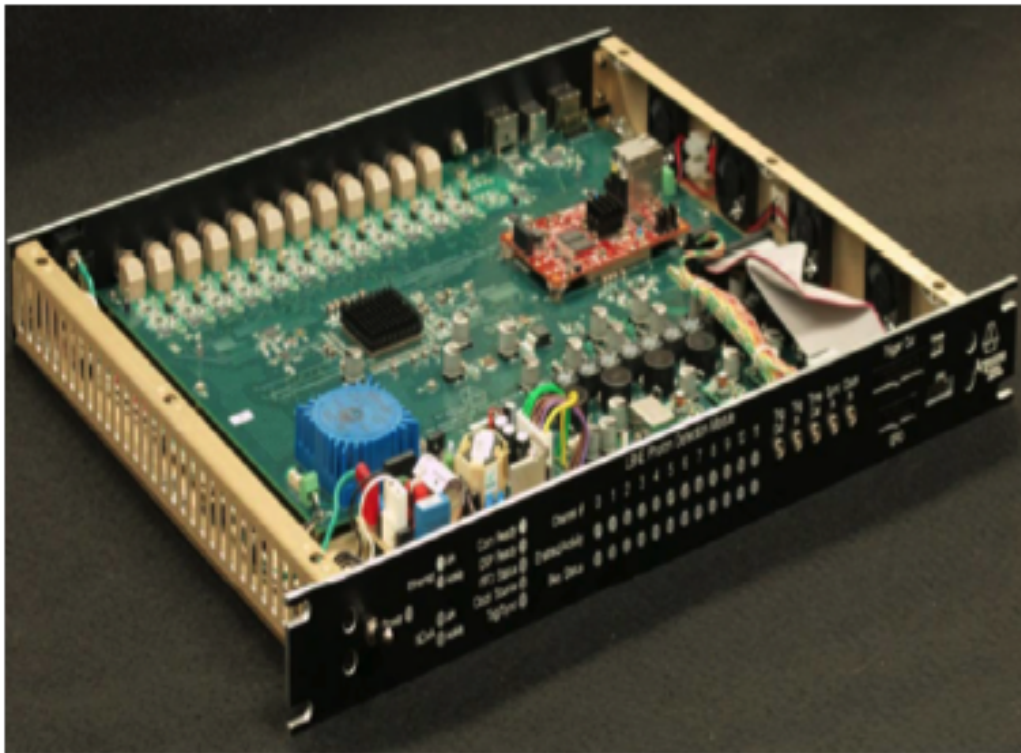


Figure 5.19: Picture of the SSP module

fig:fig-e-2

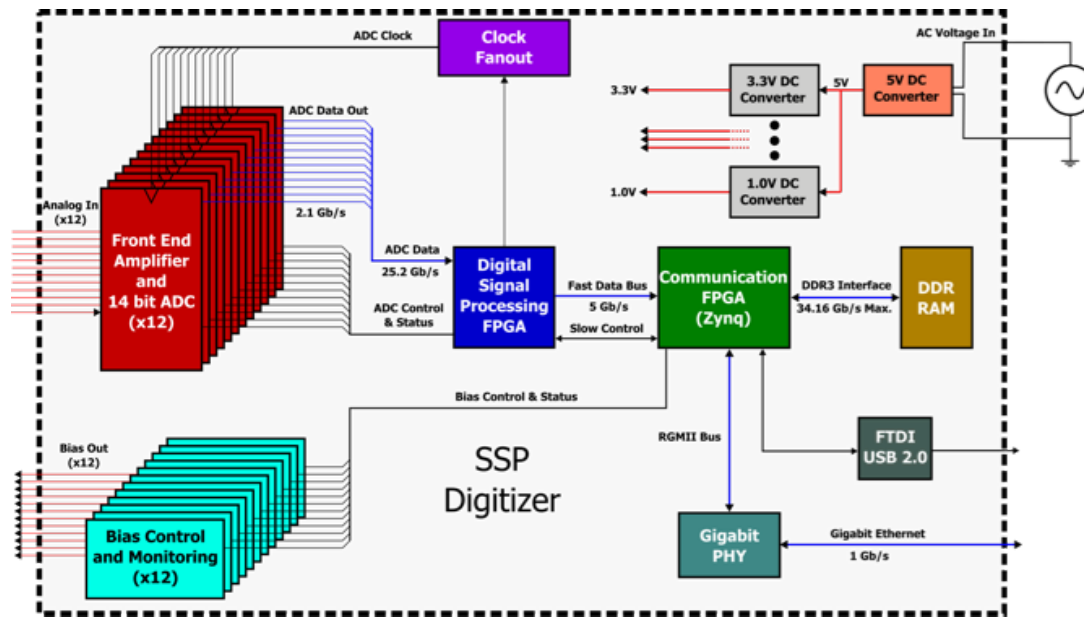


Figure 5.20: Block diagram the SSP module

fig:fig-e-3

- 1 be configured to offset, truncate or completely suppress the overlapping waveform.
- 2 Pile-up events can also be suppressed.

3 As an alternative to reading full waveforms, the DP can be configured to perform  
 4 a wide variety of data processing algorithms, e.g., measuring amplitude (via several  
 5 techniques), and also timing the event with respect to a reference clock. All timing  
 6 and amplitude values are reported in a compact event record. Each data processing  
 7 channel stores up to 340 event records when not storing waveforms.

8 In normal operation, The SSP performs pipelined processing. The module has  
 9 been designed to support several different triggering schemes, including self-triggering,  
 10 use of an external trigger, or use of an external gate to read out all events within a  
 11 time window. In order for the events measured in the photon detector to be matched  
 12 up with the corresponding events in the TPC, the front-end electronics attaches a  
 13 timestamp to the data as it is acquired. The timestamp is unique, and has a corre-  
 14 spondence with the timestamps in the TPC electronics processing. The timestamp  
 15 in the SSP is applied to the event data as it is digitized, and becomes part of the  
 16 data as the processing proceeds. In the case where zero-suppression and data spar-  
 17 sification are used, the timestamp on accepted data remains intact. To achieve this,  
 18 the TPC and PD electronics must be synchronized, including timestamp counter  
 19 resets. A known and stable calibration between the corresponding timing resolution



of the ADC conversion in the two systems must also be achieved. The electronics has been designed to support a full interface to the NO $\nu$ A timing system, which is the reference timing system for the experimental prototypes.

A Xilinx Zynq FPGA, onboard a MicroZed system-on-module, handles the slow control and event data transfer. The SSP has two parallel communication interfaces, USB 2.0 and 10/100/1000 Ethernet. The 1-Gb/s Ethernet supports full TCP/IP protocol. The module includes a separate 12-bit high-voltage DAC for each channel to provide up to 30 V of bias to each SiPM. The module also features charge injection for performing diagnostics and linearity monitoring, as well as voltage monitoring.

In tests to date, the SSP has demonstrated the ability to measure single photoelectron signals coming from the SiPMs over a cable length of 30 m when the SiPMs are operated at LAr temperature. The timing resolution of the signals has been measured to be better than 3 ns. The full-differential signal processing in the front-end circuitry is important in achieving this result.

The SSP is self-contained in that it receives 60-Hz, 120-V power, and has internal linear and DC/DC power supplies for generating the DC voltages needed for the instrumentation, as well as the bias voltage for the SiPMs. The SSP is packaged in a 1U, rack-mountable package. For the 35t prototype, the racks are located near the ports on the top of the cryostat.

## 5.6.2 Alternatives

This section describes alternative designs to the PD system readout electronics that had been considered for further study during the early stages of PD design. They are included for completeness but are no longer being considered. The performance of the SSP has been demonstrated to achieve well beyond the specifications imposed on the design.

In the reference design of the PD electronics, no electronics are placed inside of the cold volume. This results in a large number of cables and connectors. Other experiments using liquid argon have successfully implemented cold TPC electronics, thereby significantly reducing the cable plant that must come through the cryostat.

The use of cold electronics has challenges in power distribution, heat dissipation, and the performance of front-end electronics in LAr. To address serviceability, the cold electronics might be realized in a modular way and situated just below the flange in the cryostat so that it can be accessed for repair if needed. To this end the zero suppression will be important to avoid high data rates. To date the cold FPGAs have had mixed results in tests.

Performing an “analog zero suppression” with a constant-fraction discriminator

1 provides an alternative approach; it would be followed by gating the signal and  
2 performing warm digitization. This technique would, however, introduce the compli-  
3 cation of encoding the particular channel. The significant challenges in this technique  
4 include power dissipation, the increased possibility of contamination of the LAr, and  
5 extended infrastructure that must reside in the cold volume. On the other hand, it  
6 can significantly reduce the number of signal penetrations into the cold volume.

7 The electronics for the photon detector of LBNE uses fast (direct) digitization of  
8 the SiPM pulses. Another option for the front-end electronics is to use pulse shaping.  
9 Instead of digitizing the full bandwidth of the SiPM signal, in this technique the  
10 pulse is shaped using analog filtering techniques, generally producing a pulse with a  
11 prescribed shape for which the peak is proportional to the total amount of charge.  
12 By measuring the peak, both amplitude and pulse timing can be obtained. Since  
13 the pulse response follows a known transfer function, the pulse peak can be obtained  
14 using slower synchronous sampling, or using asynchronous sampling through the use  
15 of peak detection and constant fraction discrimination.

16 In either case, the data can be processed by an FPGA using algorithms optimized  
17 for the application. In particular, assuming that a sufficient number of samples of the  
18 shaped pulse are obtained, a chi-square comparison of the shape to the ideal pulse  
19 shape can be used to identify events or determine pulse corruption identification. As  
20 with direct digitization, the digitization clock and a timestamp can be synchronized  
21 using an external clock source. The data can be read out in a similar manner, using  
22 USB 2.0 or 10/100/1000 Ethernet. The virtue of this approach is that a slower  
23 ADC can be used, reducing power consumption, data load and the speed of readout  
24 links. The technique trades bandwidth for shaping, making timing and pile-up issues  
25 more important. This can result in making the interpretation of the pulse shape  
26 more complex, requiring more than direct digitization. Generally, the pulse-shaping  
27 circuitry is less expensive than the direct digitization technique, assuming similar  
28 performance requirements.

29 Another option for the photon system readout would include the use of an Appli-  
30 cation Specific Integrated circuit (ASIC) as a way to reduce cost. The large channel  
31 count in a real detector system is such that the production cost (per channel) of the  
32 system could be greatly reduced. Often, the cost of development of an ASIC from  
33 scratch is quite high, of order  $\sim 400\text{K}\$$ , and can take  $\sim 1$  to 2 years for development,  
34 so cost and schedule must be weighed carefully. However, other benefits from the  
35 ASIC approach include reduced space requirements for circuitry on the front-end,  
36 lower power dissipation, and specialized functionality in the front-end chip.

37 Several ASICs have been designed over the last few years for SiPM readout. It  
38 could be possible to explore the functionality and performance of these designs, for

1 either for warm or cold electronics, and evaluate their suitability for LBNE. This  
 2 option might be used either for warm or cold electronics. Direct digitization has  
 3 the virtue of being straight-forward from a circuit design perspective. By taking  
 4 advantage of modern high-bandwidth OP amps, high-speed, high-rate ADCs, and  
 5 powerful FPGAs with high-speed serial links, it is possible to obtain 14-bit dynamic  
 6 range digitization with  $\sim 1$ -ns timing resolution. By reading all of the samples into  
 7 an FPGA having a deep buffer, digital signal processing techniques can be employed  
 8 using the programmable logic; this could make it possible to develop powerful analysis  
 9 algorithms. The technique generally has higher power consumption and tends to be  
 10 more expensive than simpler instrumentation techniques.

## 11 5.7 Photon Detector Calibration

sec\_pd\_calib

12 The photon detector calibration is a part of a larger calibration plan that covers  
 13 all aspects of a LArTPC detector calibration. The larger plan includes methods to  
 14 convert collected charge to initial particle energy, as well as calibration techniques to  
 15 convert collected scintillation light into an estimate of a particle's interaction time,  
 16 energy and a track/vertex location for each event.

17 As already described, the reference design for the scintillation photon detectors  
 18 assumes employment of acrylic light collection paddles to reduce the required costly  
 19 photo-cathode area. Several photon detector designs are presently being developed  
 20 and are being tested in various dewars. Since none of these new elements has been  
 21 tested in a large-scale TPC, the 35t LArTPC prototype is being constructed to  
 22 provide essential design validation.

23 The current FD designs are anticipated to have sufficient sensitivity to provide  
 24 event timing information for atmospheric neutrino and proton decay channels. How-  
 25 ever, it will not provide high efficiency down to the 20-MeV neutrino energy level  
 26 desired by the supernova program. This would have the impact that the supernova  
 27 event reconstruction energy resolution would be 20% compared to the 8% achievable  
 28 with the event time determination from a photon detector. The improvement in  
 29 physics will be studied in the near future but a substantial effort in development of  
 30 improved detection techniques is desired.

31 In the absence of precise physics requirements for the photon detector system  
 32 and in order to support R&D activities on the photon detector development it was  
 33 decided that the photon detector should provide a time stamp to determine the time  
 34 of occurrence of an event (so called "time zero") with an accuracy better than  $1 \mu\text{s}$ .

35 Items relevant to the photon detector calibration are the fast and slow components  
 36 of the light, photon propagation including scattering and reflections, impact of LN<sub>2</sub>,

E-field strength, and the energy range of interest. A calibration system that addresses the issues listed above has to be both comprehensive and cost-effective, and has to be tied to the overall calibration system that includes both charge and scintillation-light calibration techniques. Such a system is planned for the future.

To support the PD R&D phase a light-flasher-based calibration system has been designed that will serve to monitor the relative performance and time resolution of the system. In particular, for the anticipated 35t performance tests the relative efficiencies of multiple light collection techniques must be evaluated in order to be able to down-select an optimal light-readout technology. The system that meets these requirements will consist of a set of LEDs as light sources or a laser with a VUV wavelength coupled to quartz fibers, thus transmitting light from outside the detector volume to desired locations at the CPA within a TPC. Therefore the 35t detector will be equipped with LEDs located and fired externally, with fibers running into the cryostat to diffusers that will emit light from the CPA to the APA.

For the 35t cryostat, installed at the surface at Fermilab, a light-flasher-based calibration system will be complementary to calibration by cosmic-ray muon tracks.

The 35t calibration measurements should be performed with an UV (245-375nm) light source. The UV light mimics physics starting from the wavelength shifter conversion, through the light guide propagation, photo-sensor detection and FEE readout. The external light-flasher calibration system is designed such that it:

- is simple to implement (has no active components within PD/APA, such as LEDs or fibers mounted within APA).
- is less-intrusive (less fiber material is within the detector than if each PD frame were equipped with individual fiber).
- provides a benchmark light-based reconstruction with the use of localized light sources distributed throughout the detector volume.
- has the potential to be adapted for deployment in a large far detector in the future

Figure 5.21 illustrates the system. It consists of a 1U rack mount Photon Detector Calibration Module (PDCM) sitting outside the cryostat. The module generates light pulses that propagate through a quartz fiber-optic cable to diffusers at cathode-plane (CPA) to distribute the light uniformly across the photon detectors mounted within an anode plane (APA). There are five diffusers on the CPA plane: one in the center and four close to the CPA corners, as shown in Figure 5.22.

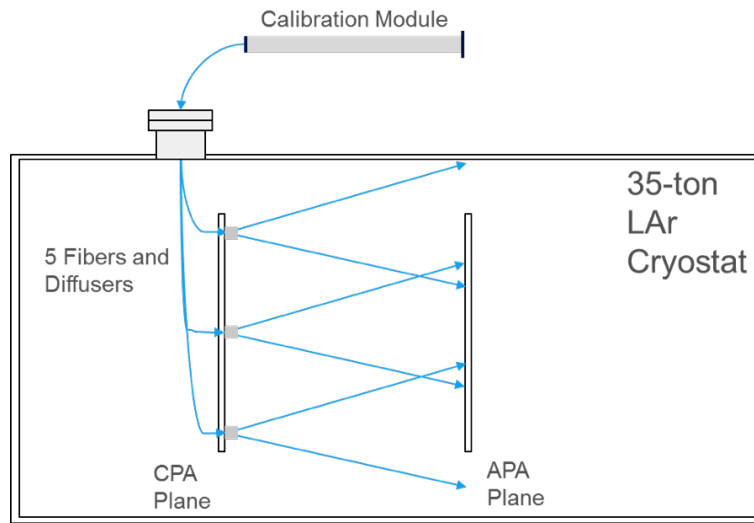


Figure 5.21: Concept of the UV-light calibration system for the photon detector in liquid argon

fig:fig-c-1

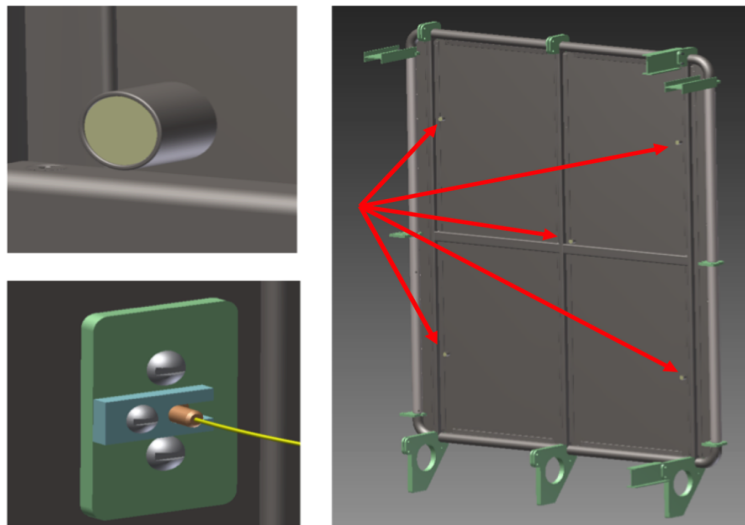


Figure 5.22: The diffuse light is emitted from diffusers (top left figure) mounted at five CPA locations, indicated by arrows (right figure). The UV light from the PDCM to diffusers is transported through quartz fiber (lower left figure).

fig:fig-c-2

1 The PDCM module layout is shown in Figure 5.23. The ANL photon calibration  
 2 module is based on a repurposed SSP unit. An SSP board will be repackaged into a  
 3 deeper rack mount chassis that will accommodate a new internal LED Pulsar Module  
 4 (LPM) and an additional bulk power supply. The LPM utilizes five digital outputs  
 5 to control the LPM pulse and its duration (arrows in black). These LVDS outputs  
 6 are derived from the charge injection control logic within the SSP's FPGA. The  
 7 even-channel SiPM bias DACs are repurposed to control the LPM pulse amplitude  
 8 (arrows in red). The adjacent odd channels are used to read out a photodiode that  
 9 is used for pulse-by-pulse monitoring of the LED light output. The output of the  
 10 monitoring diode is used to normalize the response of the SiPMs in the detector to  
 11 the calibration pulse

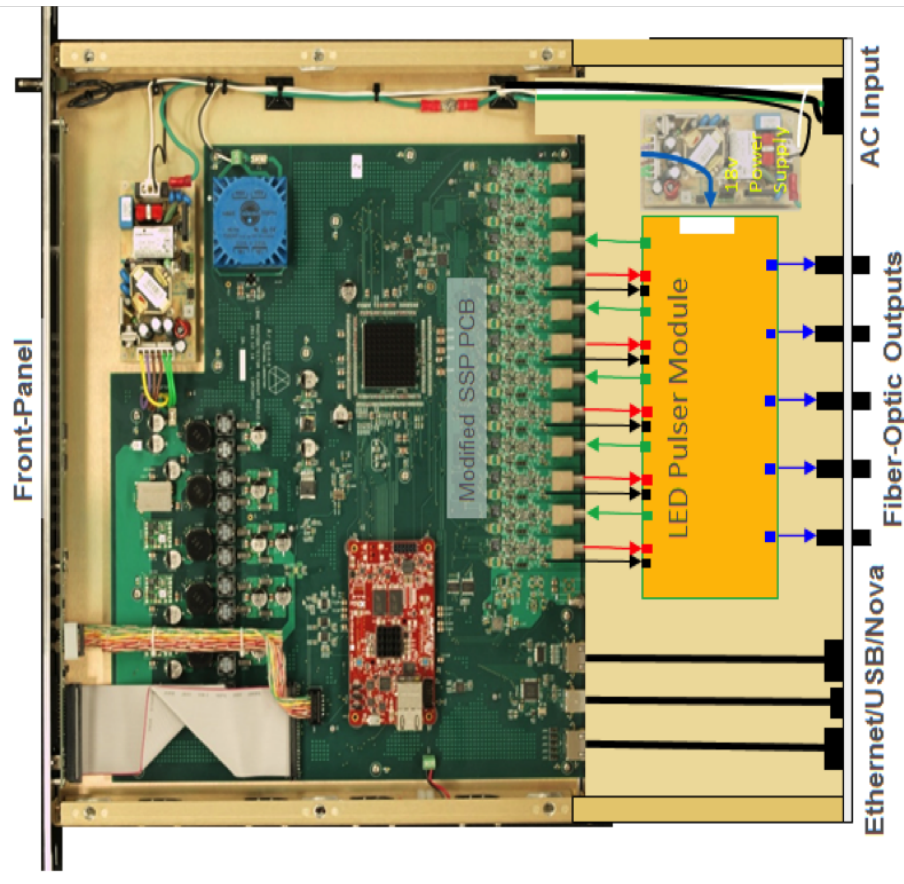


Figure 5.23: Photon detector calibration module (PDCM) layout

fig:fig-c-3

12 For the 280 nm light we have performed a simulation of the designed diffuse-light

calibration system has been performed using TracePro, a generalized 3D light ray-tracing program with the ability to include bulk optical properties such as absorption, fluorescence and birefringence in addition to surface properties such as scattering and reflection. Figure 5.24 shows simulated light distributions of the 35t APA for the cases of the VUV light emitted by either the central diffuser only (left figure), or by the outer four diffusers simultaneously (right figure). A full Geant4-based simulation of the detector will be used in the future. Using the preliminary data with the 35t-style light guides (indicating 0.5% efficiency for number of photo-electrons per incident 128-nm LAr scintillation photon 50 cm from the light guide), we estimate for 280-nm light to observe  $\sim 15$  photo-electrons per single SiPM channel when the light is emitted from the single central diffuser in 13-ns-long pulses. Similarly, we expect  $\sim 100$  photo-electrons observed by a single SiPM channel when 280-nm light is emitted in 100-ns-long pulses from the four outer diffusers at once.

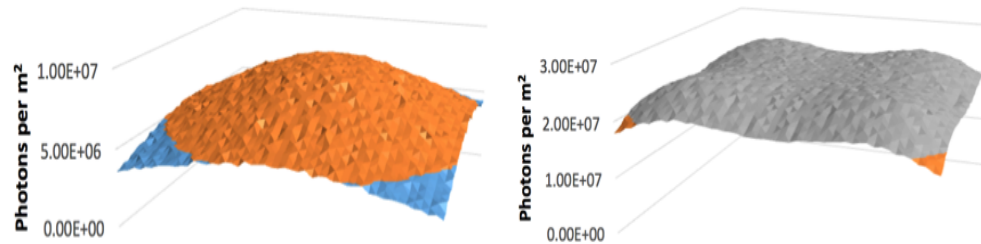


Figure 5.24: Simulated light distributions of the 35t APA for the cases of the VUV light emitted by either the central diffuser only (left), or by outer four diffusers simultaneously (right).

fig:fig-c-4

In the LBNE prototypes (i.e., the 35t) and in future far detector it will be important to check that photon-detector components are functioning properly at various stages of the detector operation. Periodic light-source deployments will monitor the system's stability as a function of time. A change in the relative difference of UV light responses will point towards potential wavelength-shifter instability; changes in SiPM gain and collection efficiencies. It is expected that much of the same monitoring can be performed with cosmic rays in the 35t (at the surface) using periodic LED/laser calibration runs complemented with cosmic-ray data tracked with an external hodoscope. With the 35t detector one could use a well-defined muon trajectory defined by the hodoscope geometry and monitor the number of p.e.'s per MeV of deposited charge. The number of p.e.'s per PD channel from a well-defined muon track can be used as a calibration constant. However, for the deep underground detector the cosmic-ray flux may be inadequate for timely monitoring of the photon detectors.

1 Two sets of calibration runs are planned for the 35t detector:

- 2 1. Calibration runs with four outer diffusers running simultaneously, in order to
  - 3 -measure response of PD channels in multi-p.e. range and get integrated
  - 4 number-of-event samples for each channel (for maximum light output)
  - 5 -test the dynamic range from 1 p.e. to maximum number of p.e.'s.
  - 6 -repeat runs periodically to track any changes in channel response.
- 7 2. Runs with central diffuser only, in order to perform
  - 8 -initial calibration runs that will reveal malfunctioning channels, if any
  - 9 -timing measurements with the 10–50-ns pulses to verify time resolution of the
  - 10 PD system.

11 The controlled source of light described here will be used to perform a relative  $t_0$   
 12 calibration, where the  $t_0$  could be absolutely calibrated with the use of the cosmic-ray  
 13 triggers available with 35t detector. Effects that contribute to a finite time resolu-  
 14 tion and relative time offset of PD channels include: scintillation time constants,  
 15 photon conversion with wavelength shifter, photon propagation through PD paddle,  
 16 SiPM jitter, and FEE resolution. Most of these effects are constant and can be in-  
 17 dividually measured on the bench, so the LED flasher system will monitor overall  
 18 stability of the photon detector. To go beyond the current R&D phase one needs  
 19 detailed MC simulations of light production, propagation and detection. This will  
 20 allow comparisons of reconstruction performance against prototype data in terms of  
 21 calorimetric energy and position reconstructions for measured event tracks. Future  
 22 light-collection systems will aim to maximize the active area of the light guide bars,  
 23 to achieve a high photon-detection efficiency with an optimized timing and granu-  
 24 larity required for improved position resolution. As in the case with the TPC charge  
 25 calibration we will need to evaluate what may be achieved with expected cosmic-ray  
 26 muons and Michels,  $\pi^0$ , and natural radioactivity events (such as  $^{39}\text{Ar}$  with end-point  
 27 energy of about 500 keV).

## 28 5.8 Installation

29 Installation of the photon detectors is one of the most significant factors driving the  
 30 mechanical design. As discussed in the section ?? the initial approach was to install  
 31 the PDs and run the SiPM twisted-pair cable down the frame side tube prior to wire-  
 32 wrapping the APA. After experience with the environmental controls (primarily UV  
 33 filtered light) required by the PDs, as well as the difficulties in dealing with the  
 34 PD readout cable ends during wire-wrapping, it was decided to change the reference



design to include inserting such that the PDs would be inserted after wire wrapping is complete. In addition to relaxing the physical constraints on the wire wrapping, this also relaxes a schedule connection between the APA and PD fabrication. It is not necessary to install the PDs into the APA frames until shortly prior to installation of the APAs into the cryostat.

As noted above, and shown in Figure 5.17, a total of 10 PDs are installed into each APA frame, with five coming in from each side. The installation will occur with the fully assembled APA frame lying flat on an insertion station table. Prior to installation, the PD cable bundle will be inserted into the APA side tubes. The cable bundle will be pre-assembled prior to installation such that the end of each cable will terminate at the correct slot for the PD to be connected. Our reference cable design has also been modified to a single cable with four individual twisted pairs in a single jacket, so each APA side tube will only require 15 cables (three per PD, 30 per APA). These cables extend approximately 30 cm past the end of the APA tubes at the cold electronics end of the APA, and following installation of the APA into the cryostat are connected to long-haul cables for the run to the readout electronics (see Figure ??).

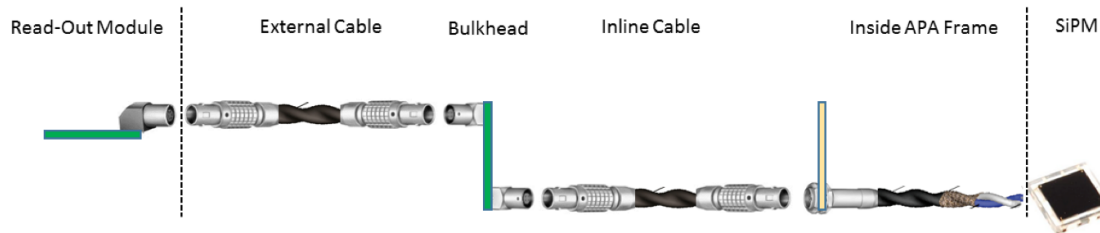


Figure 5.25: Cable assembly for each photon detector readout channel.

fig:fig:5.8-1

Following this step, five PDs will be inserted into the APA through one side frame, with connections being made between the twisted-pair cables and the SiPM PCB just as the readout end of the detector enters the tube (see Figure ??). The PD is then inserted the last 10 cm into the frame, and affixed to the inner surface of the APA tube (see Figure ??). The process is then completed for the five PDs to be inserted from the opposite side.

Following insertion of the PDs, the environmental controls required for the PD WLS materials (UV filtering, temperature and humidity control) will need to be observed for the entire APA.

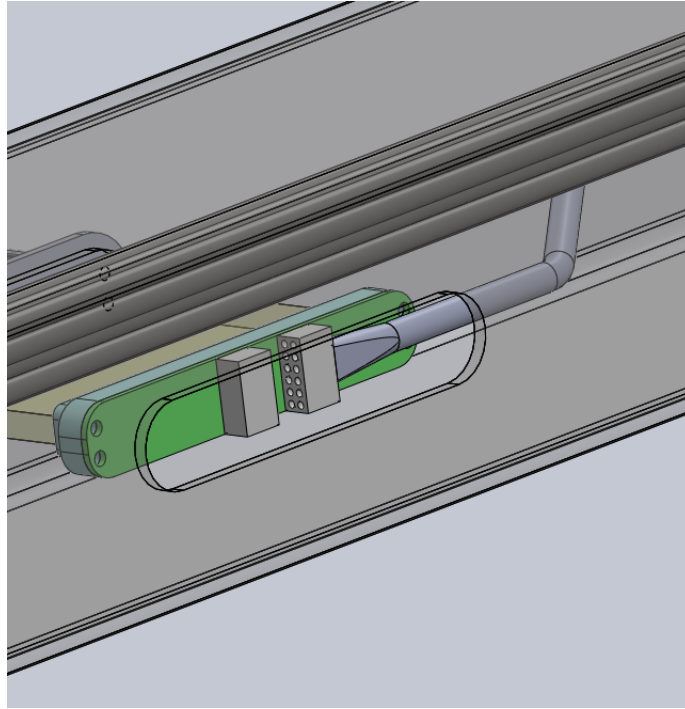


Figure 5.26: Connection between the PD twisted-pair cable and SiPM mounting board.

fig:fig:5.8-2

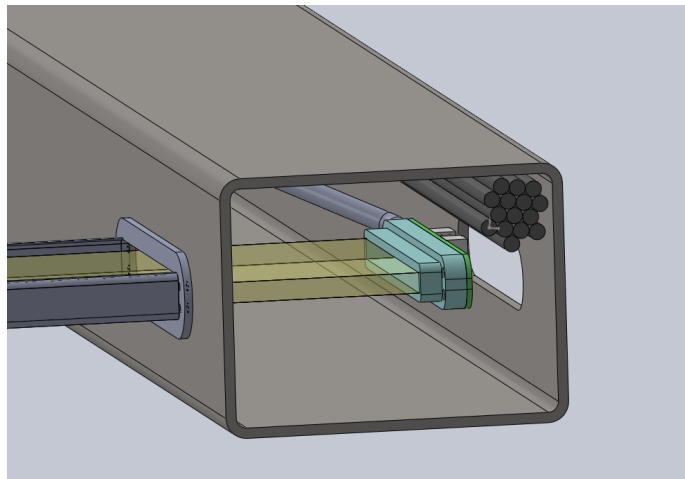


Figure 5.27: Insertion of one PD paddle

fig:fig:5.8-3

# Chapter 6

## Installation and Commissioning

`ch:install`

### 6.1 Introduction

This chapter discusses the LAr-FD Installation and Commissioning system's activities and responsibilities. LAr-FD construction and installation will occur in a series of distinct phases:

- installation planning and prototyping
- surface storage identification and operation
- excavation and outfitting of the cavern; this activity is the responsibility of the Conventional Facilities subproject (CF),
- construction and installation of the cryogenics system and cryostats by a construction management firm; this activity is the responsibility of the cryogenics system
- construction of LAr-FD components at collaborating institutions and shipment to the Far Site
- installation of detector components and installation management
- commissioning activities leading to CD-4

The Installation and Commissioning system will accept responsibility for the LAr-FD cavern, associated tunnels, infrastructure and above-ground facilities from Conventional Facilities upon completion of the Conventional Facilities contract. The cavern will be outfitted with the following utilities upon receipt of beneficial occupancy:

- 1     • ventilation in accordance with OSHA standards
- 2     • electrical power sufficient for the HVAC, cryogenics plant cooling and general
- 3       110-V service
- 4     • quiet power for the electronics with a double Faraday-shielded transformer lo-
- 5       cated some distance from the cavern to take advantage of the inductance of the
- 6       power lines. The primary shield will be connected to the main substation via
- 7       a grounded feed wire and the secondary shield will be connected to the Ufer
- 8       ground.
- 9     • communications consisting of telephone lines and computer network
- 10    • cavern lighting in accordance with OSHA regulations for industrial use
- 11    • tunnel lighting with battery-powered backup or emergency circuit backup
- 12    • environmental monitoring of oxygen, carbon monoxide, smoke and temperature
- 13    • dual isolation bulkheads separating the cavern from the existing Far-Site facility
- 14    • sump pumps for groundwater removal
- 15    • over head conveyances

16    After beneficial occupancy of the completed cavern from the CF subproject, the  
17 cavern ventilation system will be tested to assure adequate performance with regard  
18 to ODH requirements. The system will be tested with oxygen monitors distributed  
19 around the cavern and a controlled argon spill. Remedial action will be taken if  
20 required during cryostat and cryogenics construction.

21    The cryostat and cryogenics contractor will retain responsibility for the site during  
22 construction of the cryostat and cryogenics system. The Cryostat and Cryogenics  
23 System group will provide oversight during this phase. Upon completion of this  
24 contract, the facility will be in the following state:

- 25    • the LN2 refrigeration system will be constructed and commissioned with liquid
- 26      nitrogen
- 27    • the LAr systems and cryostats will be constructed and tested without the
- 28      introduction of cryogens
- 29    • the access hatches on the cryostat and the cryostat feedthroughs will be tem-
- 30      porarily sealed

- 1     • the APA- and CPA-installation support beams will be in place
- 2     • the cryostat will be connected to the steel roof structure thus connecting the
- 3         detector ground to the Ufer ground

4     The detector will utilize the cryostat pit rock bolts as part of the grounding  
 5     scheme. The rock bolts in the pit will extend through the shotcrete that lines the  
 6     cavern and be attached to the reinforcing steel network within the cryostat concrete  
 7     liner, forming an Ufer ground. The reinforcing steel will be connected to the steel  
 8     truss cover. The Ufer ground will be connected to the detector ground (the cryostat  
 9     SS liner) through a low-impedance connection.

10    The Installation and Commissioning group will be responsible for all LAr-FD-  
 11    related activities at the Far Site from this point in time until the end of the LAr-FD  
 12    project. Close coordination is clearly required between this group, system groups  
 13    that provide components and other Far Site construction activities.

14    On-project commissioning activities include the coordination of system-checkout  
 15    activities, culminating in the approval to introduce LAr into the detector modules,  
 16    and managing the steps required to meet the CD-4 goals.

## 17    **6.2    Integration - Permanent Equipment**

18    The Installation and Commissioning system will provide some permanently installed  
 19    equipment that is used by multiple Detector systems or is integral to the installation  
 20    process. This equipment includes the relay racks, cable management, support rails for  
 21    the TPC and the remaining outfitting of the detector cavern that was too detector-  
 22    specific to be included with the conventional facilities work.

### 23    **6.2.1    Relay Racks and cable management**

24    A port is located above every other APA junction and each port will serve the two  
 25    upper APAs located directly underneath it. Cables for the lower two APAs will be  
 26    routed from ports adjacent to the outer edge of the cryostat. The cables will travel  
 27    down enclosed cable trays on the two side walls of the cryostat to the floor and  
 28    over to the closest rows of APAs. Cables for the other row of APAs will be routed  
 29    similarly down the opposite side wall. The horizontal portion of the cable run will  
 30    be outside of the wire planes, so the use of double shielded cable such as Amphenol  
 31    skew clear may be adequate. If not, then custom metal shields will be mounted on  
 32    the front-end circuit boards.

The racks will be mounted either directly over the ports or adjacent to them with an extension to the rack that covers the port. All cables can be brought out of the cryostat into a grounded and shielded enclosure.. The plan is to use 36-in-deep racks and construct a shielded area on the back side of the rack to hold and shield the excess cable. 28 racks will be required for each cryostat, and rack space will be shared between the TPC and photon-detection system readout and power supplies.

A modest number of racks will be required for the DAQ. Two options are under consideration for the location main DAQ racks. One option would transport data on fibers to the surface as quickly as possible with the main DAQ racks may be located on the surface near a control room. The second option locate all DAQ racks underground with an environmental enclosure for the rack. For the second option a small adjoining control room would also be located underground.

All relay racks will be equipped with rack protection and monitoring. The racks will be supplied by the detector installation effort along with the labor to develop the rack plan.

## 6.2.2 Detector Electrical Ground

The LAr-FD will have approximately 200,000 channels of electronics with an intrinsic noise level of less than 1,000 electrons. These channels will be connected to wires that are seven meters long. Thus, grounding, shielding and power distribution are critical to the success of the experiment. In the reference design the entire detector pit will be treated as the detector ground for the following reasons: For the purpose of maintaining a low-noise performance within each of the proposed cryostat detectors, the construction of the LBNE far detectors' grounding system requires that there be separate grounding structures for the cryostat tank walls and for the cavern and its utilities. Both the cryostat detectors and the cavern structures will employ an Ufer ground, or concrete encased grounding electrodes, within the concrete construction. The guiding principle for the LBNE far detector's grounding system is to minimize, as much as possible, any ground currents from flowing between the AC power distribution system and the detector cryostats. Also, any flow of ground currents, both conducted and coupled, need to be minimized between the individual detector cryostats. Therefore, there are specific requirements for the connection and spacing of the reinforcing metal bars (rebar) set in the concrete for the cryostats' construction and for the specific and controlled interconnections between these separate grounding structures.

There shall be electrical separation between the cavern's rebar/concrete/shotcrete construction and the cryostats' rebar/concrete construction. The rebar of one

1 structure and the rebar of the other structure shall not come in direct contact with  
2 each other. The rebar for all four vertical walls and the cryostat floor concrete shall  
3 be integrated together in order to form a uniform grounding structure between all  
4 five concrete cryostat surfaces. The top plate of each cryostat detector shall serve  
5 as the detector's grounding point and be connected uniformly to the detector's Ufer  
6 ground structure.

7 Since the cavern will be cored out of solid rock, there will be no integrated metal  
8 "building" support structure as normally would occur for a building constructed  
9 above ground. In addition, some metal supports for piping, water, cable trays, air  
10 ducts, etc. will be supported by anchors attached to rock. Therefore, there is the  
11 probability that various metal structures within the cavern will not be electrically  
12 connected together. To maximize the low-impedance path (back to the source) for  
13 AC ground currents and to minimize the probability of these ground currents being  
14 coupled onto the cryostats' grounding structures, these cavern metal infrastructure  
15 components need to be electrically interconnected as much as possible.

16 The substation vault, housing the 12.47 kV transformers and associated switchgear,  
17 will be to the east side of the cavern and thus will not have appreciable distance from  
18 the detectors' construction. All concrete walls, floor and ceiling of the vault will em-  
19 ploy a rebar Ufer ground system and will contain a metal ground mesh (similar to  
20 that used for surface substations' buried ground grid) constructed of copper, within  
21 these concrete surfaces. This ground mesh shall be electrically connected to the Ufer  
22 ground.

23 The metal top plate for each of the cryostats serves as the grounding point of  
24 reference for their respective cryostat. Therefore, it is very important that the metal  
25 interconnections be as uniform as possible and that any ground potentials along this  
26 top plate, and its components, be minimized. All components of the top plate, un-  
27 less specifically designated, shall be electrically isolated from the cavern's ground  
28 structure. All cryogenic piping, crossing over from the cavern ground structure to  
29 the detector ground structure, shall implement dielectric breaks so as not to make  
30 metal-to-metal electrical contact between the ground structures through the piping.  
31 The top plate shall employ a uniform copper sheeting beneath the steel plate's con-  
32 struction. This copper sheeting shall be electrically bonded to the steel plate at  
33 multiple points where the distance between the bonding points does not exceed 4  
34 feet. The cryostat's stainless steel membrane must be electrically connected to the  
35 copper component of the cryostat's top plate. The hanger bolts or rods, used to  
36 support the weight of the detector frames, shall be electrically bonded to both the  
37 top plate and to the stainless-steel membrane [30].

### 6.2.3 TPC support rails

A set of five support rails, shown in Figure 6.1 permanently mounted in each cryostat, will provide the support for the APA and CPA panels and a track for moving the APA panels into position. This rail will be supported by rods spaced at 5-m intervals from anchor points on the inner surface of the cryostat roof. The rod lengths will be adjustable so that the rails can be leveled during installation. This will be done in rail segments with the aid of a laser level. The rails shrink 2.8 mm per meter of length or about 8.4 cm along the entire length during cool-down. The rods will be installed with an angle bias that allows the rails to return to level after the cryostat and TPC is cooled.

The estimated mass of each stacked set of APA panels is 725 kg and stacked set of CPA panels is 1280 kg. The load on the TPC on the support rails comes to 315 kg/m for the APA rails and 555 kg/m for the CPA rails. The rail segments will be constructed from 20-cm-deep laser-welded, W-shaped, stainless-steel beams. The rail segments will be joined end-to-end with large pin connections. The upper support rods will be made from 15-mm-diameter stainless steel.

The rail installation can be completed most efficiently while the large scaffolding system used for cryostat construction is still in place, therefore it will be part of the cryostat-construction contract.

Early estimates indicate that the cryostat roof will deflect 4-5cm with fluctuations in the ullage pressure. If the TPC supports are connected to the roof, as described previously, the TPC will move and distort with the roof. An alternative configuration in which the TPC is supported independently from the roof with support rods passing through the roof would isolate the TPC from this roof motion. This is currently being evaluated.

### 6.2.4 Discussion of ports in the top of the cryostat

Each of the APAs will require various electrical services for operation. This includes bias voltages, power and control lines. The data will be carried out by signal cables. The photon detectors mounted inside the APAs will also have cables to carry out their signals. Inside the cryostat all of these cables will be copper. An electronics feedthrough is required at the boundary between the cold LAr volume and the warm ambient above the cryostat. These feedthroughs will be based on a standard 10-in cryogenic conflat flange mounted on an 8-in tube that will pass through the thickness of the cryostat roof. Like other LAr detectors, this flange will either have a series of connectors or printed circuit boards with connectors to transition from the cold to warm side. On the cold side, the cables will be routed from the APAs up to and



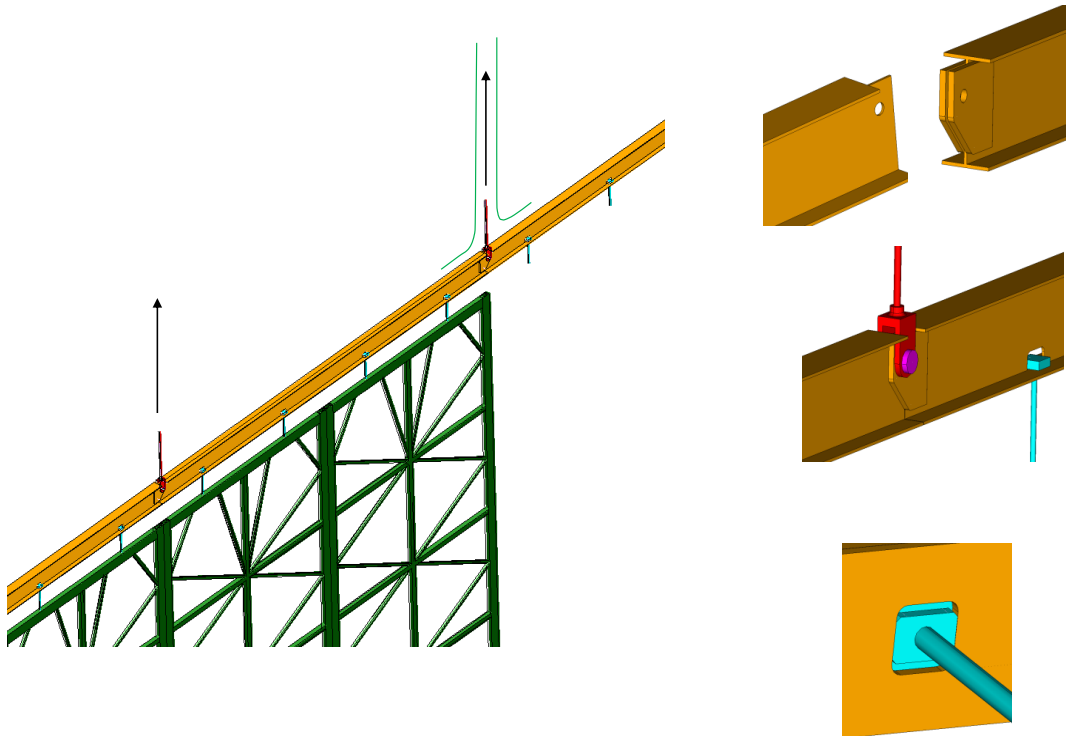


Figure 6.1: Support rails inside cryostat

fig:support-ra

connected to the cold side of the feedthrough flange. On the warm side, the cables and data fibers will be routed from the flange to various electronics racks positioned on top of the cryostat. Each feedthrough will serve two APAs. A conceptual layout for the feedthroughs is shown in Figure 6.2. For the upper APAs, the cables will be preinstalled and routed from the cold side of the feedthrough down and along the support rail to the place where they will connect to their corresponding APA. The feedthrough flanges will be positioned along the length of the APA rows and spaced based on the widths of two APAs or about every 5-m. For the lower APAs with the electronics near the floor of the cryostat, the cables will be routed from the cold side of the feedthrough down the side walls of the cryostat. When the cables reach the floor they will be routed over to their corresponding APAs. The lower APA cables will be routed in cable trays supported from the cryostat. The feedthroughs will be positioned near the outer edges of the cryostat to minimize the cable lengths. Their spacing will also be approximately every 5-m.

## 6.3 Installation Equipment - Temporary Equipment

The below-ground pre-installation activities must be completed prior to the start of TPC installation into the cryostat. These activities include design, procurement and installation of detector-specific infrastructure such as man-lifts, lifting fixtures, catwalks, ladders, tools, and so on. The major items include a clean space for the unpacking and preparation of the TPC components, the support rails for the TPC panels, the staging platform for joining two panels, installation monorails for moving the panels inside and outside of the cryostat, and a mobile scaffold for providing access to the top and middle of stacked TPC panels.

### 6.3.1 Clean Area Outside cryostat

A clean-area enclosure in the range of class 10,000 (ISO 7 equivalent) will be constructed near the entrance to the cryostat to keep the area around the open hatch isolated. The assembly practices used by the MicroBooNe experiment may serve as an example of what is required for a surface detector. The enclosure will have an area for personnel to gown with the appropriate clean-room clothing and safety shoes. A large, closable door, next to which the TPC-storage containers can be parked, will allow unloading of the TPC components directly from the container into the clean area. The TPC components will be cleaned and protected to a level suitable for installation into the cryostat as part of the TPC production process and will be delivered to the Far Site in clean containers.

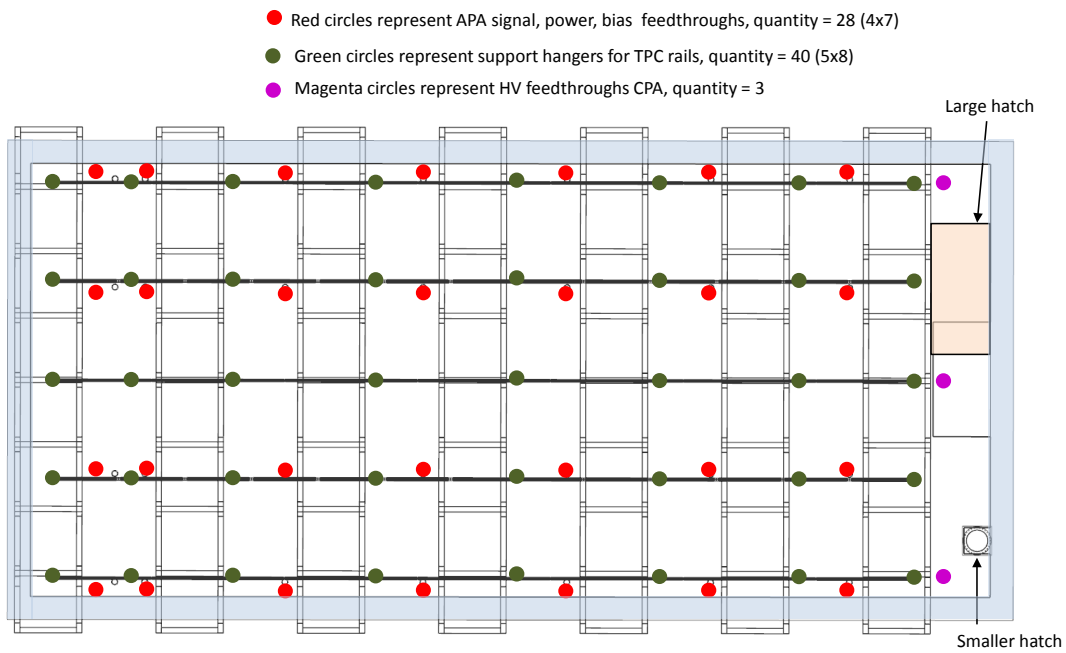


Figure 6.2: Feedthroughs

fig:tpc-instal

1 The Double Chooz detector developed a cleanliness plan to ensure that dust con-  
 2 tamination did not contribute more than a specified amount to the detector signal.  
 3 Measurements were made of the activity of rock in that experiment's underground  
 4 laboratory which was assumed to be the source of airborne dust. Maximum allowable  
 5 dust concentrations and the clean-room class and cleanliness practices were deter-  
 6 mined such as to meet the requirements for contamination. The Installation and  
 7 Commissioning group will need to evaluate the dust sources in the LAr-FD detector  
 8 pit and determine if a similar approach to setting the clean room requirements is  
 9 appropriate.

### 10 6.3.2 Inside cryostat

11 Several items will be installed in the cryostat for use during TPC installation, and  
 12 removed before the cryostat is filled with argon.

- 13 • A temporary lighting system inside the cryostat with emergency backup light-  
 14 ing will be in place for TPC installation and removed in sections as the TPC  
 15 is installed and be completely removed before filling the cryostat with Argon.  
 16 This lighting system will also be filtered to the appropriate spectrum to protect  
 17 the photon detection system installed in the APAs.
- 18 • A ventilation system and air-monitoring sensors with alarms will assure ade-  
 19 quate air quality for the personnel working inside the cryostat. The system will  
 20 also include a high-sensitivity smoke-detection system that is interlocked to the  
 21 power for all devices inside the cryostat. The blowers and temperature control  
 22 will be located outside of the cryostat and polyester ducts will be located inside  
 23 the cryostat to distribute the air properly.
- 24 • A raised-panel floor to protect the cryostat floor; see Figure 6.3. The raised-  
 25 panel floor will have support spacers located between the convolutions in the  
 26 stainless-steel primary membrane to provide a flat surface for moving equip-  
 27 ment around within the cryostat. The pressure limit for the insulation in the  
 28 floor is 0.5 MPa and the load of the vacuum that will be used to monitor leak-  
 29 age during installation reduces the effective limit to 0.4 MPa. The stock round  
 30 spacers in the raised-panel floor are 10-cm diameter and would support a load  
 31 of 310 kg. The load can be increased by adding larger-diameter plates under  
 32 the standard spacers. Since the raised floor is modular, it can be removed in  
 33 sections as the TPC installation progresses. A perforated pipe manifold will  
 34 be located on the cryostat floor to distribute the argon during the gas piston

[fig:raised-floor-protect](#)

purge and during liquid recirculation. Depending on the details of the membrane cryostat corrugation height, the distribution piping may fit under the temporary floor or be installed in sections as the floor is removed.

- Tooling for APA and CPA panels including fixtures to insert the lower APA and CPA panels. The top and bottom TPC panels of a stacked pair will be moved into the cryostat separately and connected together below the cryostat equipment hatch. A lower panel holding fixture will temporarily hold the bottom APA and CPA panels when they are inserted into the cryostat. See Figure 6.9.
- Two fixed scaffolds with integral stair towers will be installed temporarily inside the cryostat. One tower will be located in the work area of the large hatches. This tower will provide access for personnel to make the connections between stacked panels and to connect stacked panels to the installation rail inside the cryostat. The second fixed tower will be located near the smaller hatch and will provide a second route of egress from the cryostat.
- A rolling scaffold with an integral stair tower will allow personnel to access the top of the stacked panel after they are in the final position. The rolling scaffold will be moved around the cryostat floor as the TPC installation progresses.

### 6.3.3 Full-scale Mockup

A full-height mock TPC section will be constructed as part of an installation prototype in a suitable location at Fermilab, e.g. the Wideband lab or D-zero assembly hall. See Figure 6.4. The installation equipment prototype is intended to test and verify the key elements of the equipment and the process for TPC installation and to serve as a training tool for personnel who will perform the TPC installation. The initial testing of the equipment at Fermilab will be used to verify or refine the installation concepts. Complete testing of the final equipment and operations will occur at Fermilab before the installation equipment is moved to the Far Site.

This prototype will include APA and CPA rail supports and cable routing features. Multiple mock-ups of APA and CPA stacked panels will be installed. The APAs will include all mechanical mounting points and some electrical connections such as optical-fiber readout cables and power cables. Prototype versions of the special equipment required for TPC installation will be used, including the trolley, lower-panel staging platform, and a rolling-cart scaffolding. Scaffolding elements will

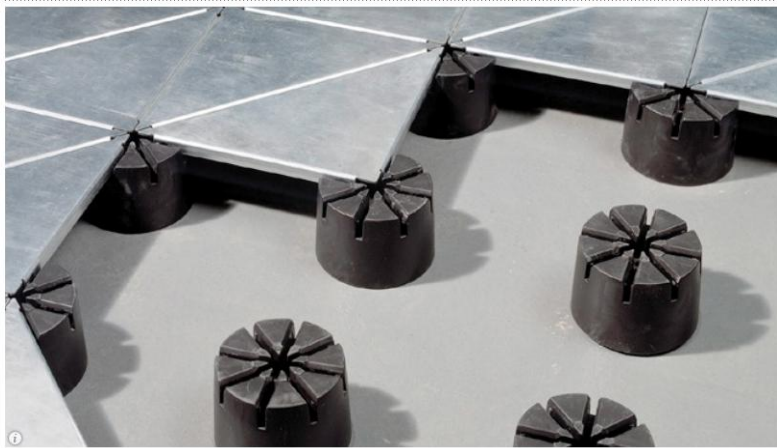


Figure 6.3: Raised-panel floor to protect the cryostat's primary membrane

fig:raised-flo

1 be rented and the scaffolding will be erected by a contract or as part of a training  
2 program.

3 Initial tests, where appropriate, will be performed at a low elevation. For example,  
4 the installation trolley and rail segment will be tested at a low elevation with a  
5 dummy weight. After successful demonstration of the features in this position, the  
6 components will be moved to a high elevation for testing with full-size mock-up  
7 panels.

### 8 **6.3.4 Surface at SURF**

9 Materials for the TPC will be transported down the Ross shaft from the surface to  
10 the 4850-ft level. It is planned that most of the material for the TPC can be sized  
11 such that it will fit inside and be transported by the cages in the Ross shaft. The  
12 APAs are too large and will be slung underneath the cage inside a specially designed  
13 container. Space and equipment will be required to move the standard and special  
14 container into the cages and attach the slung loads underneath the cage.

## 15 **6.4 Far Site Installation**

### 16 **6.4.1 Far site activities overview**

17 Local storage in the SURF region will be required because Detector installation  
18 is much shorter duration than the detector fabrication/assembly time. The local  
19 storage facility will also be used for checkout and testing of Detector components.  
20 The installation space in the cavern is very limited and so material will be moved from  
21 the local storage to the cavern at the rate of installation. Prior to installation, a clean  
22 area will need to be setup in the cavern just outside of the cryostat (Figure 6.5). After  
23 the clean area is configured, temporary installation equipment will be installed in the  
24 first cryostat. TPC installation will proceed in the first cryostat and as temporary  
25 equipment is removed from the first cryostat it will be installed into the second  
26 cryostat to prepare for installing the second TPC.

27 The following list of detector components and systems will be installed in the  
28 Detector Hall and cryostats:

- 29 • Relay Racks with rack protection (28 on each cryostat plus a few in the control  
30 room)
- 31 • Cable trays and power distribution to racks from power panels provided by CF



Figure 6.4: An Installation equipment mockup of a TPC section, in blue, will be built and tested in a Fermilab assembly building like the Wideband lab shown here

fig:installati



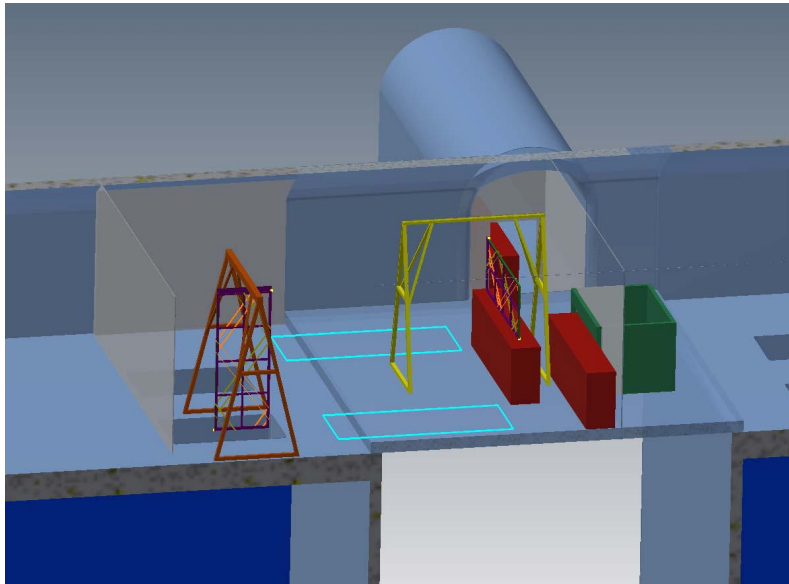


Figure 6.5: Underground clean area arrangement

fig:clean\_area

- 1 • Cable inside and outside of the cryostat including cable feedthrough flanges
- 2 • DAQ crates and power supplies in the relay racks
- 3 • The 52 APAs per cryostat with integrated photon detectors
- 4 • Three times the equivalent active area of the APAs of CPAs per cryostat
- 5 • Cryogenic instrumentation not installed by the cryostat construction vendor
- 6 (e.g. purity monitors)
- 7 • Temporary ventilation, lighting and access equipment
- 8 • Note: Support rails and hangers are installed during cryostat construction

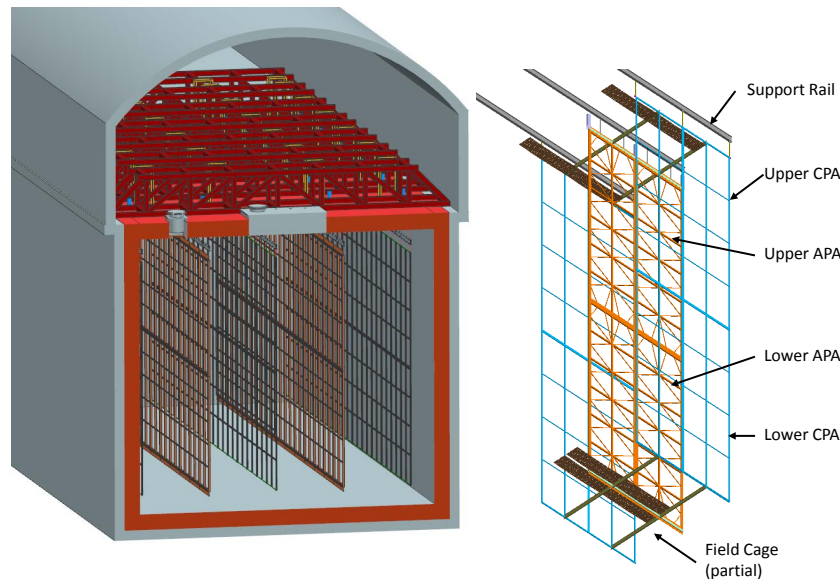


Figure 6.6: TPC panels installed in cryostats

fig:tpc-panels

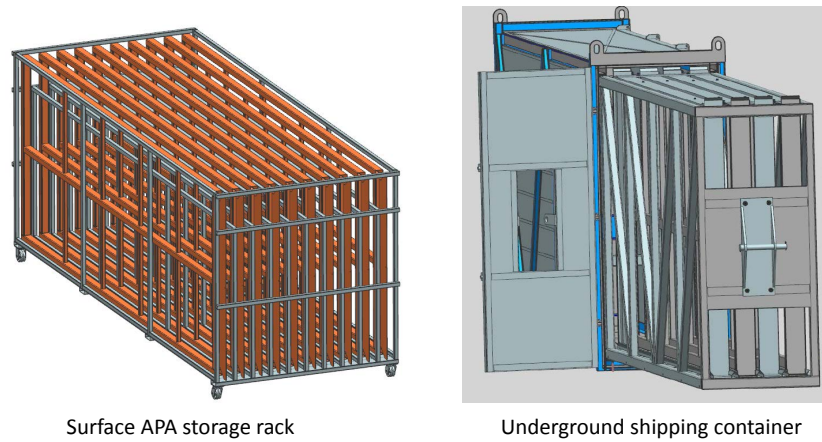
## 6.4.2 Detector material storage /testing above ground

Detector components will be delivered to the Far Site over a period of many months and will need to be stored in a storage facility. This will allow the supply of material to be maintained ready for installation. The facility will also be used for testing and checkout of the APA after the shipment from the manufacturing sites. Depending on the APA design and assembly flow the storage/testing facility may also be used for installation of the photon detectors and/or the installation of cold electronics on to the APAs. A facility for this purpose will be identified in the SURF region and arrangements will be made for its use during LAr-FD construction. Each system group is responsible for delivery of its components to the storage/testing facility. The Installation and Commissioning group will provide the management and labor resources for inventory control, material handling and transport from the off-site facility to the Detector Cavern.

The majority of the storage/testing facility space will be required for storage and testing of APAs. The APA will be shipped from the APA assembly sites to the SURF area in semitrailers or 40 ft long cargo containers. The APAs will be held in a vertical plane in a rack with one rack of about 10 APAs fitting in each trailer or container. It is expected that the racks can be removed from shipping container (Figure 6.7) and the APAs can remain in the racks as they are moved and stored. The racks will have an approximate footprint of 8' x 22'. About 12 such racks will be needed for each cryostat approximately with 2500 ft<sup>2</sup> required for all APA storage. The CPA and field cages material can be packed more compactly and will require additional space of approximately 2,500 square feet.

The facility will also be used for checkout and testing of the APAs after the long distance shipment from the assembly sites. In addition, the facility may also be used for some assembly tasks such as installing the photon detectors. Since the APAs will be exposed during these operations, the work lighting will have UV filters installed and air recirculation units will be used to maintain a clean area in the range of class 10,000 (ISO 7 equivalent). There will be a few of stations for check out, inspection and transfer of the APAs. Approximately 5000 ft<sup>2</sup> will be required for these functions with a clear height of approximately 20ft to allow the APAs to be lifted out of storage racks and stations. With a modest weight less than 1/2 ton, a free standing workstation crane would be sufficient for lifting the APAs.

The storage/testing facility should be located with a one hour drive of SURF. The facility could be in Rapid City or in the area close to SURF. The final choice of location will be a compromise of many factors including available lease space, workforce availability and cost.



Surface APA storage rack

Underground shipping container

Figure 6.7: Concept for APA shipping containers

fig:apa\_ship

### 6.4.3 Material movement to cavern

Material will be transferred from the storage facility to the Detector Hall for installation, as required to sustain the installation rate. The Ross shaft will be used to move material underground. It is possible that the CPA and field cage materials can be sized such that they will fit into the Ross shaft cage. However the APAs are too long and must be slung underneath the Ross cage.

A conceptual design for a special APA transportation container has been developed that will hold 4 APAs in horizontal and vertical orientations for movement in the Ross shaft. The 60" distance between the rails of the Ross shaft limits the width of objects that can be lowered down the shaft.

The Ross shaft lift has provisions to attach long objects to the bottom of the cage. The APA in a special container will descend the shaft in a vertical orientation (the same orientation as they will be installed), be rotated to a horizontal orientation as they are extracted from the shaft, then moved along the access drift on a cart to the cavern. The APA transportation container consists of an internal rack that can be extracted from the outer container thus avoiding moving the outer container into the clean area used for installation. The internal rack will be used to hold the APA in the installation area until they are installed. Empty racks will be returned to the warehouse for reloading in the transportation container. Figure 6.8 shows the warehouse arrangement.

### 6.4.4 TPC installation details

Each APA and CPA panel will be carefully tested after transport into the clean area at the septum and before installation into one of the cryostats. Immediately after a panel is installed it will be rechecked. Throughout the installation period it will be checked periodically. The serial stacking of the APA panels along the rails means that removing and replacing one of the early panels in the row after several others are installed would be very costly in effort and time. Therefore, to minimize the risk of damage, as much work around already-installed panels as possible will be completed before proceeding with further panels.

The installation sequence is planned to proceed as follows:

1. Install the monorail or crane in the staging area outside the cryostat, near the equipment hatch.
2. Install the relay racks on the top of the cryostat and load with the DAQ and power-supply crates.

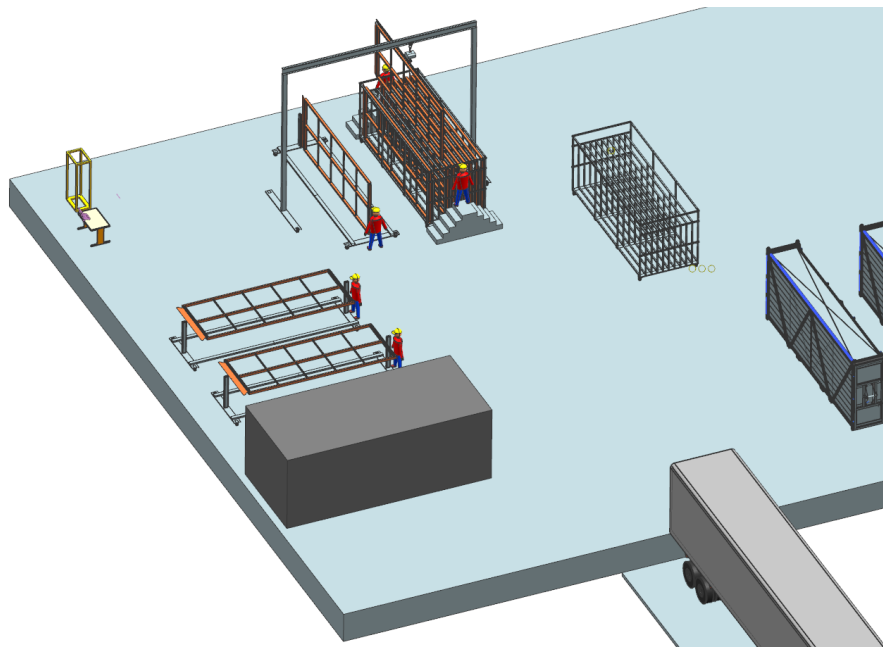


Figure 6.8: Warehouse arrangement

fig:warehouse\_

- 1     3. Dress cables from the DAQ on the top of the cryostat to remote racks.
- 2     4. Construct the clean-room vestibule outside the cryostat hatch.
- 3     5. Install the raised-panel floor inside the cryostat.
- 4     6. Insert and assemble the stair tower and mobile scaffold.
- 5     7. Install the staging platform inside the cryostat.
- 6     8. Install protection on (or remove) existing cryogenics instrumentation in the  
7       cryostat.
- 8     9. Install the cryostat feedthroughs and dress cables inside the cryostat along the  
9       support beams.
- 10    10. Begin regular transport of TPC panels in shipping boxes into the cavern.
- 11    11. Install TPC panels:
  - 12       (a) Install the two outer CPA wall assemblies. This is done by building the  
13          CPA one horizontal strip at a time. Once a strip is assembled, it is lifted  
14          and another strip is attached below until the entire height is reached. It  
15          is unclear at this point what length of strip is feasible to install at once.  
16          This length is expected to correspond to some multiple of the distance  
17          between the support hangers.
  - 18       (b) Install the center CPA.
  - 19       (c) Install the end wall field cage between the two outer CPAs and the existing  
20          center row.
  - 21       (d) Begin the installation of the first row of APAs.
  - 22       (e) Lower the first APA with the electronics toward the bottom of the cryostat  
23          and fix in the transfer fixture.
  - 24       (f) Lower the second APA with the electronics toward the top of the cryostat.
  - 25       (g) Mechanically join the two APAs in the center.
  - 26       (h) Lift the connected pair of APAs onto the support rail.
  - 27       (i) Move the stacked pair of APAs down the rail to their installed position.
  - 28       (j) Link the stacked pair to the adjacent stacked pair of APAs.
  - 29       (k) Connect power and signal cables.

- 1       (l) Test each APA wire for expected electronics noise. Spot-check electronics  
2       noise while cryogenics equipment is operating.
- 3       (m) Connect field cage in sections as the APA and CPA installation progresses  
4       at the top.
- 5       (n) Perform electrical test on CPAs and field cage.
- 6       (o) Remove temporary floor sections as the TPC installation progresses.
- 7       (p) When a row of APAs is completed, install any argon distribution piping  
8       under the APAs and associated CPAs.
- 9       (q) Install the lower field cage panels for this row of APAs.
- 10      (r) Install the end field cage for this row of APAs and associated CPAs.
- 11      (s) Move the mobile scaffold to the second row of APAs.
- 12      (t) Move installation scaffold and transfer fixture to the second installation  
13      hatch.
- 14      (u) Repeat the APA installation on the second row of APAs.
- 15    12. Complete the end field cage.
- 16    13. Remove the transfer fixture, moving platform and stair tower from the cryostat.
- 17    14. Temporarily seal the cryostat and test all channels for expected electronics  
18      noise.
- 19    15. Seal the access hatch.
- 20    16. Perform final test of all channels for expected electronics noise.

21       In general, APAs and CPAs will be installed in order starting with the panels  
22       furthest from the hatch side of the cryostat and progressing back towards the hatch.  
23       The field cage will be installed in stages as the installation of APA and CPA panels  
24       progresses at the top to utilize the mobile access platform. The only requirement  
25       for survey or alignment is to maintain the edges of a row of APA panels to 3-mm  
26       alignment along each beam. A laser guide or optical transit in combination with  
27       the adjustment features of the support rods will be used to establish the alignment.  
28       After the stacked panel is attached to the support rods the electrical connections  
29       will be made to cables that were already dressed to the support rail and electrical  
30       testing will begin. Periodic electrical testing will continue to assure that nothing gets  
31       damaged during the additional work around the installed panel.



After the CPAs have been installed, the APA installation will be performed in three stages, each in a separate location; the locations, or zones, are shown in Figure 6.9. First, in the clean room vestibule, a crew will move the APA panels from storage racks, rotate to the vertical position and move them into the cryostat. Secondly, in the panel-staging area immediately below the equipment hatch of the cryostat, a second crew will transfer the lower APA panels from the crane to the staging platform, connect the upper and lower panels together. After connection, a motorized trolley will move the stacked panels from the hatch area to their final position. Since the duty cycle of the trolley is rather low, the trolley could be battery-powered to avoid the need for cable festooning. The trolley initially moves along a rail until it reaches the end where the stacked panel will be permanently mounted. A third crew will reposition the movable scaffolding and use the scaffold to make the mechanical and electrical connections at the top for each APA. The rails inside and outside the cryostat will each have motorized trolleys so that work can be conducted by all three crews in parallel. The steady-state rate for installation, given this work plan and a single-shift schedule, is estimated to be two stacked panels per day.

Signal and power cables will be installed from the cryostat feedthrough ports next to the APA support rods, shown in Figure 6.2, along the rails to the point where the connection to the APAs will be made. The cables will be preplaced and tested before APA installation begins. Editor's Note: Figure 6.2 is for a 17-kton fiducial mass cryostat. The 5-kton cryostat is shorter and has fewer rows.

The detector installation system is also responsible for developing and implementing the procedure for monitoring the integrity of the membrane-cryostat primary liner during installation. The space between the primary liner and the secondary liner will be held under vacuum during installation. The vacuum level will be automatically monitored and will alarm if any leaks develop in the primary membrane during TPC installation.

## 6.5 Training

Installation and Commissioning will be responsible for the personnel, equipment and procedures for providing Detector Hall access controls after cryostat construction is complete. Members of the installation crew will be trained on specific installation tasks and must pass a qualification test. The training will use mock-up APAs constructed for the installation equipment prototype. The training program will be developed in collaboration with Fermilab and SURF ES&H personnel.

Installation and Commissioning will provide all of the general tools and equipment needed to support the personnel in their installation work. It will include hand

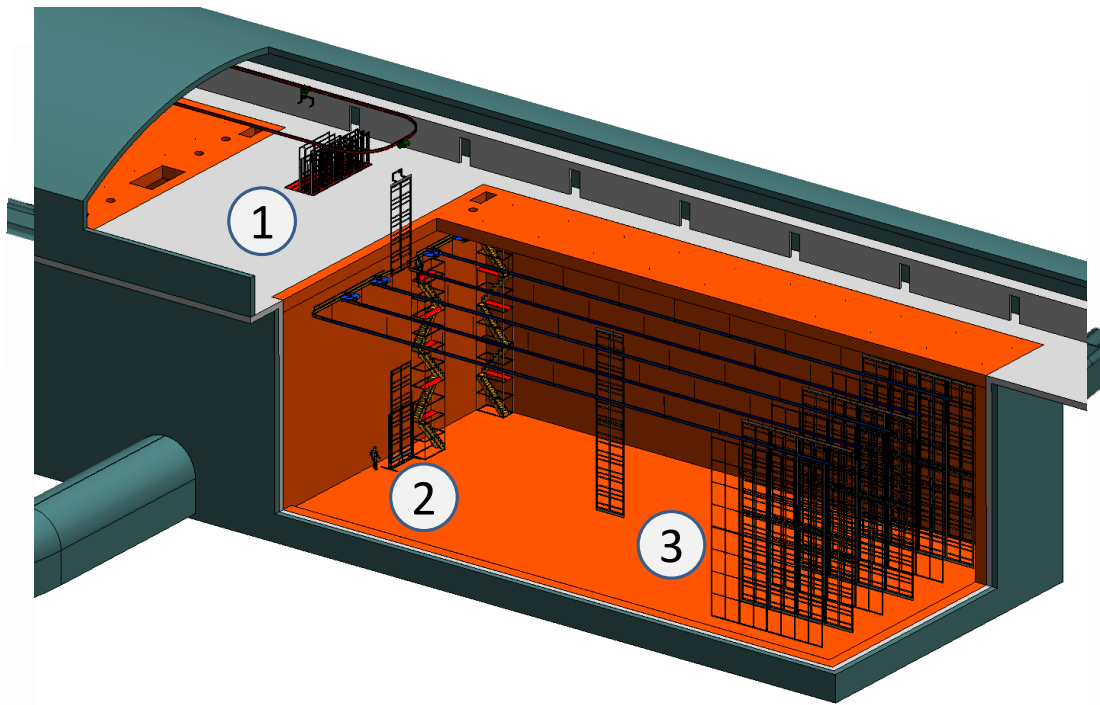


Figure 6.9: The three main work zones for TPC Installation. TPC components are lowered into the cryostat in zone 1. TPC components are connected together in zone 2, transferred to the support rails and then rolled into final position (zone 3).

fig:tpc-instal

1 tools, power tools, material-handling equipment, ladders, lifts, electrical meters and  
 2 personal protective equipment (PPE). The detector system groups will provide any  
 3 special equipment to check out or debug the power and read-out chain of the detec-  
 4 tors. The detector groups will also provide system experts at the far site to check  
 5 out the detector systems before and after installation.

## 6 6.6 Far Detector commissioning

7 The detector installation and commissioning activities will be staged such that both  
 8 TPCs can be tested cold while one cryostat still remains available as a potential  
 9 storage vessel in case a repair is needed. The LAr in one cryostat can be transferred  
 10 to the other and back again, if necessary, to allow access for a repair. Once both  
 11 TPCs are known to work properly at LAr temperature, the second fill will take place.

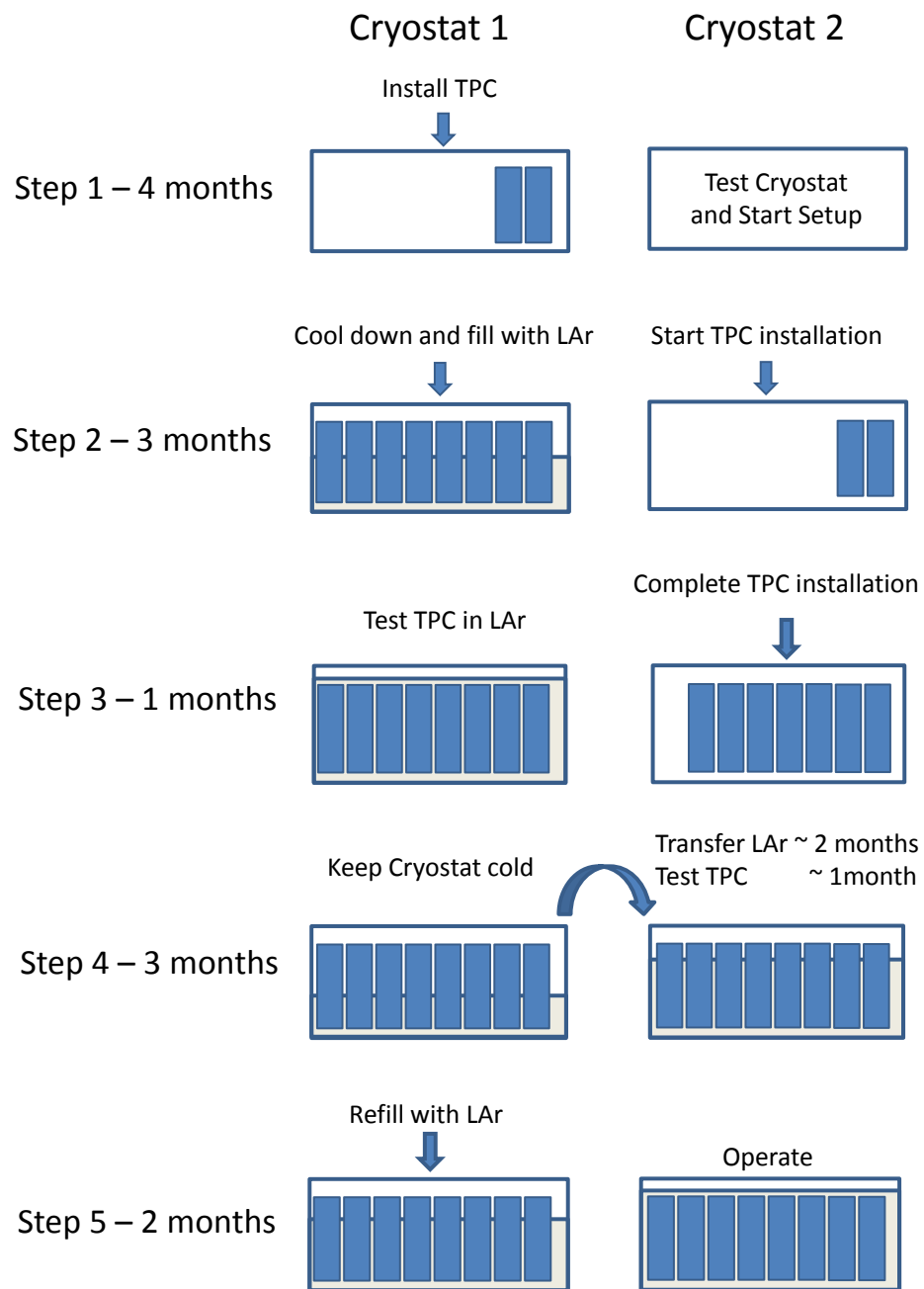
### 12 Commissioning Sequence

13 The commissioning sequence, illustrated in Figure 6.10, will start with the in-  
 14 stallation of the TPC into cryostat 1 (installed on the north side). During this time,  
 15 the leak testing and cleaning of cryostat 2 will be completed and, where possible,  
 16 the setup for TPC installation will begin. After the TPC is completely installed  
 17 in cryostat 1, its purge and cool-down can begin. Filling the cryostat with room-  
 18 temperature gaseous Ar, injected from the bottom in order to displace the air upward  
 19 through the top ports.

20 Following the purge and cool-down, the LAr fill of cryostat 1 will take approxi-  
 21 mately two months, assuming continuous LAr deliveries. LAr purification will begin  
 22 when the liquid level is high enough to start the recirculation pumps. The commis-  
 23 sioning of the cryogenics system can also begin at this point, but its full commission-  
 24 ing will require a fully loaded cryostat. In-vessel purity monitors will operate during  
 25 this time.

26 When the cryostat is full with LAr, the TPC will undergo testing for approx-  
 27 imately one month to establish that the TPC will be able to achieve the tracking  
 28 requirements and to confirm that no further access will be needed to the cryostat  
 29 and TPC. Additional testing will occur after the other cryostat is filled and is thus  
 30 no longer available as a storage vessel.

31 Installation of the TPC in cryostat 2 will begin during the LAr fill of cryostat 1.  
 32 After TPC installation and electronics testing, the purging and cooling for cryostat 2  
 33 can proceed. The LAr from cryostat 1 will be transferred to cryostat 2, and once it is  
 34 full, its TPC will undergo a month of initial testing. During this time, cryostat 1 will  
 35 be maintained cold via continuous circulation of gaseous Ar. After it is established  
 36 that no further access will be required, cryostat 1 will be refilled with LAr and begin



Design for a Deep Underground Single-Phase LArTPC

Figure 6.10: Startup and Commissioning Sequence

fig:tpc-instal

a five-month commissioning period. Testing during the commissioning period will demonstrate that the detector performance parameters for CD-4 have been achieved.

This sequence provides for a continuous flow of work and optimizes the use of the crews that will install the detectors and maintain the cryogenics systems. The operations crew is required from the start of the purge and cool down of the first cryostat through the commissioning phase. possible but these in general will require breaks in the work for the installation crew and a longer duration for the work of the operations crew. The cost/risk management benefit of other sequences will be evaluated as more experience is gained with the detector systems.

Several opportunities for system checkout arise throughout the detector installation, startup and commissioning phases as illustrated in Figure 6.10. Since the full DAQ system will be operational at the start of TPC installation, a full suite of tests can be made within the HV operating limits.

### 6.6.1 Argon receipt

Liquid Argon will be delivered at the surface by an over the road tank truck. These tank trucks have a capacity of 18.7 metric tons. Each 5-kT cryostat will require 9 ktons to fill. This will equate to 500 number of tank trucks at the surface over estimated two months for filling the cryostat. Each load of LAr will be tested for purity before it is allowed to unload. Once approved, the LAr will be transferred to a large dewar on the surface. From the dewar, the LAr will be evaporated into a gaseous state and sent down to the detector in a stainless steel pipe in the shaft. Once it reaches the detector hall, it will be recondensed and piped to the cryostat. When the liquid reaches a certain level, the internal cryogenic pumps will begin to recirculate the LAr through the purification system. More details of this process are detailed in the cryogenic section of this report.

### 6.6.2 Testing

After delivery to the Far Site and before installation, the following tests will be performed on the TPCs:

- The wires of the APA will be visually inspected for breakage or sagging.
- The leakage current will be measured on the APA wire bias terminals.
- A DAQ station will be connected to the APA cables to run electronics calibration to identify bad channel/wire connections.

- 1     • The CPA and field cages will be visually inspected. The resistance will be
- 2       measured between the frame and the bias electrodes.
- 3     • The integrity of the resistors and the resistance between the field-cage strips
- 4       will be measured.

5       These tests will be repeated and the mechanical connections will be checked after  
 6   the APA and CPA are installed in a cryostat and the field cage is connected. The  
 7   resistance between the field cage and the APA will be measured, and any individual  
 8   broken or sagging APA wires will be removed. Wire integrity will be confirmed by  
 9   measuring the Equivalent Noise Charge (ENC) of each electronics channel and com-  
 10   paring it with the expected noise for a properly connected wire. The wire-integrity  
 11   test also ensures that coherent noise sources, e.g., a mechanical connection between  
 12   the detector ground and the Ufer ground, are discovered promptly. As the TPC in-  
 13   stallation progresses, periodic electrical testing will continue on previously installed  
 14   panels to ensure the wire and electronics integrity and the collective noise perfor-  
 15   mance. Error budgeting, regular noise monitoring and mitigation will ensure that  
 16   the TPC reaches and maintains the required noise performance before the cryostat  
 17   is cooled down.

18     After cool-down and during LAr filling the electronics and wire integrity will be  
 19   tested to ensure that no damage occurred during the temperature drop. Once the  
 20   fill is complete, the TPC can be tested at full high voltage for the first time. The  
 21   electronics testing at this point will be relatively quick, however, a demonstration  
 22   that the TPC is fully operational, i.e., observation of tracks in each drift cell, re-  
 23   quires achieving sufficient electron lifetimes in the LAr, which may take some time.  
 24   Information from operation of the 35-ton prototype (Section 7.5) is expected to in-  
 25   form and confirm the simulations and to help estimate the time required to achieve  
 26   sufficient LAr purity for testing operations.

### 27   6.6.3   ES&H

28   Careful consideration for ES&H will be demonstrated in the planning and execution  
 29   of the installation and commissioning. Safety professionals will be involved in all  
 30   phases. Hazards of note for the TPC installation include work at elevated heights  
 31   and work in the confined space of the cryostat. During the detector installation no  
 32   atmospheric hazards are expected inside the cryostat, thus for normal TPC instal-  
 33   lation work the cryostat should not require any special access permits. Procedures  
 34   for access and egress will be prepared that include sign-in and sign-out for cryo-  
 35   stat entry and for two-person work. Communication equipment will be available

- 1 that works within the cryostat and between the interior and exterior of the cryostat.
- 2 Emergency response procedures will be developed that include provisions for evac-
- 3 uation and rescue from the cryostat. Temporary ventilation and light systems will
- 4 include air monitoring and high-sensitivity smoke detection. Crane operation and
- 5 operator certification methods will be established. In general the detector installa-
- 6 tion operations are such that most of the installation tasks will involve preparing a
- 7 written hazard analysis.

# Chapter 7

## Detector Development Program

ch:randd

### 7.1 Introduction

This chapter describes the development program designed to ensure a successful and cost-effective construction and operation of the massive, dual-cryostat LArTPC detector for LBNE and to investigate possibilities for enhancing the performance of the detector. The feasibility of the LArTPC as a detector has been demonstrated most impressively by the ICARUS experiment.

add ref? CERN prototype proposal doesn't have one, as was suggested

It is understood that for successful operation an LArTPC has stringent requirements on

- argon purity, which must be of order 200 ppt O<sub>2</sub> equivalent or better
- long-term reliability of components located within the liquid argon; in particular, the TPC and field cage must be robust against wire-breakage and must support a cool-down of over 200 K
- the front-end electronics, which must achieve a noise level ENC of 1000e or better

The design of the LBNE LArTPC has evolved significantly from earlier concepts based on standard, above-ground, upright cylindrical LNG storage tanks which envisioned single TPC sense and high-voltage planes spanning the full width of the tank – essentially a direct scaling of previous detectors. Problems with the actual construction of such massive planes and with the logistics of being able to construct the TPC only after the cryostat was complete are avoided in the present design. In this



design, TPC ‘panels’ are fully assembled and tested — including the electronics — independently of the cryostat construction. This modular approach is a key feature of the design. It has the benefit not only of improving the logistics of detector construction, but also the individual components can be of manageable size. It should also be noted that the cryostat itself is formed of modular panels designed for quick and convenient assembly.

This chapter does not provide a comprehensive overview of the liquid argon detector development efforts worldwide; it discusses several that are closely related to the LBNE detector, including the Material Test System, TPC design, the 35-t membrane cryostat prototype at Fermilab and its testing program, and the single-phase prototype detector proposed for construction at CERN.

## 7.2 Materials Test System

sec:mts

An area for LAr detector development, shown in Figure 7.1, has been established in the Proton Assembly Building at Fermilab. The Materials Test System (MTS) has been developed to determine the effect on electron-drift lifetime of materials and components that are candidates for inclusion in LAr-FD. The system essentially consists of a source of clean argon ( $< 30$  ppt  $O_2$  equivalent), a cryostat, a sample chamber that can be purged or evacuated, a mechanism for transferring a sample from the sample chamber into the cryostat, a mechanism for setting the sample height in the cryostat so that it can be placed either in the liquid or in the gas ullage above the liquid, a temperature probe to measure the temperature of the sample, and an electron-lifetime monitor. The system is fully automated and the lifetime data are stored in a single database along with the state of the cryogenic system.

A noteworthy feature is the novel bubble-pump filter inside the cryostat. In case of argon contamination, this can filter the cryostat volume in a few hours, allowing continuation of studies without having to refill. A schematic of the MTS is shown in Figure 7.2.

The major conclusions of the studies are summarized here. No material has been found that affects the electron-drift lifetime when the material is immersed in liquid argon — this includes, for example, the common G-10 substitute, FR-4. On the other hand, materials in the ullage can contaminate the liquid; this contamination is dominated by the water outgassed by the materials and as a result is strongly temperature-dependent. Any convection currents that transport water-laden argon into the LAr and any cold surfaces on which water-laden argon can condense will fall into the LAr and reduce the electron lifetime. Conversely, a steady flow of gaseous argon of a few ft/hr away from the LAr prevents any material in the gas volume



Figure 7.1: Liquid argon area at the Proton Assembly Building at Fermilab

fig:PAB

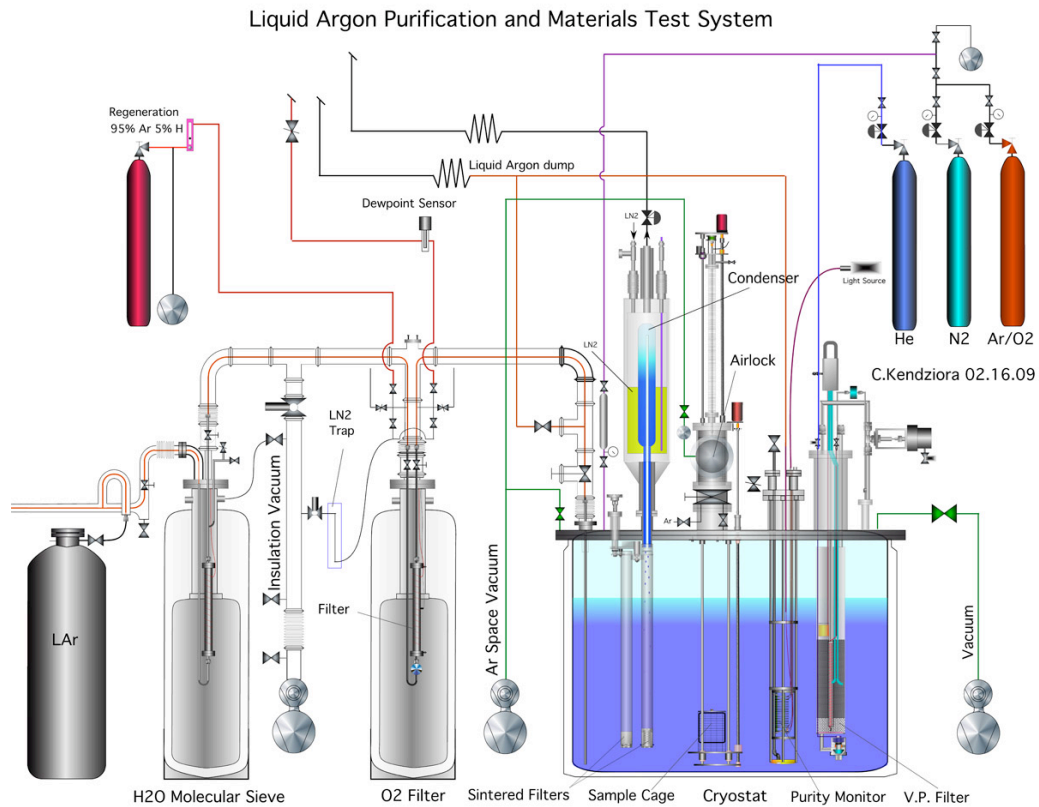


Figure 7.2: Schematic of the Materials Test System (MTS) cryostat at Fermilab

fig:MTS\_Schem

1 from contaminating the LAr.

2 These results are taken into account in the design of both MicroBooNE and LAr-  
3 FD. For LBNE they have been cast as detector requirements. The MTS will continue  
4 to be used by MicroBooNE and LBNE to test detector materials such as cables that  
5 will reside in the ullage.

## 6 7.3 TPC Design

7 A string of recent events in several liquid argon setups, such as Long Bo, DarkSide50,  
8 ArgonTube and MicroBooNE, in which the sustainable high voltage (HV) was much  
9 lower than designed voltages, prompted a reevaluation of the breakdown strength of  
10 liquid argon, especially at “detector grade” purity. Recent studies [31][32] have re-  
11 vealed that the HV-breakdown strength depends on factors such as electrode feature  
12 size, distance, stress area/volume, and LAr purity. Although no conclusive threshold  
13 was found, the results indicate that the safe operating field in LAr is well under  
14 100 kV/cm.

15 With the uncertainty in the liquid argon HV dielectric strength, attention will  
16 be focused on the HV-related aspects of the TPC design involving the CPAs and  
17 field cage modules. An R&D document has been compiled for the far detector [33]  
18 that contains a section on the proposed R&D topics and activities to reduce the HV-  
19 related risks. Apart from the HV feedthrough, which will be designed and tested  
20 above the operating voltages, there is a plan to improve the designs of the CPAs and  
21 field cage modules.

22 The current TPC design directly interconnects all CPAs on a cathode plane. Two  
23 of the outer cathode planes face the grounded cryostat walls. The stored energy be-  
24 tween one of the outer cathode planes and the cryostat wall, with the full bias voltage  
25 applied, is more than 150 joules[34]. This amount of energy, if released suddenly in  
26 an event of a high voltage discharge, is sufficient to raise the temperature of a cube  
27 of stainless steel with 2-mm sides by 4000°K, resulting in a leak in the membrane  
28 cryostat. Moreover, a sudden collapse of the cathode voltage will also inject very  
29 large current pulses into the front-end ASICs connected to the first induction plane  
30 wires, causing damage to the electronics.

31 To minimize these risks, the logical steps are:

- 32 • minimize the stored energy when possible by swapping the locations of the  
33 APA and CPA planes such that no CPAs are against the cryostat wall.
- 34 • slow the voltage collapse in a discharge by constructing the cathode planes out  
35 of highly resistive material to form a long RC time constant for discharge

- 1           – study the electrical behavior of CPAs constructed from highly resistive
- 2           material
- 3           – identify and test a resistive coating that is robust at cryogenic temperature
- 4           and able to maintain good adhesion to the cathode structure
- 5           – design the new CPAs with all resistive elements

6       Techniques for applying a highly resistive coating over the current 35t-style  
 7       printed circuit board-based panels on the field cage are being developed in order  
 8       to remove field concentration around the conductor edges. In parallel, a fall back  
 9       solution for reducing the field using roll-formed electrodes with a much larger edge  
 10      radius is being developed.

11      For the APAs, a simple and effective method to contain a broken outer layer wire  
 12      must be developed; such a wire must be prevented from drifting far into the drift  
 13      volume and making contact with the field cage.

## 14   7.4   35-ton Prototype: Phase 1

15   When first conceived, the 35t prototype cryostat was constructed to demonstrate that  
 16   a non-evacuatable membrane cryostat can satisfy the less-than-200-parts-per-trillion  
 17   (ppt) requirement on oxygen contamination of the liquid argon in the detector and  
 18   maintain that level stably. It was intended to prototype a wide variety of issues that  
 19   construction and operation of the far detector would need to address, including pro-  
 20   curement of materials and services, safety and the processes involved with ensuring  
 21   the cryostat can maintain high-purity liquid argon.

22   Later it was decided to extend its scope, and to install and operate a small-scale  
 23   LArTPC and photon detector in the cryostat; this phase (discussed in Section 7.5)  
 24   will focus on the performance of active detector elements placed directly in the volume  
 25   of liquid argon. The membrane cryostat demonstration, completed in 2014, is now  
 26   referred to as “Phase 1” and the operation of the TPC is called “Phase 2.” Phase 2  
 27   is currently under construction and it is planned to take data in summer 2015.

### 28   7.4.1   Phase 1 Construction

29   The construction of the 35t cryostat addressed a number of issues. First were  
 30   project-related issues, such as gaining detailed construction experience, developing  
 31   the procurement and contracting model, and incorporating the design and approval  
 32   mechanism in the Fermilab ES&H manual, which was necessary because membrane

1 cryostats are designed in accordance with European and Japanese standards. Sec-  
 2 ondly, it addressed technical issues such as high-purity operation in this type of  
 3 cryostat and the suitability of the planned LAr-FD construction techniques and ma-  
 4 terials.

5 The LBNE project contracted with the Japanese company IHI to build the 35t  
 6 cryostat at Fermilab. It was built in Fermilab's PC-4 facility where the Liquid Argon  
 7 Purity Demonstrator (LAPD) [35] is also located, which allowed for re-use of a large  
 8 portion of the cryogenic-process equipment installed for LAPD. The proximity and  
 9 size (30 tons) of LAPD also offers the possibility using LAPD as a partial storage  
 10 vessel for LAr if the 35t ever needs to be emptied. The 35t employs a submersible  
 11 pump to pump the LAr from the cryostat to the filters. Two pumps were installed  
 12 for redundancy, but only one is used at a time. Figure 7.3 shows the layout of the  
 13 35t prototype at Fermilab's PC-4 facility. Figure 7.4 shows a cutaway view of the  
 14 cryostat and a photograph of the interior of the completed cryostat.

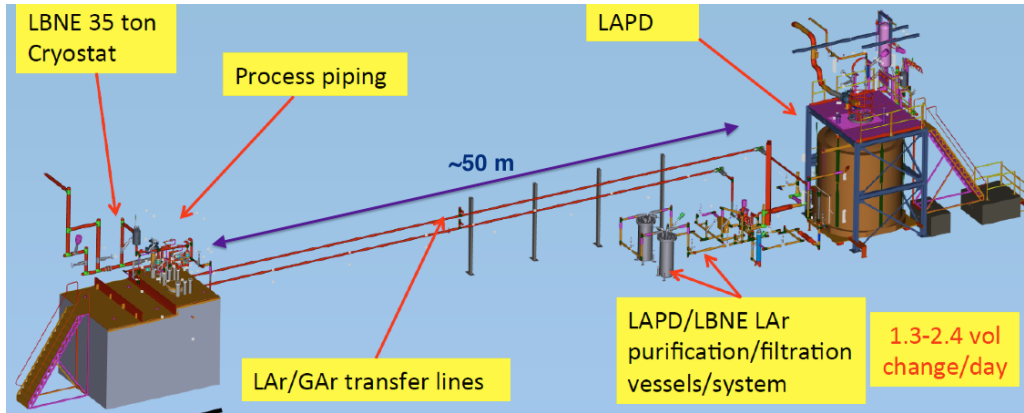


Figure 7.3: Layout of 35t prototype at Fermilab's PC-4 facility.

fig:35cryo

15 Table 7.1 gives the details of the construction materials and the dimensions for  
 16 the 35t. More information can be found in [36]. The insulation thickness is 0.4 m  
 17 rather than the 1.0 m chosen for the reference design. The techniques of membrane-  
 18 cryostat construction were demonstrated to be a fit for high-purity TPC service.  
 19 Welding of corrugated panels, removal of leak-checking dye penetrant or ammonia-  
 20 activated leak-detecting paints, and post-construction-cleaning methods were tested  
 21 for suitability of service.

22 In principle, a thin-walled membrane cryostat is as suitable as a thick-walled  
 23 cryostat for use with high-purity LAr. Both are constructed with 304 stainless steel  
 24 with a polished surface finish. Both use passive insulation. The total length of

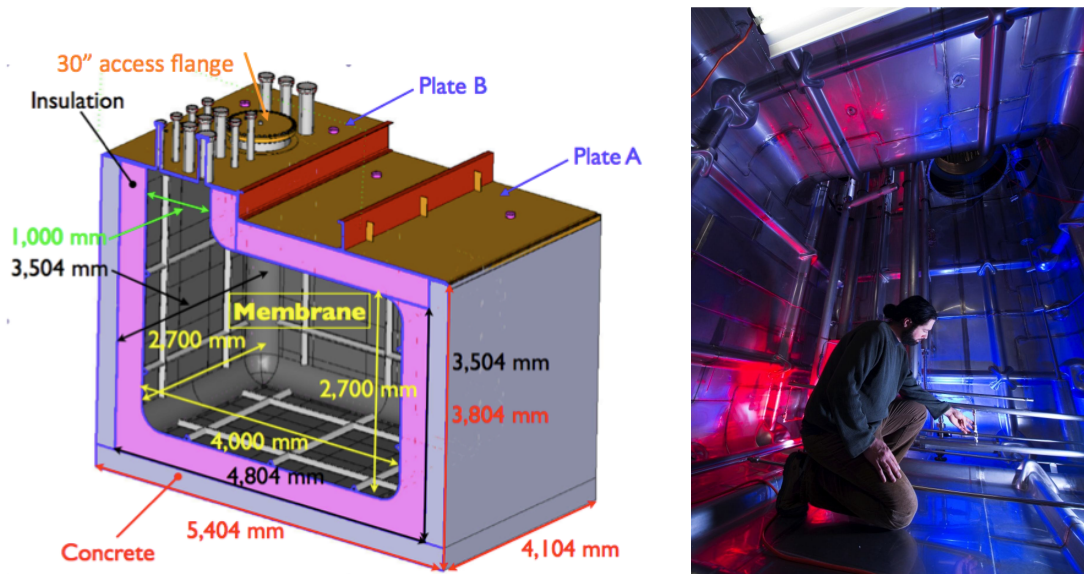


Figure 7.4: (left) Cutaway view of the 35t cryostat; (right) Interior photograph of the completed cryostat.

fig:35cutaway

Table 7.1: 35t Details and Dimensions

Parameter	Value
Cryostat Volume	29.16 m <sup>3</sup>
Liquid Argon total mass	38.6 metric tons
Inner dimensions	4.0 m (L) x 2.7 m (W) x 2.7 m (H)
Outer dimensions	5.4 m (L) x 4.1 m (W) x 4.1 m (H)
Membrane	2.0 mm thick corrugated 304 SS
Insulation	0.4 m polyurethane foam
Secondary barrier system	0.1 mm thick fiberglass
Vapor barrier Normal	1.2 mm thick carbon steel
Steel reinforced concrete	0.3 m thick layer

:35Tdimensions



interior welds required for construction would be similar in both cases. The leak-checking procedure would be the same in both cases.

The significant difference between membrane cryostats and thick-walled cryostats is the depth of the welds used to construct the vessel. The majority of membrane-cryostat welds are completed in one or two passes with automatic welding machines. A second difference, and a major advantage, is that the membrane cryostat is a standard industrial design that has been in use for over 40 years. A thick-walled cryostat vessel would be custom designed and would require significant engineering and testing. A third difference, and another major advantage, is the ability to purge the membrane cryostat insulation space with argon gas so that a leak cannot affect the purity if it escapes detection and repair.

## 7.4.2 Phase 1 Cryogenics Instrumentation

The 35t includes a full complement of standard commercial transducers and sensors that are used to monitor and control the cryogenic environment. They include temperature sensors, pressure transducers (absolute and gauge), flow meters, and level sensors. These devices are typically read out directly into the Control System and data-logged.

A number of commercial gas analyzers measure trace impurity levels ( $O_2$ ,  $H_2O$ , and  $N_2$ ) in the argon. Some have sensitivities at the 100 ppt level. A gas distribution switchyard feeding the gas analyzers allows the sampling points in the 35t to be reconfigured.

There were also two purpose-built pieces of instrumentation for the monitoring of the high-purity LAr environment, the purity monitors (PrMs) and the RTD Spooler. The PrMs are used to measure electron lifetimes in the LAr, and the RTD Spooler is used to make precision measurements of the temperature profile of the cryostat as a function of depth. These instruments were originally constructed for the LAPD run and are fully described in [35].

## 7.4.3 Phase 1 Operations

The operational portion of Phase 1 involved three main steps:

1. pushing the air up and out of the cryostat, leaving only Ar gas (the Piston Purge)
2. controlled cooldown and fill of the cryostat with high-purity LAr



3. circulation of the LAr through filters to remove residual impurities

4. maintenance of the high purity level of the LAr

LAPD, referred to in Section 7.4.1 and in progress while the 35t cryostat was being built, demonstrated that it is not necessary to evacuate a cryostat in order to achieve LAr purity levels sufficient for LBNE. The 35t prototype has demonstrated the same thing in a membrane cryostat. This is of paramount importance since the costs of multi-kiloton cryostats that could withstand evacuation is prohibitive. The 35t followed the procedure LAPD [35] established to obtain and maintain pure LAr.

## Gas Phase

When the phase 1 test began, “dry” air had been purging the cryostat for approximately three weeks.

The first step of the “gas phase” portion of the process, the Piston Purge, removes the air in the cryostat; during this step argon gas is flooded into the bottom of the cryostat. Since argon is heavier than air, the argon layer rises, analogous to a mechanical piston, pushing the air up and out of the cryostat. This gas, initially all air, is vented to the outside atmosphere. The venting stage continues for 32 hours, approximately the equivalent of 12 volume changes. Figure 7.5 graphically shows step 1 of the purification process, removal of the ambient air. The initial state,  $t = 0$ , reflects the initial values for oxygen, water and nitrogen in the “dry air” state. This is followed by the Piston Purge. These measurements are made by a variety of monitors that sample the gas in the cryostat.

After the purge, the exiting argon gas is re-routed to circulate through the filtration system that removes  $O_2$  and  $H_2O$ . ( $N_2$  is not materially removed by the filters.) Any leaks to the outside atmosphere can be detected during this step. As shown in “Debugging” gap in Figure 7.5, a leak was found and mitigated. Once leaks have been eliminated the recirculation continues until the  $O_2$  level drops to the sub-ppm level. As can be seen in the plot, the  $H_2O$  level plateaus at a much higher level than  $O_2$ . This is due to the outgassing of materials inside the 35t, including the cryostat walls, which remain at room temperature throughout the recirculation step.

## Cooldown and LAr Fill

A gas/liquid spray method is used to cool down the cryostat. This generates a turbulent mixing of cold gas in the cryostat and cools the entire surface. The cooldown rate was maintained lower (slower) than the maximum rate specified by the membrane cryostat manufacturer. The cooldown, as well as the initial fill, is shown in

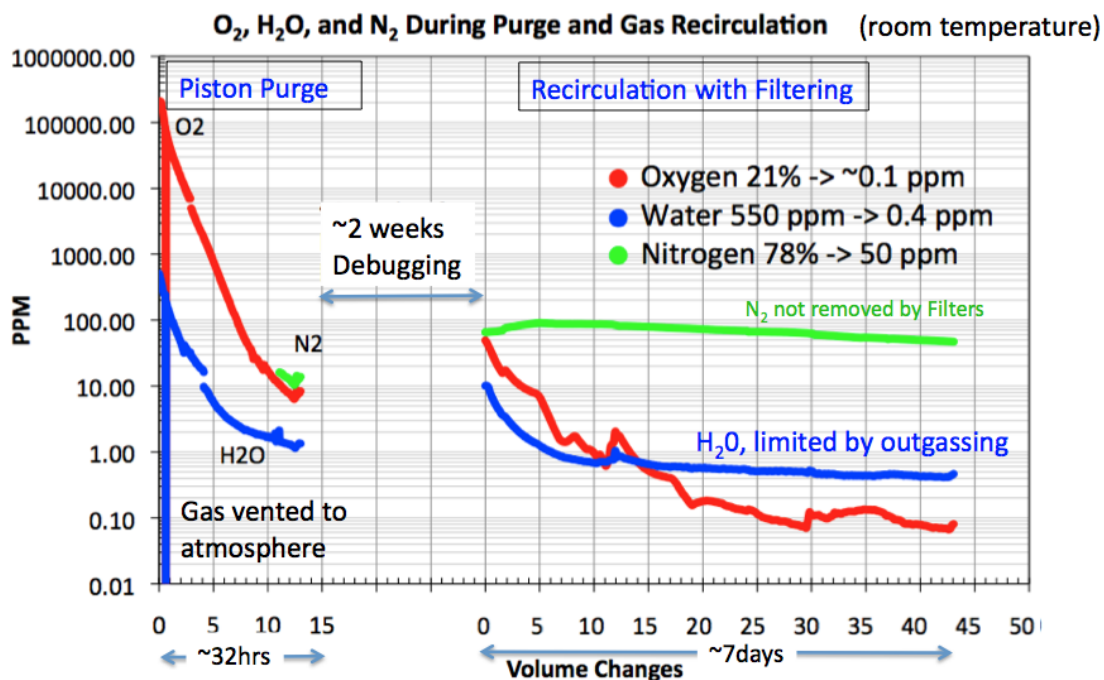


Figure 7.5: Gas phase of removing impurities in the 35t. These quantities are being measured by various gas analyzers. The first stage of the purification is a process called the “Piston Purge”. The second stage is “Recirculation with Filtering”. The gap between the two steps was due to troubleshooting a leak.

fig:35TPurge

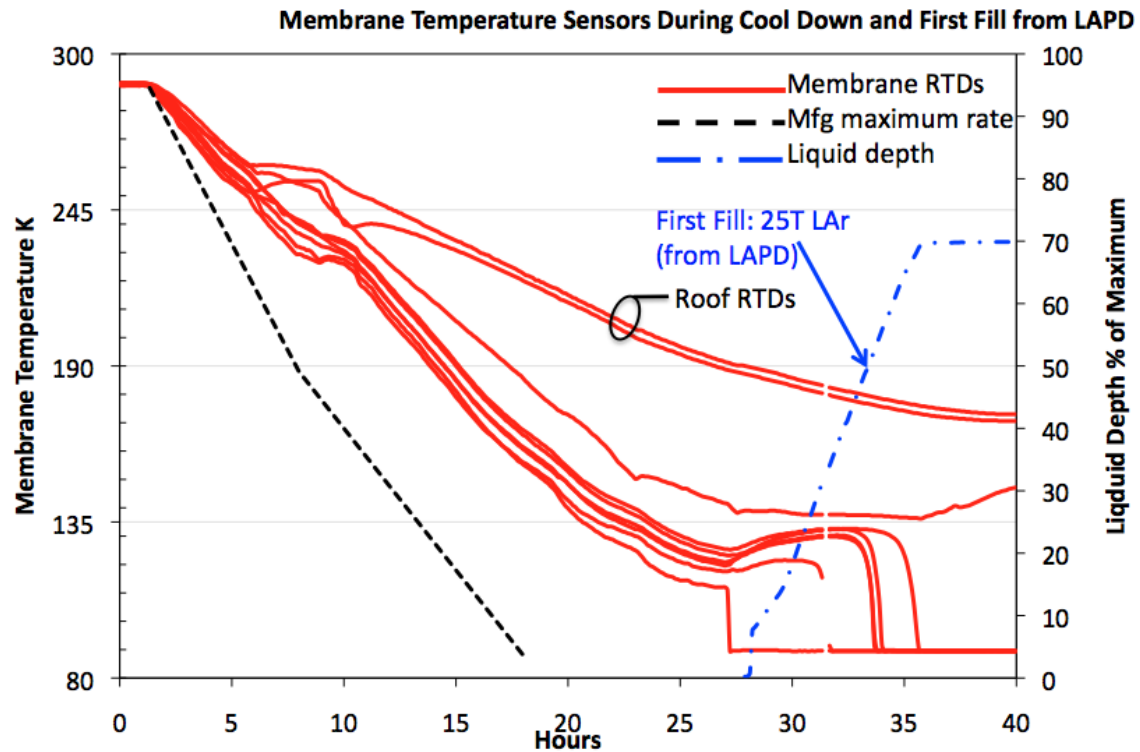


Figure 7.6: Cooldown and filling the 35t. The measurements (red trace) are made from RTDs afixed to the cryostat walls. The black dashed curve is the manufacturer's maximum allowed cooldown rate. The filling (blue trace) was from the transfer of LAr from LAPD. This quantity of LAr is less than the capacity of the 35t. The RTD traces drop to the LAr temperature when the level of the LAr covers reaches their mounting height.

fig:35TCooldown

Figure 7.6. The temperature measurements (red traces) in this plot were made by RTDs that are glued to the membrane walls of the cryostat. The black dashed trace is the manufacturer specification for the cooldown rate.

Once the cooldown was complete, the LAr transfer into the cryostat began. In this case the LAr came from LAPD, where it had been used by that system in its own recently completed second run[35].

LAPD contained about 30 tons of LAr, of which only 25 tons could be transferred to the 35t providing a  $\sim 70\%$  fill. It was decided to begin the initial commissioning of the Phase 1 run at this point since several components of the 35t could be commissioned at this fill level. After running with the partial fill for approximately eighteen days, additional LAr was added to bring the capacity to 100%, the full 35 tons.

## LAr Purification

The Fermilab Material Test System (MTS)[37, 38] (see Section 7.2) has shown that contaminants released inside LAr-filled cryostats come from materials outgassing in the warm ullage regions above the LAr surface. Typically, detector materials submersed in LAr have negligible impact on LAr purity levels.

Figure 7.7 depicts how impurities generated by outgassing materials in the relatively warm ullage under Plate B are swept up by the normal Ar boil-off in the 35t. This impure vapor is condensed in the LN<sub>2</sub>-cooled LAr condensor. The impure condensate is returned to the 35t just inside the intake manifold of the interior submersible LAr pump. From there it is pumped to the filtration system where the impurities are removed.

It is worth noting that the purity, in terms of electron lifetime, of the LAr exiting the filters, as measured by the inline PrM was always  $> 30$  ms (corresponding to a purity  $\sim 10$  ppt O<sub>2</sub> equivalent). This indicates that the filters are very efficient at removing all trace amounts of O<sub>2</sub> and H<sub>2</sub>O. This was true for the entire 35t phase 1 run, including the filling periods.

Figure 7.8 plots the electron lifetime from the start of the LAr Pump operation until the end of the Phase 1 run. In general, the electron lifetime improved as a function of pump “on-time,” but a few incidents, shown on the plot, impacted the lifetime. These will be discussed in the next section.

### 7.4.4 Phase 1 Stability of Operation

The goals of the 35t Phase 1 run included not only achieving the required purity/lifetime levels, but to also hold those levels and demonstrate a stable operation of

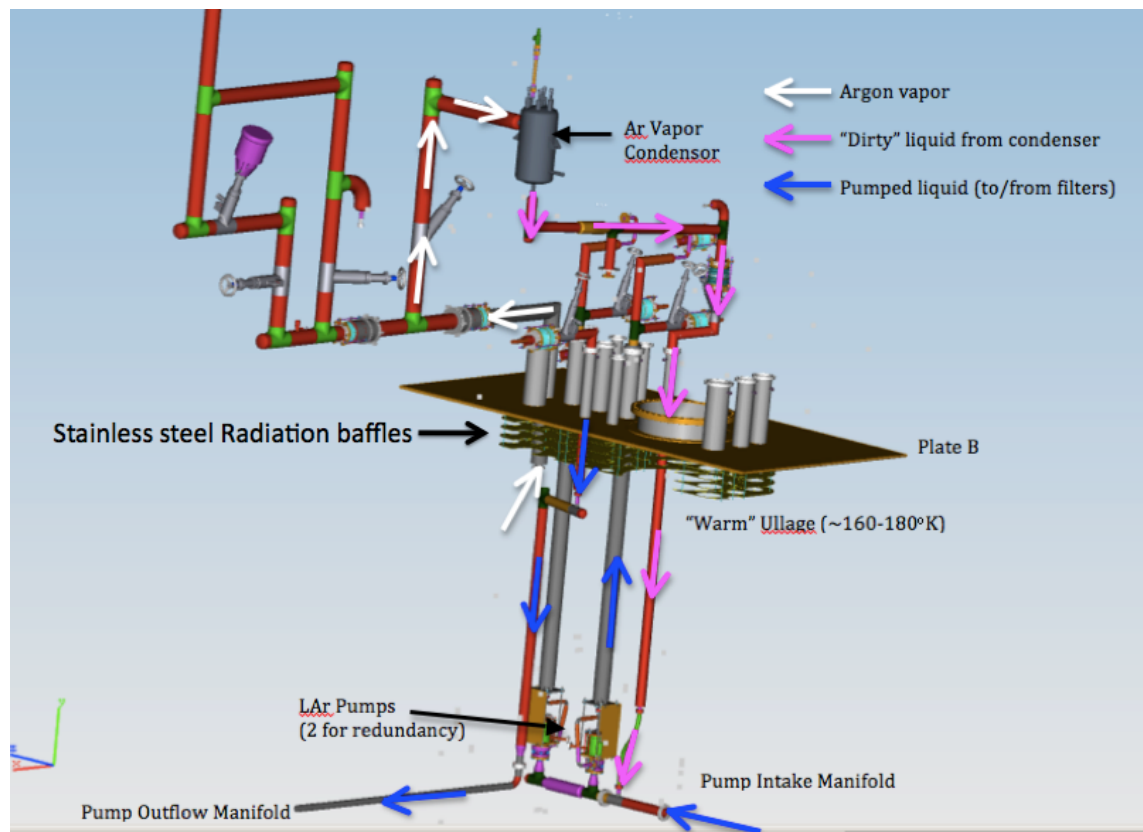


Figure 7.7: Drawing of Boiloff/Outgassing Vapor Flow (white arrows) from the 35t cryostat, with condensate return (violet arrows) from the condensor into the Pump Intake Manifold. LAr flow into the pump, and return from the Purification filters are shown by blue arrows. Also shown is the location of the Stainless Steel Radiation baffles beneath Plate B. This location just beneath Plate B is the warmest location and presumably the principal source of outgassing within the cryostat.

fig:35TVaporFl

the cryostat. The 35t Phase 1 LAr run lasted a relatively short  $\sim 2$  months. Electron lifetimes in the 2-3 ms range were achieved, as can be seen in Figure 7.8.

The electron lifetimes were severely impacted, however, whenever one LAr pump would switch to another. The drops in purity coincided with the turn on of the previously-inactive pump (see annotations in Figure 7.8). The issue is believed to lie with the procedure used to start the pumps; it will be modified for future operations in the 35t Phase 2 run.

A second stability question is keeping the temperature stable in the cryostat. Currently the 35t controls system regulates the gauge pressure of the cryostat, keeping the internal pressure to 6.69(02) kPa above ambient atmospheric pressure. However this leaves the thermodynamics of the LAr sensitive to normal atmospheric pressure changes.

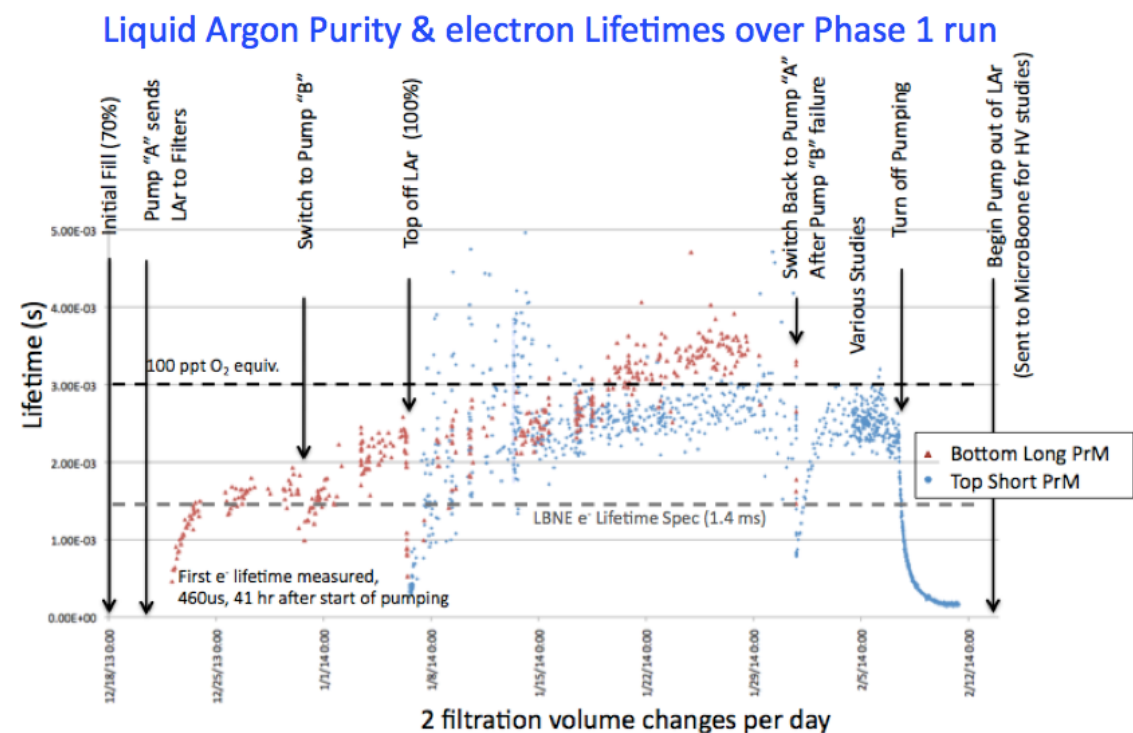


Figure 7.8: LAr electron lifetimes as measured by Cryostat Purity Monitors. Significant events are annotated on the plot. Major divisions on horizontal axis are one week periods. Equivalent purity levels are shown as dashed horizontal lines.

Figure 7.9 shows a plot over a nine-day period of the cryostat absolute pres-

sure (blue trace), bulk LAr temperature (white dashed trace) and the normalized drift time of three PrMs, one short and one long inside the cryostat, and the long inline PrM exterior to the cryostat. The temperature is obtained from resistive temperature detectors (RTDs) which make high-precision measurements. Although the temperature curve lags the pressure changes ( $\Delta P \sim 3.5$  kPa over this period) due to the thermal inertia of the LAr, the normalized drift time (= drift time/(average drift time for this period)) is directly correlated to the LAr temperature. The LAr temperature excursion range was  $\Delta T \sim 0.3$  K. Fitting the normalized drift velocity (inverse of normalized drift time) gives the result

$$\Delta_{\text{driftspeed}/\overline{\text{driftspeed}}} = -0.022/1 \text{ K}$$

The electron drift velocities for these three PrMs varied from (0.3 to 0.4) mm/ $\mu$ s depending on the individual PrM's drift field.

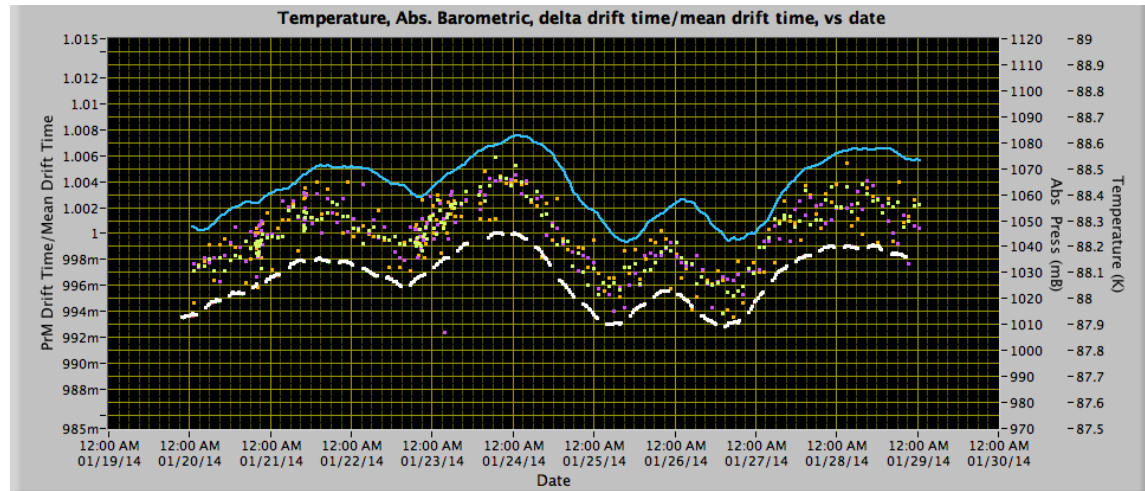


Figure 7.9: Interior Cryostat Absolute Pressure (blue trace), bulk LAr temperature (white dashed trace), and PrM drift times (dots) over a nine-day period. Major divisions on horizontal axis are one day intervals. The PrM drift times are from three PrMs, two in the cryostat, and the third from the inline PrM. The lag between the temperature and pressure is due to the thermal inertia of the LAr.

fig:35TTempSta

The RTD Spooler was intended to provide a precision measurement of the vertical temperature profile. This measurement is a means of testing the Computational Fluid Dynamics Simulations [39] that are being made on the fluid motion in the cryostat. Experimentally measuring the actual motion does not appear to be feasible

at this time. The CFD calculations are being used to understand whether there might be dead areas in the cryostat where impurities might collect. Figure 7.10 shows the result of one RTD scan. This scan was taken from a period where the barometric pressure was relatively constant so that the temperature would remain constant during the scan. Since a scan takes up to 6 hours in one direction (up or down) and as can be seen in Figure 7.9, pressure changes can impact the bulk temperature of the LAr. These profiles seen in Figure 7.10 are in nominal agreement with the current CFD calculations in [39].

### 7.4.5 Phase 1 Conclusions

The 35t Phase 1 run has shown that the membrane cryostat technology has no innate difficulties with achieving the stated goals of the LBNE Conceptual Design Far Detector. Some of the 35t issues (e.g., loss of purity when pumps are switched) are most likely unique to the 35t. It also seems likely that in a future design, the pumps will be externally located, to avoid coupling acoustical vibrations into the Far Detector cryostat and to facilitate maintenance and repair.

## 7.5 35t Prototype Phase 2

Phase 2 of the the 35t prototype involves installing a fully operational TPC and photon detector into the previously built cryostat. The prototype will be filled with liquid argon and operated for a several-month-long cosmic ray run. External plastic scintillator paddles placed around the cryostat will be used to produce trigger signals as well as rough position measurements of the incoming cosmic rays. Installation of the TPC into the cryostat is expected in April 2015 and commissioning is expected to begin in June 2015. Figure 7.11 shows a model of the TPC inside the cryostat and a trial assembly of the TPC done outside of the cryostat.

### 7.5.1 35t Phase 2 TPC Design

The Phase 2 prototype incorporates many of the design elements described in previous sections of this document. In many cases, these include novel features that have never previously been tested in an operational TPC. Rather than reiterate them all here, some of the more important aspects are collected in Table 7.2.



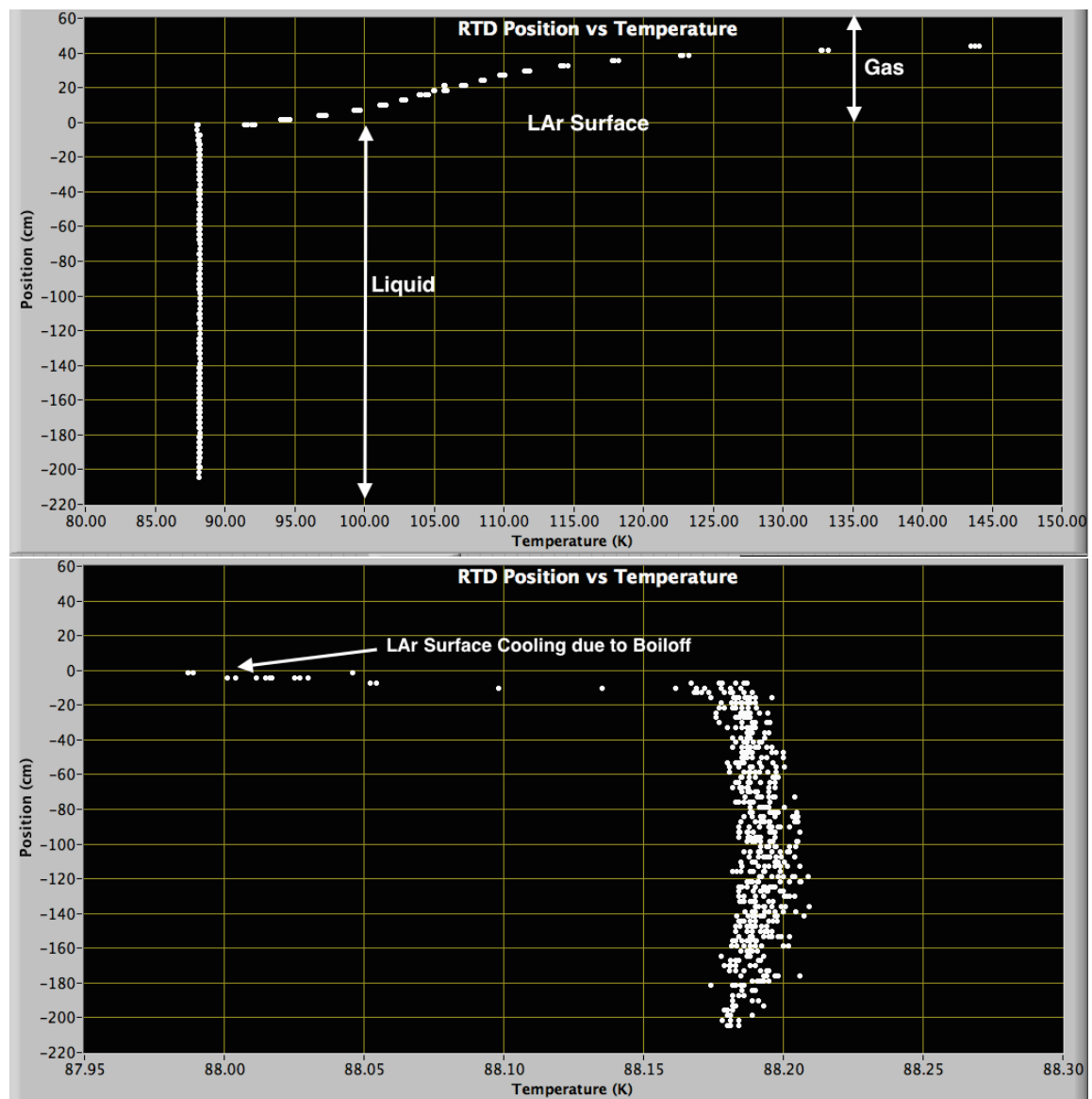


Figure 7.10: (top) RTD Spooler Vertical Temperature scan of the 35t Cryostat under Plate B showing both the liquid and vapor temperature. (bottom) Expanded horizontal axis around 88.12 K. Note that the horizontal divisions on the lower plot are 50 mK.

fig:SpoolerSca

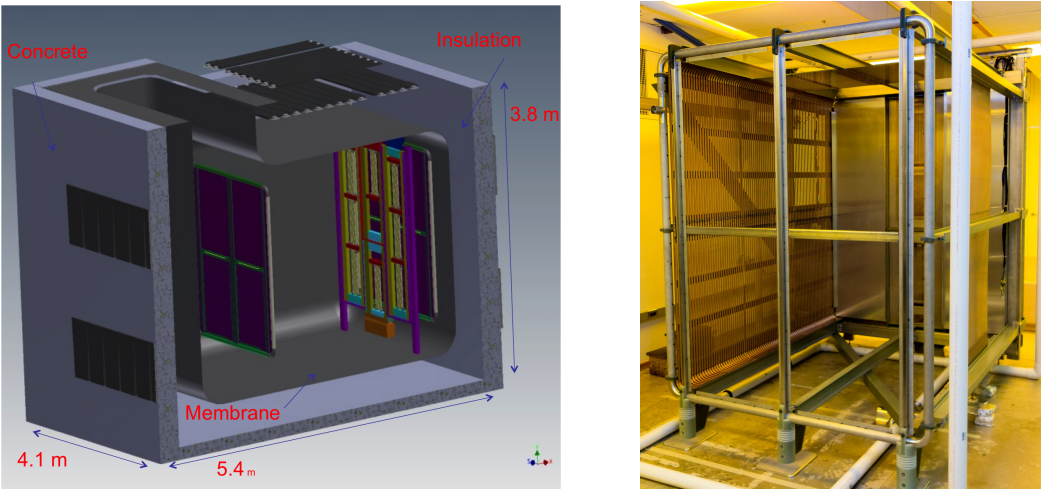


Figure 7.11: (left) 35t Cryostat with TPC and photon detectors installed. Note separate drift regions on “near” and “far” sides. The near side drift length is close to what is proposed for the far detector. The far side has a shorter drift length due to lack of space. (right) A trial assembly of the TPC.

fig:35TTPC

Table 7.2: 35t Design Elements

Design Aspect	Section	How Tested
Modular APAs with wrapped wires	2.3	Build small-scale APA Modules with FD design
Vertical Gaps between APAs	2.3	Assemble APAs side-by-side. Study reco'd tracks that cross the gaps.
Horizontal Gaps between APAs	2.3	Build two shorter APAs and stack vertically Study reco'd tracks that cross the gaps
APAs immersed in active volume	2.3	Study reco'd tracks that cross APAs
Cold Digital Electronics	3.4.2	Measure noise performance etc. <i>in situ</i>
Waveguide-style Photon Detector	3.4.2	Install in APAs. Measure lightyield
Triggerless-capable DAQ	4.1	Take data using multiple DAQ modes

tab:35TDesign

## 7.5.2 Phase 2 Simulation, Reconstruction and Analysis

As can be seen from Table 7.2, successful tests of many of the new design features requires simulation, reconstruction and analysis of 35t data. This will be done with the help of the LarSoft package, which is also used to simulate and reconstruct data from the ArgoNeuT and MicroBoone experiments. Reuse of software developed for those experiments can greatly facilitate 35t development. However, the novel hardware features of the 35t prototype necessitate new software developments as well. Among the required new software developments are:

- Code to break up the wrapped wires into as many as five individual linear segments. A hit on a single electronic channel can, in principle, be related to an induced signal on any of these segments.
- “Disambiguation” code to identify which of the possible wire segments was actually responsible for the observed hit
- Code for determining the start time of the event ( $t_0$ ). Since the 35t prototype DAQ can run “triggerless,” methods are needed for finding the  $t_0$  in data. Information from the external scintillator paddles as well as the internal photon detectors can be used.
- Code for “stitching” together track segments observed in different tracking volumes. Since hits can come from either side of the four APAs, there are effectively eight separate tracking volumes, which are treated as separate TPCs.

With these simulation and reconstruction tools in hand, “physics” analysis of the data can be undertaken. In addition to the analyses needed to validate the new detector design elements, there are also some analyses of basic LArTPC performance that are needed as well. Among the highest priority analysis tasks are:

- Basic detector performance: signal/noise, purity measured with tracks, track direction resolution, photon detector light yield
- Measurement of distortions due to space charge and field non-uniformity
- Measurements of different types of particles: muons, protons, neutrons, pions

The results obtained by operating the 35t Phase 2 prototype and the analysis of its data are expected to be very valuable in defining the final far detector design.

## 7.6 Prototype Detector at CERN to Test Physics Sensitivity

The physics sensitivity of LBNE has been estimated based on detector-performance characteristics published in the literature, simulation-based estimates and on a variety of assumptions about the anticipated performance of the future detector, event reconstruction and particle-identification algorithms. A single-phase LAr prototype detector has been proposed for testing in a CERN beam with the goal of replacing these assumptions with measurements. The prototype will implement a full-scale detector element; this will mitigate the risks associated with extrapolating from small-scale versions of the single-phase LAr TPC technology and allow benchmarking of the operation of full-scale detector elements in a well-characterized charged-particle beam.

The detector will need to accurately identify and measure the energy of the particles produced in the neutrino interaction with argon, which will range from hundreds of MeV to several GeV. The beam measurements will serve as a calibration data set to tune the Monte Carlo simulations and serve as a reference data set for the detector.

The prototype is expected to identify any potentially problematic components and lead to future improvements and optimizations of the detector design.

## 7.7 Summary

Impressive progress has been made in the development of LArTPC technology over the last few years. All elements of the development program have completed the R&D phase. Credible conceptual designs exist for all systems in LAr-FD. The technical activities described in this chapter are properly characterized as preliminary engineering design.

The most significant deficiency is the lack of fully-automated event reconstruction. Algorithms have been developed within the LAr community and are being successfully applied to ArgoNeuT data as well as to simulated MicroBooNE data. The algorithms have individually shown that the high efficiency and excellent background rejection capabilities of a LArTPC are achievable. The task remains to combine them into a single package.

# Bibliography

- [1] S. Amerio *et al.*, “Design, construction and tests of the ICARUS T600 detector,” *Nucl. Instrum. Meth. A*, no. 527, 329, 2004.
- [2] <http://t962.fnal.gov/>.
- [3] <http://www-microboone.fnal.gov/>.
- [4] LBNE LAr-FD L2 Project, “LAr-FD Requirements spreadsheets.” LBNE Doc 3747.
- [5] “The long-baseline neutrino experiment: Exploring fundamental symmetries of the universe.” arXiv:1307.7335.
- [6] M. Bass *et al.*, “Baseline optimization for the measurement of CP violation, mass hierarchy, and  $\theta_{23}$  octant in a long-baseline neutrino oscillation experiment,” *Phys.Rev.*, vol. D91, no. 5, p. 052015, 2015.
- [7] K. Scholberg *et al.*, “Far detector requirements documents.” LBNE DocDB 8741, 2014.
- [8] T. Junk *et al.*, “Wire angle change request.” LBNE DocDB 9374, 2014.
- [9] R. Rucinski *et al.*, “Fd technical board meeting on wire angle change from 45 to 36 degrees.” LBNE DocDB 8981, 2015.
- [10] L. Greenler *et al.*, “Fd technical board meeting: Anode plane assembly length change (trade study).” LBNE DocDB 9886, 2015.
- [11] B. Baller, “TPC Wire Angle Optimization.” LBNE Doc 2836, 2010.
- [12] B. Norris *et al.*, “Lbnf cryogenics infrastructure reference design.” LBNE DocDB 10719, 2015.

- [13] MicroBooNE Collaboration, “The MicroBooNE Conceptual Design Report.” <http://microboone-docdb.fnal.gov/cgi-bin/ShowDocument?docid=1821>, 2010.
- [14] H. Jostlein, “Be-Cu wire properties and recent epoxy wire holding tests,” tech. rep., FNAL, 2011. LBNE:DocDB-3657.
- [15] G. De Geronimo *et al.*, “Front-end ASIC for a Si Compton telescope,” *IEEE Trans. Nucl. Sci.*, vol. 55, no. 4, 2008.
- [16] IEEE The International Conference on Dependable Systems and Networks (DSN-04), *The impact of technology scaling on lifetime reliability*, June 2004.
- [17] M. A. Alam and S. Mahapatra, “A comprehensive model of PMOS NBTI degradation,” *Microelectronics Reliability*, vol. 45, no. 1, pp. 71–81, 2005.
- [18] IEEE International Semiconductor Device Research Symposium, *CMOS device reliability for emerging cryogenic space electronics applications*, 2005.
- [19] D. Axen *et al.*, “Signal feedthroughs for the ATLAS barrel and endcap calorimeters,” *Rev. Sci. Instrum.*, vol. 76, p. 063306, 2005.
- [20] NOvA Collaboration, “The NOvA Experiment Technical Design Report.” <http://lss.fnal.gov/archive/design/fermilab-design-2007-01.pdf>, 2007.
- [21] K. S. Beattie and D. Glowacki, “Searching for Neutrinos Using Python at the Bottom of the World,” in *PyCon 2009*, 2009. <http://us.pycon.org/2009/conference/schedule/event/19/>.
- [22] E. Grace and J. A. Nikkel, “Index of refraction, rayleigh scattering length, and sellmeier coefficients in solid and liquid argon and xenon.” ArXiv: 1502.04213, 2015.
- [23] A. Himmel, “Transmission vs. angle.” LBNE DocDB 7599-v2, 2013.
- [24] V. Gehman *et al.*, “Fluorescence efficiency and visible re-emission spectrum of tetraphenyl butadiene films at extreme ultraviolet wavelengths,” *Nucl. Instrum. Meth. A*, vol. 654, p. 116, 2011.
- [25] L. Bugel *et al.*, “Demonstration of a lightguide detector for liquid argon TPCs,” *Nucl. Instrum. & Meth.*, vol. A640, p. 69, 2011.

- [26] B. Baptista and S. Mufson, "Comparison of TPB and bis-MSB as VUV waveshifters in prototype LBNE photon detector paddles," *JINST*, vol. 8, p. C09006, 2013.
- [27] S. Mufson and B. Baptista, "Light guide production for LBNE and the effects of UV exposure on VUV waveshifter efficiency," *JINST*, vol. 8, p. C09012, 2013.
- [28] B. Baller *et al.*, "Liquid Argon Time Projection Chamber research and development in the United States," *J. Inst.*, vol. 9, p. T05005, 2014.
- [29] P. K. Lightfoot *et al.*, "Readout electronics for the central drift chamber of the belle ii detector," *IEEE (NSS/MIC)*, vol. 10, pp. 694-698, 2011.
- [30] L. Bagby *et al.*, "Lbne far detector electrical grounding." LBNE DocDB 7310, 2014.
- [31] A. Blatter *et al.*, "Experimental study of electric breakdowns in liquid argon at centimeter scale." arXiv:1401.6693.
- [32] B. Acciarri *et al.*, "Liquid argon dielectric breakdown studies with the micro-boone purification system." arXiv:1408.0264.
- [33] J. Stewart *et al.*, "Far detector research and engineering development plan." LBNE DocDB 10006, 2014.
- [34] B. Yu *et al.*, "Ve-fd-025 place apa or short drift cell nearest wall." LBNE DocDB 8920, 2014.
- [35] M. Adamowski *et al.*, "The liquid argon purity demonstrator," *JINST*, vol. 9, p. P07005, July 2014.
- [36] Cryogenic Engineering Conference: Advances in Cryogenic Engineering, *First Scientific Application of the Membrane Cryostat Technology*, 2014.
- [37] E. Voiron *et al.*, "35 ton cryostat liquid argon flow, temperature, and charge density cfd simulation." LBNE DocDB 9940-v1, November 2014.
- [38] B. Rebel *et al.*, "Results from the fermilab material test stand and status of the liquid argon purity demonstrator," *Journal of Physics: Conference Series*, vol. 308, 2011.
- [39] E. Voirin *et al.*, "35 ton cryostat - liquid argon flow, temperature, and charge density cfd simulation." LBNE DocDB 9940, 2015.